UNIVERSITÉ DU QUÉBEC À TROIS-RIVIÈRES

MODELING THE MICROSTRUCTURE OF A HETEROGENEOUS PARTICLE-BASED MATERIAL WITH HIGH-VOLUME FRACTION

THÈSE PRÉSENTÉE

COMME EXIGENCE PARTIELLE DU DOCTORAT EN INGÉNIERIE

PAR

GHAZAL AFSHAR

MAI 2025

UNIVERSITÉ DU QUÉBEC À TROIS-RIVIÈRES

DOCTORAT EN INGÉNIERIE (Concentration génie mécanique) (PH. D.)

Direction de recherche :

M. Jean-Christophe CUILLIÈRE, directeur de recherche

Département de génie mécanique, Université du Québec à Trois-Rivières

M. Vincent FRANÇOIS, codirecteur de recherche

Département de génie mécanique, Université du Québec à Trois-Rivières

M. Adrien COUTURE, co-superviseur de thèse

Professionnel Technique Senior, Cascades Inc.

Jury d'évaluation

Mohamed HABIBI Département de génie mécanique, Université du Québec à Trois-Rivières	Président du jury
Jean-Christophe CUILLIÈRE Département de génie mécanique, Université du Québec à Trois-Rivières	Directeur de thèse
Vincent FRANÇOIS Département de génie mécanique, Université du Québec à Trois-Rivières	Co-directeur de thèse
Lotfi TOUBAL Département de génie mécanique, Université du Québec à Trois-Rivières	Évaluateur interne
Marie-Laure DANO Département de génie mécanique et de génie industriel, Université Laval	Évaluatrice externe

Thèse soutenue le 29 août 2025

To my dear parents

and

To my beloved Ali

ACKNOWLEDGEMENTS

First and foremost, I would like to express my deepest gratitude to my supervisors, Professor Jean-Christophe Cuillière and Professor Vincent François, for their unwavering support, invaluable guidance, and the time and energy they have devoted throughout my research journey. Their expertise, encouragement, and constructive feedback were instrumental in shaping the direction of this work and helping me overcome numerous challenges along the way.

I would also like to extend my sincere thanks to Dr. Adrien Couture for his generous and selfless support. His willingness to share his knowledge, provide technical insights, and contribute directly to the advancement of my project has been truly exceptional. Adrien's input was not only technically valuable but also motivating, and I am sincerely grateful for his collaboration and kindness throughout this endeavor.

A very special thank you goes to my husband, Ali for his continuous support, patience, and encouragement during these years. His understanding and love were essential to the completion of this work, and I am deeply grateful for his presence by my side throughout this journey.

This work would not have been possible without the support and contributions of all these individuals, and I feel truly fortunate to have had them accompany me in this important chapter of my life.

RÉSUMÉ

Les composites à base de particules ont suscité un intérêt croissant dans les applications d'ingénierie en raison de leur capacité à améliorer les propriétés mécaniques, thermiques et fonctionnelles grâce à l'inclusion contrôlée de particules de renforcement. La prédiction précise des propriétés mécaniques effectives de ces composites est essentielle pour optimiser leurs performances et leur conception. L'homogénéisation numérique, en particulier l'utilisation de la Méthode des Éléments Finis (MEF), constitue un outil puissant pour estimer ces propriétés en analysant des Volumes Élémentaires Statistique (VES). Cependant, les approches de modélisation traditionnelles rencontrent souvent des défis pour atteindre des fractions volumiques élevées de particules tout en maintenant une efficacité et une précision computationnelle optimales.

Les recherches précédentes menées par notre équipe (ERICCA) ont abouti au développement d'une approche de modélisation numérique automatisée intégrant la Conception Assistée par Ordinateur (CAO), le maillage et l'analyse par éléments finis afin de faciliter la génération et l'évaluation des VES. Cette méthode présente une technique d'érosion des résultats, qui supprime les résultats situés près des bords du VES pour compenser la présence de vides et garantir une distribution uniforme des particules. Bien que cette approche ait permis d'atteindre des fractions volumiques élevées, elle soulève des préoccupations quant à la suppression de données computationnelles et son impact sur la précision des résultats.

Pour surmonter ces préoccupations, cette étude propose deux nouvelles méthodologies, la Méthode de Correction Géométrique (MCG) et la Méthode de Découpe du Maillage (MCM), visant à obtenir de fortes fractions volumiques sans recourir à la technique d'érosion des résultats. La MCG modifie les positions et caractéristiques géométriques des particules afin de maximiser la fraction volumique tout en assurant la cohérence géométrique, tandis que la MCM découpe directement la structure du maillage pour adapter la taille du VES à partir d'un domaine de génération plus grand et pour intégrer des particules à rapport d'aspect élevé. L'analyse comparative montre que la MCM atteint efficacement la fraction volumique souhaitée tout en préservant la précision computationnelle, tandis que la MCG, bien que performante, ne permet pas d'éliminer complètement les vides aux frontières. Néanmoins, ces deux méthodes peuvent être combinées pour améliorer les performances globales du modèle.

Les résultats obtenus avec ces méthodes sont validés en les comparant à la méthode d'érosion des résultats précédemment utilisée, démontrant une forte correspondance dans la prédiction des propriétés élastiques. De plus, la MCM est appliquée à un composite renforcé par des fibres naturelles très allongées, et ses prédictions numériques sont confrontées à des données expérimentales. Les résultats confirment la validité de cette méthode pour représenter précisément la réponse mécanique de ces matériaux. En outre, un ensemble de fibres de plus faible allongement est également modélisé afin d'analyser l'influence du rapport d'aspect sur les propriétés élastiques du composite.

Cette recherche constitue une avancée significative dans la modélisation numérique automatisée des composites à base de particules en supprimant le recours aux ajustements basés sur l’érosion des résultats, tout en maintenant une grande précision dans la prédiction de la fraction volumique et des propriétés mécaniques. Les méthodologies proposées offrent un cadre fiable pour les études futures sur la modélisation microstructurale et l'optimisation des matériaux composites avancés.

ABSTRACT

Particle-based composites have gained significant attention in engineering applications due to their ability to enhance mechanical, thermal, and functional properties through the controlled inclusion of reinforcement particles. Accurately predicting the effective mechanical properties of these composites is essential for optimizing their performance and design. Numerical homogenization, particularly using the Finite Element Method (FEM), provides a powerful tool for estimating these properties by analyzing Statistical Volume Elements (SVEs). However, traditional modeling approaches often face challenges in achieving high particle volume fractions while maintaining computational efficiency and accuracy.

Previous research by our team (ERICCA) developed an automated numerical modeling approach that integrates Computer-Aided Design (CAD), meshing, and Finite Element Analysis (FEA) to streamline the generation and evaluation of SVEs. This method presents an erosion of results technique, which removes results of elements near the edges of the SVE to compensate for voids and ensure a uniform particle distribution. While effective in achieving high volume fractions, this approach raises concerns about the removal of computational data and its impact on accuracy.

To address these concerns, this study introduces two novel methodologies, the Geometry Correction Method (GCM) and the Mesh Cutting Method (MCM), designed to achieve high particle volume fractions without relying on the erosion of results technique. The GCM modifies particle positions and geometrical characterisations to maximize

volume fraction while maintaining geometric consistency, whereas the MCM directly cuts the mesh structure to reach the dimension of SVE from a bigger generational domain and accommodate high-aspect-ratio particles within the SVE. Comparative analysis shows that the MCM successfully achieves the desired volume fraction while preserving computational accuracy, whereas the GCM, though effective, falls short in fully eliminating boundary voids. Nonetheless, these two methods can be integrated for enhanced performance.

The results of these methods are validated by comparison with the previously used erosion of results approach, demonstrating strong agreement in the predicted elastic properties. Furthermore, the MCM is applied to a natural fiber-reinforced composite containing highly elongated fibers, with its numerical predictions compared against experimental data. The results confirm the validity of the method in accurately capturing the mechanical response of these materials. Additionally, a range of lower fiber elongations is modeled to evaluate the influence of aspect ratio on the composite's elastic properties.

This research presents a significant advancement in automated numerical modeling of particle-based composites by eliminating the need for erosion-based adjustments while maintaining high accuracy in volume fraction and material property predictions. The proposed methodologies provide a reliable framework for future studies on microstructural modeling and optimization of advanced composite materials.

TABLE OF CONTENTS

LIST OF TABLES

LIST OF FIGURES

LIST OF ALGORITHMS

NOMENCLATURE AND ACRONYMS

MATHEMATICAL NOTATIONS

A	Scalar
$\underline{A}$	Vector (A_i)
$\underline{\underline{A}}$	Second-order tensor (A_{ij})
$\mathbb{A}$	Fourth-order tensor (A_{ijkl})
δ_{ij}	Kronecker delta
μ_{ijk}	Permutation tensor
$\times$	Cross product ($\mu_{ijk}\underline{a}_i\underline{b}_j$)
$\otimes$	Tensor product ($\underline{a}_i\underline{b}_j$)
$\cdot$	Single contraction of tensor product ($\underline{a}_i\underline{b}_i$)
:	Double contraction of tensor product ($\underline{a}_{ij}\underline{b}_{ij}$)
$Tr(\underline{\underline{a}})$	Tensor trace (a_{ii})
$div(\underline{\underline{a}})$	Divergence of a tensor ($\underline{\underline{a}}_{ij,i}$)
$==$	Equality comparison operator
$\cup$	Boolean union operation
$\cap$	Boolean intersection operation
$\pm$	Standard deviation
$\langle A \rangle_V$	Average of field A over volume V

THERMAL NOTATIONS

T	Temperature field

$\underline{\phi}$	Heat flux vector at the mesoscale
$\underline{\Phi}$	Heat flux vector at the macroscale
$\underline{g}$	Temperature gradient vector at the mesoscale
$\underline{G}$	Temperature gradient vector at the macroscale
λ	Thermal conductivity
$\underline{\underline{\Lambda}}$	Thermal conductivity tensor

MECHANICAL NOTATIONS

$\underline{x}$	Coordinate vector
$\underline{u}$	Displacement vector
$\underline{\underline{\mathcal{E}}}$	Strain tensor at the mesoscale
$\underline{\underline{E}}$	Strain tensor at the macroscale
$\underline{\underline{\sigma}}$	Stress tensor at the mesoscale
$\underline{\underline{\Sigma}}$	Stress tensor at the macroscale
$\mathbb{C}$	Stiffness tensor
$\mathbb{S}$	Compliance tensor
K	Bulk modulus (compressibility modulus)
G	Shear modulus
E	Young's modulus
υ	Poisson's ratio

MICROSTRUCTURE NOTATIONS

$\mathcal{M}$	Matrix

$\mathcal{P}$	Particle
$\mathcal{C}$	Constituent
f_{vol}	Volume fraction
Ω_{SVE}	SVE domain
$\underline{p}$	Orientation vector
$\underline{\underline{a_2}}$	Orientation tensor
d_e	Erosion distance

LIST OF ACRONYMS

PMC	Polymer Matrix Composite
MMC	Metal Matrix Composite
CMC	Ceramic Matrix Composite
NFRC	Natural Fiber-Reinforced Composite
FEM	Finite Element Method
CAD	Computer-Aided Design
SVE	Statistical Volume Element
FEA	Finite Element Analysis
MBD	Multi-Body Dynamics
BVP	Boundary Value Problem
RVE	Representative Volume Element
FDM	Finite Difference Method
FVM	Finite Volume Method
FFT	Fast Fourier Transform
CT	Computed Tomography
RSA	Random Sequential Adsorption
RDSF	Randomly Distributed Short cylindrical Fiber
TRDSF	Transversely Randomly Distributed Short cylindrical Fiber

SEM	Scanning Electron Microscopy
UTM	Unified Topology Model
BREP	Boundary REPresentation
CAE	Computer-Aided Engineering
OOP	Object-Oriented Programming
GCM	Geometry Correction Method
MCM	Mesh Cutting Method
SUBC	Static Uniform Boundary Condition
KUBC	Kinematic Uniform Boundary Condition

CHAPTER 1

INTRODUCTION

1.1- Background and motivation

The advancement of composite materials has led to significant developments in various engineering fields, particularly in aerospace, automotive, and biomedical industries. The continuous advancements in composite material production and the rapid evolution of technology highlight their significant advantages, including high strength-to-weight ratio, durability, and versatility.

Composite materials are multiphase materials composed of a discontinuous reinforcement phase embedded within a continuous matrix phase. The matrix phase can be metallic, ceramic, or polymeric, while the reinforcement phase can take the form of synthetic fibers (e.g., glass, carbon, aramid), natural fibers (e.g., sisal, ramie, jute, cotton, kenaf, pineapple), or particles (e.g., clay, mica, tungsten carbide, titanium carbide). Based on their matrix material, composites are categorized into three main types: Polymer Matrix

Composites (PMCs), Metal Matrix Composites (MMCs), and Ceramic Matrix Composites (CMCs) (Figure 1-1).

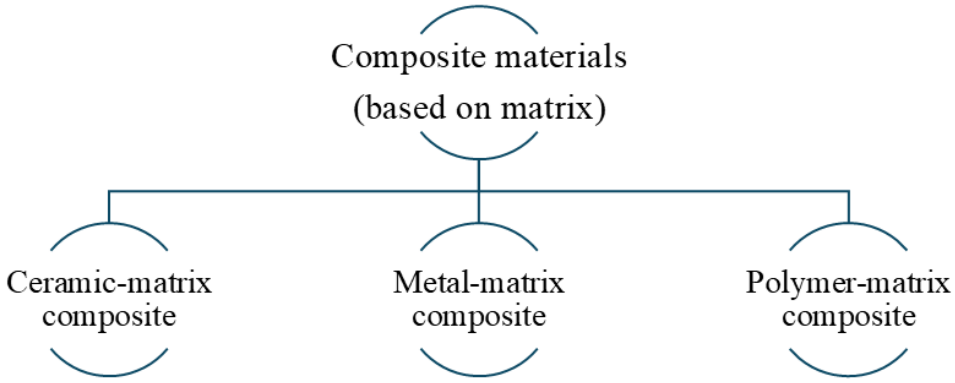

Figure 1-1. Classification of composite materials based on matrix.

Additionally, depending on the reinforcement type, composites can be classified into particulate composites, fiber-reinforced composites, and structural composites (Figure 1-2).

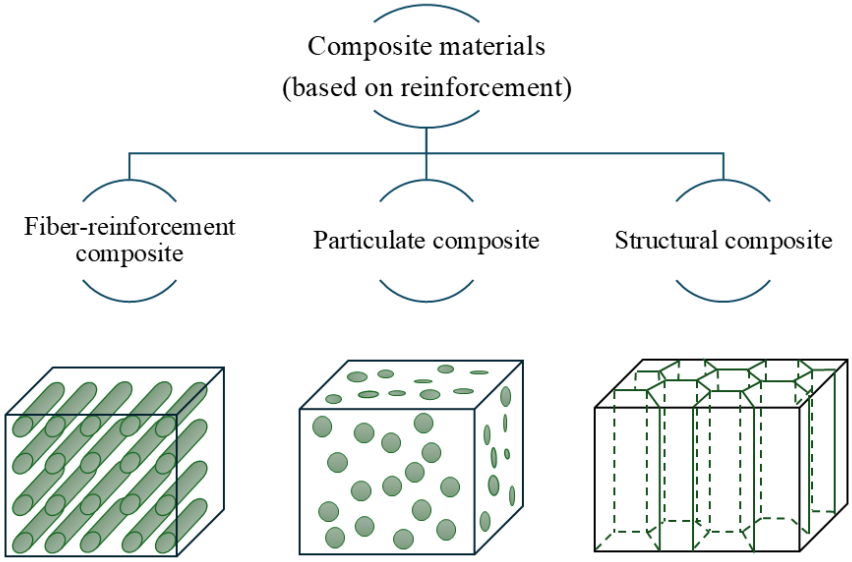

Figure 1-2. Classification of composite materials based on reinforcement.

While these categories define composite materials, a growing focus is placed on exploring reinforcements that align with industry demands for enhanced performance, sustainability, and efficiency. The shift from traditional metal and ceramic materials to synthetic fiber-reinforced composites reflects an ongoing drive toward more sustainable engineering solution. This transition has been further reinforced by the increasing adoption of Natural Fiber-Reinforced Composites (NFRCs), which offer several advantages, including environmental sustainability, biodegradability, and cost-effectiveness.

NFRCs have gained significant attention in recent years due to their ability to provide lightweight, high-strength alternatives to conventional materials. Industries such as automotive, construction, and aerospace are increasingly exploring NFRCs to reduce material costs and environmental impact while maintaining mechanical integrity. As research continues to advance in this field, optimizing the properties of NFRCs will be crucial to meeting evolving industry requirements and achieving a balance between performance and sustainability.

These fibers, derived from renewable sources such as hemp, jute, flax, sisal, bamboo, and coconut, offer adequate reinforcement capabilities, making them attractive alternatives to synthetic fibers like glass and carbon fibers. Although their mechanical properties, such as tensile strength and modulus, are generally lower than those of polymeric fibers, their higher elongation provides improved damage tolerance. However, challenges such as high moisture absorption, lower thermal stability, and weaker

interfacial bonding need to be addressed for their broader application. The growing interest in sustainable engineering solutions has further accelerated research on NFRCs, focusing on improving their mechanical performance and durability [1-4]. Advanced modeling and characterization techniques are essential for accurately predicting their material behavior and optimizing their performance.

A fundamental challenge in the adoption of NFRCs is their heterogeneous nature, which results in complex mechanical interactions between the reinforcing fibers and the matrix. NFRCs exhibit highly variable properties due to inconsistencies in fiber structure, composition, and processing conditions. Therefore, developing computational models capable of capturing the microstructural complexity of these materials is crucial for optimizing their performance and expanding their use in various engineering fields.

The numerical modeling of composite materials has become an essential tool for predicting their mechanical behavior and optimizing their microstructural design. The Finite Element Method (FEM) provides a robust framework for simulating the mechanical response of heterogeneous materials, allowing for an in-depth understanding of their structural performance under various loading conditions.

1.2- Research Objectives

This thesis aims to explore and implement an automated numerical modeling approach that can accurately predict the effective mechanical properties of particle-reinforced composites, with a particular focus on high volume fraction of particles. The study incorporates advanced meshing techniques, homogenization methods, and boundary

condition applications to establish a comprehensive numerical framework. The study builds upon prior research by our research team (ERICCA) in microstructural modeling, integrating Computer-Aided Design (CAD) tools, mesh generation, and FEM simulations within a unified topology model [5]. By leveraging Statistical Volume Elements (SVEs) and Finite Element Analysis (FEA), the research seeks to provide accurate estimations of effective mechanical properties and investigates the influence of microstructural parameters, such as particle aspect ratio, volume fraction, and spatial distribution.

One of the key objectives of this research is to generate a number of SVEs that achieves higher percentage of fiber volume fraction and can subsequently be submitted to FEA without requiring erosion of results, which was developed in previous work of our research team and means any removal of results. This approach seeks to overcome common issues in modeling, such as lack of particles and voids near SVE boundaries and non-uniform particle distribution, using automated methods based on the rigid Multi-Body Dynamics (MBD) generation algorithm.

This is significant because existing RVE or SVE generation methods, such as Random Sequential Adsorption and rigid MBD, are restricted to moderate fractions and often lead to unrealistic overlaps, boundary voids, or anisotropy. The geometric correction method (GCM) and the mesh cutting method (MCM) developed in this work are designed to overcome these limitations. GCM introduces an automated correction strategy that ensures a isotropic particle arrangement while preventing overlap and preserving minimum geometric constraints, thereby enabling higher volume fractions to be modeled

reliably. MCM further extends this capability by allowing particles to be generated in a larger domain and then trimmed into the target SVE size. This eliminates boundary voids, maintains uniform particle distribution, and preserves mesh quality even at high aspect ratios and volume fractions. Together, these approaches provide a robust framework for investigating particle-reinforced composites in regimes that are inaccessible to traditional methods, thereby extending the scientific and practical applicability of numerical homogenization.

Another important goal of this thesis is to improve computational efficiency in modeling particle-reinforced composites. Given the complex geometry and material heterogeneity of these composites, traditional simulation approaches often require significant computational resources. This study seeks to optimize meshing strategies and automate model generation to enhance simulation performance without compromising accuracy. Finally, the numerical predictions will be validated against experimental data to ensure robustness and reliability.

1.3- Dissertation Structure

The structure of this dissertation is organized as follows:

Chapter 2 provides a comprehensive literature review on particle-reinforced composites, highlighting key advancements in their modeling, processing, and applications. It discusses various homogenization techniques, including analytical and numerical methods, as well as a recently developed automated numerical approach by our team, and their role in predicting effective mechanical properties. Additionally, the

chapter explores the challenges associated with microstructural modeling and the latest computational techniques used to overcome them. It also examines the influence of different parameters on the final evaluated properties, offering insights into their impact on composite performance.

Chapter 3 first presents a review of the erosion of results method developed by our research team. Building upon this foundation, it then introduces the geometric correction and mesh-cutting methods utilized for particle-based composite modeling. It elaborates on the importance of accurate geometry representation in numerical simulations and discusses the procedures for generating SVEs.

Chapter 4 presents the finite element simulations and homogenization results obtained through two methodologies: the geometry correction method and the mesh cutting method. Finally, a comparison of the results from these two methods is presented. It evaluates their effectiveness through a comparative analysis of their results. Additionally, the chapter discusses the strengths and limitations of each method, highlighting their applicability to different scenarios.

Chapter 5 applies the proposed mesh cutting methodology to NFRPCs. The chapter also discusses the validation process through comparison with experimental data and explores the sensitivity of the results to different modeling parameters. It examines the effects of fiber aspect ratios and volume fractions on mechanical performance. Additionally, the chapter offers insights into the practical applications of these materials,

the implications of the numerical findings, and a discussion on their limitations and potential improvements.

Chapter 6 concludes the study by summarizing the key findings and their contributions to the field of particle-reinforced composites. The limitations of the proposed methodology are discussed, along with recommendations for future research directions, such as incorporating more advanced constitutive models.

CHAPTER 2

LITERATURE REVIEW

Particle-based composites have emerged as a versatile class of materials that combine the properties of a matrix with dispersed particles to achieve tailored performance for specific applications. These materials, also referred to as matrix-inclusion systems, consist of non-overlapping particles distributed throughout a continuous matrix. This structure enhances properties such as specific strength in lightweight construction, fracture toughness, and thermal or electrical performance, depending on the choice of inclusions and matrix. One of the primary advantages of these composites lies in their ability to be customized for diverse applications, ranging from aerospace and automotive industries to electronics and biomedical fields. For instance, ceramic particles significantly enhance thermal stability and mechanical strength, making them ideal for high-temperature applications [6]. Similarly, incorporating conductive particles, such as metals or carbon-based materials, into polymer matrices improves electrical conductivity

for electronic devices [7, 8]. Despite their advantages, particle-based composites also face challenges, particularly in achieving strong interfacial bonding between the matrix and inclusions. Poor interfacial adhesion can lead to debonding under stress, compromising structural integrity. Strategies such as surface treatments, functionalization of particles, and the use of coupling agents are essential to improving compatibility and enhancing interfacial strength.

In summary, particle-based composites represent a dynamic and rapidly evolving field with broad implications across various industries. Their ability to integrate diverse properties into a single material system underscores their importance in advancing modern engineering and technology. However, to effectively design and optimize these materials for specific applications, it is essential to accurately estimate their effective mechanical behavior. In particular, predicting the elastic properties of particle-based composites plays a critical role in material selection and performance assessment. Therefore, the following subsection of this chapter will explore the various theoretical, numerical, and experimental approaches used to evaluate and predict the elastic properties of these composites, providing insight into their mechanical behavior and guiding their practical applications.

2.1- Comprehensive review of evaluation methods for elastic properties of particle-based composites

The evaluation of mechanical properties of composites is crucial due to their broad applications in industries like aerospace, automotive, and defense. Composites'

mechanical behavior is strongly influenced by the properties and characteristics of the reinforcement materials. A clear understanding of how microstructural constituents influence the macroscale response of composite materials allows for better optimization of their mechanical properties to meet specific requirements. Traditionally, the mechanical properties of composites are assessed through experimental methods. However, while experimental testing offers valuable insights, it doesn't provide a comprehensive understanding of how microstructural aspects such as particle size, shape, orientation, interfacial strength, porosity, and thermal mismatch between the matrix and reinforcement impact the overall mechanical properties. As a result, numerous analytical and numerical techniques have been developed to better understand the micromechanics of composite materials. These methods allow for the examination and optimization of factors such as the size, shape, distribution, and interphase bonding of reinforcements, all of which affect the macroscopic behavior of composites. Then, utilizing methods such as homogenization [9-15], there will be a transfer between macro- and micro- scales. In another word, through this approach the heterogeneous material is transformed into a homogeneous one with equivalent mechanical behavior as shown in Figure 2-1. Additionally, these techniques provide insight into stress–strain relationships at the microscale, as well as the dynamic evolution of failure during loading. They also enable the application of multi-axial loading conditions to composite materials, a task that is often difficult to achieve with conventional experimental setups. Given the significant advantages offered by these analytical and computational approaches, many researchers now rely on them to predict

the mechanical performance of new composite materials before conducting physical experiments, ultimately saving time and reducing costs.

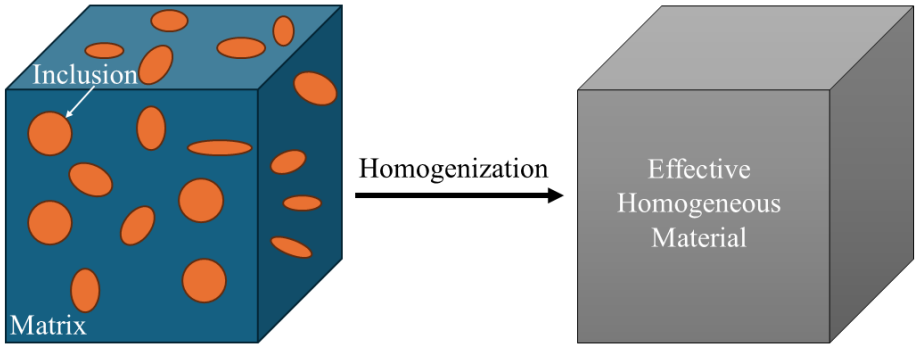

Figure 2-1. Transforming a heterogeneous material into a homogeneous material by homogenization technique.

2.1.1- Analytical homogenization:

The objective of homogenization is to obtain the effective stiffness matrix $\mathbb{C}^{eff}$ such that:

$$\underline{\underline{\Sigma}} = \mathbb{C}^{eff} : \underline{\underline{E}} \qquad \text{Eq. 2-1}$$

where $\underline{\underline{\Sigma}}$ and $\underline{\underline{E}}$ are the macroscopic stress and strain responses of the composite. Macroscopic stress and strain can be calculated by averaging the local fields of stress and strain respectively over the volume domain of study:

$$\underline{\underline{\Sigma}} = \left\langle \underline{\underline{\sigma}}(\underline{x}) \right\rangle \qquad \text{Eq. 2-2}$$

$$\underline{\underline{E}} = \left\langle \underline{\underline{\varepsilon}}(\underline{x}) \right\rangle \qquad \text{Eq. 2-3}$$

where $\underline{\underline{\sigma}}$ and $\underline{\underline{\varepsilon}}$ are the local strain and stress fields, respectively, and $\langle\ \rangle$ denotes the volume averaging operation:

$$\langle f \rangle_V = \frac{1}{V}\int_V f(\underline{x})dv \qquad \text{Eq. 2-4}$$

where V is the volume of the composite sample that is being homogenized.

On the other hand, two localization tensors $\mathbb{A}(\underline{x})$ and $\mathbb{B}(\underline{x})$ are introduced to calculate the microscopic fields from the macroscopic scale:

$$\underline{\underline{\sigma}}(\underline{x}) = \mathbb{B}(\underline{x}) : \underline{\underline{\Sigma}} \qquad \text{Eq. 2-5}$$

$$\underline{\underline{\varepsilon}}(\underline{x}) = \mathbb{A}(\underline{x}) : \underline{\underline{E}} \qquad \text{Eq. 2-6}$$

There is a condition named Hill condition [16] that establishes the equivalence in strain energy between the equivalent medium and the heterogeneous medium. This equivalence provides the connection required for transitioning between microscale heterogeneity and macroscale effective behavior:

$$\frac{1}{2}\left\langle \underline{\underline{\varepsilon}} : \underline{\underline{\sigma}} \right\rangle_V = \frac{1}{2}\underline{\underline{E}} : \underline{\underline{\Sigma}} \qquad \text{Eq. 2-7}$$

Three types of boundary conditions can be prescribed on a RVE such that the Hill condition holds [17].

- Kinematic uniform boundary condition:

$$\underline{u}(\underline{x}) = \left\langle \underline{\underline{\varepsilon}} \right\rangle . \underline{x} \qquad \forall \underline{x} \in \partial\Omega \tag{Eq. 2-8}$$

- Static uniform boundary conditions:

$$\underline{t}(\underline{x}) = \left\langle \underline{\underline{\sigma}} \right\rangle . \underline{n} \qquad \forall x \in \partial\Omega \tag{Eq. 2-9}$$

- Periodicity boundary conditions:

$$\underline{u}(\underline{x} + \underline{L}) = \underline{u}(\underline{x}) + \left\langle \underline{\underline{\varepsilon}} \right\rangle . L; \quad \underline{t}(\underline{x} + \underline{L}) = -\underline{t}(\underline{x}) \qquad \forall \underline{x} \in \partial\Omega \tag{Eq. 2-10}$$

It should be noted that in the equations above, the localization tensors and subsequently their local fields are calculated approximately not accurately. Thus, these methods usually lead to some bounds for effective properties. Based on the type of assumption and approach that are adopted to calculate the localization tensor, different analytical methods are generated. Two simplest and well-known bounds named as rule of mixture for composites, were defined by Voigt [18] and Reuss [19] providing the upper and lower bounds for effective elastic properties.

Voigt assumed the strain field remains constant throughout the material when subjected an arbitrary average stress field (Figure 2-2). The Voigt upper bound of the effective elastic modulus, $\mathbb{M}_V$, of N phases is:

$$\mathbb{M}_V = \sum_{i=1}^{N} f_i \mathbb{M}_i \tag{Eq. 2-11}$$

Where $\mathbb{M}_i$ is the elastic modulus of the ith phase and f_i is the volume fraction of the ith phase**,** defined as the ratio of the volume of that phase (V_i) to the total composite volume (V):

$$f_i = \frac{V_i}{V} \qquad \text{Eq. 2-12}$$

and thus $\sum_i f_i = 1$.

While Reuss assumed the stress field remains constant throughout the material when subjected an arbitrary average strain field (Figure 2-2). The Reuss lower bound of the effective elastic modulus, $\mathbb{M}_R$, is:

$$\mathbb{M}_R^{-1} = \sum_{i=1}^{N} f_i \mathbb{M}_i^{-1} \qquad \text{Eq. 2-13}$$

The assumption of these bounds is that each constituent is isotropic, linear, and elastic.

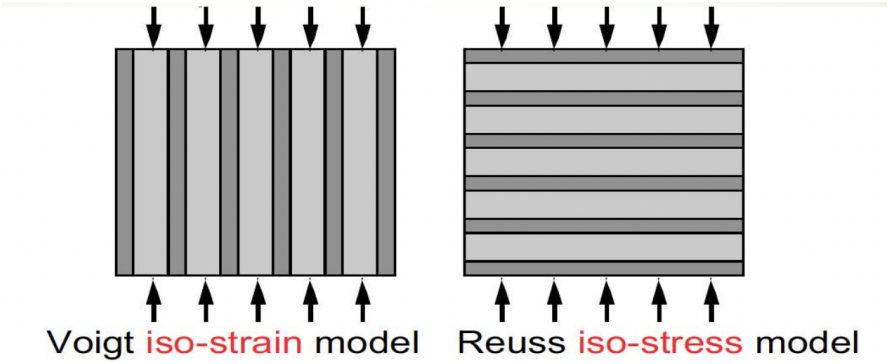

Figure 2-2. Voigt and Reuss model [20].

Other bounds for an isotropic linear elastic composite, defined as giving the narrowest possible range without specifying anything about the geometries of the constituents, are the Hashin–Shtrikman bounds [21].

The Hashin-Shtrikman treat the composite as an isotropic aggregate and instead of averaging stress and strain fields, it minimizes the strain energy and uses variational principles from linear elasticity to derive bounds. When there are only two constituents, the bounds are written as:

$$K^{HS\pm} = K_1 + \frac{f_2}{(K_2 - K_1)^{-1} + f_1(K_1 + \frac{4}{3}\mu_1)^{-1}} \qquad \text{Eq. 2-14}$$

and

$$\mu^{HS\pm} = \mu_1 + \frac{f_2}{(\mu_2 - \mu_1)^{-1} + \frac{2f_1(K_1 + 2\mu_1)}{\left[5\mu_1(K_1 + \frac{4}{3}\mu_1)\right]}} \qquad \text{Eq. 2-15}$$

where K_1 and K_2 are the bulk moduli of individual phases; μ_1 and μ_2 are the shear moduli of individual phases; and f_1 and f_2 are the volume fractions of individual phases. With these equations, upper and lower bounds are computed by interchanging which material is termed 1 and which is termed 2. The expressions yield the upper bound when the stiffest material is termed 1 and the lower bound when the softest material is termed 1. This method too has its limitations, especially in accurately predicting the behavior of materials with complex microstructures.

Many others tried to improve each of these bounds. Using perturbations, Milton and Phan-Thein [22] introduced more geometrical features of the microstructure and improved the accuracy of the Hashin–Shtrikman bounds. Using variational principles, others tried to generalize methods to include accounting for anisotropy [23], and random microstructures [24].

To enhance the predictive capability, the modified Rule-of-Mixtures was introduced by researchers like Tomoda, Williamson, and Giannakopoulos [25-27]. This modification takes into account factors such as microstructural arrangements and internal constraints. By incorporating these factors, the modified method gives a better approximation of the composite's Young's modulus.

Another group of analytical methods drops into ones based on Eshelby [28]. The Eshelby model is fundamental in micromechanics where he derived a solution for the stress and strain fields within ellipsoidal inhomogeneities in an infinite matrix subjected to uniform remote tractions. He showed that the resulting strain field in the constrained inclusion is uniform and is given by:

$$\underline{\varepsilon_i} = \mathbb{S} : \underline{\varepsilon_t} \qquad \text{Eq. 2-16}$$

where $\mathbb{S}$ is Eshelby's tensor, $\underline{\varepsilon_i}$ is the uniform strain in the constrained inclusion and $\underline{\varepsilon_t}$ is a uniform stress-free strain.

While Eshelby's approach offers useful insights into the effect of particle reinforcement on material properties, it assumes infinite matrix behavior, which might not be realistic for all composites.

The Mori-Tanaka method [29-31] is an extension of Eshelby's solution, which uses eigenstrains to calculate the average stress in a composite. The Mori–Tanaka method is a direct averaging scheme, which is based on the following relation:

$$\mathbb{C}^* = \mathbb{C}_2 + c(\mathbb{C}_1 - \mathbb{C}_2)\mathbb{S}((1-c)I + c\mathbb{S})^{-1} \quad \text{Eq. 2-17}$$

Where $\mathbb{C}_1, \mathbb{C}_2, \mathbb{C}^*$ are the elastic tensors of inclusion, the matrix, and the equivalent homogeneous media, respectively. c is the inclusion volume fraction and $\mathbb{S}$ is Eshelby's tensor. This method has gained popularity due to its ability to provide a closed-form expression for the effective stiffness tensor. However, it works best for composites with low reinforcement concentrations and is less accurate when the volume fraction of reinforcement becomes large.

For composites with higher reinforcement volume fractions (above 50 %), the self-consistent method is used. Proposed by Kroner [32] and Budiansky [33], this method assumes that the composite's overall moduli are equal to the moduli of the infinite medium, defined as a hypothetical homogeneous and unbounded material in which each inclusion is embedded and interacts with an effective medium representing the composite itself. This approach works well for spherical inclusions and is useful when dealing with large volume fractions of reinforcement. To provide a clearer overview of the more

common analytical homogenization approaches discussed, Table 2-1 summarizes their key principles, underlying assumptions, typical domains of application, and main limitations.

Table 2-1. Analytical homogenization methods: assumptions, applications, and limitations.

Method	Key Idea / Equation	Main Assumptions	Typical Use / Scope	Limitations
Voigt (Upper Bound)	$\mathbb{M}_V = \sum_{i=1}^{N} f_i \mathbb{M}_i$	Uuniform deformation across phases.	Quick upper bound on stiffness.	Strongly overestimates stiffness when inclusions are compliant.
Reuss (Lower Bound)	$\mathbb{M}_R^{-1} = \sum_{i=1}^{N} f_i \mathbb{M}_i^{-1}$	Uniform stress across phases.	Quick lower bound on stiffness.	Strongly underestimates stiffness when inclusions are stiff.
Hashin–Shtrikman (HS) Bounds	Variational principles for $K^{HS\pm}$, $\mu^{HS\pm}$	Isotropic, linear elastic phases, perfect bonding.	Best possible theoretical bounds; benchmark for validation.	Provide only bounds, not exact values.
Eshelby's Inclusion Solution	Inclusions induce strain via Eshelby tensor.	Ellipsoidal inclusion in infinite isotropic matrix.	Foundation for MT and SC methods; micromechanics.	Exact only for single inclusion in infinite medium.
Mori–Tanaka (MT)	Averages inclusion response weighted by the surrounding matrix.	Ellipsoidal inclusions, moderate volume fraction.	Widely used for short-fiber or particulate composites.	Less accurate at high volume fractions; assumes dilute interactions.
Self-Consistent (SC)	Effective medium approach: inclusions embedded in the unknown effective medium.	Randomly distributed inclusions; isotropic, linear elastic phases; ellipsoidal shapes.	Balanced estimate for randomly distributed inclusions.	Can deviate at high contrast or elongated particles.
Generalized Self-Consistent (GSC)	Three-phase model: inclusion–matrix–effective medium.	Inclusions surrounded by concentric shells.	More accurate for coated particles or core–shell systems.	Still approximate; computationally more involved.
Composite Spheres Assemblage (CSA)	For spherical inclusions.	Concentric spheres; isotropic matrix.	Exact solution for certain particle composites.	Restricted to spheres; not generalizable.
Differential Scheme (DS)	Incremental addition of inclusions.	Inclusions added progressively to matrix.	Effective for highly filled composites.	Path-dependent; results can vary with addition order.

Analytical models typically assume an idealized, infinite interface strength between matrix and reinforcement. However, in real composites, the interface strength is

finite and can vary across the interface thickness. Researchers like Christensen [34] and Yao [35] have incorporated the interface's role by including an interphase region in their models. These modifications improve the predictions of elastic properties like Young's modulus and Poisson's ratio.

Despite their foundational role in composite mechanics, one of the most important limitations of analytical methods is that for microstructures with high contrast of properties, they give us far apart bounds on effective properties that are not practically useful. These methods simplify the microstructure by approximating inclusion shapes to simple geometries (e.g., ellipsoids or spheres), which can overlook essential microstructural features such as irregular particle morphology, inhomogeneous particle distribution, and anisotropy in particle orientation.

To overcome these limitations, homogenization approaches based on numerical methods, such as FEA, have been developed. These methods provide a more detailed representation of the material's microstructure and enable more accurate predictions of macroscopic deformation, failure, and damage mechanisms.

2.1.2- Numerical homogenization

In numerical homogenization, instead of estimating the localization tensors, the response of material is calculated by numerical methods as Boundary Value Problems (BVPs) on a Representative Volume Element (RVE). Some of the numerical methods that are available for solving the BVPs required for the implementation of homogenization to

predict mechanical properties are Finite Difference Method (FDM), Finite Volume Method (FVM), Finite Element Method (FEM), and Fast Fourier Transform (FFT) [36-45]. It has been shown by Michel et al. [46] that FFT cannot converge when dealing with composites having constituents of high contrast or non-linearities. Among all, FEM have been extensively employed in numerical homogenization of mechanical properties, with significantly more research dedicated to its implementation compared to other numerical methods.

The RVE is a key concept in numerical homogenization, representing a small section of the composite that reflects the overall microstructure. By ensuring the RVE includes features such as particle volume fraction, shape, and distribution, FEM simulations can predict the macroscopic properties of the composite more reliably. Thus, defining and generating a volume element that can be statistically a representation of material microstructure is the first important step.

Generating the RVE geometry, assigning material to it, choosing a numerical method, calculating the material response, and homogenization are other steps of this approach. Each of these steps has been studied by researchers and some important conclusions of those studies will be discussed in the following sections.

2.1.2.1- Definition and Generation of RVE

The definition of a RVE is a critical step in the simulation of material behavior. It should be performed carefully to ensure that the results are both time and cost-effective

while accurately representing the material's behavior. The RVE must be sufficiently representative of the material's microstructure to capture its essential properties but also optimized to minimize computational cost and time. Key factors that influence RVE design include the size of the RVE, the types of microstructural heterogeneities included, and the shapes and distribution of inclusions within the volume. A suitable RVE will accurately reflect the material's behavior under different loading conditions.

Some researchers developed methods to determine a suitable RVE size such as analytical methods or statistical-numerical methods [47]. They are mostly based on first considering a number of criteria then obtaining results for different size of RVEs and finally check the results of these volumes with the criteria to determine the size of RVE which satisfies them. This process is shown in Figure 2-3. In this figure, the error is evaluated by comparing the predictions of the effective property with either the mean value obtained from several RVE sizes or with available experimental/analytical reference values. The main differences between existing methods lie in the type of criteria considered and in how the responses of different RVE sizes are evaluated. For example, Drugan and Willis [48] considered a linear elastic composite with non-overlapping inclusions, used error on constant overall modulus as their criteria, and adopted analytical methods to obtain the response of each size of RVE. They concluded that the minimum size of RVE could be as small as two times the sphere diameter for error of 5 % and 4.5 times the reinforcement diameter for error of 1 %. Kanit et. al [49] have performed a statistical analysis of the numerical examples in order to define the REV size in the case of linear elasticity and thermal conductivity. A model is provided that one can define the

estimation error and number of realizations of interest and find the suitable RVE size. Before that, generating several realizations on different volume sizes and then calculating the mean value, variance of properties and integral range is needed. They also pointed out that RVE size must be considered as a function of five parameters: the physical property, the variance of computed apparent properties, the contrast of properties, the volume fraction, the wanted relative precision for the estimation of the effective property and the number of realizations of the microstructure associated with computations that one is ready to carry out.

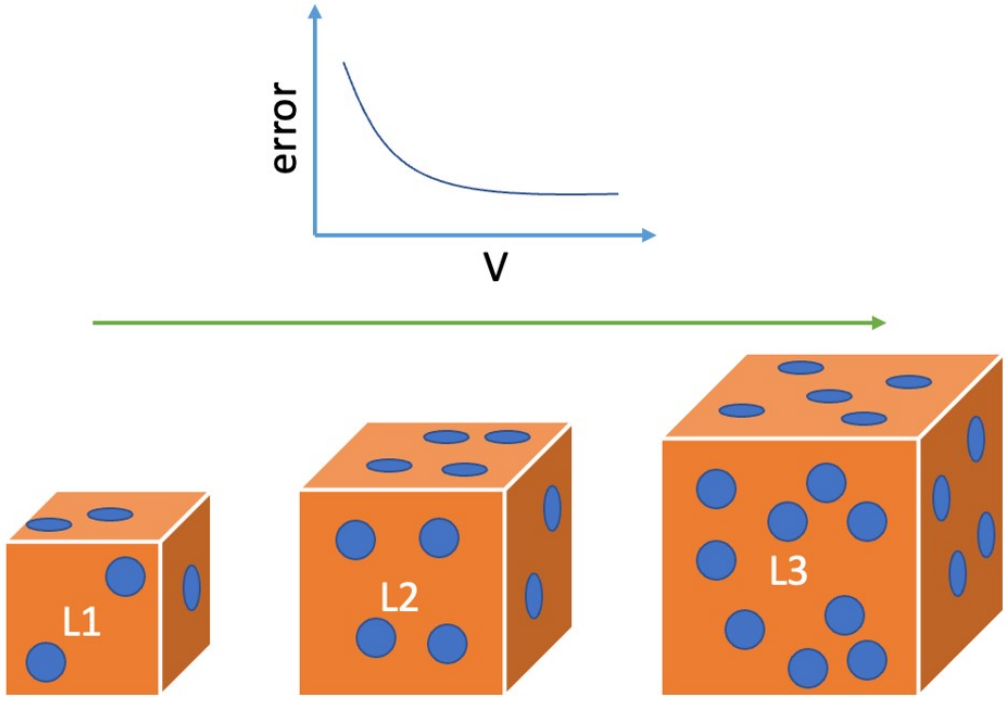

Figure 2-3. Convergence of effective properties with increasing RVE size. The error is defined as the deviation between the predicted property and the chosen reference, which may be the mean value from several RVE sizes or available experimental/analytical data.

On the other hand, Huet [17] demonstrated that it is not always possible to relate a RVE to the structure. In some cases, like cement or wood, because of the shape or size of the structure or its heterogeneities, the related RVE would be too big for calculation. Thus, he proposed the use of volumes that are smaller than RVE and calculate the properties by averaging over a number of those volumes named Statistical Volume Element (SVE) as shown in Figure 2-4. The properties calculated by SVEs are named as "apparent properties" while the properties obtained from RVEs are named "effective properties".

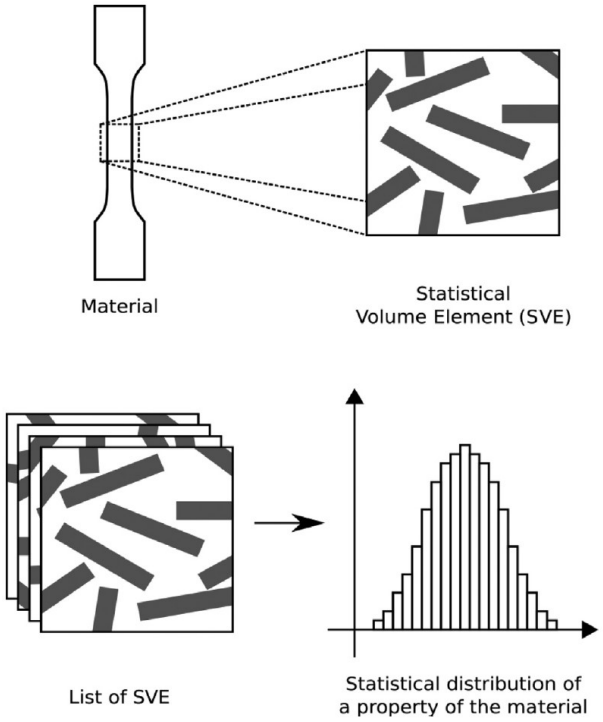

Figure 2-4. Several statistical volume elements representing the material and finally distribution of material property based on result of each realization [50].

Based on the type of material under study, different types of micro-structural heterogeneities should be included in the representation of material. For example, the composite could be a n-phase composite, and each phase could be of different shape. One could specify voids or cracks as additional microstructure in the volume. Figure 2-5 shows variety of microstructures inside the RVE.

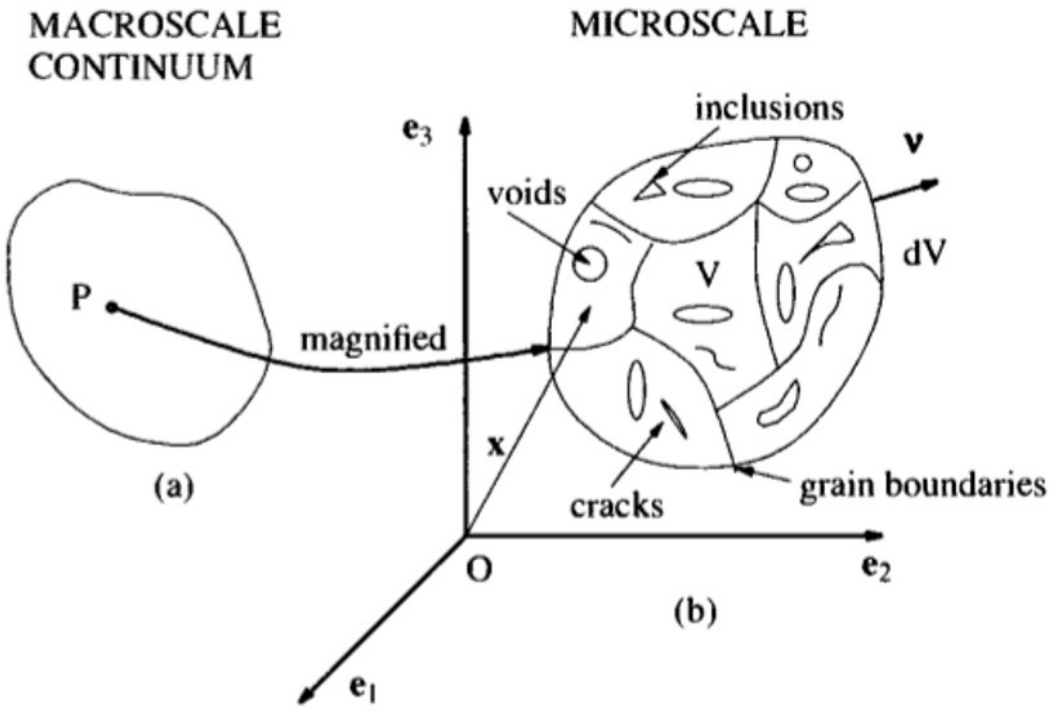

Figure 2-5. (a) P is a material point or material element surrounded by a material neighborhood; (b) Possible microstructure of an RVE for the material neighborhood of P [51].

The process of generating an RVE for inclusion-based composites materials, where one phase (inclusions) is embedded within a matrix, can be achieved through several techniques that focus on replicating the distribution, morphology, and spatial arrangement of the inclusions. These methods can generally be classified into three

categories: experimental reconstruction, physics-based simulations, and geometry-driven approaches. Each category offers specific strengths and is chosen depending on the needs of the simulation, such as precision, computational efficiency, and the availability of data.

2.1.2.1.1- Experimental Reconstruction Methods

Experimental reconstruction techniques are primarily used when it is necessary to replicate the actual, real-world microstructure of a material. These methods involve imaging techniques that can accurately reconstruct a material's microstructure, which is particularly useful for complex, heterogeneous materials such as inclusion-based composites. Common techniques include:

Serial Sectioning [52]: This destructive technique involves slicing the material into thin layers, imaging the exposed surfaces, and reconstructing the three-dimensional structure using computational interpolation. While effective, serial sectioning presents challenges such as alignment errors, surface artifacts, and anisotropic resolution. Forsman et al. [53] demonstrated this method for metallic materials, though the technique was hindered by these limitations.

X-ray Tomography: Non-destructive X-ray Computed Tomography (CT) imaging allows high-resolution scans of materials and provides detailed insights into inclusion morphology and crystallographic orientation. For instance, Figure 2-6, shows the overall dispersion state of graphene nanoflakes in the composites observed by 3D-micro-CT. However, resolution can be limited by the contrast between the inclusions and the matrix,

which is affected by the atomic number contrast between phases. Advanced techniques like differential X-ray absorption and diffraction contrast tomography help overcome some of these challenges [54].

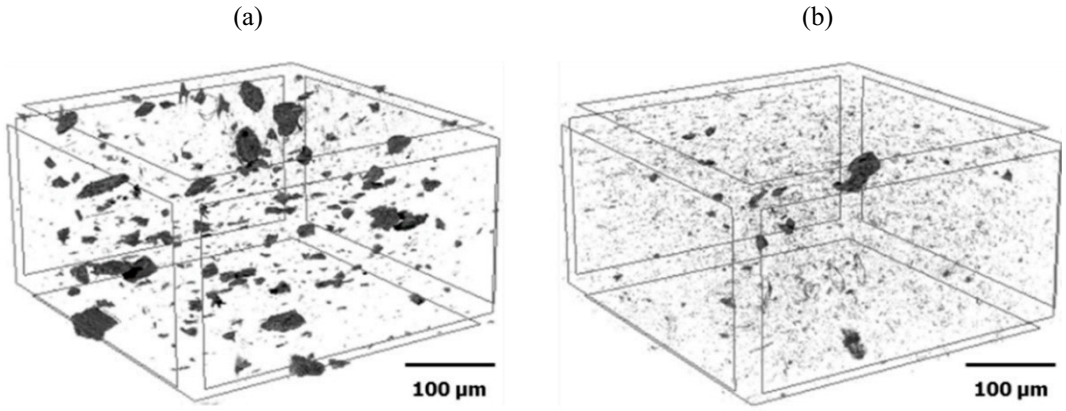

Figure 2-6. Three-dimensional non-destructive X-ray micro-computed tomography images of (a) polypropylene/reduced graphene oxide and (b) polypropylene/fluorinated graphene oxide composites [55].

Despite their high accuracy, these experimental methods are often limited by high costs, time consumption, and the availability of advanced equipment, thus leading to the development of complementary computational methods.

2.1.2.1.2- Physics-Based Simulations and Geometry-Based Techniques

Instead of directly reconstructing from experiments, physics-based models simulate the natural processes leading to the formation of matrix-inclusion composites. Physics-based approaches model the physical processes that drive the formation of microstructures, such as nucleation, growth, and interactions of inclusions. For example, Monte Carlo Simulation is a probabilistic method which is effective for simulating energy-driven processes such as grain boundary evolution. It has been successfully used to model

the annealing and recrystallization behaviors in polycrystalline materials as demonstrated by Anderson et al [56]. Phase-field models [57, 58] describe the evolution of material interfaces using field variables that transition smoothly between phases. They are particularly effective in capturing complex phenomena like coarsening and inclusion interactions under varying thermal and mechanical conditions. A phase-field model is employed to simulate the kinetics and topology of three-dimensional grain growth in an ideal polycrystal with uniform grain-boundary properties in [59]. Cellular Automata is a voxel-based simulation technique [60, 61] allowing for modeling the discrete spatial and temporal evolution of inclusions in a computationally efficient manner. It is commonly used to model processes such as recrystallization and phase transformations.

In many instances, modeling the actual physical processes involved in the creation of matrix-inclusion microstructures is impractical. Bulk or mixing simulations tend to be overly complicated, and the time required for such simulations often does not justify the insights gained regarding particle distributions. Nevertheless, several methods, such as shakedown, particle motion, growth simulations, and molecular dynamics, are inspired by physical processes and offer alternative approaches.

Unlike physics-based methods, geometrical techniques focus on parameterized shape generation and placement within a matrix. Geometry-based methods focus on replicating the spatial distribution and morphology of inclusions in a computationally efficient manner. These methods do not directly simulate the physical processes but instead use algorithms to place inclusions based on predefined spatial rules. Voronoi

tessellations is one of these methods that divide space into cells based on the distance to predefined seed points [62, 63]. This approach is widely used due to its flexibility and ability to generate periodic microstructures. Variations, such as centroidal and weighted Voronoi tessellations, allow for more control over the size distribution of inclusions, making it ideal for modeling composites with inclusions of varying sizes.

Random Sequential Adsorption (RSA) is a widely used numerical technique for generating representative microstructures of particulate composites due to its simplicity and effectiveness in modeling non-overlapping particle distributions. Its popularity in homogenization studies stems from its ability to accurately represent realistic packing densities and spatial distributions, making it highly applicable for predicting elastic properties of composites. In RSA, inclusions are placed randomly in a predefined domain while avoiding overlaps. In this method, as illustrated in Figure 2-7, the position of the first particle and subsequently other particles are randomly generated. The particles are added one by one into a cube and at each adding step, some criteria will be checked to see if the particle is accepted or not. These criteria ensure that no particles overlap and that a minimum geometrical distance is maintained both between particles and between each particle and the boundary of the volume element. If the particle is accepted, the next inclusion will be added and if not, the particle will be removed, and another one will be generated. This algorithm repeats until the final particle volume fraction is reached. This method is computationally efficient but becomes less effective as the volume fraction of inclusions increases due to the difficulty of inserting additional inclusions at high packing densities known as the jamming limit [64, 65]. Essentially, this means that once a specific

volume fraction is reached, where the space between inclusions becomes smaller than the size of inclusions, it is no longer possible to add additional inclusions. This occurs because, with the classical RSA algorithm, once inserted, each accepted inclusion cannot move or be modified to make space for additional inclusions.

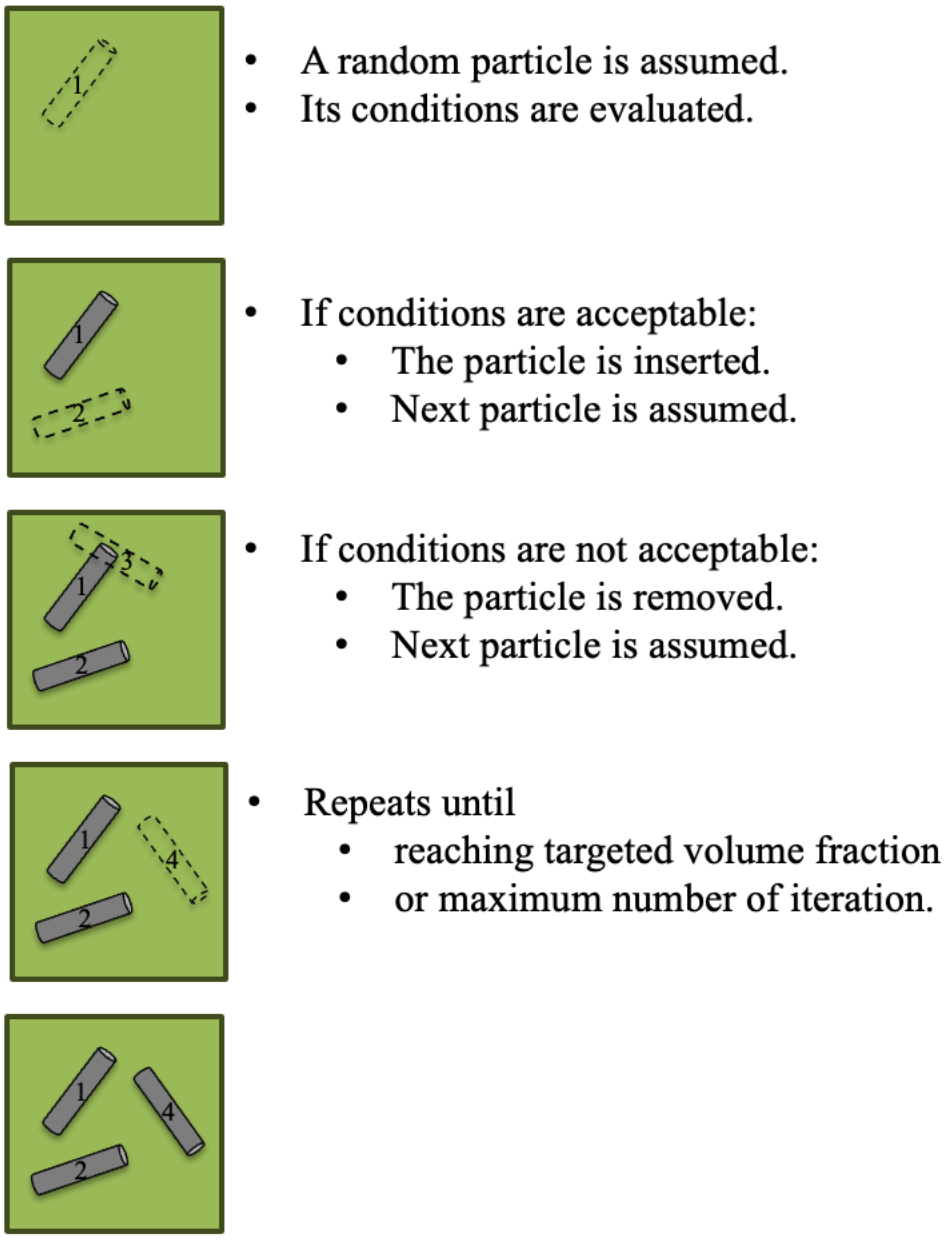

Figure 2-7. RSA algorithm.

Several modifications to the classical RSA have been proposed to achieve higher volume fractions. Kari et al. [66] suggest that once the jamming limit is reached with several fibers of a specific aspect ratio, fibers with lower aspect ratios can be introduced into the cube. This process can be repeated while ensuring that the newly introduced fibers are not too small. This method is illustrated in Figure 2-8. They report that this modified RSA approach enables achieving higher volume fractions than with previous versions of the RSA algorithm. Tian et al. [67] introduce a fiber growth method that builds on the principles of RSA but utilizes a different approach for fiber insertion. Instead of inserting a fiber and checking for intersections with other fibers, the inserted fiber grows from zero length until it intersects with existing fibers.

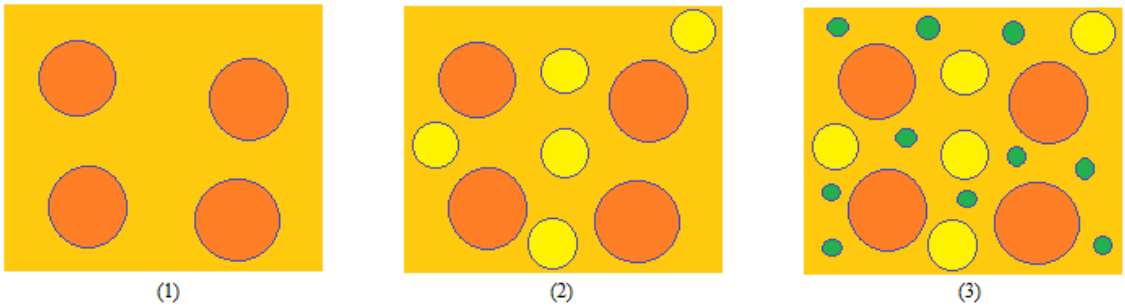

Figure 2-8. Steps of modified RSA, 1) reaching jamming limit, 2) inserting next possible biggest particles (but smaller than previous ones), 3) repeating previous step in a descending manner.

Another well stablished method is rigid multibody dynamics. MBD simulates the motion and collision of inclusions within the matrix. This approach is based on letting the inclusions move and collide with each other. This approach is generally categorized into two groups, referred to as event-driven and time-driven approaches [68]. Figure 2-9 illustrates the fundamental distinction in how interacting particles are handled between

conventional time-stepping molecular dynamics and event-driven molecular dynamics methods.

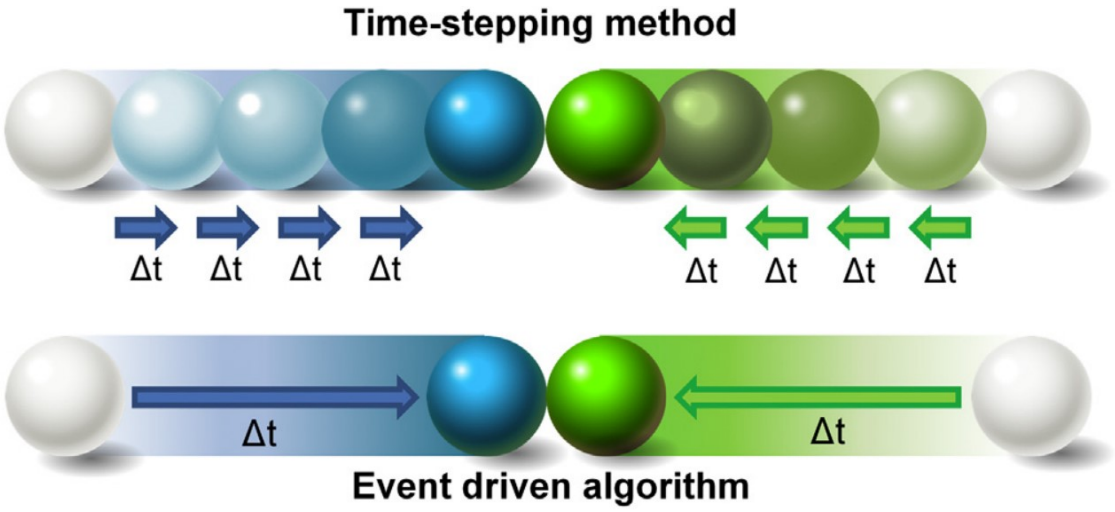

Figure 2-9. Schematic of time-stepping method and event-driven algorithm [69].

Event-driven algorithms calculate the next event at a specific moment, such as the collision between two particles or between one particle and boundaries of the domain, after which the state of the system is updated. This includes determining the new position of each particle, its speed, angular velocity, mass and its orientation in the case of a non-spherical particle. Consequently, the state of the system is not computed at regular time intervals; instead, the duration of time steps is adjusted according to time intervals between each event. Lobachevsky et al. [70, 71] propose an event-driven method based on Molecular Dynamics (MD), applying it to discs and spheres. The initial state is established by randomly generating the positions of N points (representing the centers of all particles) within a closed domain. Each point is assigned an initial velocity vector, with its components also drawn randomly. Initially, these points represent spheres with a zero

diameter. As each particle moves according to its initial velocity vector, its diameters increase over time. Along this movement and growth, the particles collide elastically. This algorithm requires calculating the positions and velocities of particles at each time step, as well as predicting future collisions. The growth of spheres allows increasing the volume fraction of particles over time, and the process stops once the desired volume fraction is achieved.

Li et al. [69] developed an algorithm based on the event-driven MD theory to rapidly generate periodic RVEs with nonuniform distributions for both unidirectional fibre-reinforced and spherical particle-reinforced composites. Figure 2-10 shows an example of a generated RVE with random particle distribution and periodic geometry along all directions with this new algorithm. The model is a RVE with spherical particles with volume fraction of 30 %.

In [72], a novel algorithm referred to as the sequential adsorption algorithm is introduced for generating RVEs of composites reinforced with randomly distributed spherical particles. This method combines the RSA algorithm with the MD-based approach. The proposed algorithm addresses limitations of the RSA method and can efficiently produce RVEs with high particle volume fractions (around 50 %).

Despite the developments mentioned above, event-driven MD-based methods are constrained by their limitations regarding collision detection, which restricts all these approaches to spherical particles. Achieving high volume fractions of particles with more

complex shapes, such as cylindrical particles, particularly those with high aspect ratios, remains a significant challenge.

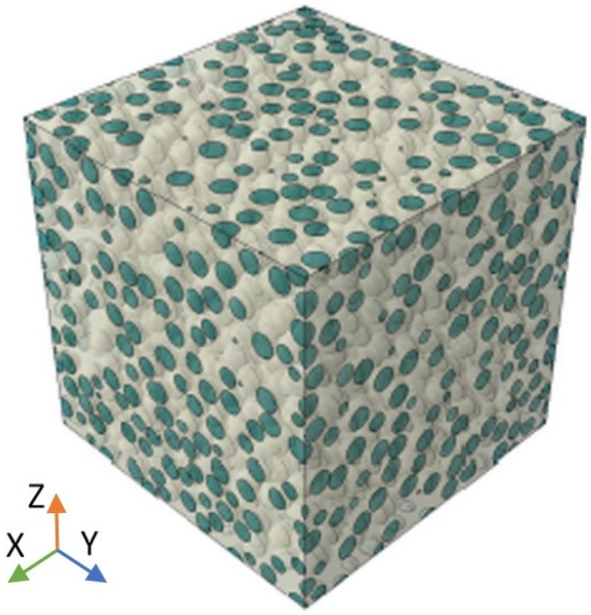

Figure 2-10. Generated 3D RVE with randomly distributed spherical particles and volume fraction = 30 % [69].

In contrast, time-driven MBD approaches calculate the system's state at regular time intervals, updating collision detection at each step. This method is not constrained to specific particle shapes and employs surface triangulations along with bounding boxes for effective collision detection.

This approach, employed by our research team (ERICCA) and presented in [73], is used for the modeling and analysis of particle-based composites with spherical and cylindrical shapes. The developed method automatically generates the geometry of SVEs using time-driven rigid MBD techniques in conjunction with solid modeling concepts.

Figure 2-11 illustrates an example of this method performed with 100 spheres stacked in the same location.

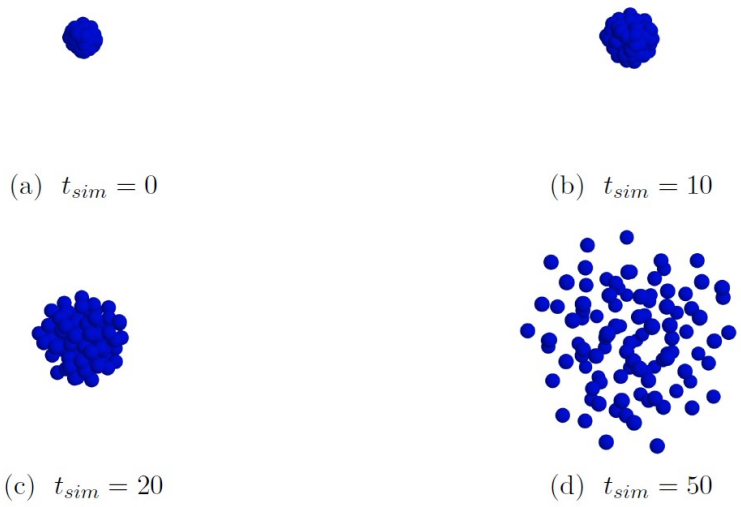

Figure 2-11. Simulation of 100 spheres with time-driven MBD. a) Stacking of the spheres. b-c) Overlap elimination. d) Final positions of the spheres [74].

When particles are too close to each other or to the SVE boundary, mesh elements can become ill-shaped or impossible to generate, leading to failure of the meshing algorithm or poor element quality. To ensure mesh convergence and avoid automatic mesh generation failure, specific criteria related to minimum distance and minimum angle between geometric entities must be respected during particle generation. This requirement results in the elimination of a significant number of particles, particularly those located near boundaries of the SVE. To address this issue, after FEA results on the entire model are obtained, an erosion-based approach that involves not taking into account results for layers of elements from boundaries of the SVE is integrated into the method. This erosion-based approach, reviewed in next section, is applied to both the RSA method and the MBD

method [50, 73], achieving a volume fraction of approximately 30 % for both spherical and cylindrical particles. In this erosion-based method, to reach the target volume fraction, results inside a distance from the six faces of the SVE, known as the erosion distance (d_e) are eroded. This results in a smaller homogenization domain if compared to the original SVE used for FEA. While this approach addresses the issue of inhomogeneity near the boundaries, it raises important questions about the exclusion of boundary elements results. Specifically, it is necessary to determine whether a high volume fraction with a uniform particle distribution can be achieved without removing these boundary elements results or encountering inhomogeneity at the SVE boundaries.

Periodic RVE Generation is another method. To eliminate artificial boundary effects, periodic boundary conditions are applied to RVEs, ensuring continuity across the RVE's edges. Periodic versions of RSA, and Voronoi tessellations are commonly used for studies involving computational homogenization.

2.1.2.1.3- Hybrid Approaches and Integration

Hybrid methods combine the strengths of experimental data and computational models. For instance, statistical metrics derived from experimental imaging can inform the parameters for computational models, ensuring that the generated RVEs accurately reflect the material's actual microstructure. Techniques like statistical stereology, which extracts 3D information from 2D images, can also be used to supplement computational methods and improve the accuracy of RVE generation.

In summary, microstructure generation methods for inclusion-based composites span a wide spectrum of techniques, each suited to specific applications. Experimental methods provide unmatched accuracy but are limited in scalability. Physics-based and geometry-driven techniques offer computational efficiency and flexibility, enabling high-throughput exploration of material behavior. Geometry-based methods like RSA, and Voronoi tessellations, in particular, provide a balance of efficiency and realism, making them indispensable for modern materials design. Future advancements in hybrid methods and the integration of machine learning promise to enhance the accuracy and predictive power of RVE generation techniques further.

2.1.2.2- Material assignment

Most of studies focused on isotropic constituents (both fibers and matrix) which when assigned to a randomly distributed short fibers, will lead to resultant isotropic material. Isotropic materials have only two independent coefficients and their stiffness matrix is as the following matrix.

$$\frac{E}{(1-2\nu)(1+\nu)}\begin{bmatrix} 1-\nu & \nu & \nu & 0 & 0 & 0 \\ \nu & 1-\nu & \nu & 0 & 0 & 0 \\ \nu & \nu & 1-\nu & 0 & 0 & 0 \\ 0 & 0 & 0 & \frac{1-2\nu}{2} & 0 & 0 \\ 0 & 0 & 0 & 0 & \frac{1-2\nu}{2} & 0 \\ 0 & 0 & 0 & 0 & 0 & \frac{1-2\nu}{2} \end{bmatrix} \quad \text{Eq. 2-18}$$

Also, it is possible to find shear and bulk modulus of the material using its elastic modulus and Poisson's ration:

$$G = \frac{E}{2(1+\nu)} \quad \text{Eq. 2-19}$$

$$K = \frac{E}{3(1-2\nu)} \quad \text{Eq. 2-20}$$

However, lots of fibers especially natural fibers show different behavior such as orthotropic (9 independent coefficients) or more generally behavior as anisotropic (21 independent coefficients). The stiffness tensor of anisotropic material with 21 independent coefficients is such that:

$$\begin{bmatrix} C_{11} & C_{12} & C_{13} & C_{14} & C_{15} & C_{16} \\ & C_{22} & C_{23} & C_{24} & C_{25} & C_{26} \\ & & C_{33} & C_{34} & C_{35} & C_{36} \\ & & & C_{44} & C_{45} & C_{46} \\ & Sym. & & & C_{55} & C_{56} \\ & & & & & C_{66} \end{bmatrix} \quad \text{Eq. 2-21}$$

In addition to mechanical properties, the thermal behavior of materials must be considered when modeling the response of composites under thermal loading or combined thermomechanical effects. Similar to mechanical behavior, the assignment of thermal properties depends on the nature of the constituents.

For isotropic materials, thermal conductivity is characterized by a single scalar value λ, representing an identical conductivity in all directions. In the case of orthotropic or anisotropic constituents, thermal conductivity is represented by a second-order tensor $\underline{\underline{\Lambda}}$, typically diagonal in orthotropic materials, with distinct conductivities along the principal material directions.

The local thermal behavior follows Fourier's law, relating the heat flux vector Φ to the temperature gradient T:

$$\underline{\Phi} = -\underline{\underline{\Lambda}}.\underline{T} \qquad \text{Eq. 2-22}$$

2.1.2.3- Calculation method: FEM

One of the mostly used numerical method to simulate the micromechanical behavior of materials is the FEM. Using FEM can solve partial differential equations that describe the behavior of a physical system. The partial differential equations consist of equilibrium equations on the domain of study and the imposed boundary conditions. We are looking for the displacement field that is the solution of these equations and satisfies the boundary conditions [75]. We consider a domain of $\Omega \subset R^D$, where D is the space dimension as illustrated in Figure 2-12. The boundary of the domain is denoted by $\partial\Omega$, and is composed of disjoint and complementary parts denoted by $\partial\Omega_u$ and $\partial\Omega_F$, on which are prescribed the displacements u^* (Dirichlet boundary conditions) and tractions F^* (Neumann boundary conditions).

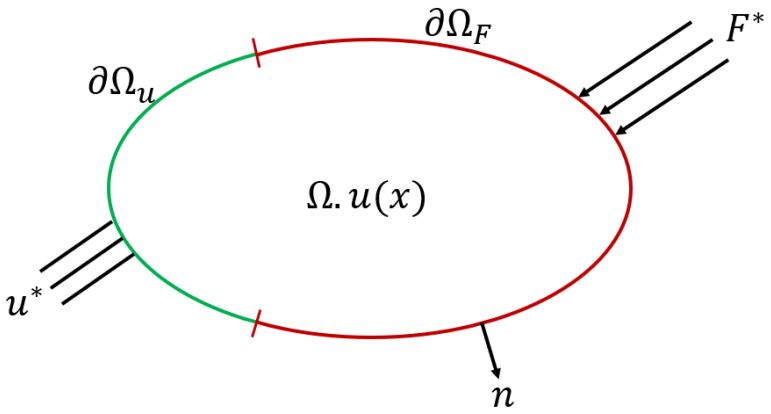

Figure 2-12. Boundary conditions for the linear elasticity problem.

The equations of the problem, also called as "strong form" of equations, for the unknown displacement field $\underline{u}(\underline{x})$ are:

$$\nabla . \underline{\underline{\sigma}}(\underline{x}) + \underline{f}(\underline{x}) = 0 \qquad in\ \Omega \tag{Eq. 2-23}$$

$$\underline{\underline{\sigma}}(\underline{x}) = \mathbb{C} : \underline{\underline{\varepsilon}}(\underline{x}) \tag{Eq. 2-24}$$

$$\underline{\underline{\sigma}}(\underline{x}) . \underline{n}(\underline{x}) = \underline{F^*}(\underline{x}) \qquad on\ \partial\Omega_F \tag{Eq. 2-25}$$

$$\underline{u}(\underline{x}) = \underline{u^*}(\underline{x}) \qquad on\ \partial\Omega_u \tag{Eq. 2-26}$$

where $\underline{\underline{\sigma}}$ is the Cauchy stress second-order tensor, $\underline{f}$ is a body force, $\mathbb{C}$ is the fourth-order elasticity tensor, $\underline{u}$ denotes the displacement vector, $\underline{n}$ is a unitary vector normal to $\partial\Omega$, and the linearized strain tensor is as below:

$$\underline{\underline{\varepsilon}} = \frac{1}{2}\left(\nabla \underline{u} + \nabla^T \underline{u}\right) \tag{Eq. 2-27}$$

Then using a set of methods, these equations and boundary conditions are transferred into an integral formulation known as weak form as type below:

$$\int_V \nabla\delta\underline{u} : \underline{\underline{\sigma}} dV - \oint_{Sf} \delta\underline{u} \,.\, \underline{F}^* dS - \int_V \delta\underline{u} : \underline{f} dV = 0 \qquad \text{Eq. 2-28}$$

From a discretization of the domain Ω into small-sized elements and the choice of interpolation functions of the unknown fields, it is possible to finally replace the partial differential equations in linear algebraic equations. The set of equations forms a linear system for linear elasticity problems assuming small disturbances:

$$\underline{\underline{K}} . \underline{U_{Nd}} = \underline{F} \qquad \text{Eq. 2-29}$$

where $\underline{\underline{K}}$ represents the stiffness matrix, $\underline{U_{Nd}}$ the vector of nodal displacements and $\underline{F}$ the vector of nodal forces.

The thermal behavior of the microstructures is also analyzed using the FEM, following a procedure similar to the mechanical simulations. In this case, the governing partial differential equation expresses the balance of heat flux within the domain, associated with prescribed thermal boundary conditions.

The thermal problem seeks the temperature field $\underline{T}(\underline{x})$ that satisfies the steady-state heat conduction equation over the domain $\Omega \subset R^D$:

$$\nabla . \underline{\Phi}(\underline{x}) + \underline{q}(\underline{x}) = 0 \qquad on\ \Omega \tag{Eq. 2-30}$$

$$\underline{\Phi}(\underline{x}) = -\underline{\underline{\Lambda}} . \underline{T}(\underline{x}) \tag{Eq. 2-31}$$

where $\underline{\Phi}(\underline{x})$ is the local heat flux vector, $\underline{\underline{\Lambda}}$ is the thermal conductivity tensor (or scalar if isotropic), $\underline{T}(\underline{x})$ is the temperature field, and $\underline{q}(\underline{x})$ represents the internal heat generation per unit volume (assumed to be zero in most cases).

Boundary conditions are applied on the domain boundary $\partial\Omega$, consisting of:

- Prescribed temperatures $\underline{T}^*$ on $\partial\Omega_T$ (Dirichlet conditions),
- Prescribed heat fluxes $\underline{\Phi}^*$ on $\partial\Omega_\Phi$ (Neumann conditions).

The boundary conditions are thus:

$$\underline{T}(\underline{x}) = \underline{T}^*(\underline{x}) \qquad on\ \partial\Omega_T \tag{Eq. 2-32}$$

$$\underline{\Phi}(\underline{x}) . \underline{n}(\underline{x}) = \underline{\Phi}^*(\underline{x}) \qquad on\ \partial\Omega_\Phi \tag{Eq. 2-33}$$

where n_x is the outward unit normal vector at the boundary.

Similar to the mechanical case, the strong form is transformed into the weak form:

$$\int_V \nabla \delta\underline{T} . \underline{\underline{\Lambda}} \nabla \underline{T} dV - \oint_{Sf} \delta\underline{T}\, \underline{\Phi}^* dS - \int_V \delta\underline{T}\, \underline{q} dV = 0 \tag{Eq. 2-34}$$

where $\delta\underline{T}$ is a virtual temperature variation field.

After discretization into finite elements and interpolation of the unknown temperature field, the system of equations becomes:

$$\underline{\underline{K}}.\underline{T_N} = \underline{Q} \qquad \text{Eq. 2-35}$$

Where $\underline{\underline{K}}$ is the thermal conductivity matrix, $\underline{T_N}$ is the vector of nodal temperatures, and $\underline{Q}$ is the vector of nodal heat fluxes.

Thus, the FEM provides the distribution of temperature fields within the heterogeneous material, allowing the evaluation of the apparent thermal conductivity through homogenization.

Section 2.1 provided a comprehensive overview of methods used to predict the elastic properties of particle-based composites. It began with analytical homogenization, covering classical bounds (Voigt, Reuss, Hashin–Shtrikman) as well as micromechanical models (Eshelby's solution, Mori–Tanaka, self-consistent schemes) and their inherent assumptions and limitations. It then turned to numerical homogenization, highlighting the central role of RVEs and SVEs and detailing various RVE-generation approaches, experimental reconstruction (e.g., X-ray CT), physics-based simulations (phase-field, molecular dynamics), and geometry-driven algorithms (RSA, rigid multibody dynamics). The discussion also addressed material assignment, meshing criteria, and the formulation and solution of finite-element boundary-value problems. Together, these methods form a robust framework for estimating effective elastic behavior. In the next section 2.2, this

foundation is built upon by examining how particle shape and volume fraction affect the composite's elastic response.

2.2- Effect of particle shape and volume fraction on elastic properties or even other properties

The reinforcement shape in particle-reinforced composites significantly affects their physical properties and the accuracy of predictions derived from RVEs. The morphology of the inclusions, characterized by their shape, aspect ratio (the ratio of a particle's length to its width or diameter), and orientation, determines the mechanical response of the composite under various loading conditions. This chapter explores the influence of reinforcement shape on key macroscopic properties, such as stiffness, strength, and elasticity, and examines how these factors integrate with RVE-based modeling approaches to predict composite behavior.

In RVEs, inclusions are frequently modeled as idealized convex shapes, such as spheres and polyhedral, or more complex shapes such as capsules, cylinders, ellipsoids, or cylinders. Observational studies reveal that inclusions exhibit a wide range of geometries, as illustrated in Figure 2-13, spanning from aspect ratios close to unity to much larger values.

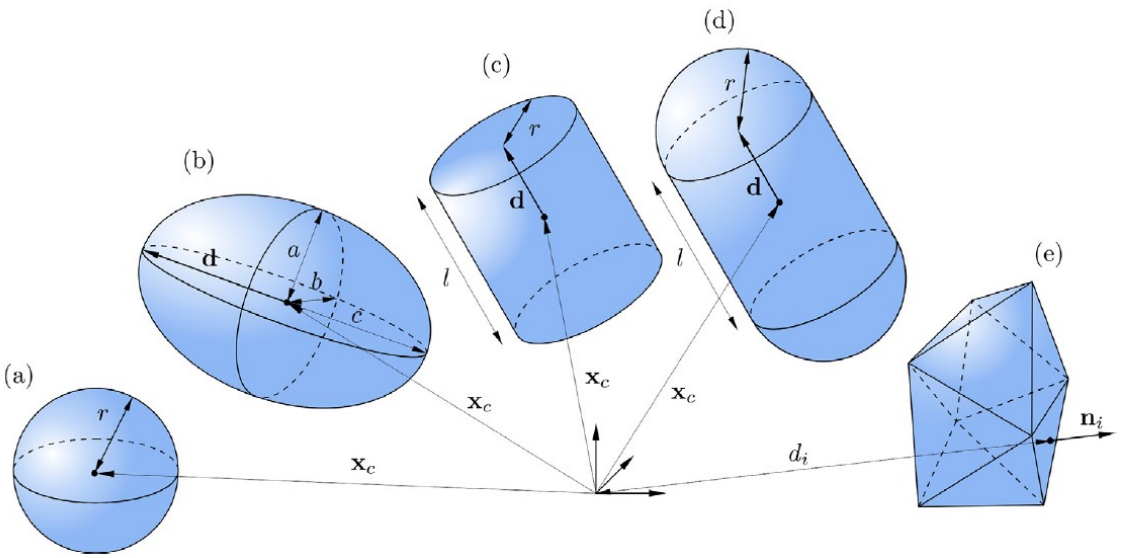

Figure 2-13. Geometric primitives: (a) sphere, (b) ellipsoid, (c) cylinder, (d) capsule, (e) polyhedron. Spheres are isotropic and do not have an orientation, thus are described via the center point X_c and the radius r. For ellipsoids, capsules and cylinders, the orientation d needs to be considered. In addition, for ellipsoids, the three half-axes are described by a; b; and c, for capsules and cylinders the radius r and length l need to be stated. Convex polyhedral are defined by the intersection of half spaces [76].

These geometries, along with factors like particle size, aspect ratio, and volume fraction, is important in determining the overall mechanical and physical properties of the composite. In the literature, particle volume fractions below 20 to 25 % are typically considered moderate, as they can be modeled reliably using classical RSA or similar approaches. Fractions exceeding ~30 % are generally referred to as high-volume fractions in the modeling context, since particle–particle interactions, packing limitations, and meshing difficulties make accurate numerical homogenization increasingly challenging.

It should be emphasized that this definition is not absolute. The notion of what constitutes “high” depends on several factors, including particle geometry, aspect ratio,

and the numerical method employed. For elongated particles in particular, the effective difficulty of modeling increases substantially, meaning that even lower volume fractions may already behave as high volume fraction cases. However, in real materials and experimental studies, particle volume fractions can reach much higher values, in some cases exceeding 50 %. The distinction lies in the fact that what is considered “high” for modeling is defined by the limitations of numerical generation and meshing methods, rather than by the physical upper bound achievable in manufacturing.

Additionally, statistical and stereological parameters such as size distribution, orientation, and pair correlation functions provide insights into microstructural influences on composite performance.

The performance of particle-based composites is heavily influenced by the uniformity of both particle distribution and orientation (in case of non-spherical particles) within the matrix. Achieving this uniformity is critical to avoiding stress concentrations and ensuring optimal performance.

The shape of reinforcement particles directly impacts stress distribution, load transfer, and the overall mechanical performance of composites. Reinforcements with low aspect ratios, such as spheres, offer simplicity in modeling and fabrication, generally lead to isotropic material properties. However, their ability to reinforce the matrix is limited due to reduced surface area for load transfer. Conversely, elongated shapes, like fibers or ellipsoids, introduce anisotropy, enhancing properties in specific directions but potentially

leading to stress concentrations and localized failures. Ellipsoidal and cylindrical inclusions provide better load transfer efficiency due to their increased surface area and directional alignment. These shapes enhance the stiffness and strength of the composite along specific axes but may require careful alignment during manufacturing. Particles with polyhedral or irregular geometries can introduce complex interactions within the matrix, affecting the stress distribution and fracture mechanisms. These shapes are more representative of natural or industrial particles, offering insights into real-world applications. Reinforcements with high aspect ratios, such as fibers, significantly enhance tensile strength and stiffness in the direction of alignment. However, their effectiveness diminishes with misalignment or clustering.

The RVE is a critical concept in multiscale modeling, capturing the statistical and geometrical features of the microstructure to predict macroscopic properties. The shape and distribution of reinforcements within the RVE influence its representativeness and accuracy. Smaller RVEs are sensitive to particle geometry, with significant variations in predicted properties observed for irregular or elongated shapes. Larger RVEs reduce this variability, providing more reliable results. Studies indicate that increasing the aspect ratio of particles enhances directional stiffness and strength but may lead to higher computational demands for accurate modeling. Incorporating statistical measures such as size and orientation distributions, covariance, and pair correlation functions improves the representativeness of RVEs. These metrics are particularly relevant for irregular and non-spherical particles. While idealized shapes simplify computational modeling, real-world particles often deviate from these assumptions, necessitating advanced simulation

techniques and higher computational resources. Advances in 3D imaging and computational power offer opportunities to model complex particle shapes more accurately, improving the predictive capabilities of RVEs for composite materials.

The study by Kari et al. [77] investigates the influence of particle size and volume fraction on the elastic behavior of spherical particle-reinforced composites using numerical homogenization techniques based on the FEM. The research focuses on constructing RVEs with randomly distributed spherical particles, using a modified random sequential adsorption algorithm to achieve high volume fractions of up to 60 %. The findings demonstrate that particle volume fraction is the primary determinant of effective elastic properties, including Young's modulus, Poisson's ratio, and shear modulus, while particle size has negligible influence in the linear elastic regime. The study emphasizes the importance of RVE size in accurately representing the composite's macroscopic properties, with specific guidelines provided to minimize errors in homogenization predictions. By comparing the numerical results with analytical models such as Torquato's third-order approximations and the Hashin-Shtrikman bounds, the study validates its approach and highlights its applicability to high-volume fraction composites. Although the study exclusively evaluates spherical particles, it establishes a foundational understanding of how particle volume fraction impacts elastic behavior, paving the way for further research on the role of particle shape and its interaction with size and distribution.

The study by Kari et al. [66] examines the impact of fiber volume fraction and aspect ratio on the elastic properties of composites reinforced with Randomly Distributed Short cylindrical Fibers (RDSF) and Transversely Randomly Distributed Short cylindrical Fibers (TRDSF) (Figure 2-14).

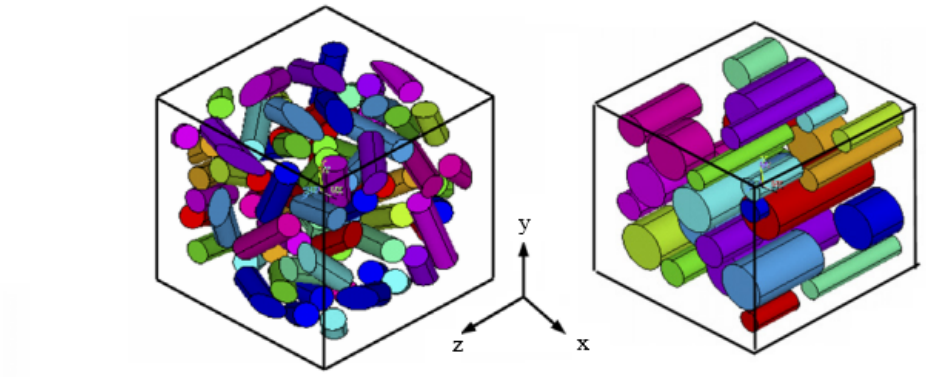

Figure 2-14. RDSF and TRDSF composites RVEs [66].

Using a finite element-based numerical homogenization approach, the authors developed RVEs to evaluate effective material properties under periodic boundary conditions. The findings reveal that the elastic properties, including Young's modulus, Poisson's ratio, and shear modulus, are strongly influenced by the volume fraction of fibers in both RDSF and TRDSF composites. For RDSF composites, the properties primarily depend on the fiber volume fraction, and minimal anisotropy is observed due to the random orientation of fibers across all three coordinate directions. In contrast, TRDSF composites show significant dependence on fiber aspect ratio, especially for the longitudinal elastic modulus (E_{33}), which increases considerably with higher aspect ratios before stabilizing at values close to those of continuous fiber composites. However, for RDSF composites, changes in fiber aspect ratio have a negligible effect on the elastic

properties. The study also emphasizes the importance of adequately sized RVEs to ensure accurate and statistically representative predictions of composite properties. The numerical results closely align with analytical models such as the Hashin-Shtrikman bounds and self-consistent methods, demonstrating the reliability of the homogenization approach. Overall, this research provides valuable insights into how fiber volume fraction and aspect ratio influence the elastic behavior of short fiber composites. The differentiation between RDSF and TRDSF composites highlights the critical role of fiber orientation and aspect ratio in designing composites with specific mechanical properties, enabling applications that demand tailored performance.

The research by Böhm and Rasool [78] provides a comprehensive exploration of how particle shapes influence the macroscopic and microscopic behaviors of particle-reinforced composites, offering significant insights into material design. Their earlier work in [79] laid the foundation for understanding particle shape effects on linear behaviors, including elastic, thermoelastic, and thermal conduction responses. As illustrated in Figure 2-15, finite element analysis was performed on multi-particle unit cells containing spheres, cubes, octahedra, and tetrahedra, each at a fixed volume fraction of 20 %. The study demonstrated that particle shape significantly influences both macroscopic and microscopic behaviors. The results indicate that polyhedral shapes enhance effective elastic moduli and thermal conductivity compared to spherical particles. However, this improvement comes at the cost of increased microscopic stress and flux concentrations, which could compromise material integrity. The study highlighted the

importance of balancing enhanced macroscopic properties with the risks of localized stresses in material design.

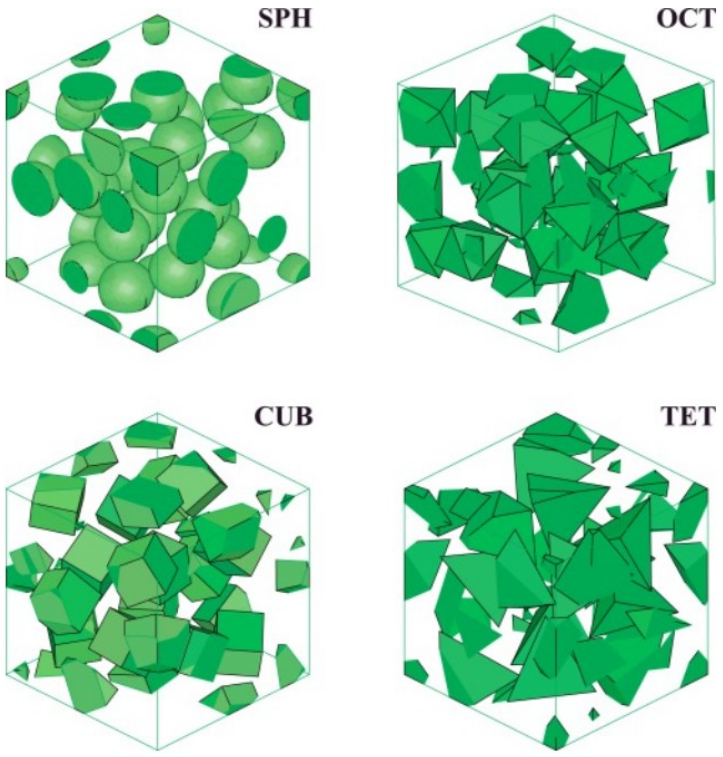

Figure 2-15. Typical periodic multi-particle volume elements, each containing some 21 identical spherical (SPH), octahedral (OCT), cube-shaped (CUB), or tetrahedral (TET) particles of volume fraction 0.2 [78].

Building on these findings, their subsequent work in 2016 [78] extended the investigation to the thermos-elasto-plastic domain, examining how particle shapes affect the non-linear behavior of composites under mechanical and thermal loading. This study revealed that tetrahedral particles exhibit the stiffest response, while spherical particles remain the most compliant. Furthermore, polyhedral particles, though beneficial for stiffness and strain hardening, introduced higher residual stresses and stress concentrations, making them more prone to microdamage under operational conditions.

This work emphasized the essential function of particle shape in tailoring composite performance, particularly in applications requiring a balance between stiffness, strength, and durability. Together, these studies underscore a progression in understanding the complexities of particle-reinforced composites, moving from linear to non-linear behavior analysis and providing a coherent framework for designing materials optimized for specific engineering requirements. The transition from fundamental to advanced investigations reflects the evolving focus on practical applications and challenges in composite material design.

The study by El Moumen et al. [80] investigates the effect of particle shape on the effective elastic properties and RVE size of two-phase composites. Using numerical homogenization techniques based on finite element simulations, the authors evaluate three particle shapes: spherical, prolate (elongated), and oblate (flattened) as illustrated in Figure 2-16. The study also incorporates statistical and morphological analyses to better understand the relationship between particle shape and composite behavior. The findings indicate that particle shape significantly affects elastic properties in volumes smaller than a representative volume of RVE, with notable variations in elastic moduli due to changes in particle geometry and orientation. However, for volumes equal to or larger than a representative volume, the influence of particle shape becomes negligible, and the effective properties converge regardless of the particle morphology. The study demonstrates that ellipsoidal particles require larger RVE sizes compared to spherical particles, reflecting increased heterogeneity in microstructures with elongated or flattened particles. The authors further establish that statistical parameters such as covariance,

variance, and integral range are critical for characterizing the microscale heterogeneity of composites. They introduce an equivalent morphology concept, where ellipsoidal particles can be replaced with spherical particles of equivalent volume to achieve similar effective elastic properties, though the RVE sizes may differ. Overall, this research highlights the importance of considering particle shape in the design and analysis of particle-reinforced composites, especially when working with volumes smaller than the RVE. It provides a comprehensive framework for linking particle morphology with mechanical behavior through combined numerical and statistical approaches.

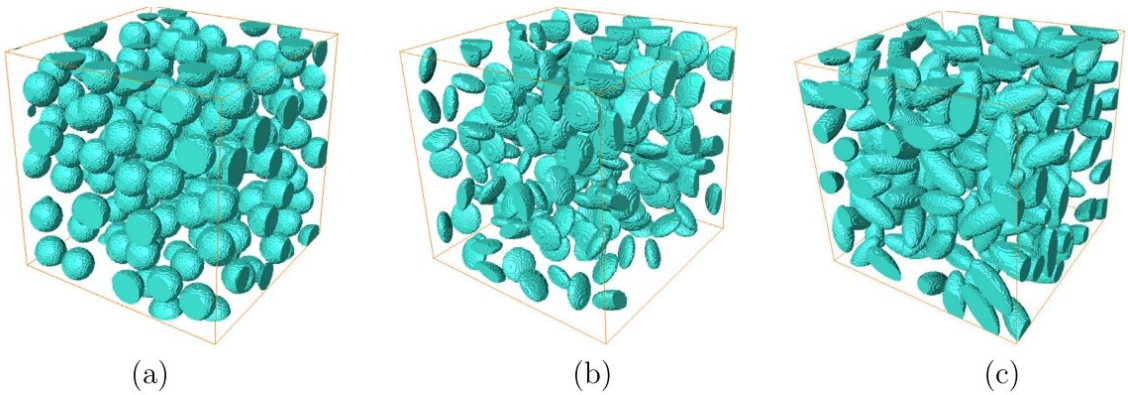

Figure 2-16. Generated RVEs: (a) spherical particles, (b) oblate spheroids, and (c) prolate spheroids [80].

The study by Rani et al. [81] investigates the impact of particle dispersion on the mechanical properties of polymer composites reinforced with Spent Coffee Bean Powder (SCBP) particles in a Polypropylene Carbonate (PPC) matrix. The analysis covered SCBP filler contents of 5 %, 10 %, 15 %, 20 %, and 25 % weight fraction. Using an automated image analysis tool developed within Python, the researchers quantitatively assessed particle and cluster size distributions and their effects on tensile strength and modulus.

The tool enabled detailed statistical analysis of microstructural features such as particle clustering and agglomeration. Key findings highlight that particle dispersion and clustering significantly influence mechanical properties. The microstructural analysis revealed a bimodal distribution of particle clusters, including the presence of a secondary phenomenon termed "clustering of clusters." This phenomenon became more prominent with higher filler content, particularly beyond 20 % of weight fraction, leading to a reduction in tensile strength and modulus. The researchers introduced a modified effective volume fraction to account for clustering effects, successfully integrating it into the rule-of-mixture model. This modification improved predictions of composite tensile strength and modulus, capturing non-linear trends observed in experimental data. The study emphasizes the necessity of quantitatively linking particle microstructure with composite mechanical performance. The proposed effective volume fraction also demonstrated applicability in other theoretical models, offering a generalized framework for enhancing the predictability of composite properties in systems with heterogeneous particle distributions.

The study by Yun et al. [82] focuses on the elastic properties of polypropylene (PP) and ultra-high molecular weight polyethylene fiber composites, investigating the effects of fiber aspect ratio and volume fraction. The authors employ FEA and the Halpin-Tsai model to predict the elastic modulus and shear modulus of these composites under varying conditions. The study examines volume fractions of 5 %, 10 %, 15 %, 20 %, and 25 %, with fiber aspect ratios ranging from 3 to 15 as illustrated in Figure 2-17.

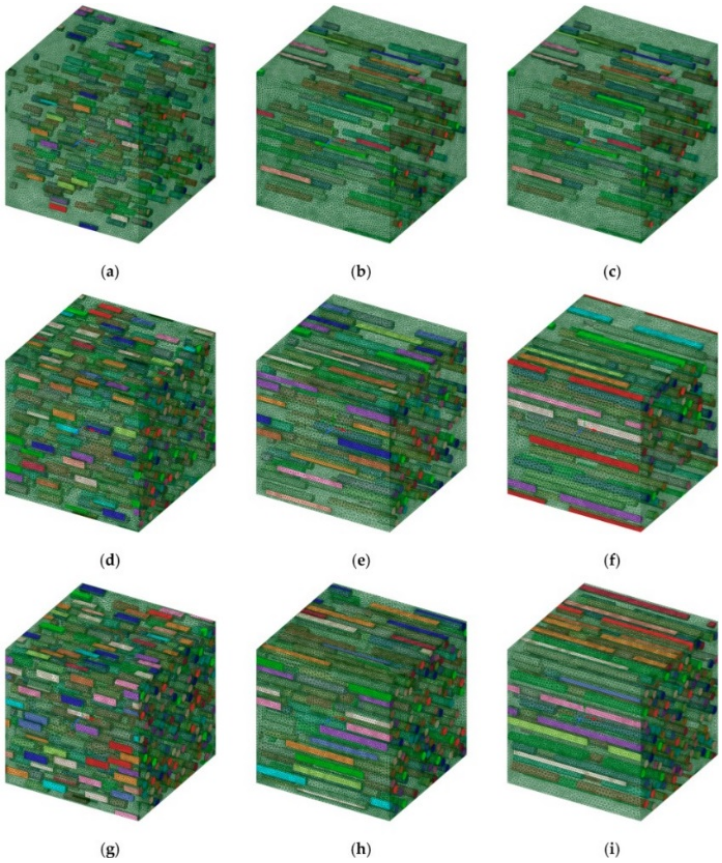

Figure 2-17. Different modeling under evaluation in [82].

Results demonstrate that the elastic modulus in the fiber length direction (E_{11}) increases proportionally with both the aspect ratio and volume fraction. At higher volume fractions (25 %) and aspect ratios (15), the elastic modulus reaches its peak value of approximately 5900 MPa in FEA simulations, though deviations from the Halpin-Tsai model grow with increasing fiber aspect ratios and volume fractions. The transverse modulus (E_{22}) is less affected by volume fraction and more by the aspect ratio, while the shear modulus (G_{12}) increases linearly with volume fraction and aspect ratio in the Halpin-Tsai model, contrasting with the FEA results. The study underscores the significance of fiber orientation and distribution, particularly at higher aspect ratios, where discrepancies

between FEA and the Halpin-Tsai model arise due to the random orientation assumed in the FEA model versus the lattice-based assumptions of the Halpin-Tsai model. A contour graph aids in predicting elastic properties based on these parameters, facilitating the optimization of PP/UHMWPE composite designs for specific mechanical requirements.

The study by Siraj et al. [83] evaluates the effects of particle characteristics, specifically size and weight fraction, on the mechanical and physical behavior of High-Density PolyEthylene (HDPE) composites reinforced with silica fillers. focuses on HDPE composites reinforced with silica fillers derived from raw sand, investigating how particle size (25 μm and 5 μm) and weight fraction (0 %, 20 %, 35 %, and 50 %) affect the mechanical properties of the resulting material. The silica particles were randomly distributed within the polymer matrix, leading to a heterogeneous microstructure in the prepared sheets. This random distribution was confirmed through Scanning Electron Microscopy (SEM), which revealed differences in particle dispersion and interparticle distance between the two particle sizes. The findings highlight significant impacts on toughness, elastic modulus, ductility, and density, with distinct trends observed for different particle sizes and filler loadings. The influence of particle size is particularly evident in the behavior of the composites. For larger particles (25 μm), toughness showed an initial improvement, peaking at 811 MPa at 20 %, compared to 611 MPa for pure HDPE. This improvement is attributed to silica clusters promoting partial stress within the matrix and altering crack propagation. However, as the filler content increased beyond 20 %, toughness declined due to stress concentrations resulting from particle agglomeration. In contrast, for smaller particles (5 μm), toughness consistently decreased with increasing

filler content, as their reduced interparticle distance facilitated agglomeration, creating structural instability and a brittle matrix. The elastic modulus also exhibited size-dependent behavior. Composites with 25 μm particles achieved higher modulus values compared to those with 5 μm particles. For example, at 20 %, the modulus increased from 1201 MPa to 1298 MPa for 25 μm particles but declined at higher filler contents due to stress concentrations. In contrast, composites with 5 μm particles displayed generally lower modulus values across all filler levels, with the exception of 50 %, where the dense packing of smaller particles contributed to localized modulus increases. This behavior underscores the role of particle size in balancing matrix integrity and reinforcement. Ductility, a measure of the material's ability to deform plastically under load, decreased substantially with increasing filler content for both particle sizes. While pure HDPE demonstrated ductility over 150 %, the value dropped by approximately 98 % at 50 % filler content. This reduction was more pronounced for 5 μm particles due to the higher tendency for agglomeration and the formation of structural voids, which weakened the matrix's ability to sustain deformation. The weight fraction of the fillers also played a significant role in the observed behavior. At lower filler levels (up to 20 %), composites benefited from enhanced particle dispersion, resulting in improved toughness and elastic modulus, especially for 25 μm particles. However, at higher filler levels (35 % and 50 %), agglomeration effects dominated, leading to declines in toughness and modulus and increased brittleness, regardless of particle size. Finally, the density of the composites increased with filler content for both particle sizes, as expected. The 25 μm particles produced slightly higher densities than the 5 μm particles, due to their larger size and

higher individual mass. Overall, the study highlights the critical influence of particle characteristics on the final behavior of the composites. Larger particles provided better performance at moderate filler contents, while smaller particles were more prone to agglomeration, limiting their effectiveness. These findings underscore the importance of optimizing particle size and filler loading to achieve desired mechanical and physical properties for specific applications.

The study by Tian et al. [84] explores the effective elastic properties of short-fiber-reinforced metal matrix composites (MMCs) using a two-step mean-field homogenization procedure. The composites under investigation consist of a magnesium alloy matrix reinforced with spatially randomly distributed short carbon fibers, characterized by an aspect ratio of 15. The fibers are distributed in a three-dimensional random orientation, as confirmed by their fiber orientation averaging procedure, which effectively captures the anisotropy introduced by the spatial randomness. This random distribution is essential to replicating realistic MMC microstructures, differing significantly from unidirectional or aligned fiber composites.

The primary objective of the study is to evaluate how fiber characteristics, including aspect ratio, volume fraction, and orientation, affect the composite's elastic behavior. The research employs multiple homogenization models, including Mori–Tanaka (M-T), double inclusion (D-I), Voigt, and Reuss models, to predict the elastic moduli and shear moduli. These predictions are validated against results from RVE-based finite element (FE) homogenization and uniaxial tensile testing.

The findings reveal that the elastic properties, such as elastic moduli and shear moduli, are strongly influenced by the fiber volume fraction. As the volume fraction of fibers increases, both elastic moduli and shear moduli improve due to enhanced load transfer between the matrix and the reinforcement. At lower volume fractions (≤ 15%), predictions from the M-T and D-I models closely match those from the RVE-FE homogenization method, indicating their reliability for accurately capturing elastic behavior at low fiber content. At higher fiber volume fractions, the predictive accuracy of these models diminishes, leading to the development of a modified two-step mean-field homogenization approach. This modified method combines the D-I and M-T models in the first homogenization step and employs a Voigt-Reuss interpolation in the second step, providing more precise results across a broader range of volume fractions.

The aspect ratio of the fibers, fixed at 15, contributes to the anisotropic mechanical properties of the composites due to their three-dimensional random orientation. The fiber orientation transformation procedure effectively incorporates these characteristics into the homogenization framework, ensuring that the influence of orientation is accurately captured in the final predictions. This approach highlights the necessity of considering not only volume fraction but also fiber orientation and distribution in designing MMCs for optimal performance.

Overall, the study demonstrates the vital part of fiber characteristics, including volume fraction and orientation, in determining the elastic behavior of short-fiber-reinforced MMCs. The proposed two-step mean-field homogenization procedure,

especially its modified version, offers a robust tool for accurately predicting the elastic properties of these composites, making it highly relevant for applications requiring lightweight materials with superior mechanical performance.

The study by Ezzaraa et al. [85] explores the elastic properties of 3D-printed wood-polylactic acid (PLA) composites using numerical homogenization techniques. The research focuses on understanding the influence of particle characteristics, such as wood volume fraction, particle shape, and internal porosity, on the mechanical performance of the composites. The samples under investigation were fabricated using fused deposition modeling (FDM), a widely used additive manufacturing technique. The wood particles were derived from beech wood and embedded in a PLA matrix. The composites exhibited randomly distributed particles with no directional alignment, reflecting the heterogeneous nature of the microstructure. RVEs were used to model the microstructure, employing a random sequential adsorption algorithm to ensure a realistic particle distribution within the composite matrix. The study evaluates the influence of particle characteristics on the composite's mechanical behavior. The elastic modulus increased with wood volume fractions ranging from 10 % to 30 %, with a 35 % enhancement observed at the highest fraction. This improvement was attributed to the significantly higher modulus of wood (14.31 GPa) compared to PLA (3.72 GPa). The particle shape was also found to play a crucial role in determining the composite's anisotropy. Ellipsoidal particles, characterized by varying aspect ratios, produced a transversely isotropic material behavior, with the longitudinal modulus (E_{11}) increasing significantly as the aspect ratio rose. Conversely,

spherical particles resulted in isotropic elastic properties. Porosity was another critical factor investigated in the study. The inclusion of pores, ranging from 0.09 mm to 0.43 mm in diameter, introduced reductions in the elastic modulus. For instance, at 10 % wood content, an increase in porosity from 2 % to 7 % caused a 9.37 % decrease in the elastic modulus. Despite this, the model showed strong agreement with experimental data, with relative errors not exceeding 10 %. Overall, the findings emphasize the importance of optimizing wood particle content, shape, and porosity to tailor the mechanical properties of wood-PLA composites for specific applications. The numerical homogenization technique effectively predicts the elastic behavior, providing a valuable tool for designing high-performance 3D-printed composites.

The study by Kouassi et al. [86] focuses on the determination of effective elastic properties of nanocomposites reinforced with organoclays using numerical and experimental methods. The research examines how dispersion, particle morphology, and weight fraction of the organoclays influence the elastic properties of the composites. The samples under investigation consisted of PMMA reinforced with organoclay fillers at weight fractions ranging from 1 % to 5 %. The microstructure of these nanocomposites was characterized as having random dispersion, as confirmed by Ripley functions and analysis of transmission electron microscopy (TEM) images. Platelet and prism inclusion types were modeled based on the morphology and size distribution of the particles, with aspect ratios of 0.01, 0.02, and 0.05 used to generate RVEs for numerical simulations. The results highlight that both the weight fraction and the aspect ratio of the particles play significant roles in determining the elastic properties of the nanocomposites. The Young's

modulus and shear modulus increased with the volume fraction of the organoclays, with higher values observed for lower aspect ratios. This trend is attributed to the lower probability of aggregation at smaller aspect ratios, which ensures better dispersion and stress transfer within the matrix. Conversely, as the aspect ratio increased, the likelihood of clustering grew, negatively impacting the mechanical properties. Prism inclusions generally provided slightly better elastic properties compared to platelets, which may be due to the differences in meshing and geometry. For weight fractions of 1 % to 2 %, the organoclays were predominantly exfoliated, resulting in superior mechanical performance. However, at higher weight fractions, the microstructure transitioned to a mix of exfoliated, intercalated, and aggregated morphologies, leading to a reduction in mechanical properties. The study further validated the numerical predictions against experimental data, with good agreement observed for intermediate aspect ratios (AR2 = 0.02). This research underscores the importance of optimizing particle dispersion, morphology, and weight fraction to achieve desired mechanical properties in PMMA-organoclay nanocomposites. The integration of Ripley functions and Digimat-FE modeling provides a robust framework for accurately predicting the effective elastic properties of complex composite materials.

The study by Wolfsgruber et al. [87] investigates the effects of filler type, shape, and volume fraction on the thermal conductivity and mechanical properties of thermoplastic matrix composites (PMCs). The materials examined include five different thermoplastics—polyamide 6 (PA6), polypropylene (PP), polycarbonate (PC), thermoplastic polyurethane (TPU), and polysulfone (PSU)—reinforced with various

inorganic fillers, including aluminum oxide (Al2O3), zinc oxide (ZnO), and boron nitride (BN). The fillers exhibited different shapes, such as cubic, needle-like, and platelet structures, and were incorporated into the matrix at weight fractions ranging from 10% to 40%. The samples under investigation were prepared using a twin-screw extrusion process followed by injection molding. This manufacturing process resulted in a heterogeneous distribution of filler particles within the thermoplastic matrices, with particle orientation influenced by the melt flow during injection molding. The microstructure displayed a "skin-core" effect, with filler orientation differing between surface and core regions, particularly for platelet-shaped fillers. The study specifically evaluates the impact of particle characteristics on the elastic modulus, tensile strength, density, and thermal conductivity of the composites. The elastic modulus increased with filler content, and the rate of increase varied depending on the filler shape and its interaction with the matrix. Platelet-shaped boron nitride exhibited the highest reinforcement effect due to its large aspect ratio and ability to form continuous thermal pathways. Conversely, cubic and needle-like particles demonstrated moderate reinforcement effects. The work of adhesion between filler and matrix was identified as a critical factor affecting the elastic modulus, with materials like PA6 and PSU exhibiting higher adhesion and thus greater stiffness compared to TPU or PP. Tensile strength results showed a contrasting behavior, with some matrices (e.g., PA6 and PSU) exhibiting reduced tensile strength at higher filler contents due to stress concentrations and reduced chain mobility. Conversely, PC exhibited improved tensile strength due to better filler-matrix interaction facilitated by siloxane modifications in the matrix. Thermal conductivity increased with filler content, with

significant differences observed based on filler shape and type. Platelet-shaped fillers, such as boron nitride, demonstrated the highest thermal conductivity improvements due to their ability to bridge larger thermal paths. The study found that semicrystalline matrices (PA6 and PP) exhibited higher thermal conductivity than amorphous matrices (PC, PSU, TPU), although crystallinity itself did not significantly change with filler addition. In summary, the findings emphasize the importance of filler type, shape, and content in determining the thermal and mechanical properties of thermoplastic composites. The results provide a foundation for optimizing filler-matrix combinations for applications requiring specific thermal and mechanical performance.

In summary, Section 2.2 examined how reinforcement shape and volume fraction govern composite behavior, evaluating inclusion geometries from simple spheres and convex polyhedra to ellipsoids, capsules, and cylinders across volume fractions from dilute (< 10 %) to around 30 %. These studies confirm that particle morphology critically influences stiffness, strength, and elasticity: spherical particles often lead to isotropic responses but impose packing limits, whereas elongated or irregular particles can enhance stiffness in preferred directions but require larger RVEs to achieve statistical representativeness. Although many works confirm the importance of geometry, most existing studies have focused on low-elongation or unidirectionally elongated particles, with limited systematic evaluation of high aspect ratio fibers. This gap stems from the difficulty of generating such models with existing RVE/SVE algorithms.

The literature also shows that increasing particle content intensifies particle–particle interactions and meshing difficulties, making homogenization significantly more challenging beyond ~30 % volume fraction. For this reason, fractions around 30 % are typically referred to as high-volume fractions in the modeling context, even though experimental composites may reach much higher reinforcement contents.

This thesis specifically addresses these modeling challenges by developing methods capable of generating and analyzing microstructures with volume fractions of 30 %, which are regarded as high in the modeling literature, while acknowledging that real-world composites may present even denser microstructures, thereby extending the range of reliable numerical homogenization.

2.3- Conclusion

Despite decades of advances, from metals and ceramics to synthetic fiber-reinforced polymers and now natural fiber-reinforced composites, the accurate prediction of effective properties remains a critical challenge for modern materials design. A wide range of analytical and numerical homogenization techniques has been developed, ranging from classical bounds (Voigt, Reuss, Hashin–Shtrikman) and micromechanical models (Eshelby, Mori–Tanaka, self-consistent schemes) to numerical methods such as finite element analysis coupled with geometry-driven (RSA, rigid multibody dynamics) or physics-based (tomography, phase field) reconstructions. Nevertheless, several persistent challenges remain. First, geometry-driven algorithms routinely stall near the

jamming limit. Second, high-fidelity reconstruction methods (e.g., serial sectioning, X-ray tomography, phase-field simulations), while accurate, incur prohibitive computational cost and equipment requirements for routine use. Finally, numerical methods struggle to accommodate reinforcements with high aspect ratios, as mesh convergence issues and boundary voids escalate with increasing aspect ratio.

FEA coupled with homogenization has emerged as one of the most reliable tools for estimating elastic moduli and other effective properties of heterogeneous materials, yet it brings its own challenges like high computational cost, the need for precise microstructural data, and the difficulty of selecting a RVE that truly reflects the material's variability. In recognition of cases where a single RVE may be impractically large (e.g., cement or wood), the use of multiple, smaller SVEs has become widespread; however, generating SVEs that faithfully reproduce fiber geometry, distribution, orientation, shape, and volume fraction, while remaining compatible with FEA mesh convergence and time-efficiency requirements, remains an active area of research.

To address these limitations, our team (ERICCA) previously developed an automated numerical homogenization framework that integrates CAD, meshing, and FEA driven by both RSA and time-driven rigid multibody dynamics generator (detailed in [50, 73, 88]). This method is a generalized modeling approach for particle-based heterogeneous materials. This pipeline efficiently produces SVEs by enforcing minimum distance and angle criteria during particle placement, then applies an erosion-of-results technique to eliminate boundary effects and achieve target volume fractions for

homogenization. Although effective in matching experimental elastic moduli, its reliance on data removal rises doubts and it cannot fully capture boundary conditions influence.

Building on this foundation, the present work introduces two novel methodologies, Geometry Correction Method (GCM) and Mesh Cutting Method (MCM), that achieve high particle volume fractions without eroding results. GCM makes subtle, geometry-preserving adjustments to particle size, position, and orientation to eliminate voids at the SVE boundaries, while MCM generates a mesh over an extended domain before precisely trimming it to the SVE bounds, thereby preserving all computed element data. These advances enable a direct comparison with the erosion-based baseline to evaluate its accuracy, support accurate modeling of very large aspect-ratio fibers and enhance both computational efficiency and fidelity. Chapter 3 will detail the theoretical foundations and algorithmic implementation of GCM and MCM, setting the stage for a comprehensive evaluation of their performance against both the traditional erosion-based pipeline in Chapter 4 and experimental benchmarks in Chapter 5.

CHAPTER 3

METHODOLOGY

This chapter begins by reviewing the automated numerical modeling approach previously developed by our research group (ERICCA), which integrates CAD, meshing, and finite element analysis for microstructural modeling of particle-reinforced composites. The complete sequence of this methodology is outlined, including the erosion of results technique, which was introduced to compensate for boundary-induced voids and to enable high particle volume fractions by excluding results near the edges of the domain.

This previously developed workflow serves as the foundation for the two new methodologies proposed in this study. Two distinct methodologies are developed to achieve high volume fraction of particles without utilizing the erosion of results methodology. The objective of these methodologies is twofold: first, to enable verification of the erosion of results approach, and second, to assess the impact of boundary condition selection on final results and their convergence.

In Section 3.1, presents the review of previous approach. In Section 3.2, the Geometry Correction Method (GCM) is presented, which modifies particle geometries near boundaries to allow denser packing without creating voids. In Section 3.3, the Mesh Cutting Method (MCM) is introduced, which enables extraction of SVEs from a larger meshed domain, preserving complex particle configurations while allowing controlled application of boundary conditions.

These methods were developed to achieve high particle volume fractions without relying on the erosion of results and offer a more complete and boundary-aware framework for the homogenization of particle-based composites at high volume fractions.

3.1- A review of existing erosion of results method

In this section, an overview of previous study by our research team (ERICCA) (detailed in [50, 73, 88]), is presented. This method is a generalized and automated numerical homogenization modeling approach for particle-based heterogeneous materials.

The entire modeling framework of this method is obtained by integrating CAD, mesh generation and FEA tools. This integration is facilitated through the Unified Topology Model (UTM) [5]. UTM is a computational framework developed by the ERICCA team. This modular, scalable, and general-purpose environment establishes a connection between Boundary REPresentation (BREP) topological entities and mesh entities used in FEA as illustrated in Figure 3-1.

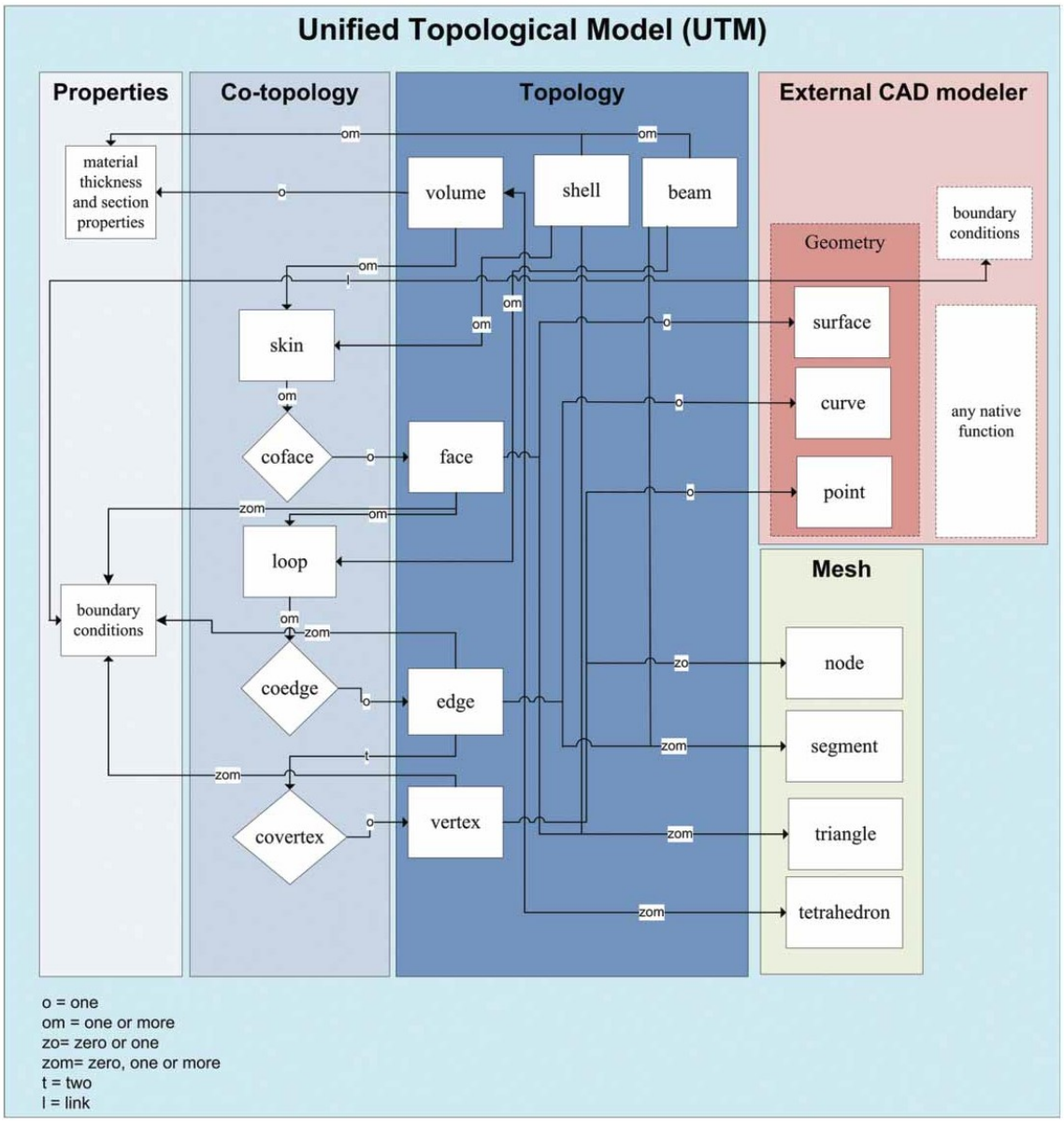

Figure 3-1. General architecture of the UTM [5].

Historically, the development of geometric modeling techniques, meshing algorithms, and FEA tools was carried out independently. This segmentation meant that little communication existed between the various steps of the numerical analysis process. A designer would first create a CAD model, then transfer it to a meshing software before

exporting the mesh to an FEA solver. Any modification based on the analysis results required starting over from scratch, making iterative refinement both time-consuming and inefficient. To address this limitation and accelerate the structural design process, significant efforts have been devoted to integrating these stages. The UTM establishes a bidirectional communication framework between these components, thereby enabling automatic updates and maintaining consistency throughout the design and analysis workflow. The UTM is built on the B-REP modeling framework while leveraging Object-Oriented Programming (OOP) principles, such as polymorphism and encapsulation, to enhance flexibility and interoperability. Encapsulation allows the UTM to interact with different CAD software without dependency on a specific modeler. Instead of rewriting compatibility functions for each new CAD tool, only the encapsulation layer needs to be adapted, significantly reducing development efforts when integrating new technologies. A key advantage of this approach is the automatic adaptation of CAD geometries for numerical analysis [89], allowing seamless modifications and direct compatibility with FEA tools. Modern Computer-Aided Engineering (CAE) software has since followed this trend, incorporating CAD modeling, meshing, and FEA solvers into a single platform with increasing levels of automation in transitions between modules.

With the UTM, boundary conditions must directly be applied to BREP topological entities, and FEA results can be mapped back to the original geometry, enabling comprehensive post-processing analysis. A key feature of the UTM is its co-topology framework, which addresses redundancies in geometric representations. In traditional B-

REP models, redundancy occurs among topological entities such as vertices and edges where two adjacent faces share a common edge, and two adjacent edges converge at a shared vertex. Furthermore, when representing two volumes that share a common face, the same problem appears for the adjacent faces. The co-topology approach eliminates these redundancies by associating each geometric entity with a single topological reference while maintaining orientation consistency. This strategy ensures that shared features between volumes, such as common faces, are uniquely defined and correctly oriented, preventing ambiguity in mesh generation, especially in particle-reinforced microstructures. Consequently, the UTM enables multidimensional modeling and simulation [90], making it well-suited for complex engineering applications.

The meshing process follows the B-REP hierarchy, associating each mesh element with a corresponding topological entity through a bidirectional link. Through its integrated approach, the UTM provides a robust computational environment for various applications, including pre-meshing optimization [91], automatic remeshing of FEA models following CAD modifications [92].

The workflow begins with node placement at vertices, followed by edge discretization, surface meshing using advancing front algorithm, and volume meshing with tetrahedral elements based on the surface triangulation. This structured approach ensures that geometric consistency is preserved, particularly when adapting CAD models for finite element simulations.

To further enhance interoperability, the FEA solver interface in the UTM employs a file-based exchange mechanism. Simulation data, including material properties, section properties (for beams and plates), and boundary conditions, are directly linked to topological entities rather than requiring manual definition of node and element groups. The solver reads the generated input files, executes the simulation, and the results are then automatically imported and associated with mesh elements in the UTM. This method simplifies model setup, accelerates the simulation process, and allows for easy solver substitution without modifying the core UTM architecture. One of the most significant applications of the UTM is in microstructural modeling of heterogeneous materials [74], where its advanced meshing strategies and co-topology framework allow accurate representation of particle-based composites.

As research advances, the UTM continues to evolve, further enhancing the seamless integration of CAD, meshing, and FEA into a unified and automated computational framework.

The methodology outlined in this study provides a structured framework that integrates geometric modeling, meshing, and FEA into a single automated process. This ensures consistency, reduces manual intervention, and enhances computational efficiency. The overall process consists of four main steps: (1) generation of the geometric model, (2) creation of the size map, (3) meshing, and (4) execution of finite element studies including post-processing and homogenization. All these steps are executed automatically and are followed by a post-processing stage, as illustrated in Figure 3-2.

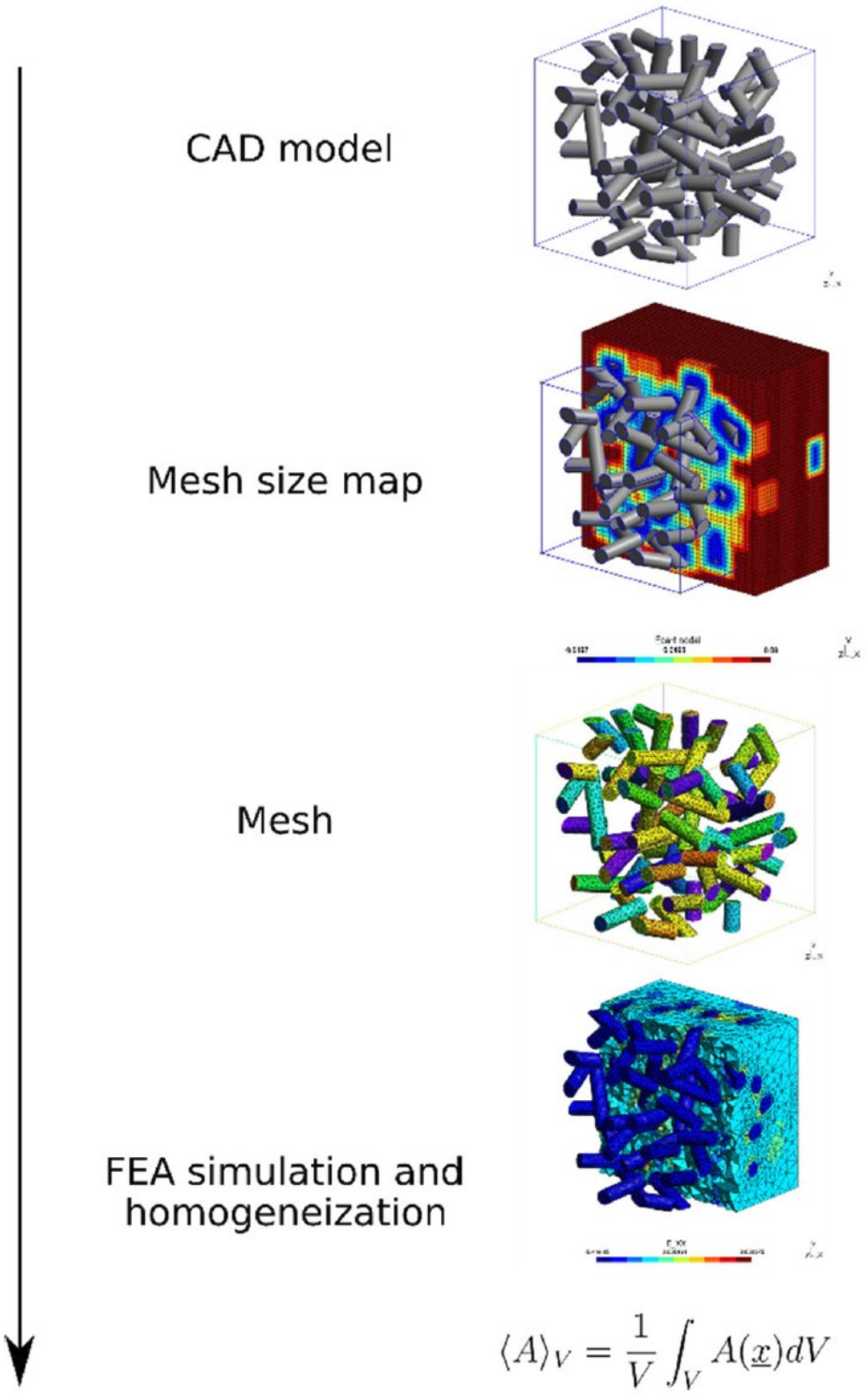

Figure 3-2. Overview of the SVE automatic generation process described in [73].

3.1.1- Generation of the geometric model

The adopted approach involves creating a RVE, composed of multiple SVEs. Each SVE is individually analyzed, and the overall properties of the RVE are determined by averaging the results obtained from all SVEs. The number and size of SVEs are carefully chosen to account for the natural variability in fiber properties. Moreover, numerical SVEs are designed to be smaller than physical samples to ensure that simulations remain computationally feasible within reasonable timeframes. To achieve realistic SVEs that accurately reflect real-world conditions, fibers must be represented with a high degree of precision.

The construction of the numerical model follows a structured sequence of steps. First, the geometric model of the microstructure is generated, where particles are inserted into the matrix while adhering to specific placement criteria. The geometric representation of the microstructure is built using a combination of Constructive Solid Geometry (CSG) and BREP techniques. These techniques allow for precise control over the placement and interaction of particles within the matrix. In this study, advanced Boolean operations, including union, intersection, and subtraction, are utilized to enable the efficient insertion of particles within the matrix. These operations ensure precise geometric construction and allow the creation of complex microstructures by accurately combining and modifying multiple volumes as required by the modeling process.

The two main approaches used for particle generation are RSA and MBD. The RSA approach sequentially inserts particles while ensuring non-overlapping conditions, but as

the volume fraction increases, available space diminishes, making further insertions difficult. The MBD approach, on the other hand, simulates particle movement and interaction by allowing dynamic rearrangement of particles until a stable configuration is reached. This method significantly improves packing density, making it more representative of real composite materials. The geometric generation process follows key stages.

In the first step, a particle distribution is generated using either RSA or MBD within a slightly larger domain of length $L + \Delta$, referred to as the generation domain, in order to avoid edge effects of particles intersecting the boundaries of the generation domain. To ensure mesh convergence in subsequent steps, minimum distance and angle criteria are applied to each particle. Only particles meeting these criteria are actually inserted into the CAD model of the SVE of length L. However, the resulting model shows a lack of particles near the boundaries of the sample, leading to a deviation from the target particle volume fraction.

3.1.2- Generation of the size map

Once the geometric model is established, the next step involves the generation of a size map, which governs the distribution of element sizes across the computational domain. The size map defines the nodal spacing for meshing, ensuring that areas near particle-matrix interfaces receive a finer discretization while bulk matrix regions use coarser elements. The size distribution is structured using a hierarchical refinement strategy, balancing computational efficiency and accuracy.

The size map is represented as a structured grid. The grid is generated by computing the bounding box of the microstructure and expanding it slightly to provide additional meshing flexibility. The process includes global nodal spacing assignment, where a baseline nodal spacing is assigned to all elements. Local refinement is applied at interfaces by refining the size near particle surfaces using distance-based constraints, ensuring at least two layers of elements exist between particle boundaries. Maintaining a minimum of two element layers is critical both for achieving mesh convergence and for allowing sufficient deformation freedom of the matrix. Specifically, this approach ensures that there are elements belonging exclusively to the matrix phase. If only a single layer of elements existed between a particle and the surrounding matrix, the elements of that layer would be shared between both the particle and the matrix, creating ambiguity in material assignment and hindering the correct representation of their mechanical behaviors. By enforcing at least two layers, elements can be clearly associated with either the matrix or the particles, preserving the physical integrity of the simulation. However, increasing the number of layers beyond the minimum requirement leads to a significant rise in the number of elements, thereby increasing computational cost and simulation time. A balance must therefore be maintained between mesh accuracy and computational efficiency. Finally, a smoothing algorithm is applied using a relaxation process to avoid abrupt size transitions, ensuring a smooth variation in element size across the domain.

3.1.3- Mesh generation

The meshing process discretizes the geometric model while ensuring topological conformity, element quality, and size map adherence. The meshing process follows a co-topology approach, where shared interfaces between particles and the matrix are meshed only once, preserving continuity and preventing redundant elements. Initially, the domain is meshed using linear tetrahedral elements, ensuring that the particle-matrix boundaries are well-defined. To improve numerical accuracy, the study employs quadratic element generation, where mid side nodes are introduced to enhance the representation of curved boundaries. To prevent poorly shaped elements, various mesh optimization techniques [93] are applied. First, on the 2D mesh composed of triangular elements, iterative node relocation and segment swapping are performed to improve the quality of the linear triangular elements. Then, during the 3D meshing stage, the quality of tetrahedral elements is continuously optimized by relocating nodes to enhance element shapes. Refinement of sharp angles is performed near corners and fiber intersections to avoid numerical instability. Aspect ratios of elements are controlled within an optimal range to ensure accurate FEA results. Near-boundary regions are refined to improve stress calculations and boundary condition enforcement. By integrating the size map with an adaptive mesh refinement strategy, the SVE model achieves a balance between accuracy and computational efficiency. The final mesh undergoes quality assessment based on the classical quality metric Q_k, defined as below, to guarantee numerical stability and convergence in FEA simulations.

$$Q_k = \frac{2\sqrt{6}r}{h_{max}} \quad \text{Eq. 3-1}$$

Where r is the inradius (the radius of the sphere inscribed within the tetrahedron), and h_{max} is the maximum edge length of the tetrahedron. This metric quantifies the element's deviation from the ideal shape, with values ranging from 0 (for a degenerate tetrahedron) to 1 (for a perfect equilateral tetrahedron). Higher values of Q_k indicate better-quality elements, which is essential for ensuring numerical stability and accuracy in finite element simulations.

3.1.4- Finite element analysis and homogenization

Following mesh generation, the FEA is conducted to evaluate the thermomechanical behavior of the composite material. The study integrates FEM solver, into the unified topology model, enabling automated execution of simulations. The FEA process involves the application of boundary conditions, including mechanical and thermal loading, followed by the computation of apparent material properties. Using volumetric averaging techniques, the study extracts effective properties such as Young's modulus, shear modulus, and thermal conductivity, ensuring a reliable characterization of the composite material. The homogenization process is conducted using Hill's macro-homogeneity condition, which ensures that the computed mechanical properties are representative of the overall material response.

Considering that mechanical properties of the glass-fiber composite are assumed to be isotropic; the macroscopically isotropic microstructure assumption is applied. Under this assumption, in the mechanical study, two principal types of macroscopic loadings are

applied to characterize the effective properties: spherical (hydrostatic) loading to determine the apparent bulk modulus (K_{app}) and deviatoric (pure shear) loading to extract the apparent shear modulus (G_{app}). Each loading is imposed under two types of boundary conditions: KUBC, prescribing uniform displacements proportional to position and SUBC, applying uniform pressures normal to the surfaces, ensuring that the deformation remains homogeneous.

Spherical loading aims to produce an isotropic expansion or contraction of the SVE, resulting in purely volumetric strain or stress without introducing shear components:

$$\underline{\underline{E}} = \begin{bmatrix} E & 0 & 0 \\ 0 & E & 0 \\ 0 & 0 & E \end{bmatrix} or \underline{\underline{\sum}} = \begin{bmatrix} \sum & 0 & 0 \\ 0 & \sum & 0 \\ 0 & 0 & \sum \end{bmatrix} \quad \text{Eq. 3-2}$$

This loading condition is used to determine the bulk modulus of the material.

Deviatoric loading aims to induce shear deformation or stress without any volumetric change, allowing the evaluation of the shear behavior of the composite microstructure:

$$\underline{\underline{E}} = \begin{bmatrix} 0 & E & E \\ E & 0 & E \\ E & E & 0 \end{bmatrix} or \underline{\underline{\sum}} = \begin{bmatrix} 0 & \sum & \sum \\ \sum & 0 & \sum \\ \sum & \sum & 0 \end{bmatrix} \quad \text{Eq. 3-3}$$

This loading is necessary for evaluating the apparent shear modulus. In both loading cases, careful constraints are added to prevent rigid body motion without interfering with the intended deformation patterns.

Once the simulation is solved, the apparent mechanical properties are extracted. The bulk modulus K_{app} is determined from the spherical loading results as:

$$K_{app} = \frac{Tr\left(\underline{\underline{\Sigma}}\right)}{3Tr\left(\underline{\underline{E}}\right)} \quad \text{Eq. 3-4}$$

The shear modulus G_{app} is extracted from deviatoric loading:

$$G_{app} = \frac{1}{3}\left(\frac{\Sigma_{xy}}{2E_{xy}} + \frac{\Sigma_{yz}}{2E_{yz}} + \frac{\Sigma_{xz}}{2E_{xz}}\right) \quad \text{Eq. 3-5}$$

In these equations, $\underline{\underline{\Sigma}}$ and $\underline{\underline{E}}$ are the volume averaged values (over the SVE) of stress and strain tensors obtained with FEA. Using this FEA homogenization, the apparent elasticity modulus for KUBC and SUBC boundary conditions is calculated

$$E_{app} = \frac{9K_{app}G_{app}}{3K_{app} + G_{app}} \quad \text{Eq. 3-6}$$

Regarding the thermal behavior, two types of thermal loadings are applied: a prescribed temperature gradient and a prescribed heat flux. In the first case, a temperature difference is imposed across two opposite faces while the others are thermally insulated. In the second case, a uniform heat flux is applied across two faces with thermal insulation on the others, and the temperature is fixed at a point to avoid rigid body motion of the temperature field.

After solving the thermal FEM problem, the apparent thermal conductivity along each principal direction is obtained from the volumetric averages of the heat flux (Φ_i) and temperature gradient (G_i):

$$\lambda_{app_i} = \frac{-\Phi_i}{G_i} \quad \text{Eq. 3-7}$$

where i represents the x, y, or z direction.

Finally, the overall thermal conductivity is calculated by averaging the three principal conductivities:

$$\lambda_{app} = \frac{\lambda_{app_x} + \lambda_{app_y} + \lambda_{app_z}}{3} \quad \text{Eq. 3-8}$$

Throughout both the mechanical and thermal analyses, the results are post-processed by volumetric averaging of fields over the entire SVE, ensuring that the extracted apparent properties are representative of the global microstructure and are not biased by local inhomogeneities or boundary effects.

3.1.5- Edge effects and erosion method

To address boundary effects that may introduce artifacts in the simulations, the study incorporates an erosion of results method, which progressively removes results of elements near the edges of the REV. This ensures that computed properties reflect the core microstructure rather than artificial boundary influences. The erosion process begins by defining a predefined erosion distance, within which elements results near the boundaries

are systematically removed. As elements results are eliminated, the remaining core structure is re-evaluated to ensure that material properties remain consistent and free from distortions introduced by edge effects. The process continues iteratively until mechanical and thermal properties stabilize, indicating that the retained volume provides an accurate representation of the material's behavior. In addition to filtering out the effects of boundary conditions, the erosion of results method also addresses geometric imperfections that arise during particle placement. Particularly when using MBD to generate microstructures, particles that do not meet strict insertion criteria near the domain edges are excluded, resulting in reduced particle density in those regions. For example, in Figure 3-3, the empty spaces near the SVE edges are visible in the resulting geometrical model of spherical and cylindrical particles with 10 % of particle volume fractions. A similar observation can be made in Figure 3-4 for the case of 30% particle volume fraction.

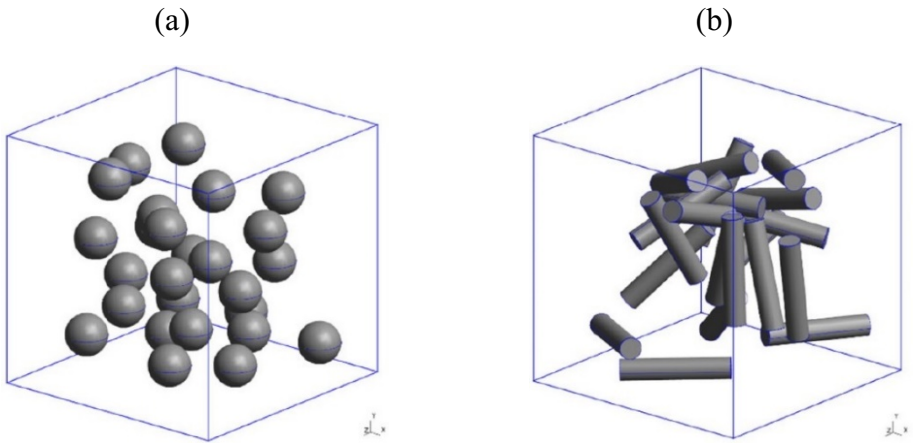

Figure 3-3. Illustration of BREP models for each MBD configurations: (a) 10 % of spheres, (b) 10 % of cylinders [73].

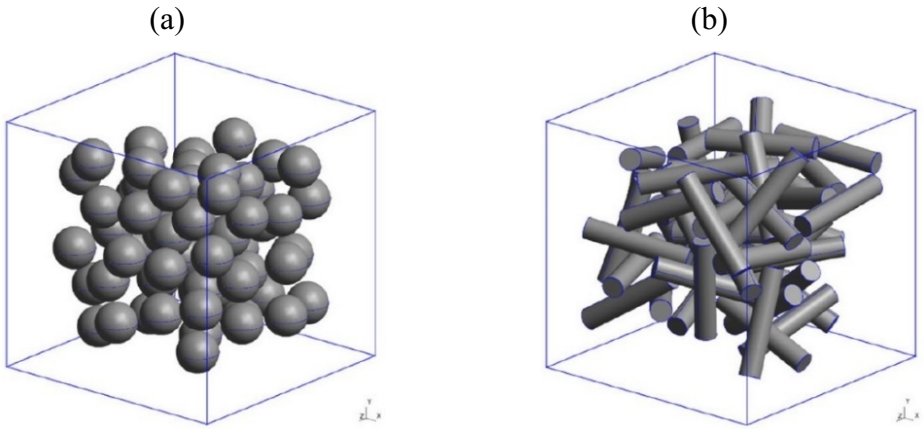

Figure 3-4. Illustration of BREP models for each MBD configurations: (a) 30 % of spheres, (b) 30 % of cylinders [73].

This incomplete geometry may distort the local response and thus the overall homogenized properties. The erosion technique avoids this by excluding the edge regions from the homogenization calculation, ensuring that only zones with complete and representative particle content contribute to the extracted properties.

Practically, the erosion method consists of defining a central subdomain by an erosion distance d_e and retaining only the finite elements whose centroids fall within this region as shown in Figure 3-5. A new volume average is then performed on this reduced domain.

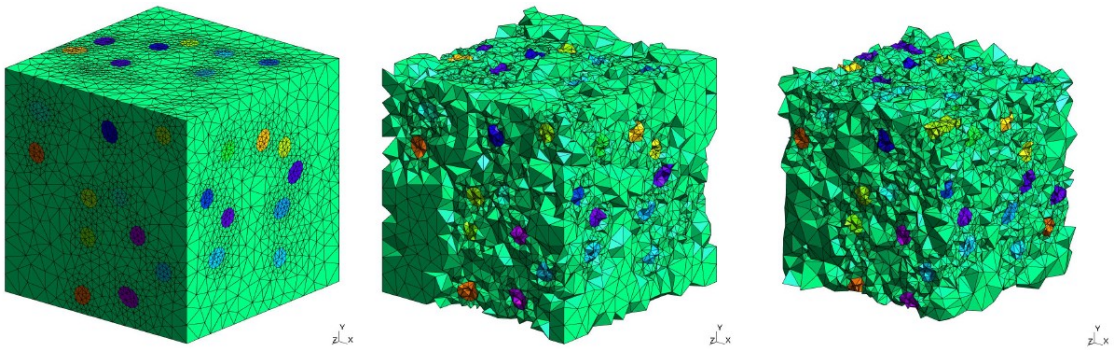

Figure 3-5. Illustration of the erosion of an SVE: (a) SVE without erosion, (b) $d_e = 0.1$, (c) $d_e = 0.2$ [74].

The evolution of apparent elasticity modulus and volume fraction by increasing the erosion distance is presented in Figure 3-6. This refined averaging improves the reliability of the calculated properties by ensuring consistency between mechanical and thermal results, regardless of the applied boundary condition.

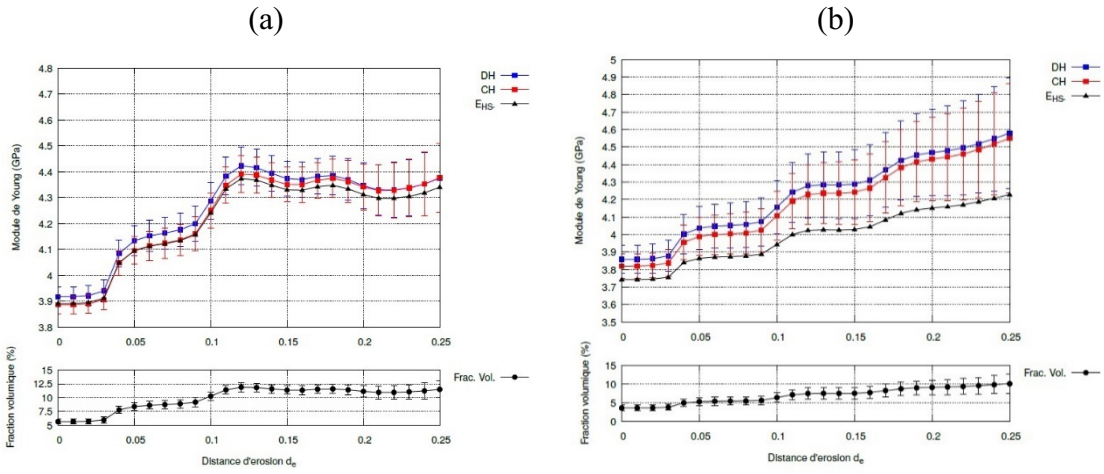

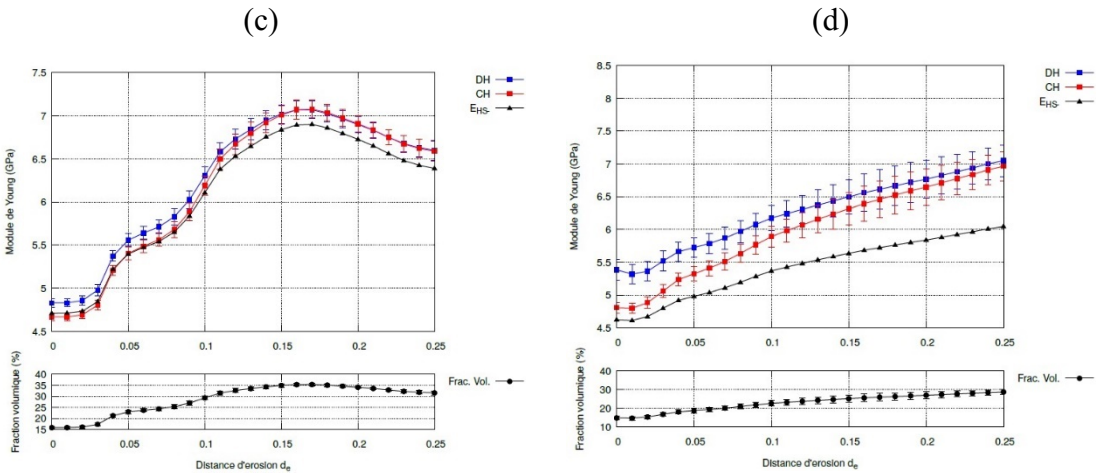

Figure 3-6. Evolution of apparent elasticity modulus E_{app} as a function of the erosion distance d_e for: (a) 10 % of spheres, (b) 10 % of cylinders, (c) 30 % of spheres, (d) 30 % of cylinders [73].

3.1.6- Conclusion

The study presents a fully automated framework for generating realistic microstructural models of particle-reinforced composites. By integrating geometric modeling, adaptive meshing, and FEM analysis, the approach provides a robust numerical tool for characterizing heterogeneous materials. The implementation of MBD-based microstructure generation and erosion methods further enhances the fidelity of mechanical property predictions, making the model highly applicable for computational material science and engineering.

This method reaches volume fractions up to approximately 30 % for both spherical and cylindrical particles. However, this is accomplished by removing certain elements results from the analysis, particularly those near the boundaries where boundary conditions are applied. As a result, the boundary conditions are no longer fully represented in the final model, effectively eliminating their influence on the computed results. The

ability to reach this volume fraction without dealing, through erosion of results, with issues such as lack of particles at SVE boundaries, boundary condition effects, or inhomogeneities, while preserving the FEA results at the boundaries, is addressed by the two approaches [94] presented in the following sections.

3.2- Geometry correction method

This paragraph details the Geometry Correction Method (GCM) presented in this work. The approach leverages MBD to achieve a higher particle volume fraction while maintaining the reliability of results without erosion of results. The main steps for generating the final geometry of particle distribution within the SVE is illustrated in Figure 3-7.To construct a CAD model of the SVE with uniformly distributed particles, the process begins by populating a slightly larger domain, referred to as the MBD generation domain, with enough particles to reach the target volume fraction. This initial domain with length of $L + \Delta$ as illustrated in Figure 3-6a, exceeds the size of the SVE with length L to minimize boundary effects caused by particles in contact with its edges. Importantly, particles are introduced without enforcing the minimum-distance and minimum-angle requirements between particles or between particles and the SVE boundary at this stage.

The MBD approach is applied using a time-driven algorithm implemented in our simulation framework to arrange the particles. This method calculates the dynamics of particle motion and collisions, assigning and iteratively updating velocity vectors for each particle. The algorithm continues to update motion and collision equations at each time step until convergence is achieved. At this point, particle velocities are near zero,

signifying the final stable distribution of particles within the domain. Following this, the SVE of length L is generated as a CAD model. To ensure mesh convergence in subsequent computational steps, specific geometric criteria must be satisfied: a minimum distance between particles and a minimum angle between particles and the SVE faces. Applying these criteria can result in the exclusion of particles, particularly those near the boundaries of the SVE, potentially reducing the particle volume fraction (Figure 3-7b). To address this issue, an algorithm is introduced to slightly adjust the geometric characteristics of particles that do not meet these two criteria, trying to make these particles compatible. This adjustment enables retaining particles that might otherwise be excluded (Figure 3-7c). Particles that are already compatible with these criteria are directly inserted into the CAD model of the SVE. The final distribution of particles within the SVE is achieved by adding the newly retained particles to those previously accepted and inserted (Figure 3-7d). For each particle that do not meet one (or more) geometric criterion, a process is iteratively applied to slightly adjust its size, position, or orientation.

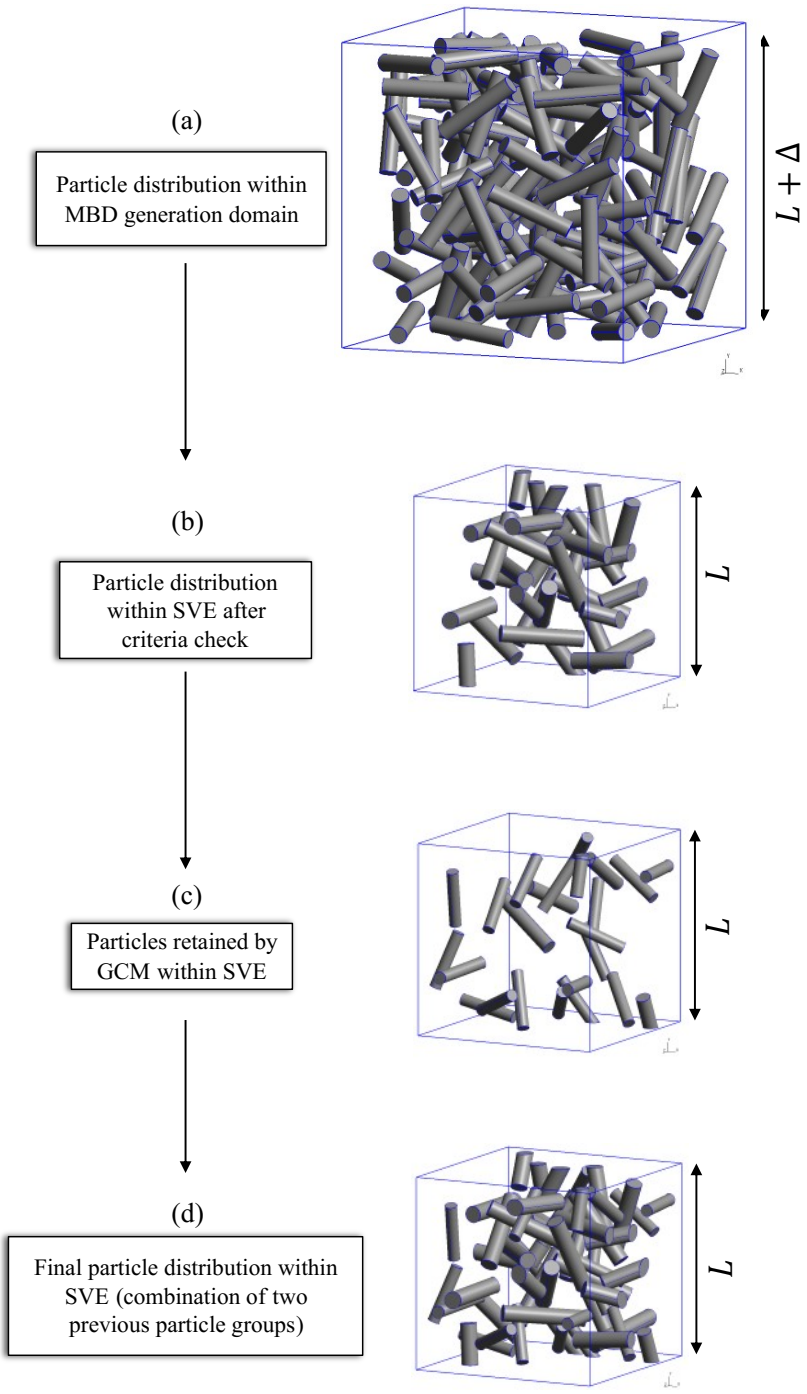

Figure 3-7. Overview of the SVE geometry generation process with geometry correction method.

The process as outlined in Algorithm 1, begins with a size adjustment phase. During this phase, an adjustment factor $\propto$ is applied iteratively to gradually reduce the particle's dimensions (length L_P for cylinders or diameter D_P for spheres). This factor must be chosen between zero and one ($0 <\propto< 1$) to reduce the particle's dimensions. The proximity of $\propto$ to one or zero controls the rate of reduction: values closer to one produce slight, incremental changes, whereas values nearer zero cause more dramatic reductions, since at each iteration, α is multiplied by the already reduced dimension in previous iteration. At each iteration of adjustment, the criteria are re-evaluated. If the criteria are satisfied, the particle is considered compatible and retained in the SVE.

If the size adjustment phase alone does not result in compatibility after a maximum number of iterations (it_{max}), the algorithm progresses to a position adjustment phase, where the particle's coordinates $(\mathrm{x}, \mathrm{y}, \mathrm{z})$ are iteratively modified. The criteria are re-evaluated at each step, and compatibility is assessed.

For cylindrical or torus particles, if neither size nor position adjustments resolve the incompatibility, the algorithm enters an orientation adjustment phase to modify the orientation angles ($\theta \; and \; \varphi$). For each adjustment phase, these adjustments continue iteratively, respecting a maximum number of iterations (it_{max}).

The primary objective is to retain as many particles as possible without significantly deviating from the original size of its random distribution. The method's algorithm is outlined in Algorithm 1.

Algorithm 1. Geometry correction method

Input: Particles list with properties (size (L_P/D_P), coordinates (x, y, z), type (sphere, cylinder), if cylinder: orientation (θ *and* φ)), $Dist_{min}$, $Angle_{min}$, Neighboring Topological entities of Particle P ($Topo_{neighboring}$)

Output: particles compatible with criteria

Initialization: Initial adjustment factor: $\propto_{initial} < 1$, Maximum number of adjustment iteration: it_{max}, $Create\ particle = False$, i=1, j=1, k=1
Foreach particle, P **do**
  Get *Dist* and *Angle* between P and $Topo_{neighboring}$
  If $Dist < Dist_{min}$ **or** $Angle < Angle_{min}$, **then next**
    While $i < it_{max}$ **and** $Create\ particle = False$, **do**
      $\propto_i = \propto_{initial}^{i}$
      In case of cylinder: $L_P = L_P \times \propto_i$
      In case of sphere: $D_P = D_P \times \propto_i$
      If $Dist \geq Dist_{min}$ **and** $Angle \geq Angle_{min}$, **then next**
        $Create\ particle = True$
    If $Create\ particle = False$ **then next**
    While j $< it_{max}$ **and** $Create\ particle = False$, **do**
      $adjust\ x, y, z$
      If $Dist \geq Dist_{min}$ **and** $Angle \geq Angle_{min}$, **then next**
        $Create\ particle = True$
    In case of cylinder or torus:
    If $Create\ particle = False$ **then next**
    While k $< it_{max}$ **and** $Create\ particle = False$, **do**
      In case of cylinder: adjust θ *and* φ
      If $Dist \geq Dist_{min}$ **and** $Angle \geq Angle_{min}$, **then next**
        $Create\ particle = True$

To provide a clearer understanding of the geometry correction method, a simplified flowchart has been developed to illustrate the correction process applied to individual particles and is shown in Figure 3-8. When a newly inserted particle does not satisfy the predefined criteria, such as minimum distance and minimum angle to neighboring

particles or domain boundaries, the correction algorithm is triggered. The flowchart outlines the sequential steps taken to adjust the particle's characteristics.

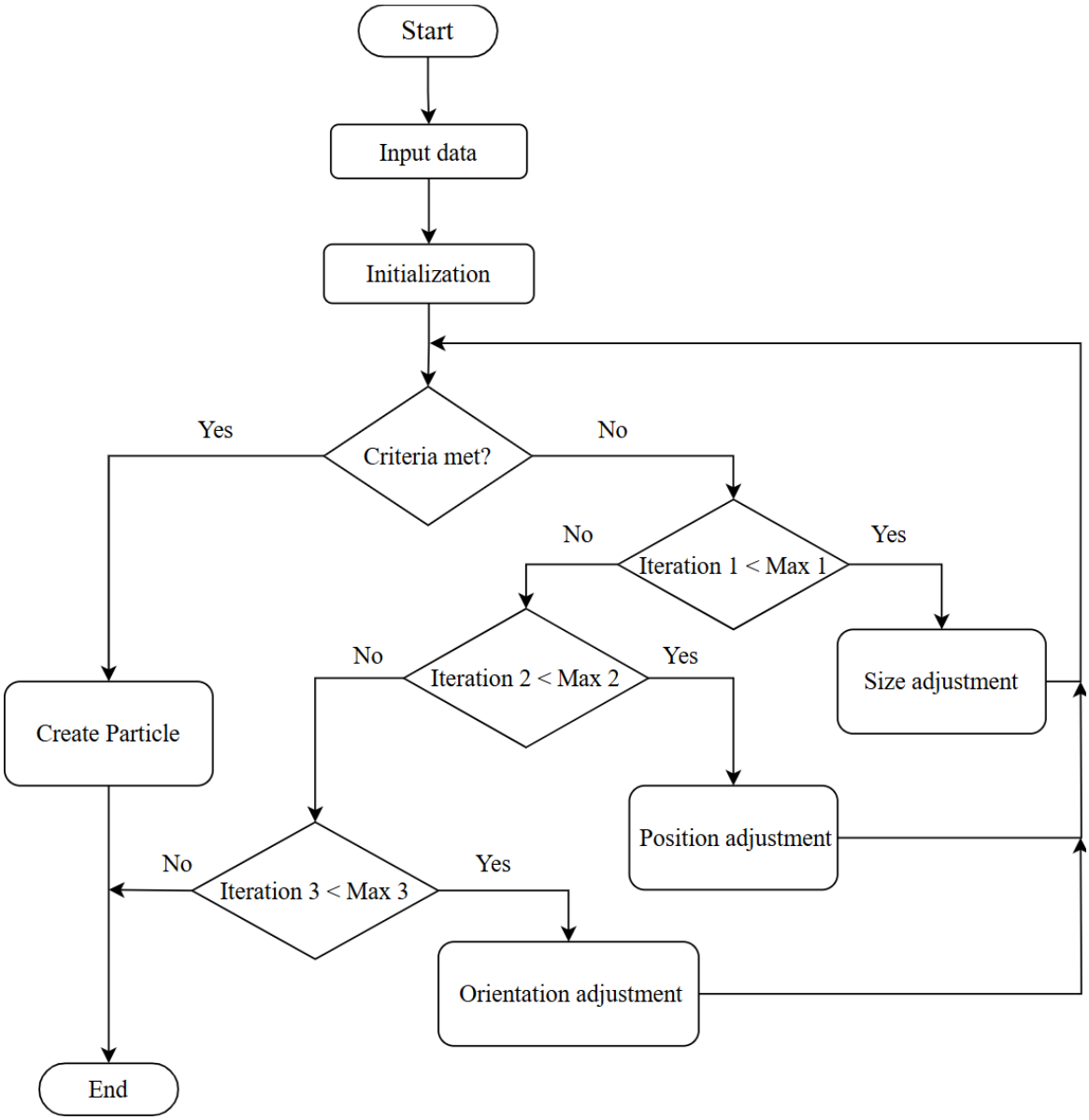

Figure 3-8. Flowchart of GCM.

Initially, a size correction is attempted by reducing the particle's dimensions to meet the criteria. If this adjustment is insufficient, a position correction is applied, aiming to

relocate the particle within a permissible region of the domain. Should repositioning also fail to satisfy the criteria, an orientation correction is attempted, particularly for elongated particles, by altering their angular alignment. If none of these correction steps successfully resolve the conflict, the particle is ultimately excluded from the microstructure.

For instance, as shown in Figure 3-9a, when attempting to insert particle 3 into the SVE, it initially fails to meet the minimum distance requirement with particles 1, which is already positioned within the SVE. The size adjustment phase (Figure 3-9b) iteratively reduces the dimensions of particle 3 until the maximum allowable number of iterations is reached or the particle becomes compatible with the criteria. In this example, by applying only the size adjustment phase, the particle 3 becomes compatible with criteria and is inserted into the SVE. Next example as shown in Figure 3-10, also starts with size adjustment on newly assumed particle 4. However, after maximum number of iterations, while this adjustment resolves the minimum distance issue with the edge of the SVE, the particle's position still results in a failure to satisfy the minimum distance criterion with particle 1 (Figure 3-10b). When the size adjustment phase alone does not result in compatibility after a maximum number of iterations (it_{max}), the algorithm progresses to a position adjustment phase. This process is illustrated in Figure 3-10c, where the position of particle 4 is adjusted to resolve the previously mentioned issue with the minimum distance criterion relative to particle 1. During this phase the compatibility of particle 4 is reached and this particle is inserted in the SVE. Figure 3-11a, b, c illustrates another example where neither size adjustment nor position adjustment resolves the

incompatibility of particle 5. In this situation, next phase as orientation adjustment is started (Figure 3-11d). Through iterative changes, the particle's orientation is refined to ensure compatibility with all geometric constraints, including minimum distances from other particles and the SVE boundary. Ultimately, this adjustment allows particle 5 to meet the required criteria, enabling its acceptance and integration into the SVE. This ensures the particle is retained in the model rather than being excluded, thereby preserving the desired volume fraction within the SVE. Figure 3-12 demonstrates an example where neither of phases cannot lead to compatibility and finally particle 6 is not inserted into the SVE.

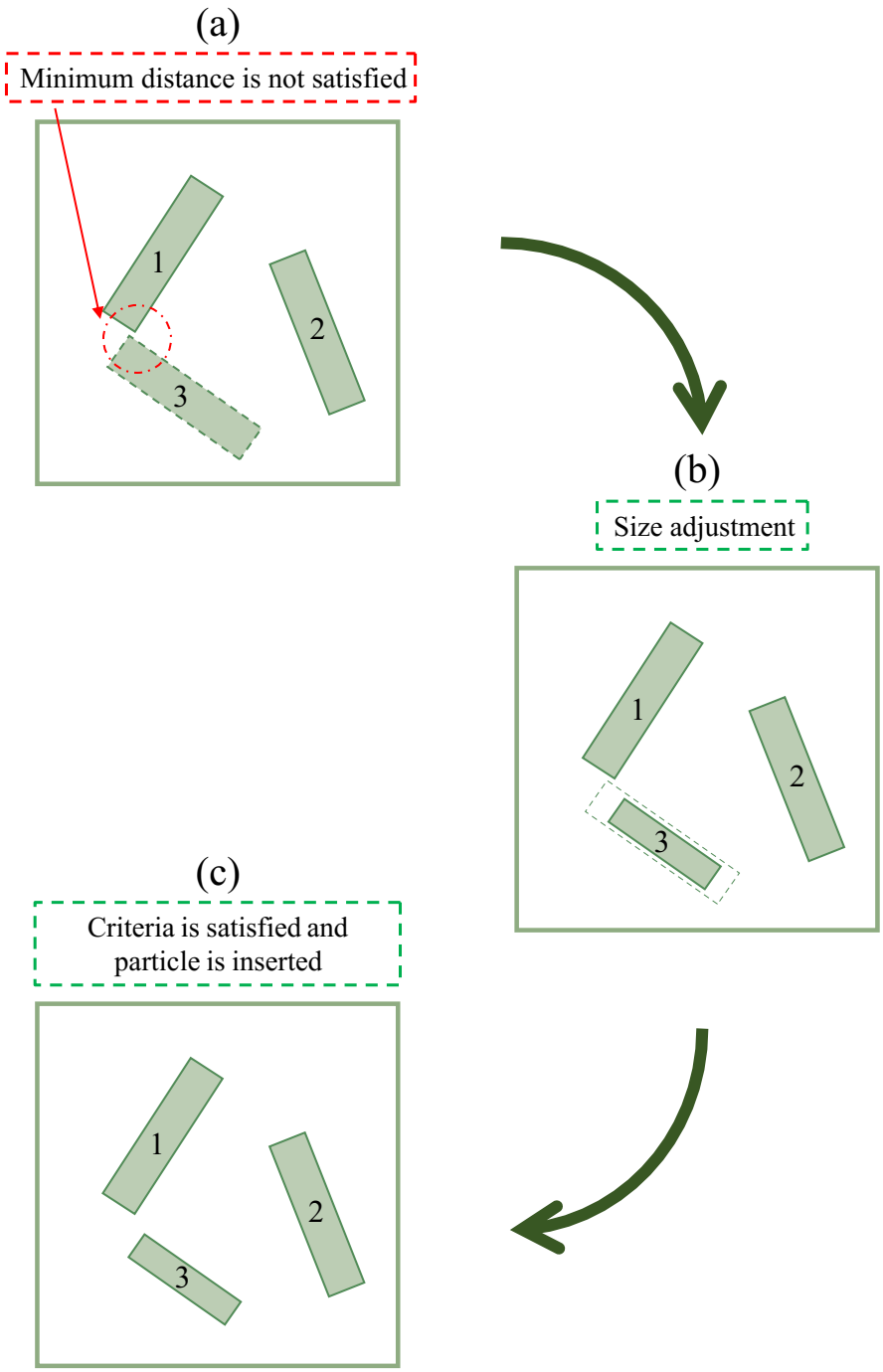

Figure 3-9. An example of applying GCM on particle 3: (a) the criteria unsatisfaction, (b) applying size adjustment, (c) compatibility with criteria and particle insertion.

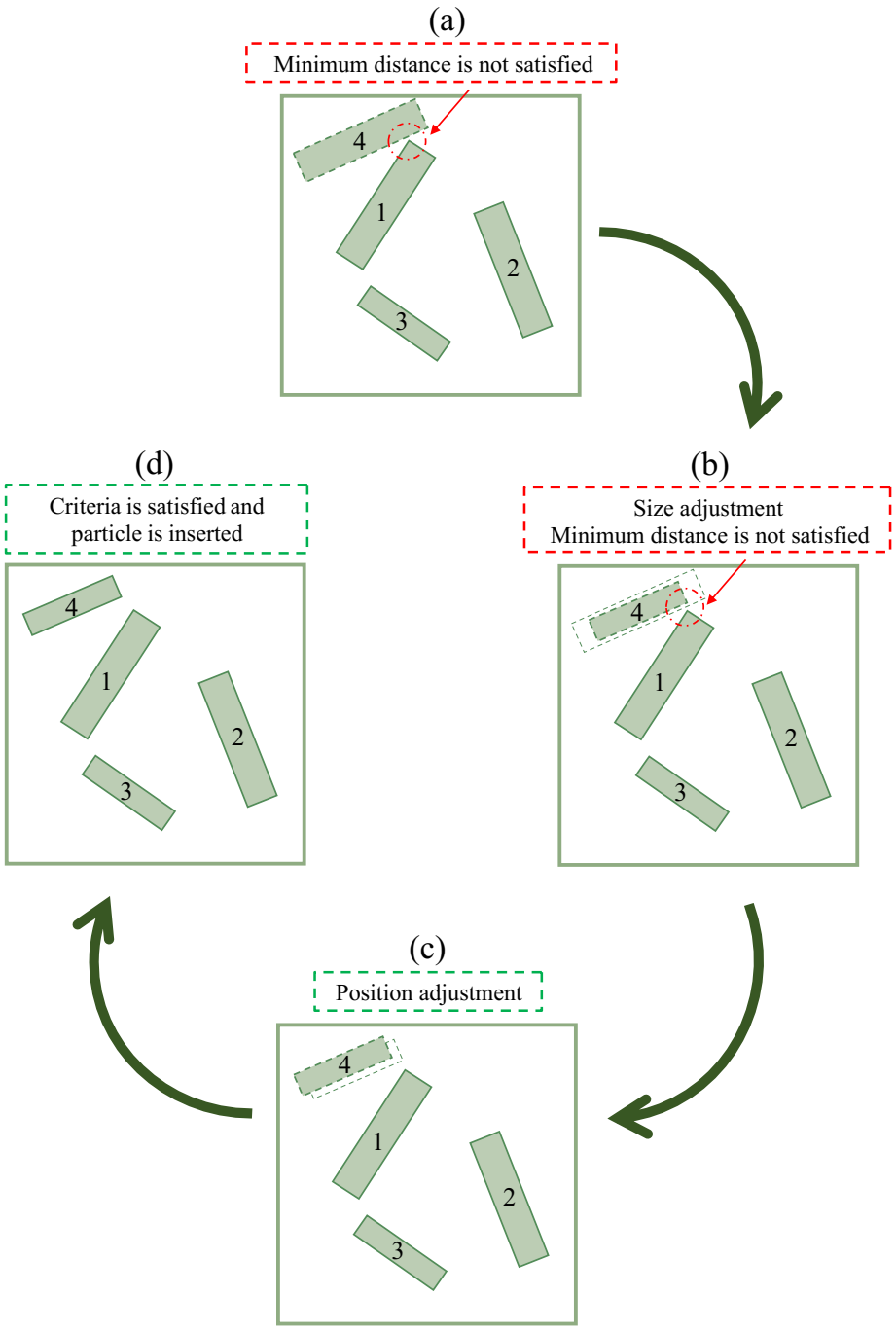

Figure 3-10. An example of applying GCM on particle 4: (a) the criteria unsatisfaction, (b) applying size adjustment, (c) applying position adjustment, (d) compatibility with criteria and particle insertion.

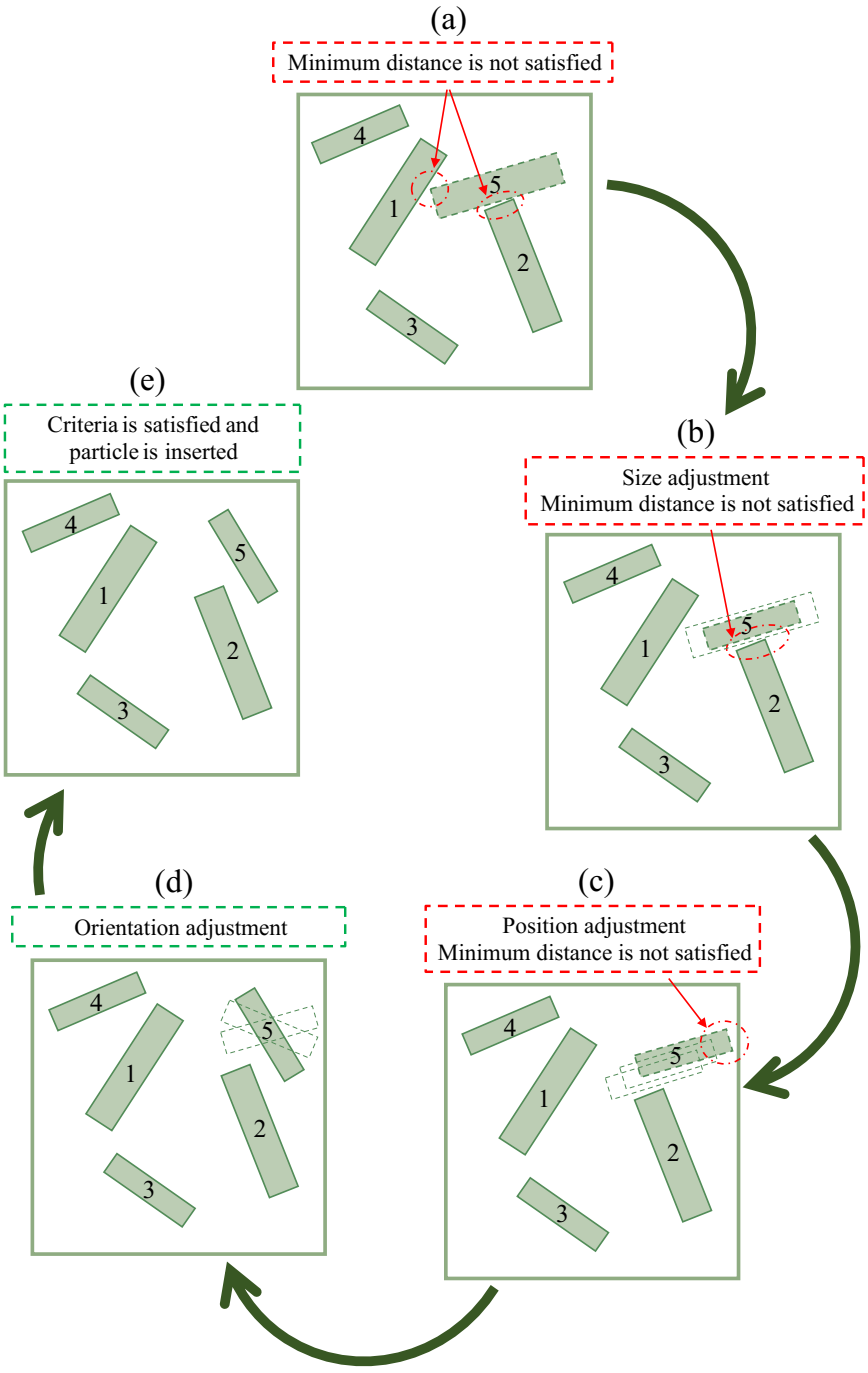

Figure 3-11. An example of applying GCM on particle 5: (a) the criteria unsatisfaction, (b) applying size adjustment, (c) applying position adjustment, (d) applying orientation adjustment, (e) compatibility with criteria and particle insertion.

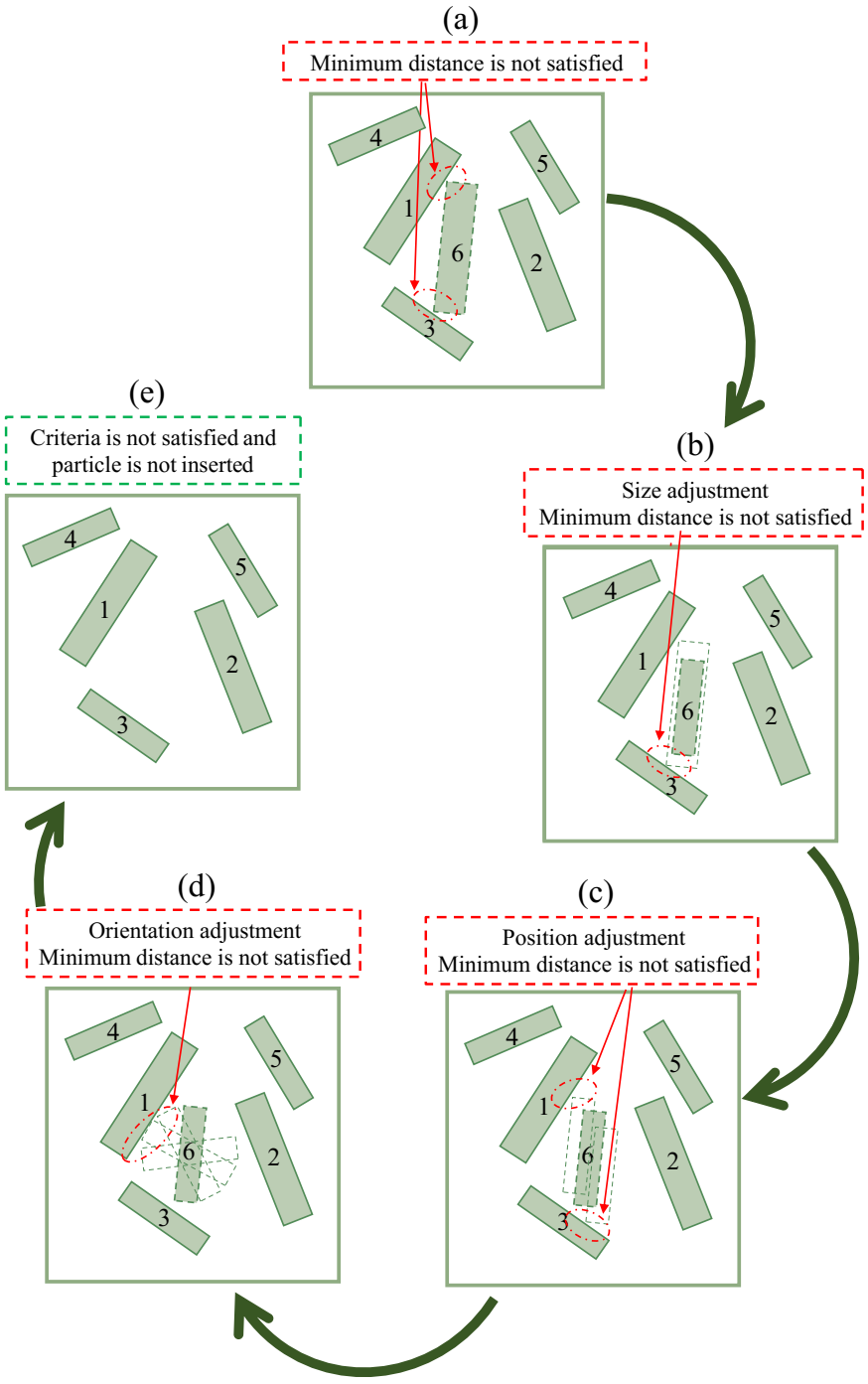

Figure 3-12. An example of applying GCM on particle 6: (a) the criteria unsatisfaction, (b) applying size adjustment, (c) applying position adjustment, (d) applying orientation adjustment, (e) compatibility is not achieved.

3.3- Mesh cutting method

This method offers an alternative approach to achieve a uniform particle distribution. Its main objective is eliminating the need for the erosion of results. A stepwise approach is used to reach the SVE of length L (Figure 3-13). First the MBD generation domain of length $L + \Delta$ is defined and all required particles are inserted while ensuring no particle intersections occur (Figure 3-13a). Then, the CAD model of a smaller domain of length $L + \varepsilon$ where $\varepsilon < \Delta$, referred to as the criteria domain, is created by applying the geometric criteria mentioned in the previous section (minimum distance and minimum angle) to achieve a compatible particle distribution (Figure 3-13b).

Once this compatible particle distribution is achieved inside the criteria domain, the CAD geometry is finalized, and material properties are assigned. As the next step, a size-map is generated to dictate element sizes throughout the criteria domain. This map [50] will later guide the automatic generation of the tetrahedral mesh.

The procedure begins by embedding the geometry in a structured hexahedral grid. Initially, a uniform nodal spacing is assigned across the domain, serving as a baseline. Local refinements are then introduced near particle interfaces by adjusting the nodal spacing according to distance-based criteria, ensuring that a minimum of two element layers separates neighboring particles. Maintaining at least two layers of elements is essential both for mesh convergence and for preserving the mechanical fidelity of the matrix material. This strategy guarantees that nodes exist which belong exclusively to the matrix, rather than being shared between particles and matrix. Without this precaution, a

single element layer would result in node-sharing between phases, leading to ambiguities in material property assignment and a loss of simulation accuracy. Nevertheless, adding more layers beyond the minimum increases the element count substantially, resulting in higher computational demands and longer simulation times. Therefore, an optimal compromise between mesh quality and computational efficiency must be achieved. To finalize the mesh, a smoothing procedure based on relaxation techniques is applied to prevent abrupt transitions in element size, promoting a gradual variation across the entire domain.

Then the model of this criteria domain is meshed, based on this size map. Linear tetrahedral elements are automatically generated first. Subsequently, the mesh is trimmed to match dimensions of the SVE (L), as detailed in Algorithm 2. Tetrahedral elements intersecting the boundary of this SVE are divided into smaller tetrahedra. All elements located outside the SVE are discarded, which results in a mesh of the SVE (Figure 3-13c). This approach effectively removes boundary areas that are subject to voids and lack of particles, leaving a uniformly and randomly dispersed particle-based SVE cube (Figure 3-13d).

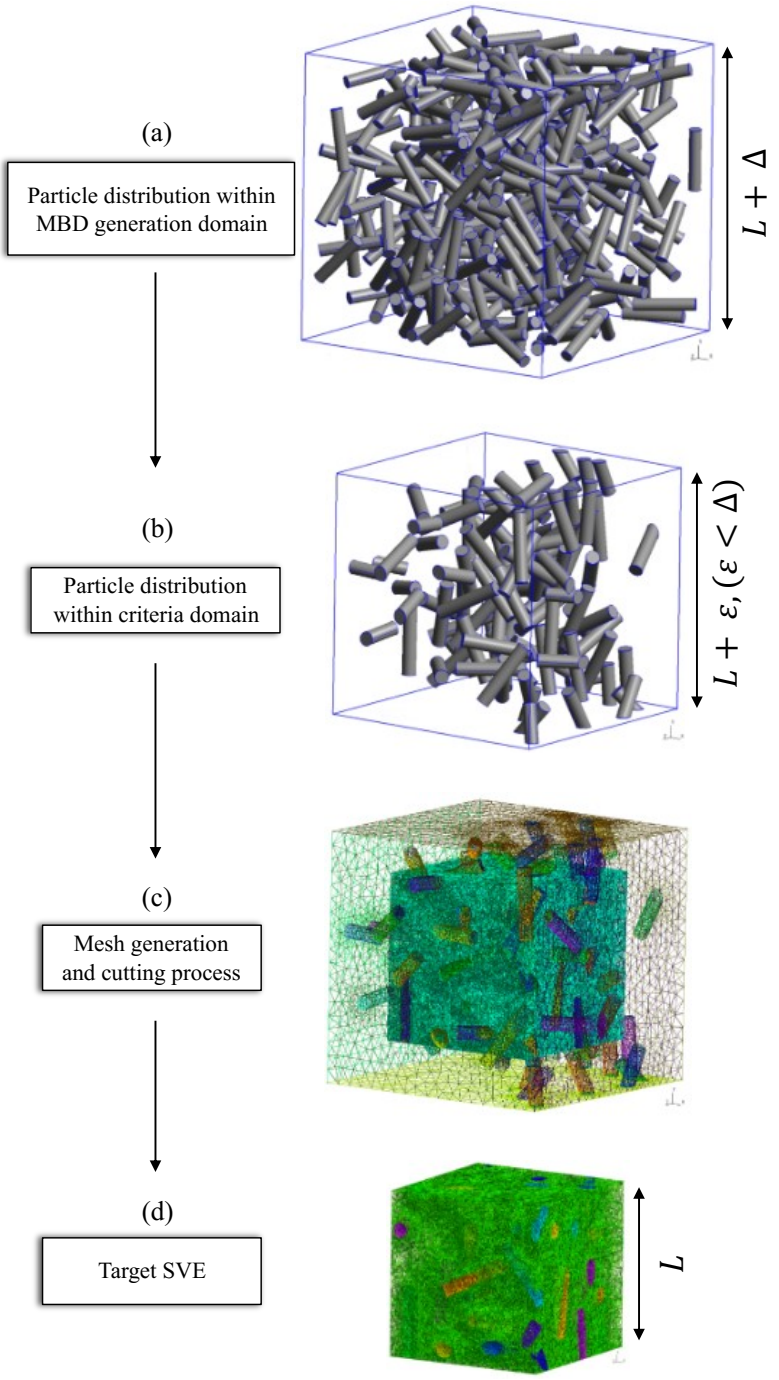

Figure 3-13. Overview of the SVE automatic generation process with mesh cutting method ($\varepsilon < \Delta$).

The algorithm for cutting the mesh by the six planes of the SVE boundary is presented as Algorithm 2. The entire process involves four loops. The first loop iterates over the six cutting planes of the SVE cube, and the next three inner loops respectively iterate over all nodes, segments, and tetrahedral elements in the mesh. For each cutting plane, the process begins with a loop over all nodes that first calculates the distance between each node and the cutting plane ($dist_{node\_n}$). There are three possible states for each node with respect to a given cutting plane: inside the SVE (represented by a positive distance, +), outside the SVE (represented by a negative distance, -), or on the plane (represented by zero distance, 0). Figure 3-14, as an example presented in 2D for clarity, demonstrates the classification of nodes on segments relative to a given cutting plane. This 2D representation serves as a simplified example to enhance understanding. Nodes with a positive distance are retained within the SVE, contributing to its internal domain, while those with a negative distance are excluded, as they lie outside the defined boundaries. Nodes with a zero distance, situated exactly on the cutting plane, act as critical transition points and are crucial for maintaining geometric accuracy and boundary integrity.

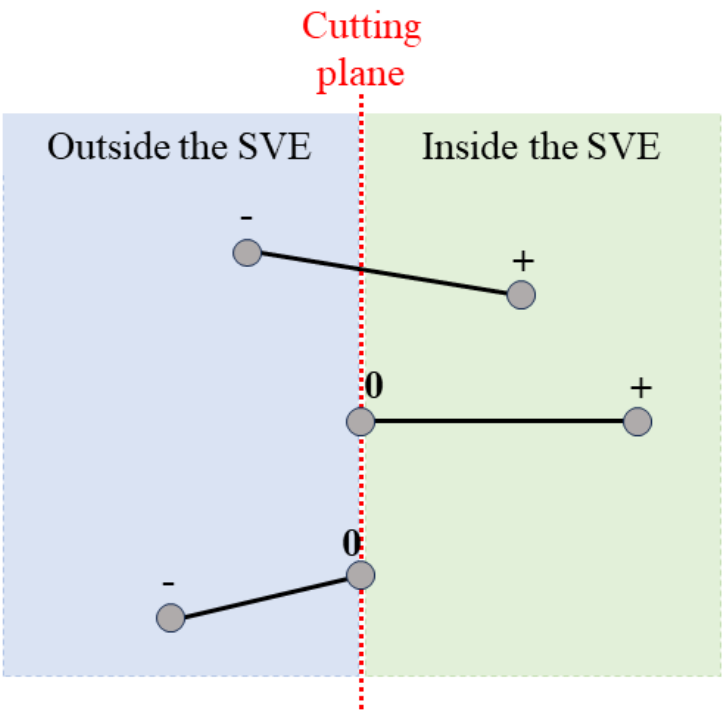

Figure 3-14. Example of three states of nodes on segments with respect to a cutting plane in 2D.

With this information, the next loop checks mesh segments and creates a list of segments being intersected by the plane ($list_{cut\_seg}$). Segments with one node inside ($dist_{node\_n} > 0$) and the other outside ($dist_{node\_n+1} < 0$) are added to this list. For each mesh segment in this list, the coordinates of the intersection between the segment and the plane are calculated, resulting in a point. A new node is created at these coordinates and assigned to its respective segment.

This process is visually represented in Figure 3-15 as a simplified 2D example. In this figure, the SVE is modeled as a 2D meshed plane composed of triangular elements, and the cutting plane is represented by a cutting line. Figure 3-15a illustrates an identified intersected segment. In the next step, the coordinates of the intersection point between this

segment, and the cutting line are calculated (Figure 3-15b). Finally, as shown in Figure 3-15c, a new node (indicated by the red marker) is created at the computed intersection point and assigned to the segment. This newly created node ensures accurate representation of the intersection, maintaining the geometric integrity of the SVE and enabling seamless refinement of the mesh.

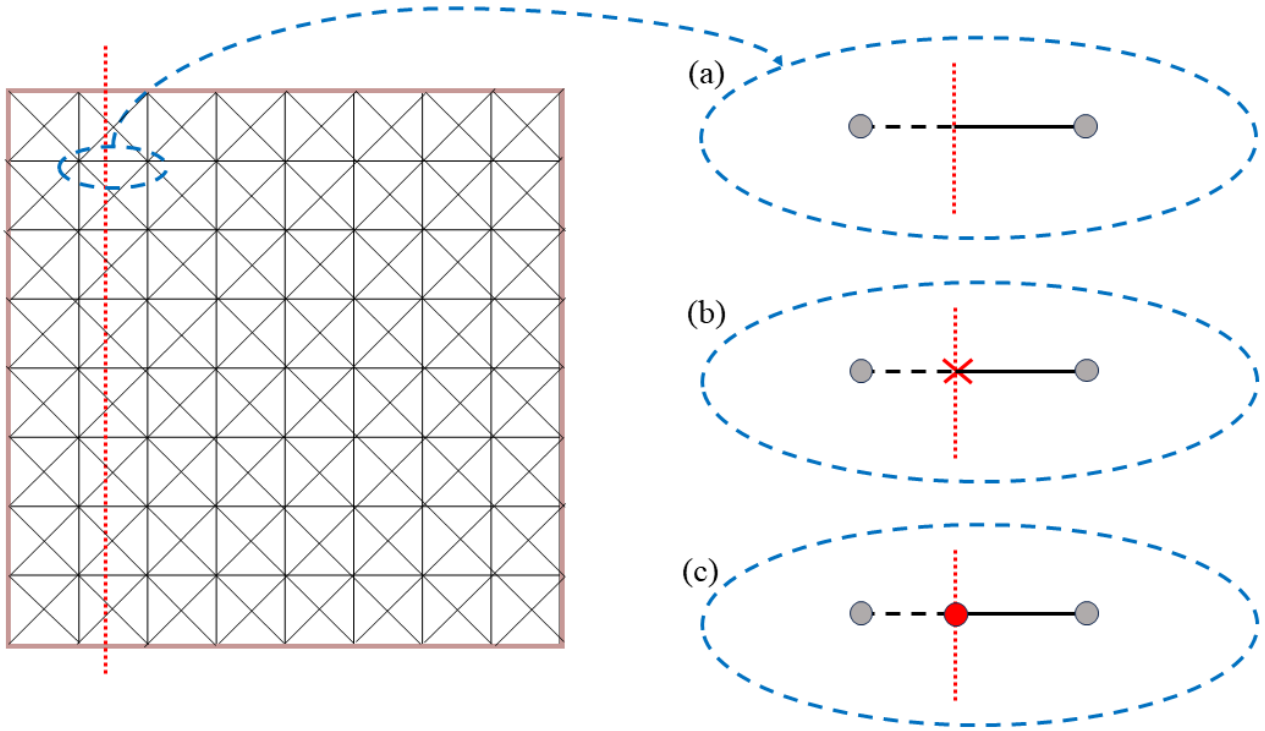

Figure 3-15. A simplified 2D example of the loop on segments, (a) An intersected segment is identified, (b) the coordinates of the intersection point between this segment, and the cutting line is calculated, (c) A new node (indicated by the red marker) is created at the computed intersection point and assigned to the segment.

One important aspect to consider in this step is that, in some cases, the intersection point may lie very close to the inside node of the segment. This situation, as illustrated in the example of Figure 3-16a, b (e.g., segments 2 and 3), can result in the creation of an extremely small segment when a new node is introduced at the computed intersection point Figure 3-16c. Such small segments lead to the generation of too small elements in the final mesh, like elements 1, 2 and 3 in the example of Figure 3-16d, which can negatively impact its overall quality. This issue can have several consequences, including a significant increase in the number of elements in the mesh, which in turn raises computational costs. Moreover, these tiny elements may lead to numerical instabilities or errors during subsequent simulations, particularly when identifying nodes that are positioned very close to one another. Proper handling of these cases is therefore essential to ensure that the mesh remains well-structured, computationally efficient, and free of artifacts that could degrade its accuracy or performance.

(a)

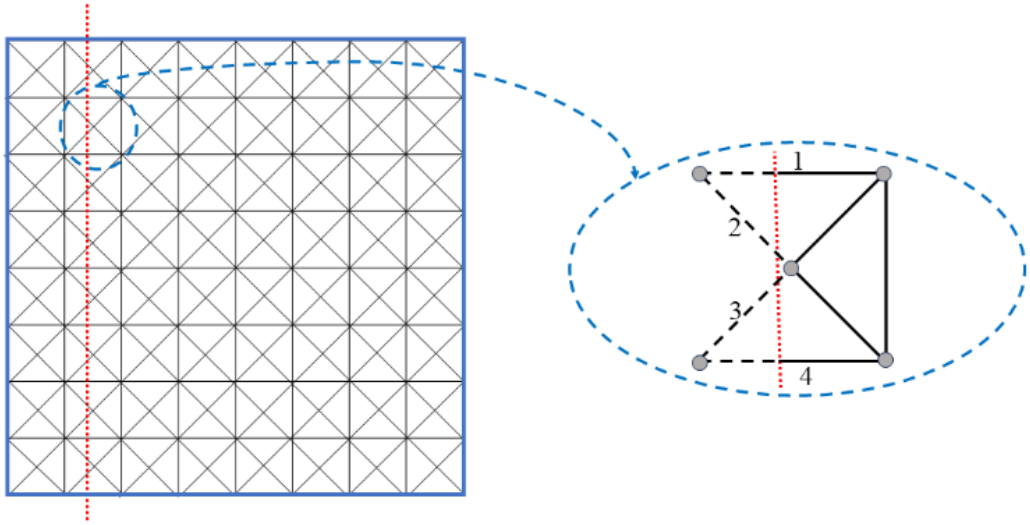

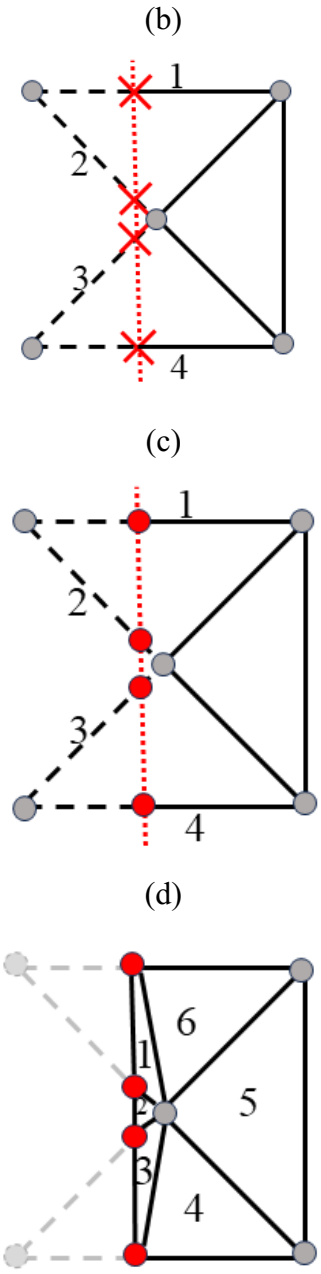

Figure 3-16. Illustration of the potential issue with intersection points lying very close to the inside node of a segment. (a, b) Segments 2 and 3 are identified as having intersection points near their inside nodes, (c) new nodes are created at the computed intersection points, resulting in extremely small segments, (d) These small segments lead to too small elements (e.g., elements 1, 2, and 3).

As a solution to this issue, when the intersection point lies very close to the inside node of the same segment (Figure 3-17a), and the distance between them (d) is less than a predefined threshold ($d < \varepsilon$) (Figure 3-17b), an alternative approach is applied. Instead of creating a new node at the intersection point, the inside node of the segment is shifted toward the intersection point (Figure 3-17c). This adjustment avoids the creation of unnecessary nodes and prevents the generation of excessively small or poor-quality elements in the mesh (Figure 3-17d, e). For instance, in the examples shown in Figures 1 and 2, this method reduces the number of new nodes from four to two. Consequently, instead of producing six elements, only three elements are generated. Additionally, this approach has the added benefit of addressing related problems automatically. By shifting the position of the inside node on segment 2, the issue of a close intersection point on segment 3 is also resolved mesh (Figure 3-17d, e), further improving the overall quality and efficiency of the mesh.

(a)

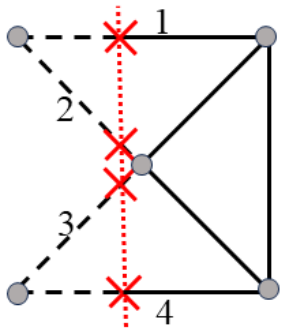

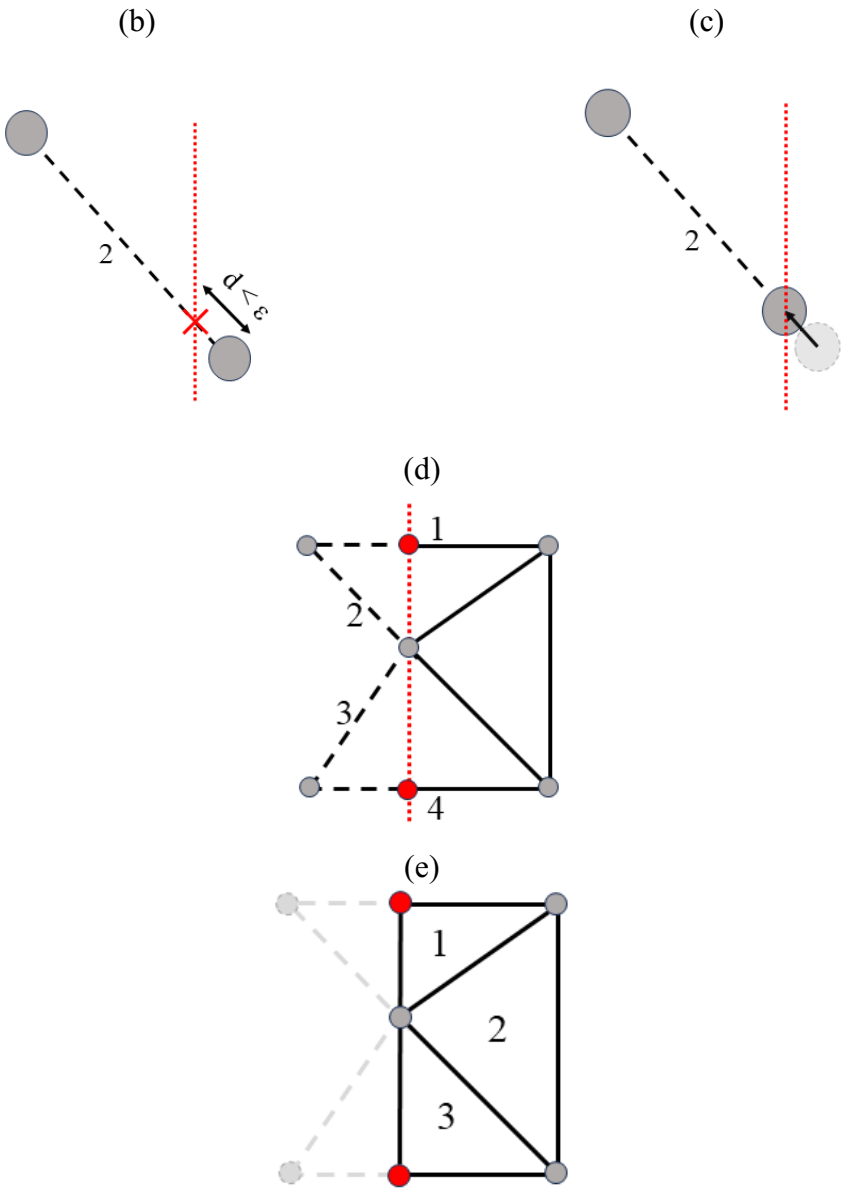

Figure 3-17. Solution for handling intersection points close to the inside node of a segment. (a) An intersection point is identified near the inside node of a segment. (b) the distance between the intersection points and the inside node is less than a predefined threshold, (c) the inside node is shifted toward the intersection point. (d) This adjustment avoids creating unnecessary nodes, reduces the number of elements, and prevents poor-quality elements, (e) creation of three element by this shifted node and two new nodes in red.

Then, the algorithm iterates over each tetrahedral element to assess the state of its four nodes. These iterations result in all tetrahedrons being classified as inside, outside, or cut by the cutting plane. All tetrahedrons located outside the SVE are removed from the mesh, while all tetrahedrons located inside the cube are retained unchanged. The classification of all possible ways of leading to an inside or outside tetrahedron, based on the state of its four nodes, is shown in Table 3-1. For tetrahedrons intersecting the cutting plane, six different cutting scenarios are shown in Figure 3-22. For each tetrahedron being cut, a list of nodes is created including inside nodes, on plane nodes, and newly created nodes at intersections with the cutting plane. Based on the number and type of nodes inside this list, the inside part of each cut tetrahedron could result in a tetrahedron itself (list of four nodes), a quadrilateral pyramid (list of five nodes) or a triangular prism (list of six nodes). This classification of cutting scenarios is summarized in Table 3-2.

To provide a clearer understanding of the mesh cutting method, a simplified flowchart has been developed to illustrate the cutting process applied to each cutting plane. A general schematic of this process, consisting of three main loops, is presented in Figure 3-18. These loops are detailed individually in Figure 3-19, Figure 3-20, and Figure 3-21 which respectively depict the loop over nodes, the loop over segments, and the final loop over tetrahedra.

Algorithm 2. Mesh cutting process.

Input: Mesh file, six cutting planes coordinates,

Output: Mesh file of cut mesh

Foreach cutting plane, $Plane_i$ (i=1 to 6)
  Foreach node **do**
    Get node distance from $Plane_i$, $dist_{node\_n}$
  Foreach segment **do**
    Get two nodes of segment ($node_n$, $node_{n+1}$) and their distances from cutting plane $dist_{node\_n}$, $dist_{node\_n+1}$
    If ($dist_{node\_n}$ >0 and $dist_{node\_n+1}$ <0) **or** ($dist_{node\_n+1}$ >0 and $dist_{node\_n}$ <0)
      Calculate segment and $Plane_i$ intersection coordinates, x, y, z
      Create a node in x, y, z and attach it to segment, $new\_node_{segment}$
  Foreach tetrahedral element, tetra **do**
    Get four nodes of tetra distance from $Plane_i$,
    If all four $dist_{node}$ are <=0 **then next**
      Remove tetra
    Else if all four $dist_{node}$ are >=0 **then next**
      Keep tetra
    Else
      Generate a list of nodes, $List_{nodes}$
      Insert nodes with $dist_{node}$ >=0
      Insert $new\_node_{segment}$ attached to tetra's segments
      Get number of nodes inside $List_{nodes}$, No_{nodes}
      If No_{nodes} = 4 **then next**
        Generate a new tetra element by these nodes
      If No_{nodes} = 5 **then next**
        Generate two new tetra elements by these nodes
      If No_{nodes} = 6 **then next**
        Generate three new tetra elements by these nodes

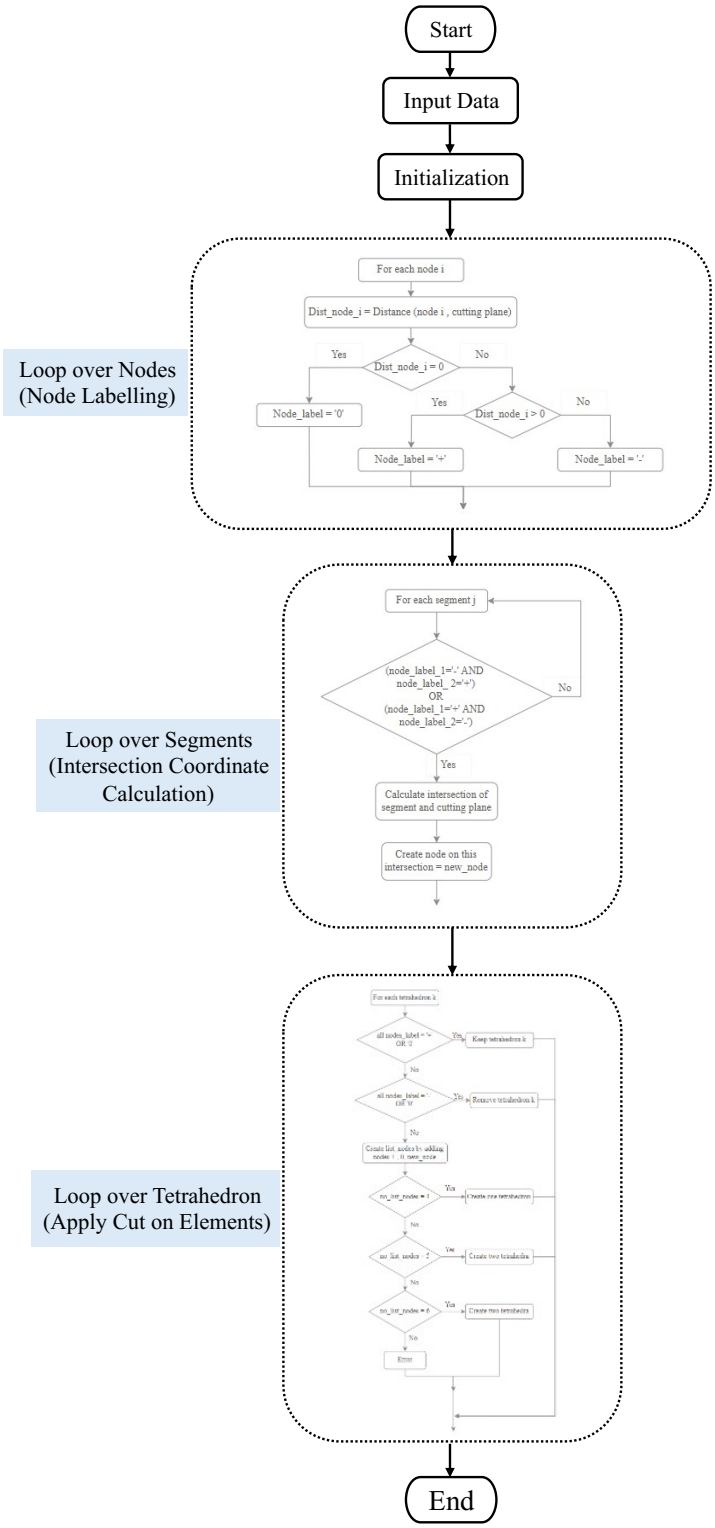

Figure 3-18. A general schematic of MCM flowchart.

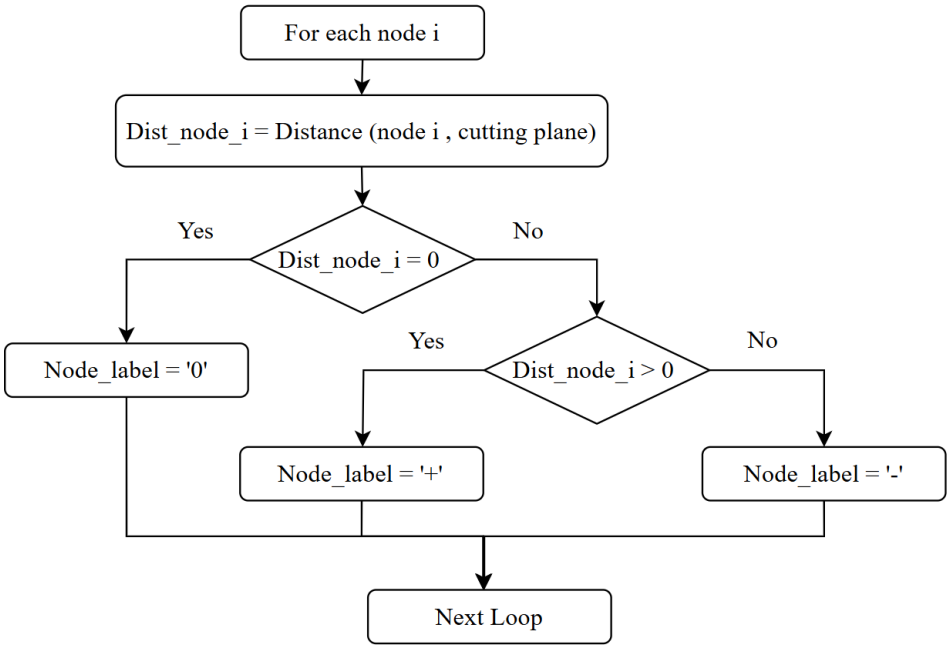

Figure 3-19. First loop of MCM flowchart.

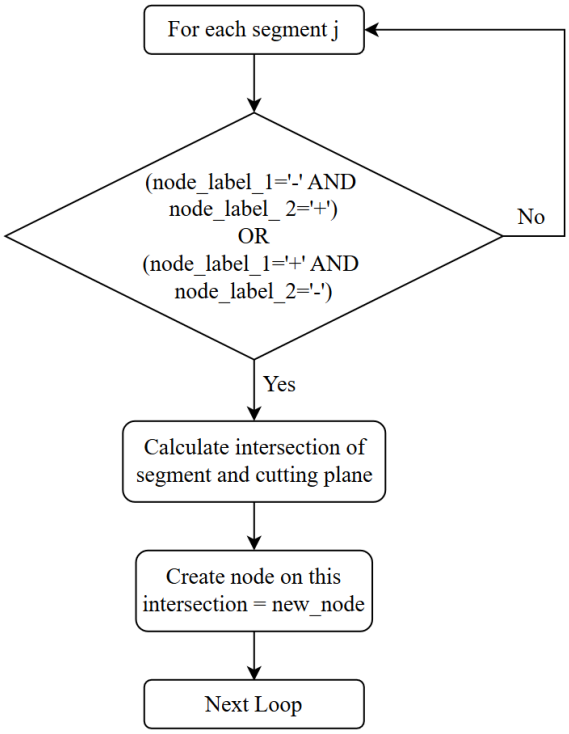

Figure 3-20. Second loop of MCM flowchart.

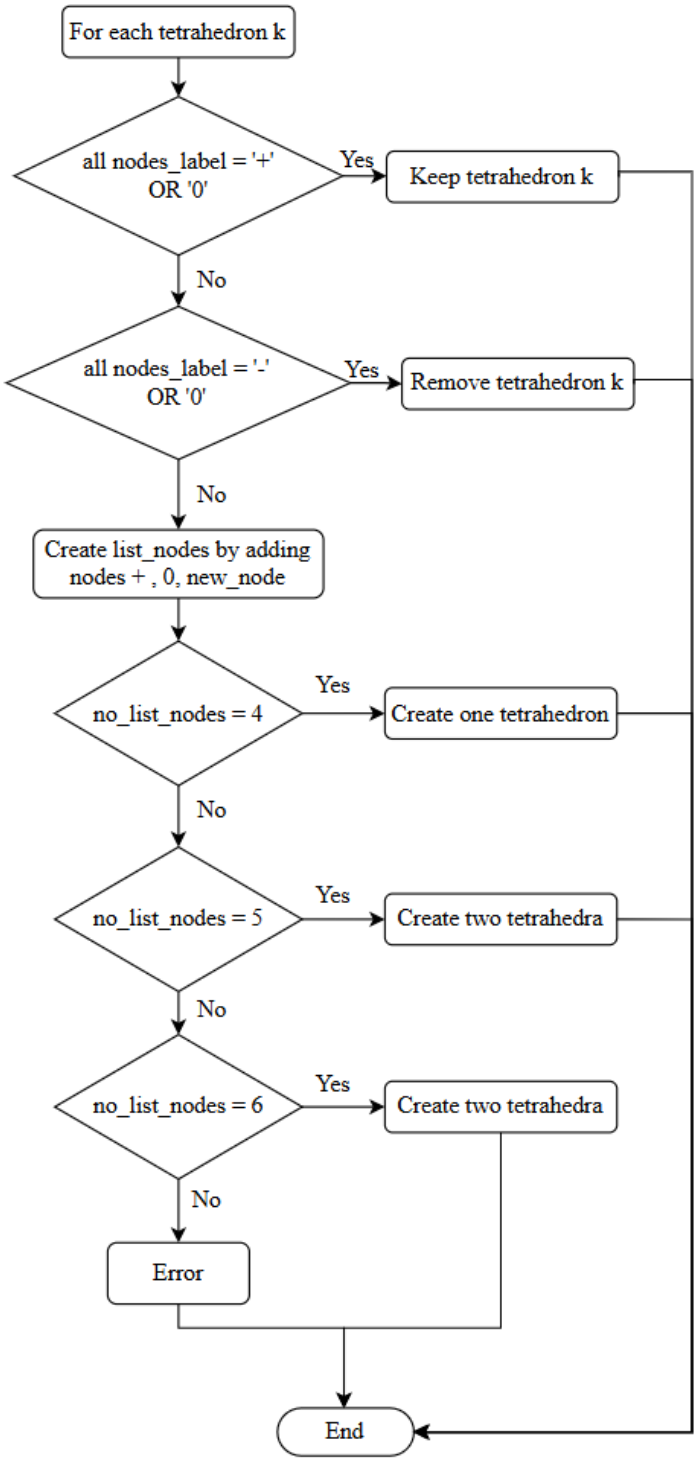

Figure 3-21. Third loop of MCM flowchart.

Table 3-1. Various configurations of a tetrahedron before cut based on the states of its four nodes: "+" (inner side of the cutting plane), "-" (outer side of the cutting plane), and "0" (on the cutting plane).

Tetrahedron node number	1	+	+	+	+	−	−	−	−
	2	+	+	+	0	0	−	−	−
	3	+	+	0	0	0	0	−	−
	4	+	0	0	0	0	0	0	−
Tetrahedron state		Inside	Inside	Inside	Inside	Outside	Outside	Outside	Outside

(a) (b)

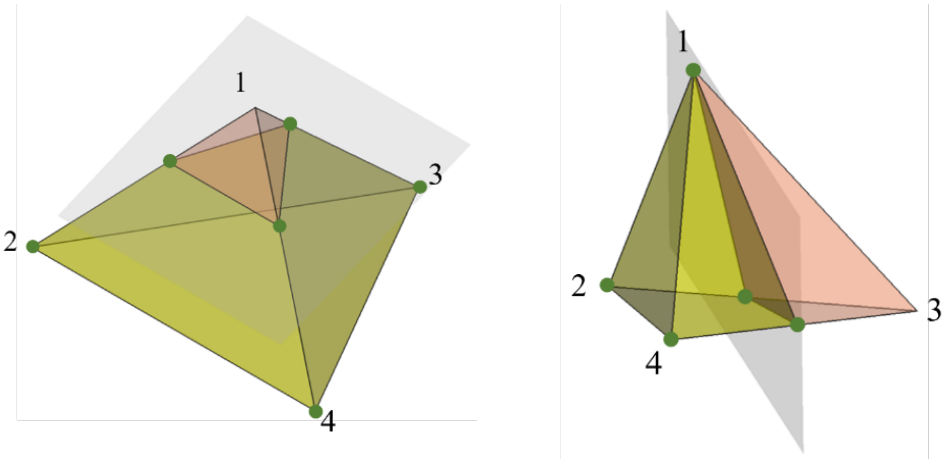

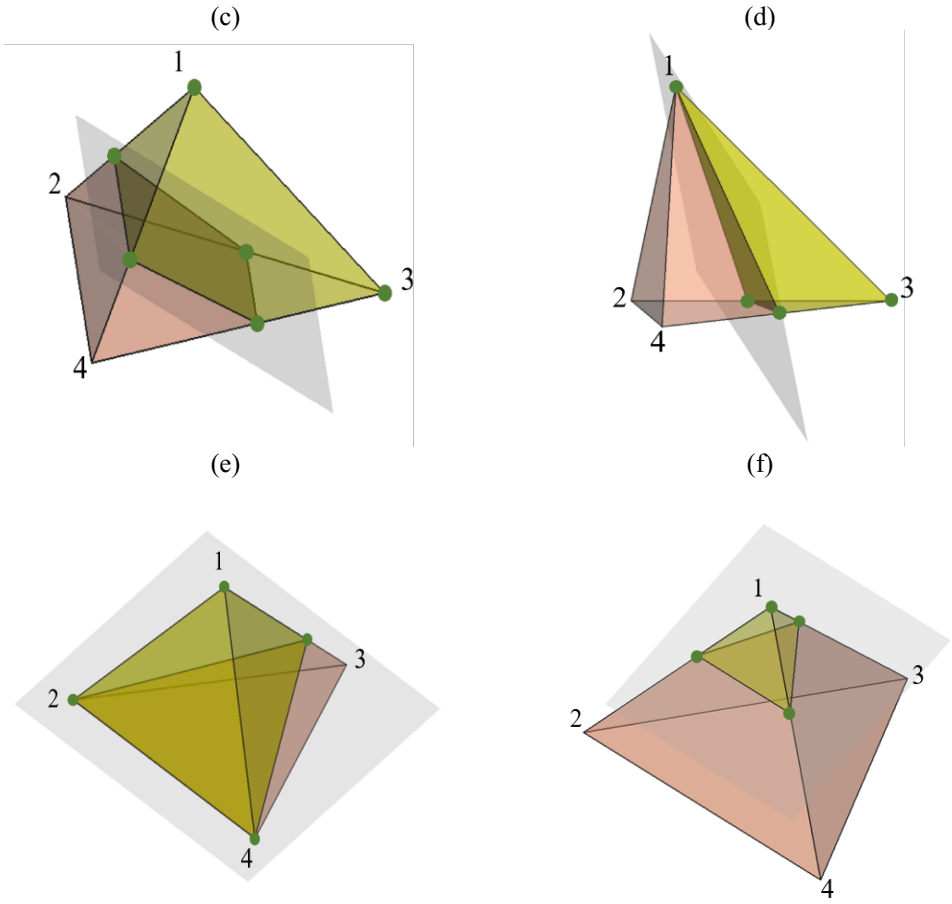

Figure 3-22. Six different configurations of a cut tetrahedron based on the state of its four nodes, yellow is the inside part of the tetrahedral element, red is the outside part of the tetrahedral element, and the final inside nodes and newly created nodes on segment and cutting plane intersection are shown in green.

When the resulting list of nodes contains four nodes, arranging them in the correct order is sufficient to form a properly oriented tetrahedral element. However, when the list contains five or six nodes, additional considerations are required.

Table 3-2. Six different configurations of a cut tetrahedron determined by the state of its four nodes.

Tetrahedron nodes	1	+	+	+	+	+	+
	2	+	+	+	0	0	−
	3	+	0	−	−	0	−
	4	−	−	−	−	−	−
Tetrahedron state		Cut tetrahedron (a)	Cut tetrahedron (b)	Cut tetrahedron (c)	Cut tetrahedron (d)	Cut tetrahedron (e)	Cut tetrahedron (f)
final number of nodes inside the list		6	5	6	4	4	4
final shape of inside part		triangular prism	quadrilateral pyramid	triangular prism	tetrahedron	tetrahedron	tetrahedron

A quadrilateral pyramid can be divided into two tetrahedra by splitting its quadrilateral face (Figure 3-23), while a triangular prism can be divided into three tetrahedra by splitting each of its three quadrilateral faces (Figure 3-24). Since a quadrilateral pyramid must be divided into two tetrahedra, splitting the quadrilateral face must take into account neighboring tetrahedra to ensure consistency in the mesh. There are two possible ways to split a quadrilateral face into two triangles and choosing the appropriate splitting diagonal depends on the configuration of neighboring elements to maintain consistency and quality of the resulting mesh. This issue also applies to splitting a triangular prism since there are three quadrilateral faces to split.

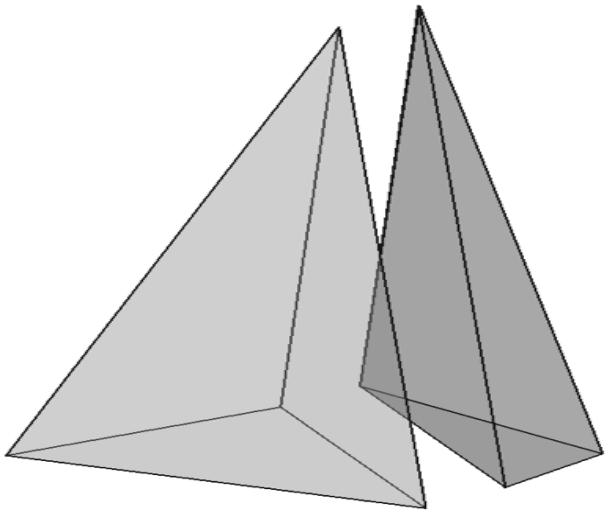

Figure 3-23. A quadrilateral pyramid being tessellated into two tetrahedra.

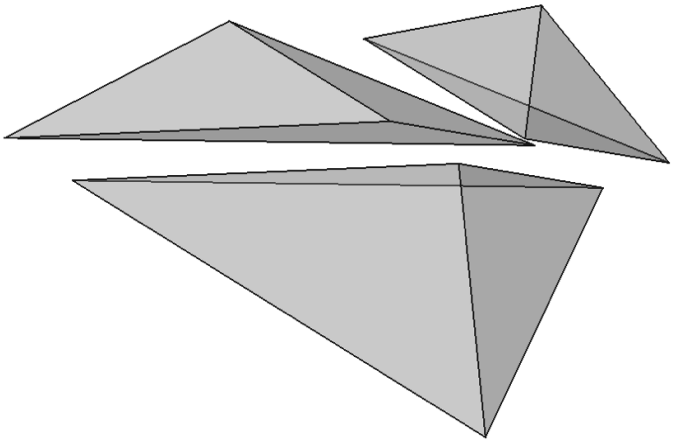

Figure 3-24. A triangular prism being tessellated into three tetrahedra.

Indeed, there are eight different ways to create diagonals and split the three quadrilateral faces of a triangular prism. However, only configurations for which two of the three diagonals coincide in one of the prism corners are valid and result in three tetrahedra. Thus, as reported in [95-97], there are six ways to create three tetrahedra from

a triangular prism (Figure 3-25). The choice of how the three quadrilateral faces is divided is important since neighboring tetrahedra should also be considered to guarantee mesh consistency. In the mesh generation algorithm, each node is associated with the triangles it belongs to. Using this information, the algorithm evaluates all six possible ways to create tetrahedra from a triangular prism and selects the one that fits with the existing triangles formed by any three of the six nodes. Another challenge is related to cases when the process leads to a dead-end because it reaches a triangular prism for which all three quadrilateral faces are already divided consistently with its neighboring tetrahedra in way that is not valid (not consistent with the six configurations shown in Figure 3-25). These dead-end cases are addressed by creating a new node inside the prism and eight tetrahedra are generated inside the prism with the help of this new node (Figure 3-26). In this work, across the entire model, dead-end scenarios usually occur for less than 0.2 % of all tetrahedra being cut. Maintaining this percentage as low as possible is important because a higher percentage would lead to increasing the number of nodes and elements, resulting in mesh refinement without added benefit and, consequently, longer computational times.

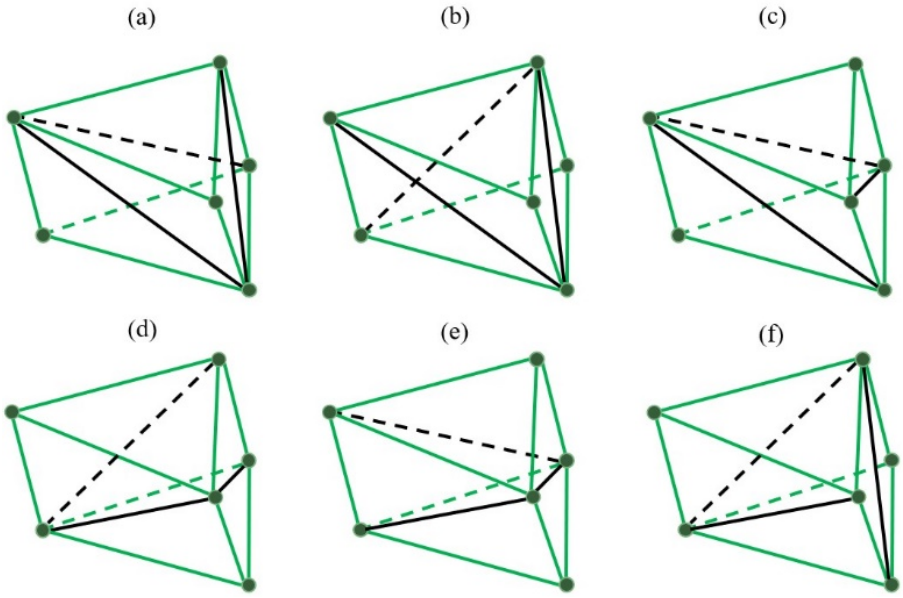

Figure 3-25. Six valid different ways to create a teras from a triangular prism.

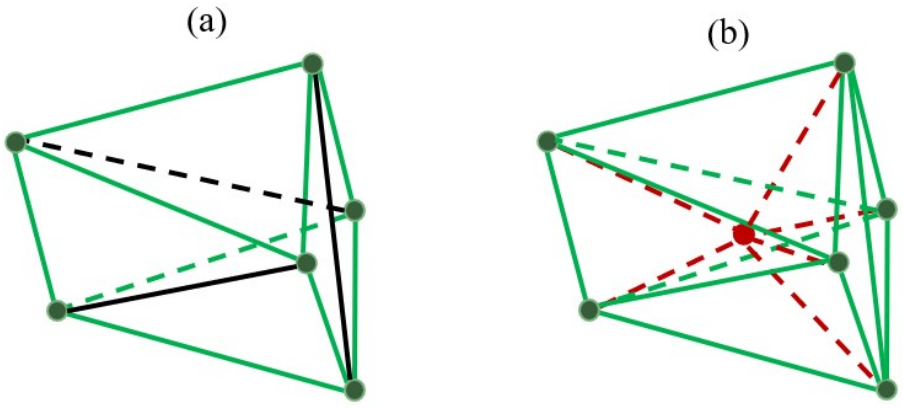

Figure 3-26. Addressing the dead-end problem in a triangular prism by adding a new node inside it.

A schematic of the cutting process is illustrated in Figure 3-28. Although the primary mesh undergoes a two-stage optimization before cutting, the new mesh exhibits poor quality around the SVE faces due to the cutting process, which is improved through another mesh optimization step. In the original pipeline, the generated linear mesh is first

smoothed in 2D. Surface triangles are optimized by iteratively relocating nodes and swapping edges to maximize minimal angles. Only once the surface quality meets its targets, the 3D advancing-front is used to fill the volume, at which point a full 3D node-relocation sweep reshapes interior tetrahedra and eliminates any negative-Jacobian elements. However, after cutting the mesh, only a single 3D optimization is applied to restore element quality. In the meantime, it must be underlined that during the cutting process, the link between the CAD model (BREP topology) and mesh components (nodes, triangles, tetrahedra) is lost since some particle geometries are removed and new mesh elements are generated. As a result, original connections between CAD and mesh components are lost. As the UTM workflow requires an associated geometric model, a virtual CAD geometry of the SVE is defined, since no geometric model initially exists for it. This virtual geometry is constructed by associating topological entities (such as edges, faces, and volumes) with geometric entities that are derived from the mesh. These geometric entities are implicitly defined using information of the original elements that were cut into these new elements during the cutting process. In other words, the mesh itself, combined with the transformation history of its elements, serves as a foundation to recreate the geometric structure indirectly. This virtual CAD geometry is not an actual representation but serves as an approximation, allowing the re-establishment of links between geometry and mesh, in order to apply the second round of mesh optimisation, boundary conditions and material properties. The second round of mesh optimisation consists of a 3D process aimed at restoring and enhancing element quality. It involves iterative node relocation to improve shape metrics, thereby reducing poorly shaped or

inverted elements and eliminating any negative-Jacobian elements that could compromise the accuracy of finite element simulations.

It is also worth noting that curvilinear quadratic tetrahedra are generated based on linear tetrahedra. The process as shown in Figure 3-27 begins with an initial mesh composed of linear tetrahedra. Each linear element is then enriched by inserting mid-side nodes at the center of each of its edges, transforming it into a quadratic tetrahedron. The mid-side nodes are projected onto an approximated curved surface representing the boundary of the particles. Since the exact analytical geometry of the particles is not available anymore, this projection relies on an estimated local discrete curvature [93]. This curvature approximation allows the reconstruction of the overall curved shape of the particles with improved fidelity. As a result, the quadratic mesh better conforms to the real geometry of the microstructure, particularly near particle-matrix interfaces.

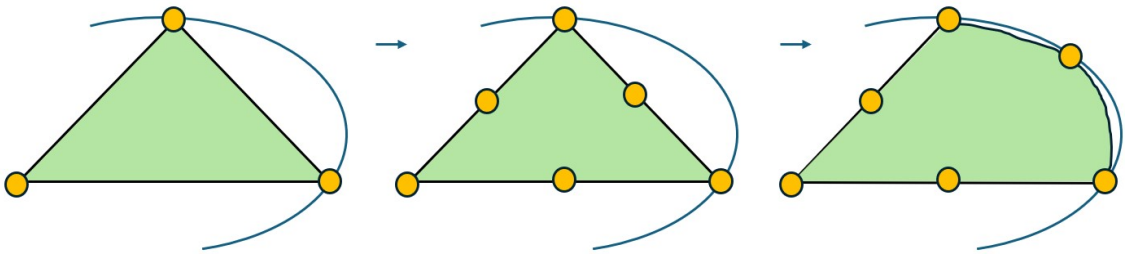

Figure 3-27. Quadratization by estimating local discrete curvature.

Once mesh optimization and quadratization completed, applying boundary conditions, FEA and homogenization of results are automatically performed. This method eliminates areas located around faces of the cut criteria domain with lower particle density, leading to a more uniform particle distribution inside the SVE itself.

(a)

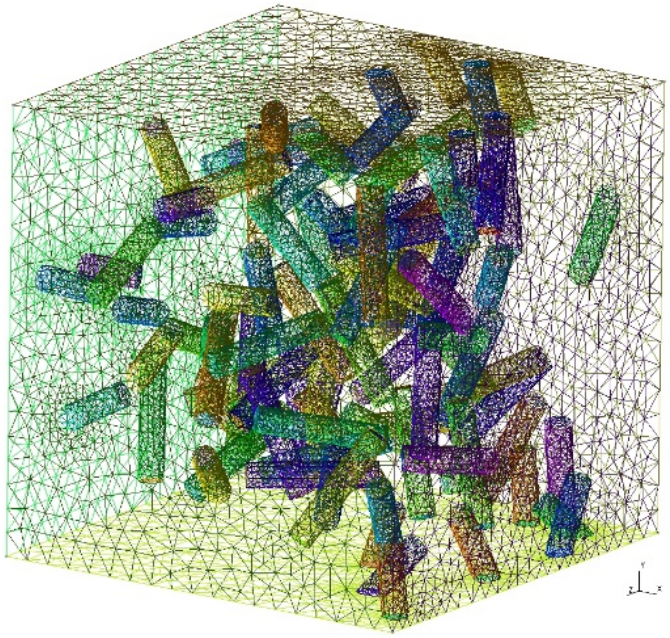

(b)

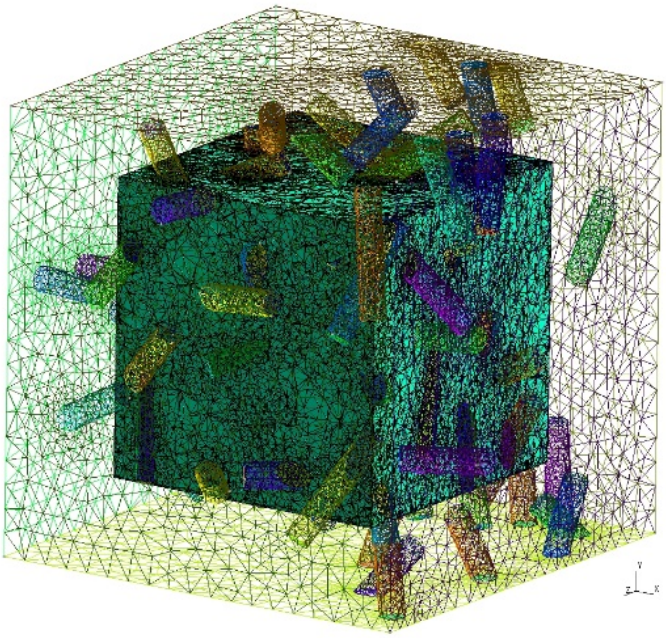

(c)

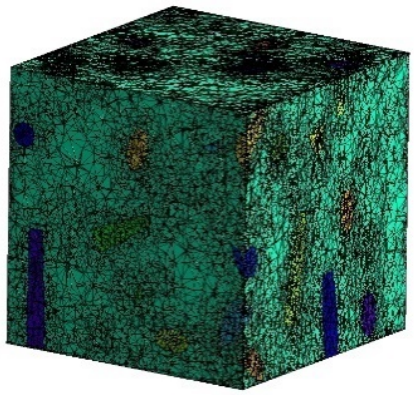

Figure 3-28. (a) meshed criteria domain, (b) cut criteria domain by target SVE and generation of new elements (the target SVE is shown by 3D elements and outer criteria domain by 2D elements for clarification.), (c) removal of outside tetrahedra leading to the target SVE.

3.4- Conclusion

This chapter presented two methodological frameworks developed in this thesis for the numerical homogenization of particle-reinforced composites at high volume fractions. GCM, which improves particle insertion through controlled adjustments, and MCM, which cut the mesh over a larger domain to reach target SVE and overcomes empty spaces at edge of SVE. These two distinct methods provide a flexible framework capable of addressing the main challenges identified in the literature, namely: achieving high reinforcement fractions, preserving isotropy in particle distributions, and ensuring stable and accurate finite element analyses. The next chapter applies these methodologies to glass–epoxy composites to evaluate their effectiveness, before extending the analysis to natural fiber reinforced composites (NFRCs) to demonstrate their practical applicability.

CHAPTER 4

RESULTS AND DISCUSSION

This chapter presents the results obtained using the methodologies described in the previous chapter. The results presented in this chapter are all obtained on unit cube dimensions (L=1). The material under investigation is glass-epoxy composite consists of an isotropic epoxy matrix reinforced with isotropic glass particles, with a perfectly bonded interface. Both constituents are treated as isotropic, and the particle–matrix interface is assumed perfect (no debonding). The mechanical properties of the glass and epoxy are summarized in Table 4-1.

Table 4-1. Material properties.

Material	E (GPa)	υ
Epoxy	3.5	0.33
Glass	72.3	0.22

Three particle shapes, spherical, cylindrical, and toroidal, are considered for modeling. Figure 4-1 illustrates these shapes and their parametrization. As shown, the sphere is characterized by its diameter (D), the cylinder by its diameter (D) and length (L) (or alternatively by its diameter and length-to-diameter elongation ratio ($\frac{L}{D}$)), and the toroidal segment by two radii: the major radius governing the overall curvature (R) and the minor radius defining the fiber's cross-sectional dimension (r), along with a specified arc angle ($\propto$).

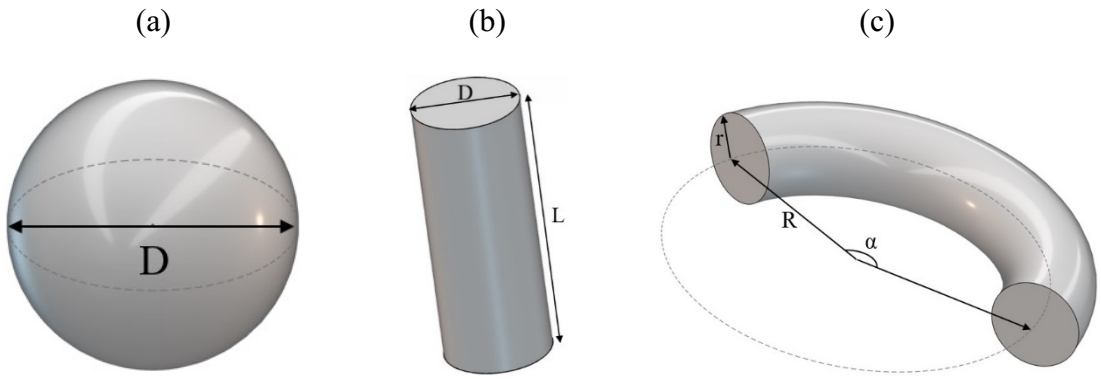

Figure 4-1. Three particle shapes available for modeling and their parametrization: (a) spherical, (b) cylindrical, (c) toroidal.

First, in Section 4.1, the results of the geometry correction method are presented and analyzed. Then, in Section 4.2, the outcomes of the mesh cutting method are introduced and discussed. Finally, Section 4.3 provides a comparative analysis of both methods to evaluate their effectiveness and determine which approach is more robust.

4.1- Results obtained with geometry correction method

This section presents results obtained for SVEs with unit cube dimensions (L=1) using the GCM only. Three types of particle shapes, spherical, cylindrical, and torus, are considered. The geometric specifications of spherical, cylindrical and torus particles used are detailed in Table 4-2.

Table 4-2. Particle characterization used in modeling.

Particle	Label	Particles intersecting the SVEs borders	Geometrical properties (mm)	Volume fraction (%)	Number of samples
Sphere	S1	Yes	$D = \frac{1}{6}$	10	15
	S2	Yes	$D = \frac{1}{6}$	30	15
Cylinder	C1	Yes	$D = 0.085, \frac{L}{D} = 5$	10	15
	C2	Yes	$D = 0.085, \frac{L}{D} = 5$	30	15
Torus	T1	Yes	$R = 2.125, r = 0.0425,$ $\propto = 0.2\ rad$	10	15
	T2	Yes	$R = 2.125, r = 0.0425,$ $\propto = 0.2\ rad$	30	15

For each particle shape, two target volume fractions are considered: 10% and 30%. As detailed earlier, using the MBD algorithm, spherical or cylindrical particles required to achieve the target volume fraction, are inserted into the MBD generation domain with the open-source Project Chrono library [98]. In the case of torus-shaped particles, the RSA algorithm is employed, as the torus primitive is not available within the MBD framework.

Geometric criteria (minimum distance and minimum angle) are then applied to all particles, and they are free to intersect with the SVEs borders. The final distribution of particles that comply with these criteria is displayed in Figure 4-2a (10 % target volume fraction) and Figure 4-2d (30 % target volume fraction) for spherical particles and Figure 4-3a (10% target volume fraction) and Figure 4-3d (30 % target volume fraction) for cylindrical particles and Figure 4-4a (10% target volume fraction) and Figure 4-4d (30 % target volume fraction) for toroidal particles. Any particle that does not meet one of the two geometric criteria undergo the geometry correction algorithm. The final distribution of particles that have been modified in shape, position, or orientation to ensure compatibility with the two geometric criteria, is illustrated in Figure 4-2b (10 % target volume fraction) and Figure 4-2e (30 % target volume fraction) for spherical particles and Figure 4-3b (10 % target volume fraction) and Figure 4-3e (30 % target volume fraction) for cylindrical particles and Figure 4-4b (10 % target volume fraction) and Figure 4-4e (30 % target volume fraction) for toroidal particles. The inclusion of these newly retained particles, combined with those already accepted and inserted, results in the final particle distribution and volume fraction as illustrated in Figure 4-2c (10% target volume fraction) and Figure 4-2f (30 % target volume fraction) for spherical particles and Figure 4-3c (10 % target volume fraction) and Figure 4-3f (30 % target volume fraction) for cylindrical particles and Figure 4-4c (10 % target volume fraction) and Figure 4-4f (30 % target volume fraction) for toroidal particles.

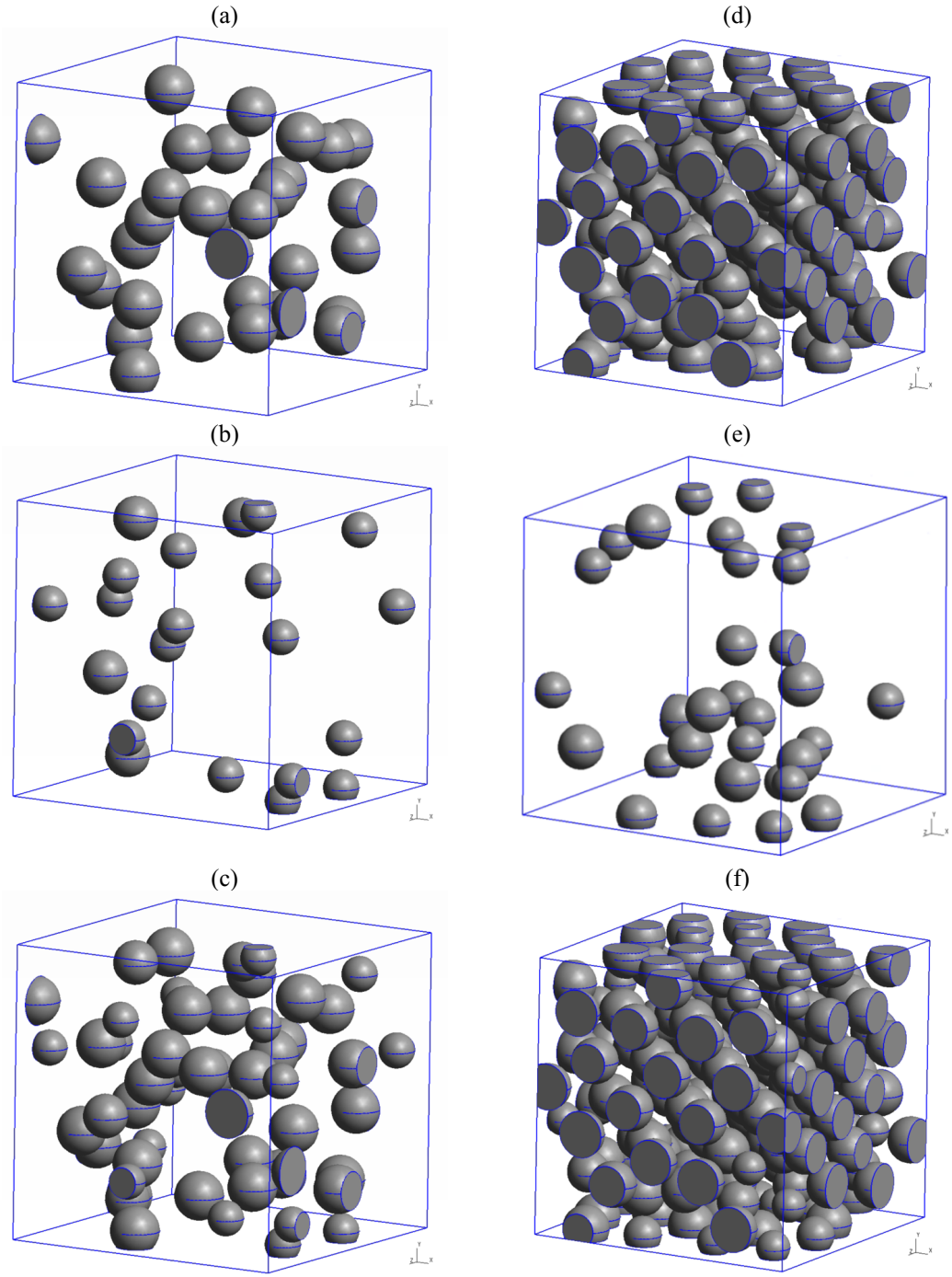

Figure 4-2. Geometry correction approach for spherical particles to achieve 10% volume fraction ((a)-(c)) and 30% volume fraction ((d)-(f)). Shown are original particle distribution ((a), (d)), corrected and accepted particles ((b), (e)), and final particle distribution ((c), (f)).

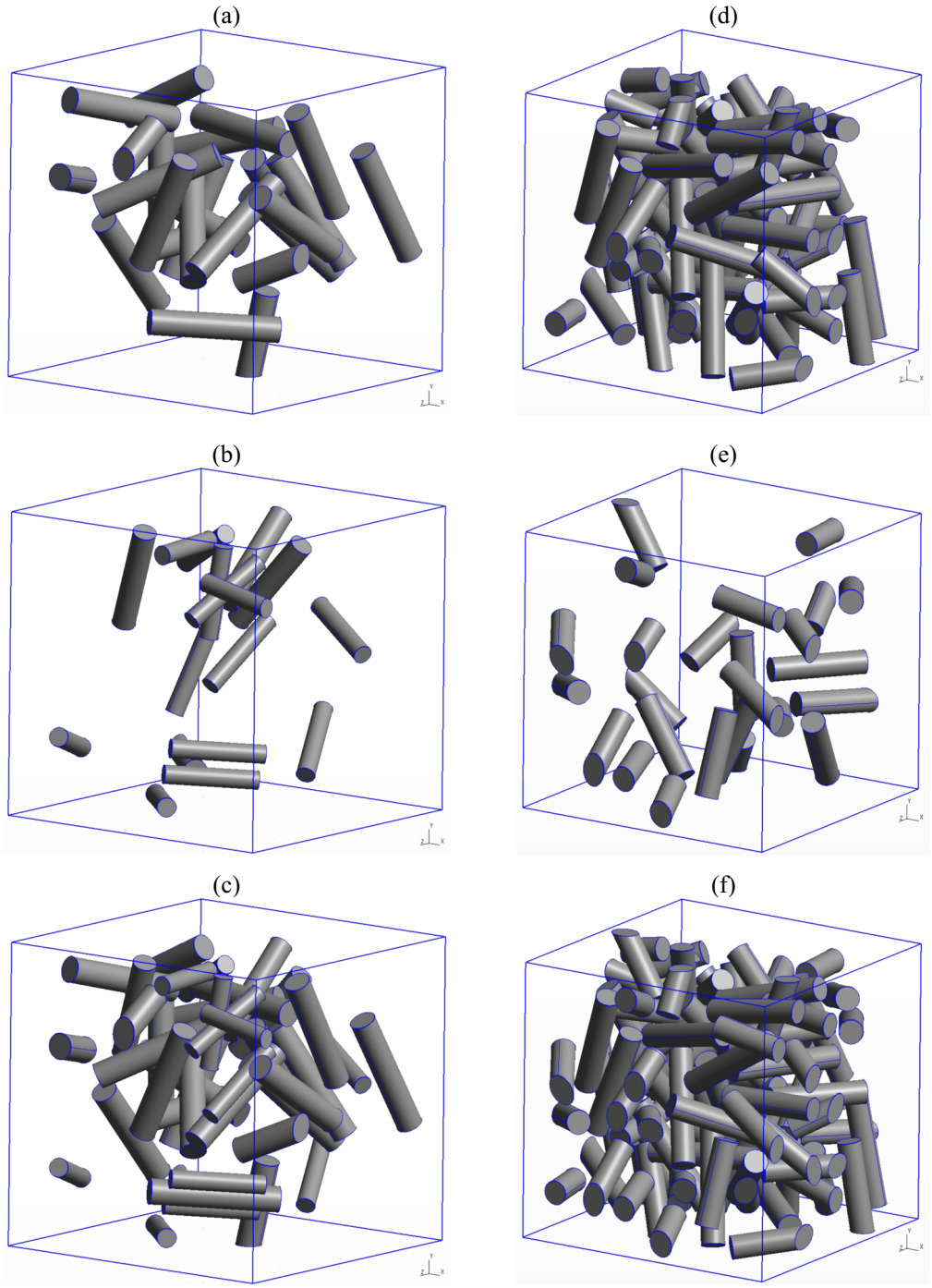

Figure 4-3. Geometry correction approach for cylindrical particles to achieve 10% volume fraction ((a)-(c)) and 30% volume fraction ((d)-(f)). Shown are original particle distribution ((a), (d)), corrected and accepted particles ((b), (e)), and final particle distribution ((c), (f)).

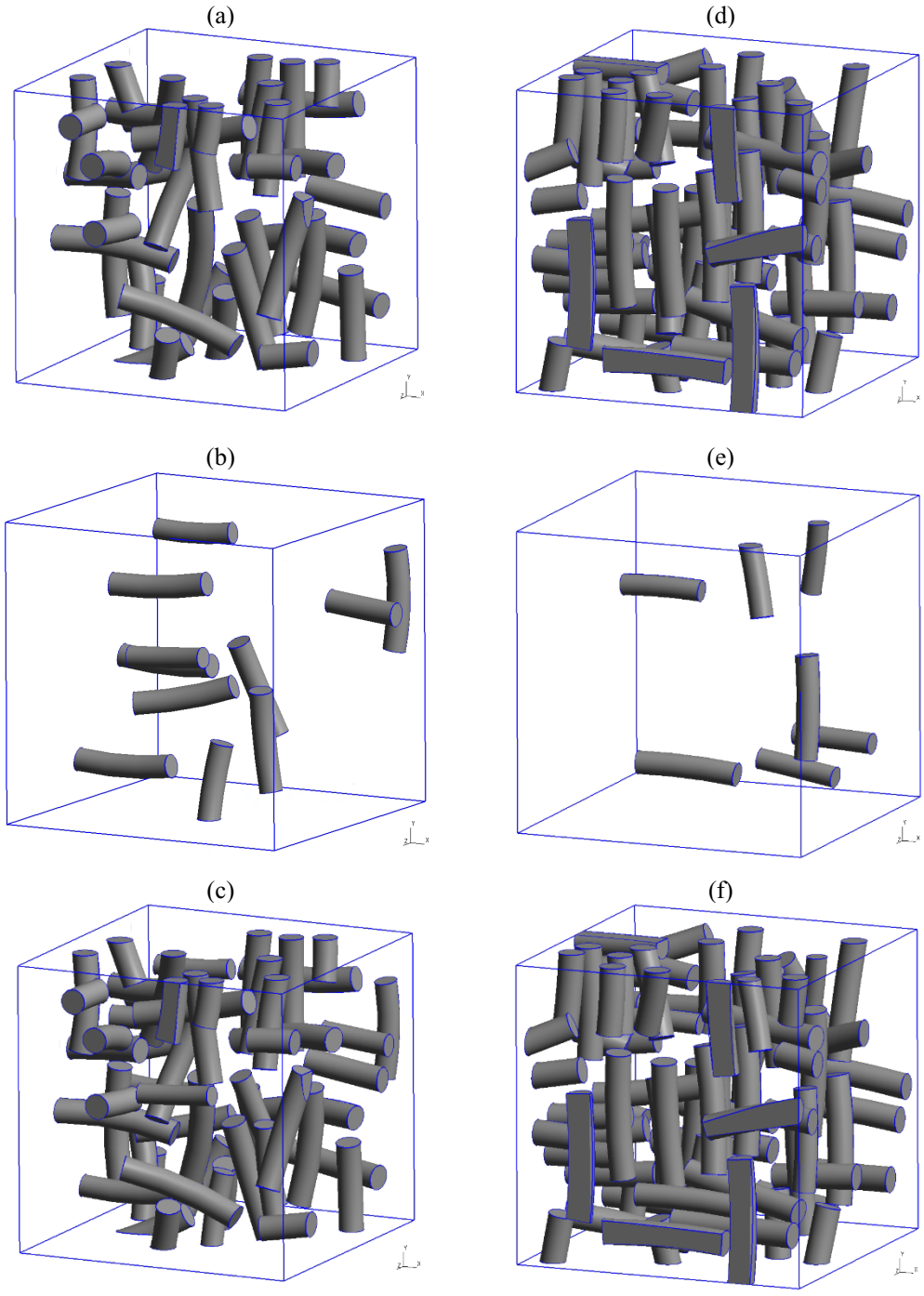

Figure 4-4. Geometry correction approach for toroidal particles to achieve 10% volume fraction ((a)-(c)) and 30% volume fraction ((d)-(f)). Shown are original particle distribution ((a), (d)), corrected and accepted particles ((b), (e)), and final particle distribution ((c), (f)).

Numerical results, including mean volume fraction and mean number of particles of 15 SVEs for each case, are summarized in Table 4-3. It is worth noting that, even for the more demanding case of cylindrical particles at 30 % volume fraction, the computational overhead of the GCM algorithm remains modest. This is because the maximum number of correction iterations per particle is deliberately limited, so that only small adjustments are attempted at each step. As a result, the algorithm does not require a high number of iterations to converge for each particle. In practice, the additional cost introduced by GCM is at most a couple of hours in the most demanding configurations, which is minor compared to the overall modeling time dominated by meshing and finite element simulations. For spherical particles, before applying the GCM, mean volume fractions around 7.17 % and 27.60 % are respectively obtained for 10 % and 30 % target volume fractions. After applying the geometry correction algorithm, these mean values increase to 9.62 % and 30.63 %. Changes to the geometry in this case are limited to changing the radius and position of spheres, which is significantly different for cylindrical-shaped and torus shaped particles. When the GCM is not applied, with cylindrical particles, mean volume fractions around 4.78 % and 15.31 % are respectively obtained for 10 % and 30 % target volume fractions. After applying the geometry correction algorithm, these mean values increase to 7.41 % and 19.75 %. Furthermore, with toroidal particles, when the GCM is not applied, mean volume fractions around 4.75 % and 6.95 % are respectively obtained for 10 % and 30 % target volume fractions. After applying the geometry correction algorithm, these mean values increase to 7.39 % and 10.74 %.

Table 4-3. Results of applying GCM on SVEs.

Case	Target volume fraction (%)	MBD without GCM (%)	MBD with GCM (%)	Number of Corrected Particles	Total Number of Particles
S1	10	7.17±0.91	9.62±0.84	19±3	52±5
C1	10	4.78±0.50	7.41±0.32	20±3	43±5
T1	10	4.75±0.33	7.39±0.72	9±2	41±6
S2	30	27.60±0.20	30.63±0.30	27±3	162±2
C2	30	15.31±0.49	19.75±0.95	31±6	106±2
T2	30	6.95±0.25	10.74±0.68	18±2	67±2

For cylindrical and toroidal particles, the algorithm tries adjustments in length, radius, position, and orientation of particles. Even if this approach enhances the volume fraction, it still falls short of achieving target volume fractions for elongated particles. This limitation arises because, although several particles are retained, their volume is often significantly reduced. Moreover, after a limited number of adjustments, a jamming limit is reached. As a particle's position or orientation is modified to resolve a compatibility issue with one neighboring particle, it can create a new compatibility problem with another neighboring particle. For instance, in Figure 4-5, even after adjusting the position of particle 2 to ensure it respects the minimum distance between the particle and the SVE boundary, a new incompatibility arises with particle 1. As a result, particle 2 is ultimately removed from the SVE model. Furthermore, when working with cylindrical particles, ensuring a final isotropic distribution necessitates careful attention to their random positioning and orientation which is checked using the orientation tensor of particles.

When the correction algorithm modifies orientation and position of cylinders to achieve a higher volume fraction, it may disrupt the random distribution of particles orientation. This issue is illustrated in Figure 4-6. The figure illustrates that the correction algorithm may tend to align particles that were randomly oriented before geometry correction, which ultimately results in a non-isotropic distribution of particles orientation. The alignment shown in Figure 4-6b is measured using the orientation tensor illustrated in Table 4-4. The orientation tensor of a perfect isotropic distribution of cylinders is as shown in Table 4-5. Indeed, the diagonal values of this tensor exhibit deviations (around 10 %) from those in the tensor of a perfectly isotropic distribution of particles.

To achieve a higher volume fraction for more complex shapes than spheres, which is generally the case for real-world particle geometry, the mesh cutting method can be applied and its results are presented in the next subsection.

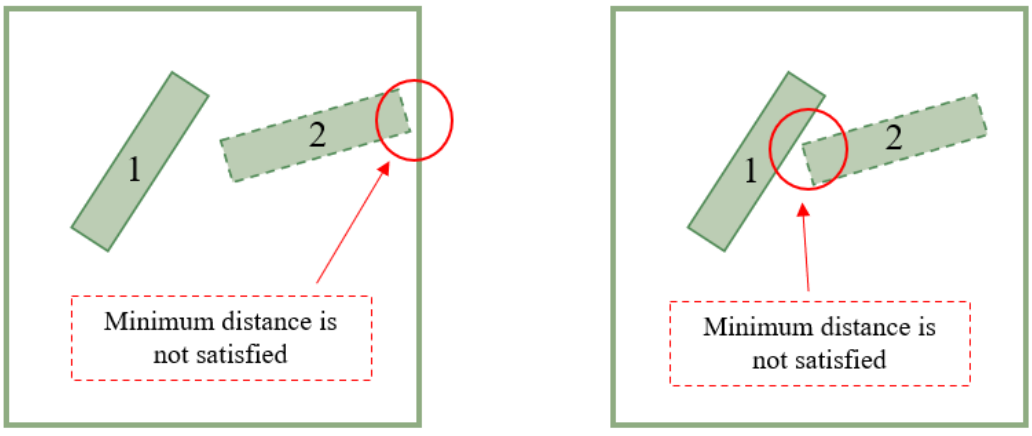

Figure 4-5. Jamming limit in GCM, min_{dist} problem of particle 2 (left) with the edge and (right) with another particle.

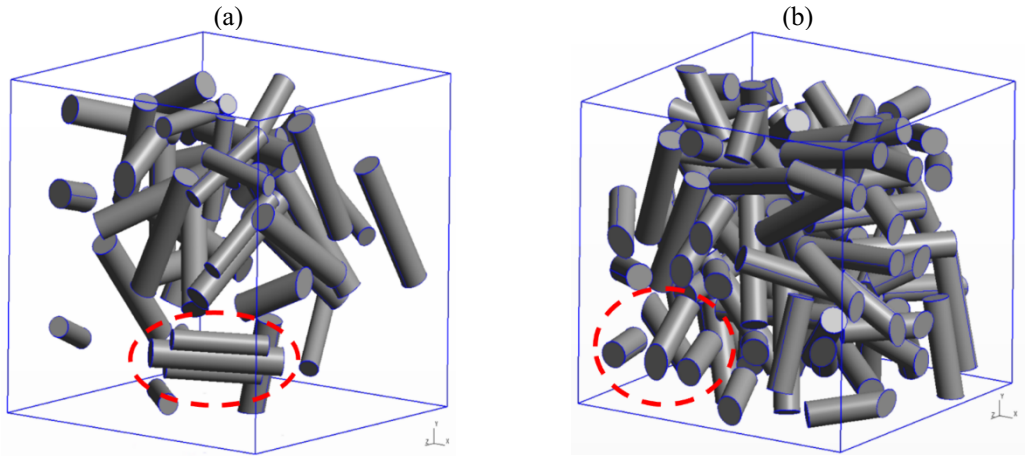

Figure 4-6. The correction algorithm tends to change the randomly oriented particles to become uniformly aligned, resulting in a non-isotropic distribution of cylinders: (a) for 10 % target volume fraction, (b) for 30 % target volume fraction.

Table 4-4. Orientation tensor for sample Figure 4-6b.

$$\begin{bmatrix} 0.294 & -0.023 & -0.015 \\ -0.023 & 0.293 & -0.015 \\ -0.015 & -0.015 & 0.411 \end{bmatrix}$$

Table 4-5. Orientation tensor for a perfectly isotropic distribution of particles.

$$\begin{bmatrix} \frac{1}{3} & 0 & 0 \\ 0 & \frac{1}{3} & 0 \\ 0 & 0 & \frac{1}{3} \end{bmatrix}$$

4.2- Results obtained with the mesh cutting method

Following models are generated and evaluated by only the mesh cutting method described in section 3. Geometric properties used for these models are listed in Table 4-6.

The results are obtained for SVEs with unit cube dimensions ($L = 1$). Furthermore, material properties of a glass-epoxy composite are already listed in Table 4-1.

Table 4-6. Particle characterization used in modeling.

Particle	Particles intersecting the SVEs borders	Geometrical properties (mm)	Volume fraction (%)	Number of samples
Cylinder	No	$D = 0.085, \frac{L}{D} = 5$	10	15
Torus	No	$R = 2.125, r = 0.0425,$ $\propto = 0.2\ rad$	10	15
Sphere	No	$D = \frac{1}{6}$	30	15
Cylinder	No	$D = 0.085, \frac{L}{D} = 5$	30	15

As presented in section 3, the final geometry and mesh of SVEs are generated focusing on mesh consistency and tetrahedral elements quality. In the case of torus-shaped particles, the RSA algorithm is utilized to generate particles, given the absence of a torus primitive in the MBD framework. As reported in our previous work [73], discarding particles intersecting the borders of SVEs reduces the number of elements and prevents the refinement of the size map near the boundaries. In this method, particles intersecting the borders of the criteria domain are similarly discarded, along with particles that do not meet specified criteria. This approach is justified since elements in these areas will be removed in subsequent steps. The volume fraction is calculated for the criteria domain for comparison purposes, which is followed by mesh generation and mesh cutting to achieve the target SVE dimensions. It is worth noting that the final SVE volume fraction of

particles is based on the volume of mesh elements and not on solid modelling calculations. The comparison between these volume fractions is presented in Table 4-7. For toroidal particles, before applying the MCM, a mean volume fraction of approximately 7.18 % was achieved, while for cylindrical particles, it was about 6.34%, both corresponding to a target volume fraction of 10 %. After applying the MCM, these mean values increased to 10.45 % and 9.97 %, respectively. Similarly, prior to the implementation of the mesh cutting method, the maximum achievable volume fractions for a target of 30 % were 19.34 % for spherical particles and 15.31 % for cylindrical particles. It is worth noting that, if compared to spheres, the volume fraction is lower for cylinders due to their geometric characteristics, which make it more challenging to fit a greater number of cylinders inside the SVE while respecting required criteria (minimum distance and angle). However, after applying the mesh cutting method, these values increase to 30.33 % for spherical particles and 30.14 % for cylindrical particles, which demonstrates the effectiveness of this method towards raising volume fractions.

The orientation tensor for cylindrical particles is presented in Table 4-8 to verify the isotropic distribution of particles orientation within the SVE. As mentioned in sub-section 4.1, this tensor provides insights into the alignment and distribution of cylindrical particles, ensuring that they are uniformly oriented which confirms effectiveness of this method towards achieving isotropic distributions of particles orientation.

The orientation tensor is a useful measure of particle alignment and provides insight into how orientation distribution affects effective properties. When the orientation

tensor is close to isotropic (diagonal components ≈ 1/3), the reinforcement is randomly oriented and the apparent moduli are lower but more uniform, reflecting balanced stiffness in all directions. In contrast, as alignment increases (anisotropic tensor), the modulus in the fiber alignment direction grows significantly, while stiffness in transverse directions decreases. This behavior reflects the fundamental role of elongated fibers in transferring load most efficiently along their main axis. The orientation tensor serves as a bridge between microstructural alignment and macroscopic anisotropy. Small variations in orientation can therefore lead to noticeable differences in apparent moduli, even for composites with identical volume fraction and aspect ratio. This confirms that orientation distribution is a critical parameter for interpreting homogenized elastic properties and must be considered alongside volume fraction and particle geometry in model validation.

Table 4-7. Comparison of volume fractions with different methods.

	Target volume fraction (%)	Volume fraction in criteria domain (%)	Volume fraction after cut in SVEs (%)	Volume fraction with erosion of results only with erosion of results distance of 0.2 (%) [73]
Torus	10	7.18 ± 0.24	10.45 ± 0.71	N/A
Cylinder	10	6.34 ± 0.35	9.97 ± 0.87	9.13 ± 1.93
Sphere	30	19.34 ± 0.34	30.33 ± 0.49	34.12 ± 0.57
Cylinder	30	15.31 ± 0.49	30.14 ± 0.53	27.01 ± 1.88

Table 4-8. Orientation tensor for cylindrical particles.

$$\begin{bmatrix} 0.323 & -0.004 & -0.003 \\ -0.004 & 0.342 & -0.006 \\ -0.003 & -0.006 & 0.334 \end{bmatrix}$$

The finite element quality distributions for both spherical and cylindrical particles calculated as described in previous chapter are illustrated in Figure 4-7. This quality values quantifies the element's deviation from the ideal shape, with values ranging from 0 (for a degenerate tetrahedron) to 1 (for a perfect equilateral tetrahedron). Higher values of Q_k indicate better-quality elements, which is essential for ensuring numerical stability and accuracy in finite element simulations. According to this figure, the great majority of tetrahedra feature quality between 0.3 and 0.8. This means that meshes generally show high quality, which is important for the accuracy of FEA results. Only a very small percentage of elements show a quality below 0.3, which can be explained considering that the quality threshold set for the automatic mesh generation algorithm is 0.2. This means that along automatic mesh generation and optimization, elements with a quality below 0.2 are eliminated and re-meshed to enhance mesh quality.

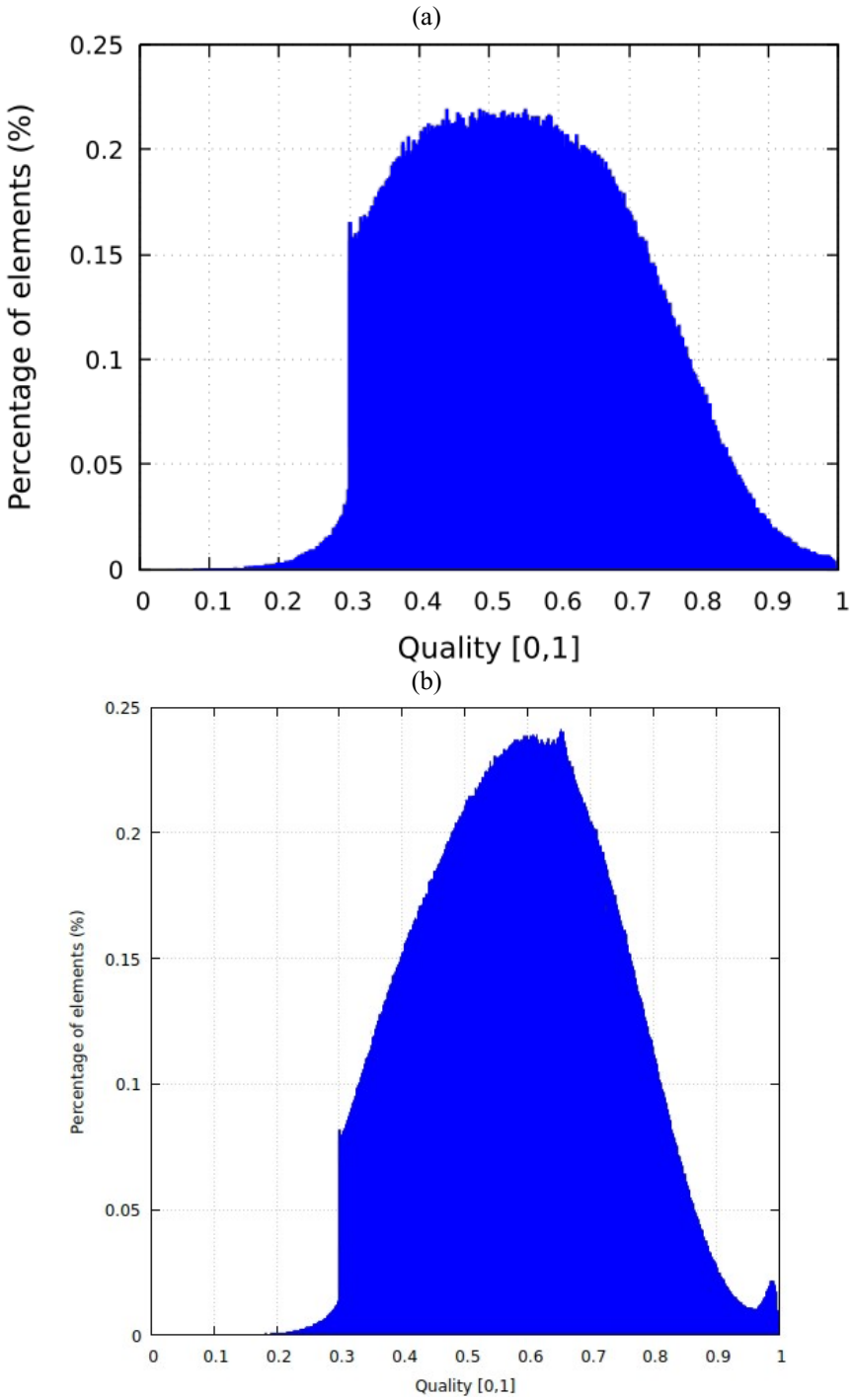

Figure 4-7. Mesh quality distribution: (a) spherical and (b) cylindrical particles with 30 % target volume fraction.

To evaluate the apparent elasticity modulus (E_{app}), three types of boundary conditions are commonly employed: Kinematic Uniform Boundary Conditions (KUBC) and Static Uniform Boundary Conditions (SUBC), and Periodic Boundary Conditions (PBCs). It is well established that PBCs are advantageous in homogenization studies, as they lead to faster convergence of homogenized material properties while requiring smaller SVEs compared to KUBCs and SUBCs [49, 99-101]. However, applying PBCs is not just a boundary condition challenge but also a geometrical and meshing one. For PBCs to be effective, the particle generation process must be intrinsically periodic before meshing, and the mesh itself must maintain periodicity, ensuring that opposite faces have matching nodes to avoid interpolation errors when enforcing PBCs. While PBCs may be useful in some cases, Schneider et al. [102] highlight that achieving a fully periodic RVE and mesh topology is inefficient and challenging, especially for complex microstructures.

In this study, the primary objective is to achieve higher volume fractions without relying on the erosion of results method. This focus makes the direct enforcement of PBCs particularly difficult due to the lack of periodicity in the particle generation process and the disruption of mesh periodicity when applying a cutting plane. Unlike structured meshes, where node pairing is straightforward, the unstructured nature of the cut tetrahedral mesh complicates the identification of periodic node pairs and the imposition of displacement constraints.

Thus, to evaluate the apparent elasticity modulus (E_{app}), two types of boundary conditions are employed: KUBC and SUBC. Considering that mechanical properties of

the glass-fiber composite are assumed to be isotropic; the macroscopically isotropic microstructure assumption is applied. Under this assumption, the apparent compressibility modulus (K_{app}), apparent shear modulus (G_{app}) and apparent elasticity modulus (E_{app}) are respectively calculated as explained in previous chapter.

Using this FEA homogenization, the apparent elasticity modulus for KUBC and SUBC boundary conditions is calculated and presented in Table 4-9. These results are compared with the apparent elasticity modulus obtained using the erosion of results method described in section 3. A notable difference is observed between apparent elasticity moduli obtained with KUBC and SUBC boundary conditions when using the mesh cutting method, which is not the case when applying the erosion of results method. Moreover, the apparent elasticity modulus with KUBC and the mesh cutting method is higher than that obtained with KUBC and the erosion of results method. This is due to the fact that the erosion of FEA results from the SVE boundary tends to supress boundary condition effects. It is also observed that KUBC results tends to overestimate elastic properties by enforcing rigid displacements on the boundaries, while SUBC underestimates these properties since it allows more boundary deformation. This difference highlights the contrasting effects of boundary conditions on the predicted material properties.

Table 4-9. Comparison of apparent elastic modulus with erosion of results method for KUBC and SUBC.

	Volume fraction with cut (%)	E_{KUBC} (GPa)	E_{SUBC} (GPa)	Volume fraction $_{\text{erosion of results}}$ with erosion distance of 0.2 (%) [73]	$E_{KUBC,\ \text{erosion of results}}$ with erosion distance of 0.2 (GPa) [73]	$E_{SUBC,\text{erosion of results}}$ with erosion distance of 0.2 (GPa) [73]
Torus	10.45 ± 0.71	4.69 ± 0.09	4.26 ± 0.05	N/A	N/A	N/A
Cylinder	9.97 ± 0.87	4.92 ± 0.14	4.39 ± 0.10	9.13 ± 1.93	4.46 ± 0.24	4.43 ± 0.23
Sphere	30.33 ± 0.49	7.41 ± 0.18	6.32 ± 0.06	34.12 ± 0.57	6.89 ± 0.09	6.90 ± 0.09
Cylinder	30.14 ± 0.53	8.45 ± 0.17	6.92 ± 0.11	27.01 ± 1.88	6.76 ± 0.29	6.64 ± 0.27

To validate results obtained, the evolution of apparent elasticity modulus with respect to the volume fraction of each SVE is also compared with analytical bounds of Reuss, Voigt and Hashin–Shtrikman (HS-, HS+) (Figure 4-8 and Figure 4-9). It appears that, for each case, the apparent elastic modulus lies between lower and upper bounds, with a significant margin from Hashin–Shtrikman lower bound (HS-). This indicates that predicted apparent elastic moduli are neither overly conservative nor overly optimistic.

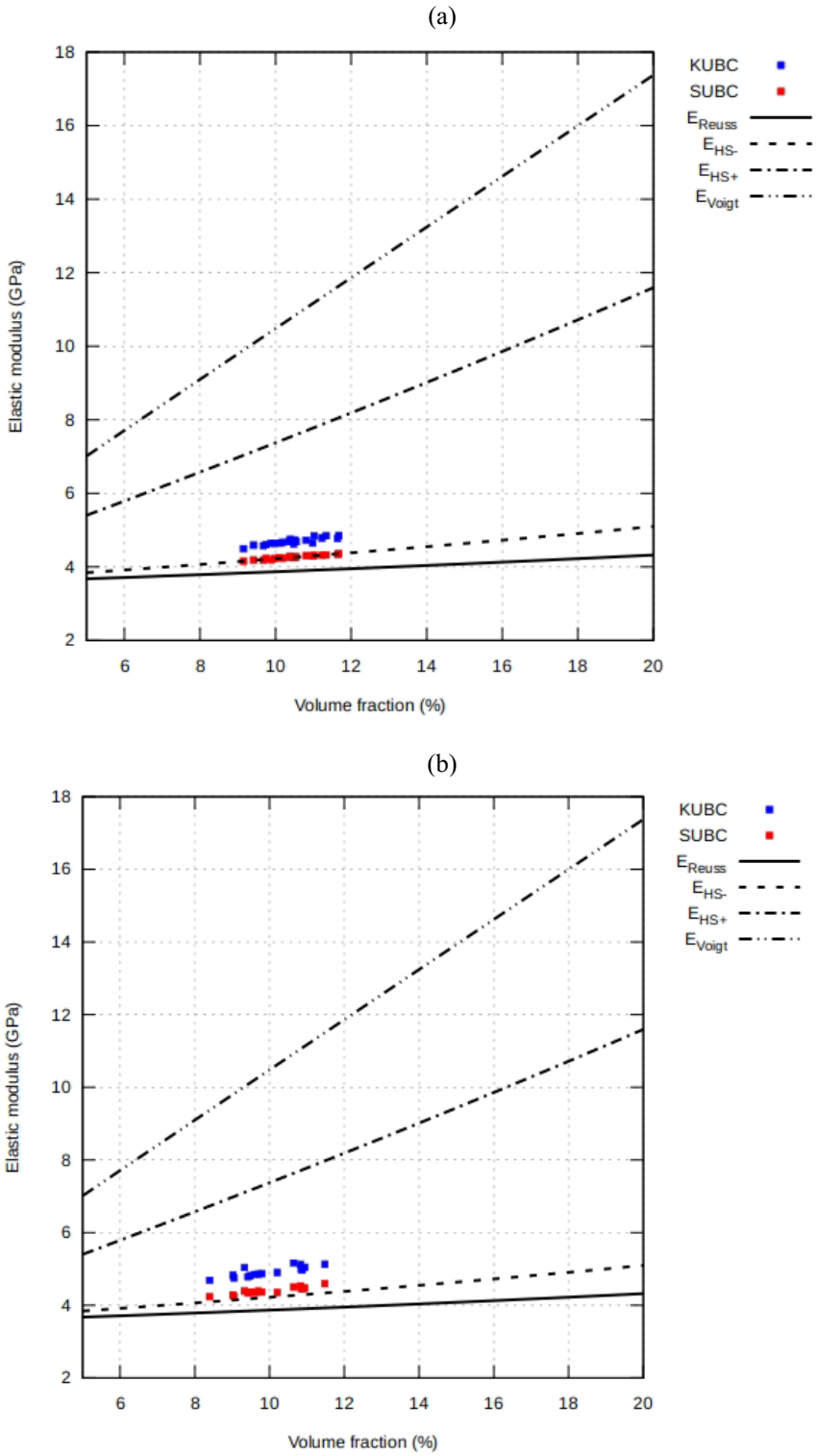

Figure 4-8. Elastic modulus scatter for different SVEs with: (a) toroidal and (b) cylindrical particles.

Figure 4-10 and Figure 4-11 provides insights about how moving toward the core of the cube, affects results. As the distance from boundary faces increases through the core of the SVE between 0 and of 0.2 (for a unit cube SVE) the change in volume fraction is not significant. This consistency confirms that the distribution of particles within the SVE is even and isotropic. In addition, as the distance from boundary faces increases, the differences between results obtained with KUBC and SUBC gradually diminish, which illustrates, as expected, that boundary conditions have very little effect at the core of the SVE. However, with the mesh cutting method, a clear difference between KUBC and SUBC results is observed, which demonstrates that the mesh cutting approach maintains the influence of boundary conditions.

(a)

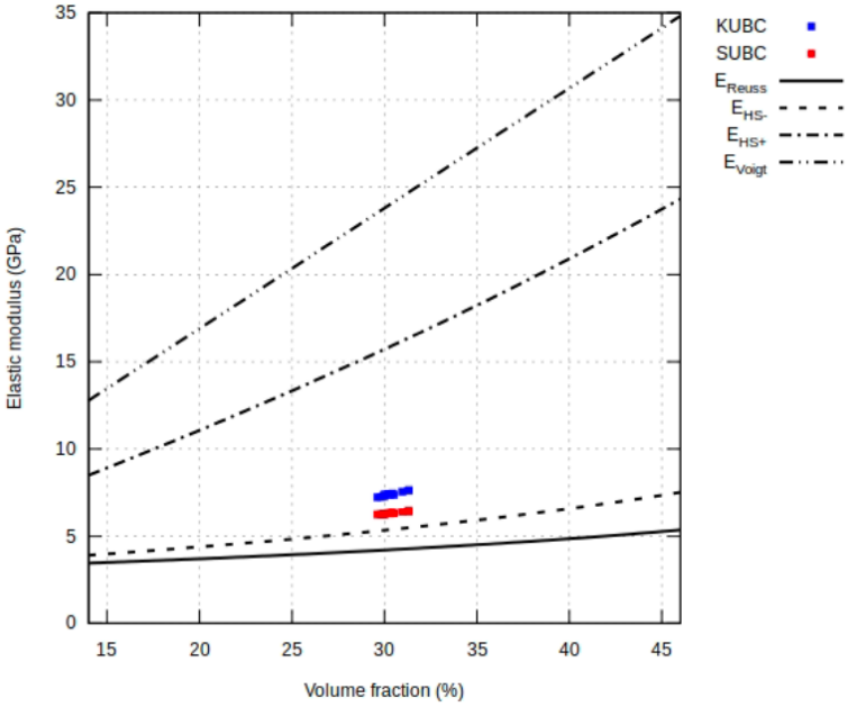

(b)

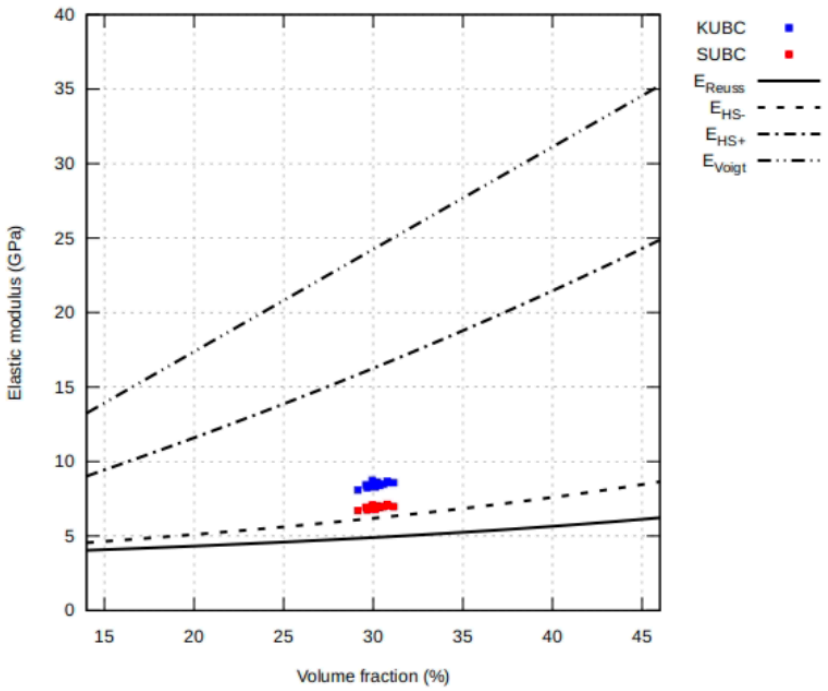

Figure 4-9. Elastic modulus scatter for different SVEs with: (a) spherical and (b) cylindrical particles.

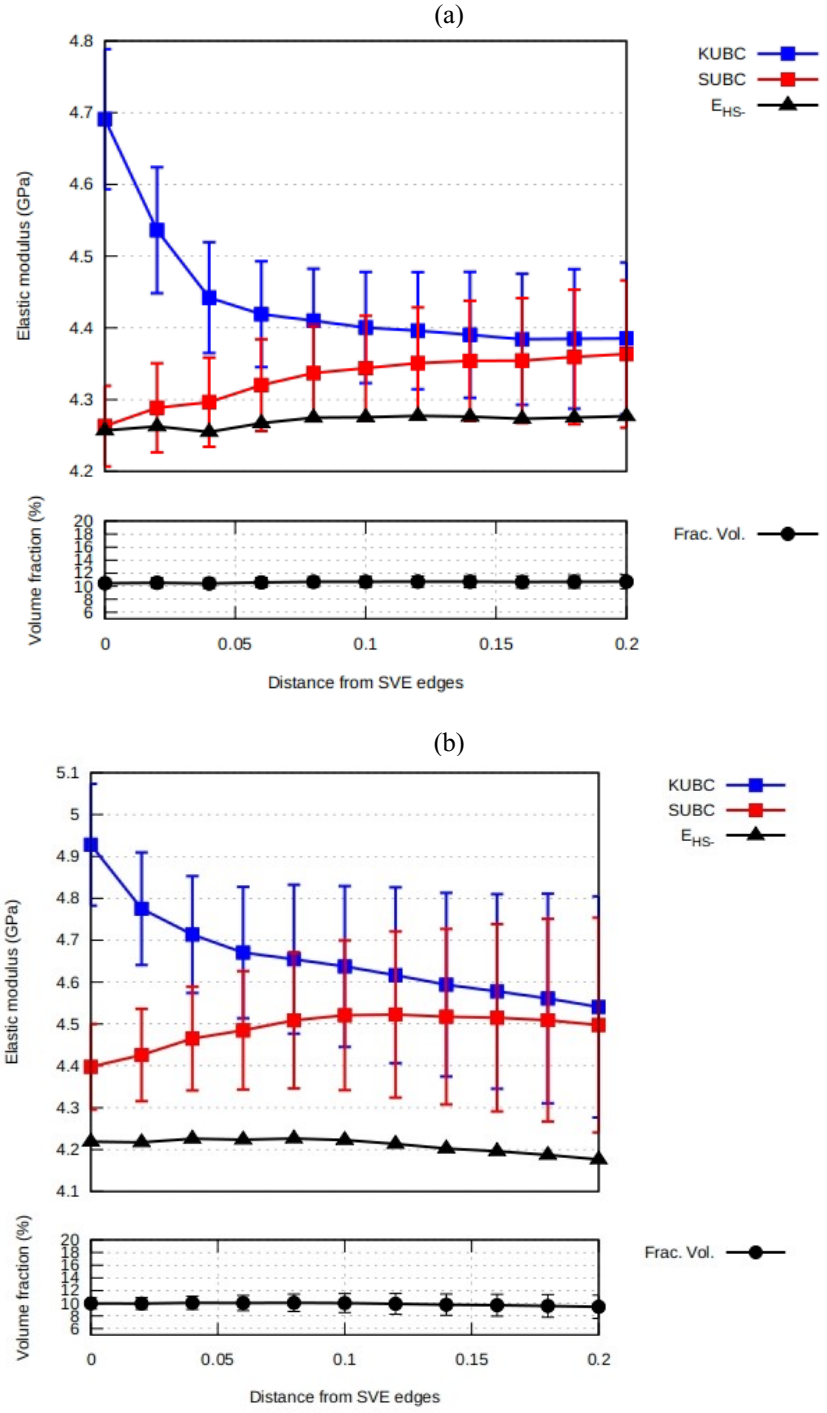

Figure 4-10. Elastic modulus scatter toward the core of the cube for a SVE with: (a) toroidal and (b) cylindrical particles.

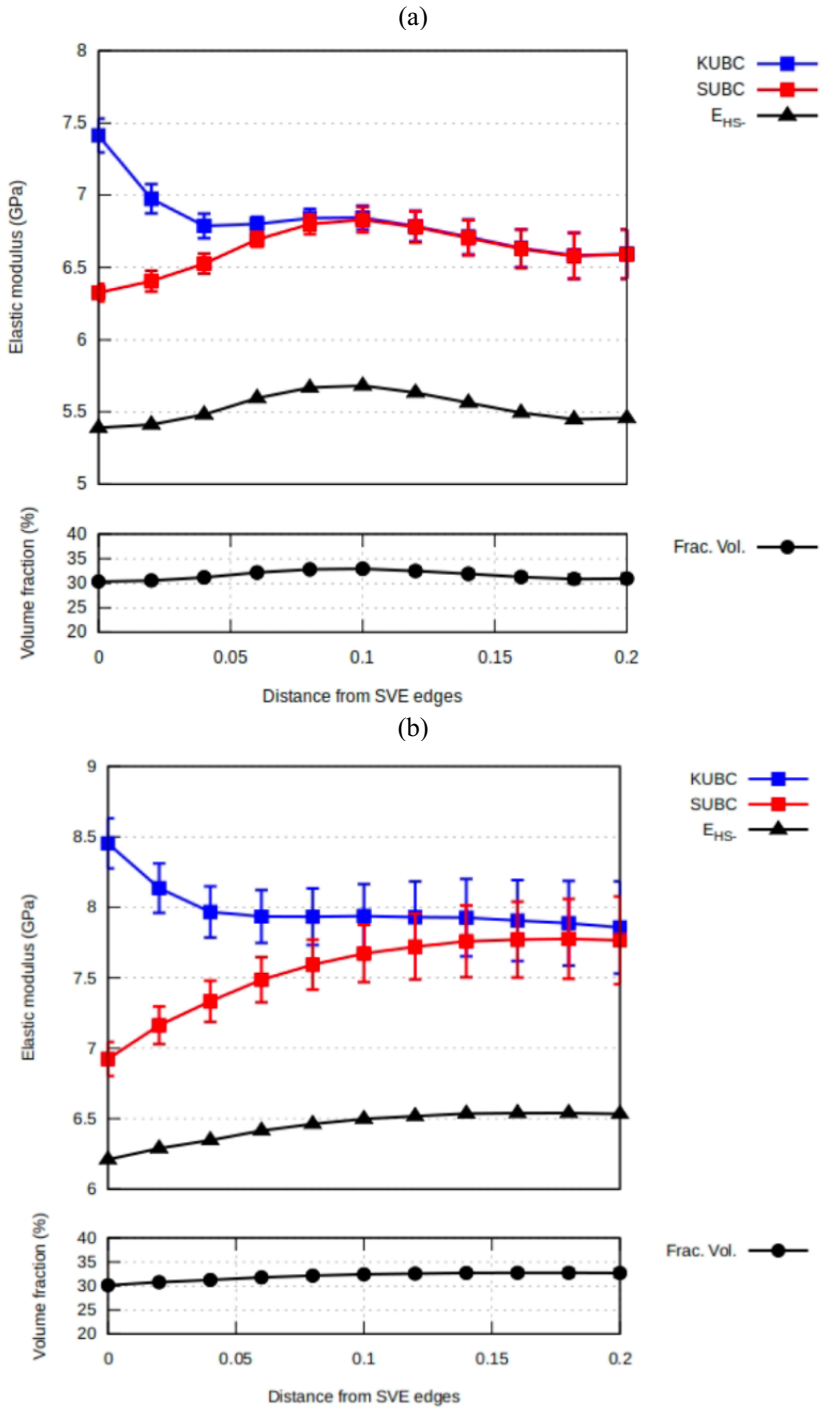

Figure 4-11. Elastic modulus scatter toward the core of the cube for a SVE with: (a) spherical and (b) cylindrical particles.

4.3- Comparing geometry correction method with mesh cutting method for sphere

A comparative analysis of the GCM and the MCM for spherical particles at a volume fraction of 30% provides key insights into their performance. Both methods successfully achieve the target volume fraction and obtain final averaged elastic modulus values, as summarized in Table 4-10. However, distinct differences emerge in their efficiency, particle distribution, and the consistency of their results. First of all, it should be mentioned that, as shown before in Chapter 3, it is not possible to reach this volume fraction with cylindrical particles using GCM, and this is the reason why only results for spherical particles are compared in this section.

Table 4-10. Comparison of apparent elastic modulus with GCM and MCM.

Sphere	Volume fraction (%)	$E_{KUBC}\,(GPa)$	$E_{SUBC}\,(GPa)$
MCM	30.33 ± 0.49	7.41 ± 0.18	6.32 ± 0.06
GCM	30.00 ± 0.53	7.95 ± 0.14	6.15 ± 0.07

From an elastic modulus perspective, both methods effectively reach the desired volume fraction, but the difference between KUBC and SUBC is more pronounced when using GCM than MCM. This discrepancy, illustrated in Table 4-10, Figure 4-12 and Figure 4-13, highlights the effect of particle distribution on numerical results. In Figure 26, which presents the elastic modulus distribution within SVEs, a larger gap between KUBC and

SUBC results is observed for GCM. This suggests that GCM induces more variability in elastic modulus estimation, likely due to its less uniform particle distribution.

The particle distribution differences between the two methods are further demonstrated in Figure 4-13, where the non-uniform volume fraction distribution in GCM-generated SVEs is evident from the sudden jumps in the volume fraction versus distance from the SVE edge curve (Figure 4-13a). In contrast, MCM maintains a more gradual and stable distribution, ensuring a more homogeneous spatial arrangement of particles (Figure 4-13b). This improved uniformity contributes to the better consistency of elastic modulus values obtained via MCM. Additionally, the distance required for KUBC and SUBC results to converge is greater in GCM than in MCM, further indicating that MCM provides a more stable and predictable numerical framework.

Another important observation comes from Figure 4-12. In Figure 4-12a, the results generated by GCM are evenly scattered around the target volume fraction of 30%, whereas in Figure 4-12b, MCM results tend to exceed the target volume fraction. This suggests that MCM has a greater capability to reach even higher volume fractions or accommodate more elongated particles, making it a more versatile approach in handling complex composite microstructures. Furthermore, the geometric integrity of particles is significantly better preserved using MCM. With GCM, some particles are artificially reduced in size to fit within the computational domain, leading to an unrealistic representation of their physical properties. On the other hand, MCM retains the original particle dimensions, ensuring that all spheres conform to the same geometric parameters.

This consistency contributes to the uniformity of particle distribution and elastic properties within the matrix. The alteration of particle size in GCM likely contributes to the uneven distribution of volume fraction observed in Figure 4-13a, further demonstrating the advantages of MCM in maintaining structural fidelity.

(a)

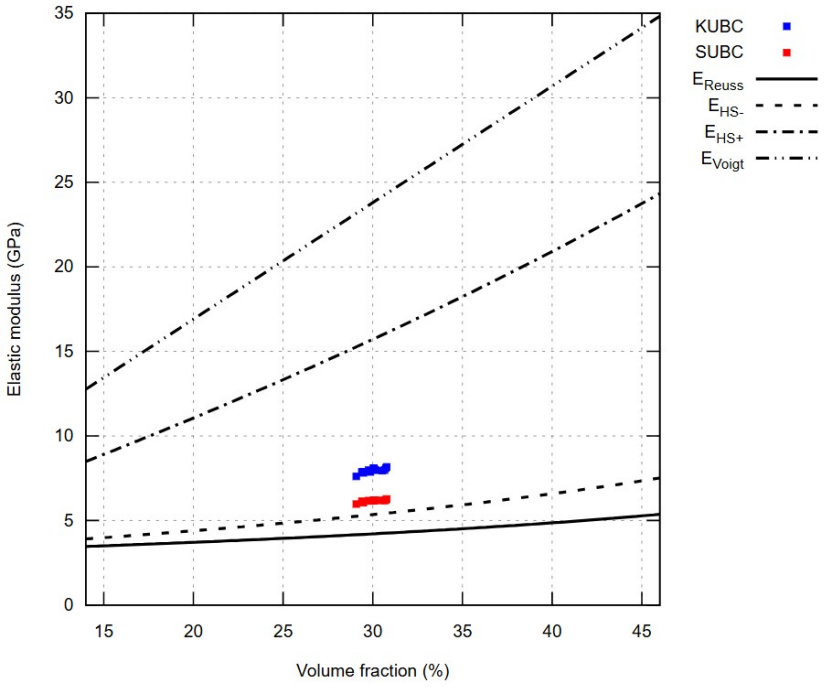

(b)

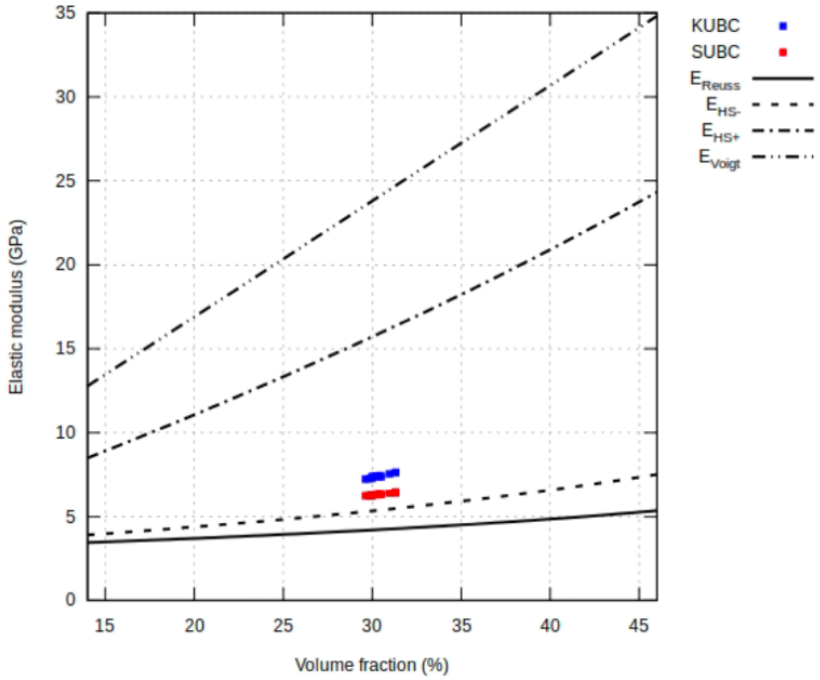

Figure 4-12. Elastic modulus scatter for different SVEs with spherical particles generated by: (a) GCM and (b) MCM.

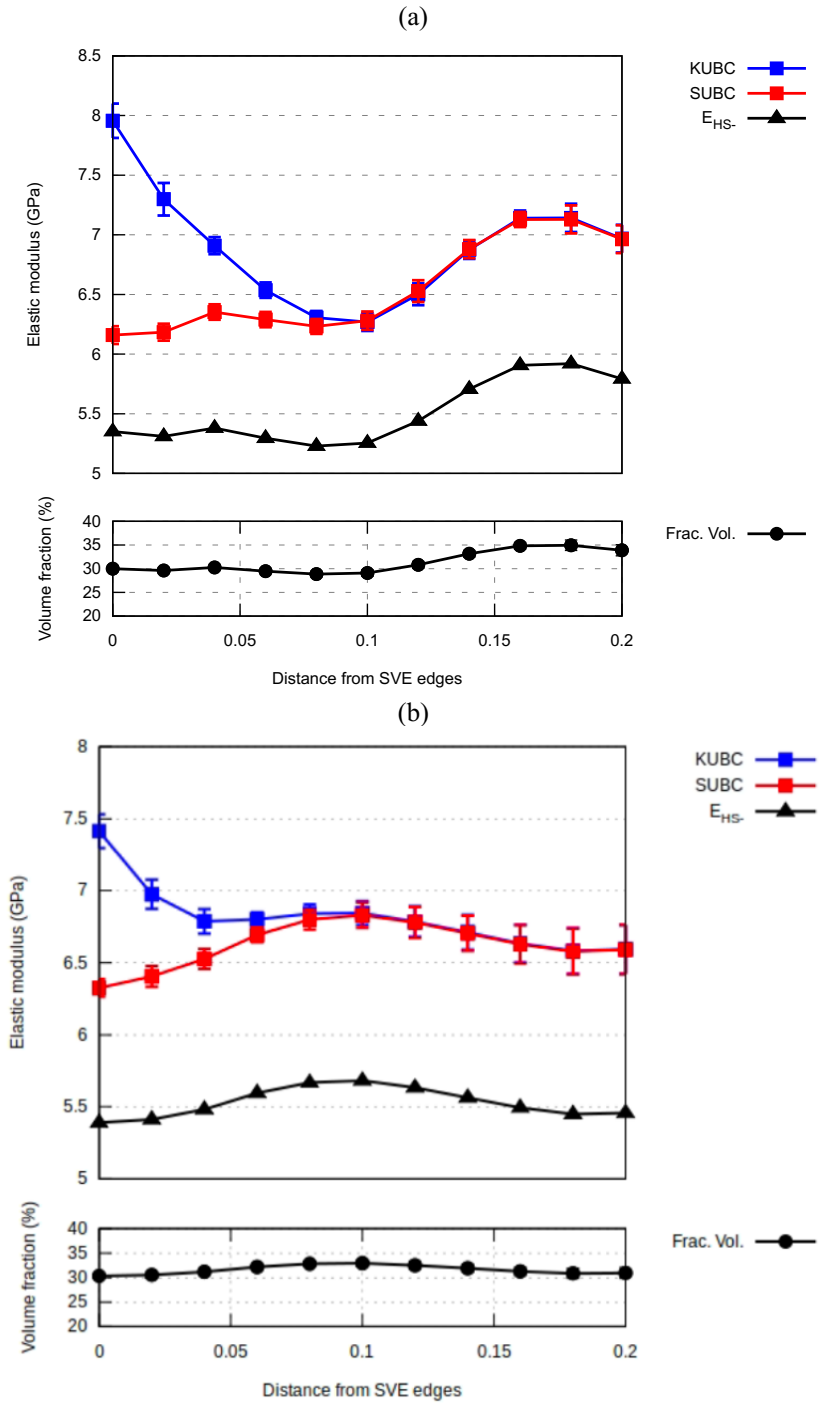

Figure 4-13. Elastic modulus scatter toward the core of the cube for a SVE with spherical particles generated by: (a) GCM and (b) MCM.

In summary, the following conclusions can be drawn from this comparative study:

1. Higher Volume Fraction Capability: MCM has the potential to achieve higher volume fractions and can be applied to more elongated particles, whereas GCM is limited in this regard.

2. Uniform Particle Distribution: MCM provides a more homogeneous distribution of particles within the SVE, while GCM results in a non-uniform arrangement due to geometric modifications and positional adjustments.

3. Reduced Variation in Elastic Modulus: Due to the maldistribution of particles, GCM exhibits a wider range of elastic modulus values between KUBC and SUBC results, whereas MCM ensures a more stable and consistent response.

4. Possibility of combining GCM and MCM: Although a combination of GCM and MCM could be considered, in the context of this study, such an approach was deemed unnecessary. The MCM alone successfully achieves the target volume fractions, maintains particle isotropy, and ensures numerical stability, making the combination redundant for the current objectives. However, future work could explore the potential benefits of hybrid strategies, particularly for applications requiring more complex particle shapes, targeted anisotropy, or multi-phase composites. Moreover, further refinement of the GCM could be investigated to enhance its compatibility with high volume fraction insertions or to tailor particle distributions for specific mechanical or thermal property optimizations.

These findings demonstrate that MCM is the superior approach for modeling spherical particles in composite materials, offering improved numerical stability, better particle representation, and enhanced predictive accuracy in elastic modulus estimation.

In addition to the comparative study between GCM and MCM, the results obtained from the erosion of results method were also compared with those from the MCM, as presented in Table 4-7 and Table 4-9. This comparison led to several important conclusions. The results indicate that MCM produces a smoother and more isotropic distribution of particles throughout the SVE ensuring uniformity both near the boundaries and within the interior, while the erosion of results method exhibits more noticeable fluctuations in local particle volume fractions. These fluctuations are inherent to the initial microstructure generation process and are not eliminated by the erosion technique. Although the erosion of results method does not fully capture the mechanical effects induced by boundary conditions, since it mitigates them by excluding affected regions, it remains effective for estimating the overall elastic properties of particle-reinforced composites. The method demonstrates good predictive capability, with acceptable errors in the estimation of elastic moduli. Therefore, while MCM provides a more robust and physically representative modeling framework, the erosion of results method offers a practical and computationally efficient alternative when a direct handling of boundary effects is not feasible or necessary.

It is important to note that the definition of high-volume fraction is not absolute but depends on the modeling context and particle geometry. In numerical homogenization,

fractions around 30 % are generally regarded as high because of the meshing and convergence difficulties they introduce. This threshold is particularly relevant when elongated particles are considered, since their shape increases the complexity of packing and numerical stability. From this perspective, the proposed Mesh Cutting Method effectively meets the stated objective of enabling reliable homogenization at high particle contents, whereas GCM represents a partial step toward that goal.

The next section extends this framework to natural fiber reinforced composites (NFRCs), where the ability of MCM to handle elongated particles is further evaluated under more realistic microstructural conditions.

CHAPTER 5

APPLICATION OF MESH CUTTING METHOD TO NATURAL FIBER-REINFORCED COMPOSITES

Natural fiber-reinforced polymer composites are the environmentally friendly materials that are getting more attention because of showing some more advantages over the synthetic fibers. The evolution from metal and ceramic materials to synthetic fiber-reinforced composites, and eventually to NFRPC, reflects the continuous effort to obtain new material characteristics that can better fulfill the demands of various industries [103-

105]. Figure 5-1 shows the path from metal and ceramic to the synthetic fiber reinforcement composite and then advancing to NFRPC.

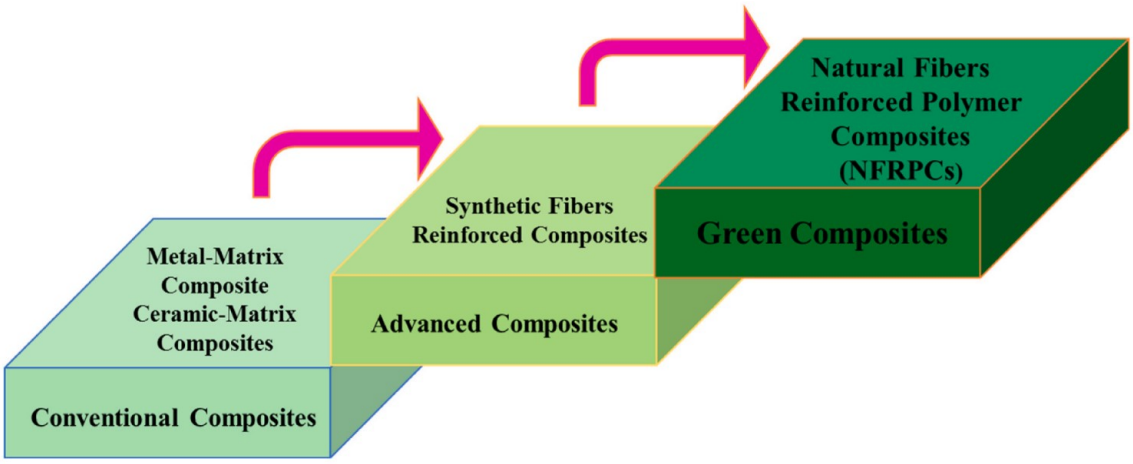

Figure 5-1. Advancement of composites [104].

Wood (hard/soft), wool, bamboo and cotton are different types of natural fibers. These materials have characteristics such as low density, light weight, inexpensiveness, non-rough surface, renewable, and able to solve environmental pollution that made them a better alternative material for glass, carbon, and human-made fibers for composite manufacturing [103]. However, natural fiber composites can show unwanted properties like high water absorption rate, inferior fire resistance, and low mechanical properties. Thus, the type of materials should be chosen carefully [103].

There are different kinds of natural fibers and polymer matrix. To obtain and choose an optimised material, one should be able to estimate the effective properties of different composite materials. Evaluating the elastic properties of heterogeneous materials can be done by experimental tests which are time consuming and cost ineffective. Another

popular method is to use homogenization to estimate the properties of heterogeneous materials. By homogenization we can estimate the macroscopic behavior (effective properties) of heterogeneous material having the material characteristics of its constituents (microstructure) and their arrangement.

In this section, the High-Density Polyethylene-birch fiber (HDPE-birch) composite is modeled using the FEM. The experimental results of the elastic properties for this composite material are presented in [106]. The study presented in [106] investigates the mechanical properties of HDPE/birch fiber composites through tensile and flexural tests, dynamic mechanical analysis, and Scanning Electron Microscopy (SEM). The materials were prepared by blending the constituents on heated rollers, followed by molding under heat and pressure, as illustrated in Figure 5-2 of the reference article.

The study evaluated five different fiber weight fractions, ranging from 10 % to 50 %, to assess their effect on mechanical properties. The experimental results demonstrated that increasing the fiber volume fraction leads to a significant enhancement in the elastic modulus. Specifically, for fiber content up to 50 % by weight, the tensile modulus increases by 210 %, while the flexural modulus shows a 236 % improvement. These results highlight the reinforcing effect of birch fibers and their potential for enhancing the mechanical performance of HDPE-based composites. Additionally, the experimental findings indicated that fiber-matrix adhesion plays a crucial role in mechanical performance, which was improved using maleic anhydride polyethylene

(MAPE) as a coupling agent. SEM images confirmed good interfacial bonding between the HDPE matrix and birch fibers. Furthermore, the thermal analysis revealed that although HDPE possesses higher thermal stability, the addition of birch fiber lowers the degradation temperature of the composite, with thermal breakdown occurring in two distinct stages.

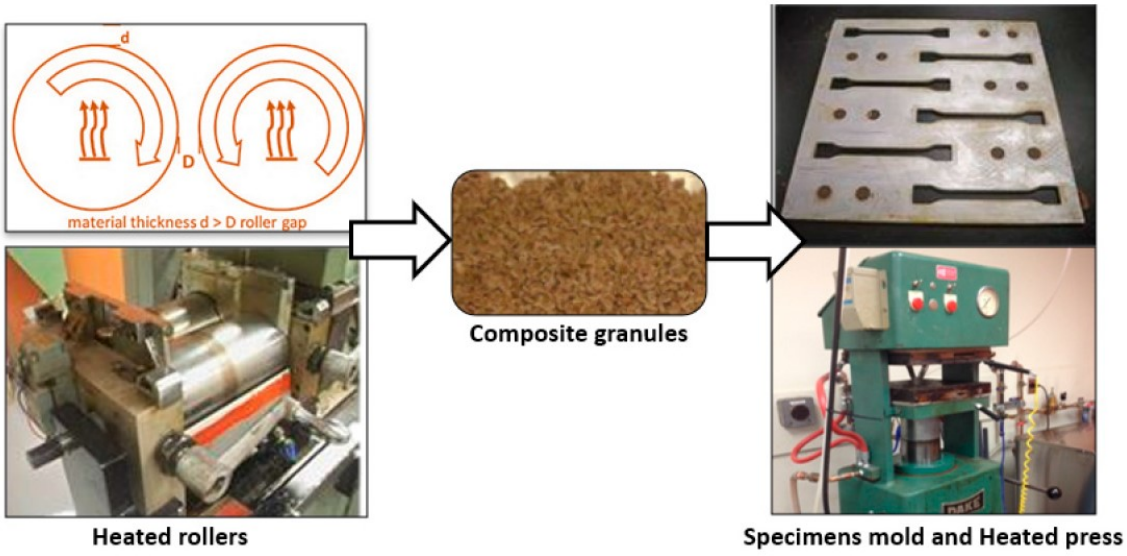

Figure 5-2. Summary of production process for composites and samples [106].

The wood fiber used in the experimental tests has a length-to-diameter ratio of 20, which is four times greater than the fiber elongation considered in previous sections of this study. Given the significant impact of fiber aspect ratio on the mechanical properties of fiber-reinforced composites, it is essential to analyze how fiber elongation influences the material's elastic response.

To systematically investigate this effect, five different fiber elongation ratios are modeled using the mesh-cutting method described in Section 3. The aim is to compare and analyze the variations in elastic properties resulting from different fiber elongations and to validate the applicability of the mesh-cutting approach for modeling fiber-reinforced composites with varying aspect ratios. The numerical results are compared against each other and ultimately validated against the experimental data reported in [106].

By integrating the mesh-cutting method into the modeling framework, this study aims to replicate these experimental findings and evaluate how the fiber elongation influences stress distribution and load transfer within the composite structure. The results from the numerical simulations provide deeper insights into the structure-property relationships of HDPE-birch fiber composites and offer a validation pathway for employing mesh-cutting techniques in microstructural modeling.

All the steps follow the methodology described earlier. However, due to the high elongation of the particles considered in this section, certain adaptations to parameters were necessary to ensure their successful insertion into the SVEs while maintaining computational efficiency. These modifications were implemented to address challenges related to both geometric constraints and the computational cost of simulating highly elongated particles.

Below, the specific parameters considered for each numerical method steps, along with the adaptations introduced to overcome the challenges associated with modeling

highly elongated cylindrical particles are outlined. Any steps not mentioned here remain unchanged from the original methodology.

5.1- Adaptations introduced into the geometry generation step

The results are obtained for SVEs with unit cube dimensions (L = 1) and a targeted volume fraction of 14.15%, which corresponds to a 10% weight fraction as reported in [106]. The average fiber dimensions used in the experimental tests are approximately 0.5 mm in length and 0.025 mm in diameter. Five models are considered in modeling, with particle aspect ratios of 1, 5, 10, 15, and 20. To represent different particle elongations ranging from 1 to 20, the length of each model is kept constant while the particle diameter is adjusted accordingly. For each of the five models, the geometric properties of the particles used are listed in Table 5-1. Furthermore, Figure 5-3 illustrates five different configurations corresponding to the particle characterization parameters presented in this table.

Table 5-1. Particle characterization used in modeling.

$\frac{L}{D}$	D (mm)	Volume fraction (%)
1	0.150	14.15
5	0.100	14.15
10	0.050	14.15
15	0.033	14.15
20	0.025	14.15

This approach is adopted for two main reasons. First, it simplifies comparisons by ensuring that only one geometric parameter, either length or diameter, is varied. Second, and more importantly, it significantly reduces computational costs. Since the SVE is fixed at dimensions of 1 × 1 × 1, maintaining a constant target volume for smaller elongations would require a much larger number of particles to reach the targeted volume fraction. This increase in particle count would, in turn, lead to a substantial rise in computational time.

(a)

(b) (c)

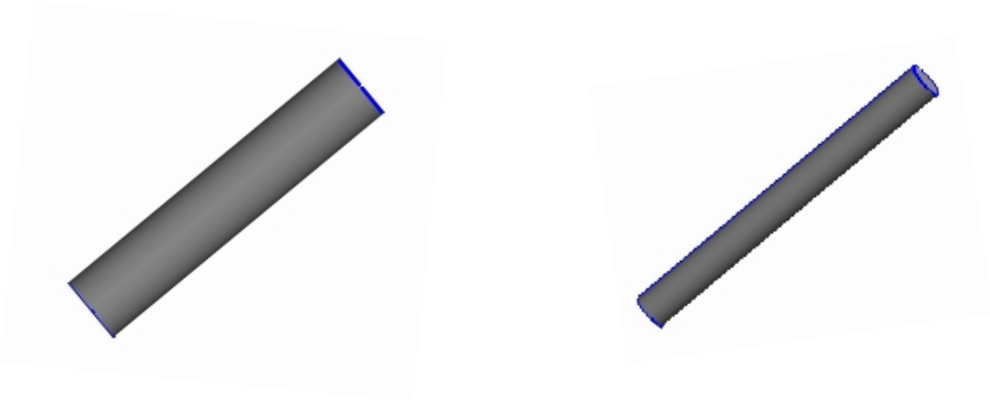

(d) (e)

Figure 5-3. Five particle configurations with L/D equal: (a) 1, (b) 5, (c) 10, (d) 15, (e) 20.

When dealing with highly elongated particles, inserting them into the SVE becomes increasingly challenging. This difficulty arises due to two primary factors.

First, as particle elongation increases, the volume of each individual particle decreases. Since the length remains fixed while the diameter becomes smaller, a larger number of particles is required to achieve the targeted volume fraction. This higher particle count not only increases computational complexity but also raises the likelihood of particle overlap, making the packing process more intricate.

Second, as the elongation increases, the insertion process becomes more difficult due to the expanding particle domain box. More elongated particles occupy a larger bounding box relative to their actual volume, which reduces the available free space within the SVE. This spatial constraint leads to a greater risk of intersection between particles, making it more computationally demanding to generate a well-distributed and non-overlapping particle arrangement.

To help with these particle placement challenges, one strategy is to minimize the acceptable minimum distance between particles or between particles and the SVE

boundary. However, it is important to recognize that there are practical limitations to minimizing this distance. As the spacing between particles decreases, the complexity of the finite element mesh increases significantly. This can lead to difficulties in achieving mesh convergence, as the element quality deteriorates, and the computational cost escalates. Extremely small distances may introduce excessive distortions in the mesh, requiring finer discretization and more refined numerical techniques to ensure accurate and stable simulations. Therefore, an optimal balance must be struck between increasing particle density and maintaining numerical efficiency.

The specific minimum distance and other geometrical parameters values used for all models are summarized in Table 5-2.

Another important strategy is the careful selection of the MBD domain and the criteria domain to maximize particle retention within the unit SVE. When cutting the MBD to fit within the unit SVE, it is essential to ensure that as many particles as possible remain inside while minimizing empty regions at the borders. To achieve this, the difference between the unit SVE and the criteria domain should be at least equal to the particle length. This approach prevents the removal of particles that partially intersect the criteria domain while still contributing to the overall volume fraction inside the unit SVE. By optimizing this cutoff process, the model maintains a more representative particle distribution and avoids unnecessary reductions in volume fraction.

Table 5-2. Geometrical parameters considered for particles.

$\frac{L}{D}$	1	5	10	15	20
Particles intersecting SVE	No	No	No	No	No
$Distance_{min}$ (mm)	0.020	0.018	0.018	0.017	0.013
$Volume_{min}$ (mm^3)	8.177e-5	1.308e-3	3.271e-4	1.425e-4	8.177e-5
$Area_{min}$ (mm^2)	1.575e-3	2.616e-3	6.542e-4	2.849e-4	1.635e-4
$Length_{min}$ (mm)	1.940e-2	2.500e-2	1.250e-2	8.250e-3	6.250e-3

This concept is visually demonstrated in Figure 5-4, which illustrates the relationship between the MBD domain dimension ($L + \Delta$), the criteria domain dimension ($L + \varepsilon$), and the unit SVE (L). The figure highlights that if the particle length is considered L_{cyl} but the difference between the criteria domain and the unit cube is smaller than this value, some particles will inevitably intersect both domains. Since intersection checks are a key criterion for particle placement, these particles would be automatically eliminated during the criteria domain evaluation. However, if these particles were retained, their partial presence within the unit SVE would contribute to the overall volume fraction, thereby improving the accuracy of the microstructural representation. This emphasizes the importance of properly defining the criteria domain to avoid unnecessary particle removal and ensure a more accurate volume fraction estimation within the SVE.

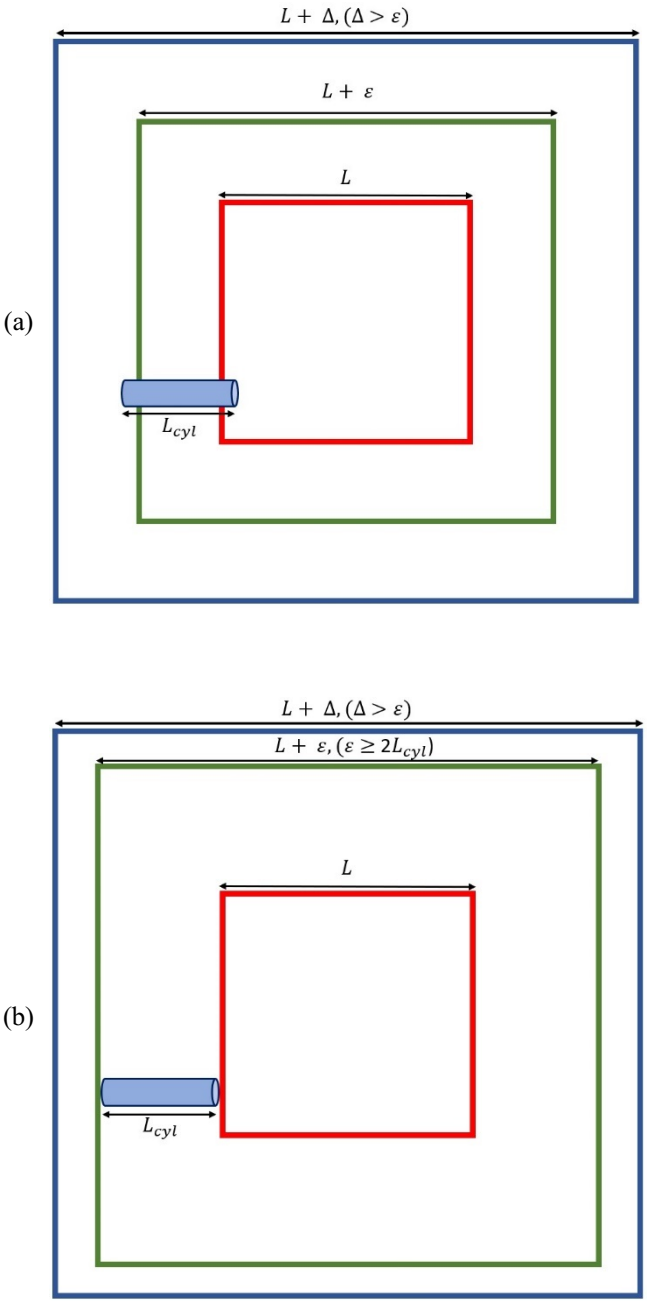

Figure 5-4. Effect of size of MBD domain (green square) and criteria domain (purple square) on maintaining more particles (or a part of particle) inside the unit cube (red square).

With this in mind, the domains are considered as in Table 5-3.

Table 5-3. Domains coordinates.

Domain	$X_{min}(mm)$	$Y_{min}(mm)$	$Z_{min}(mm)$	$X_{max}(mm)$	$Y_{max}(mm)$	$Z_{max}(mm)$
MBD	-0.6	-0.6	-0.6	1.6	1.6	1.6
Criteria	-0.5	-0.5	-0.5	1.5	1.5	1.5
SVE	0.0	0.0	0.0	1.0	1.0	1.0

Finally, the geometry of MBD domain and then the criteria domain with final particle distribution is generated (Figure 5-5).

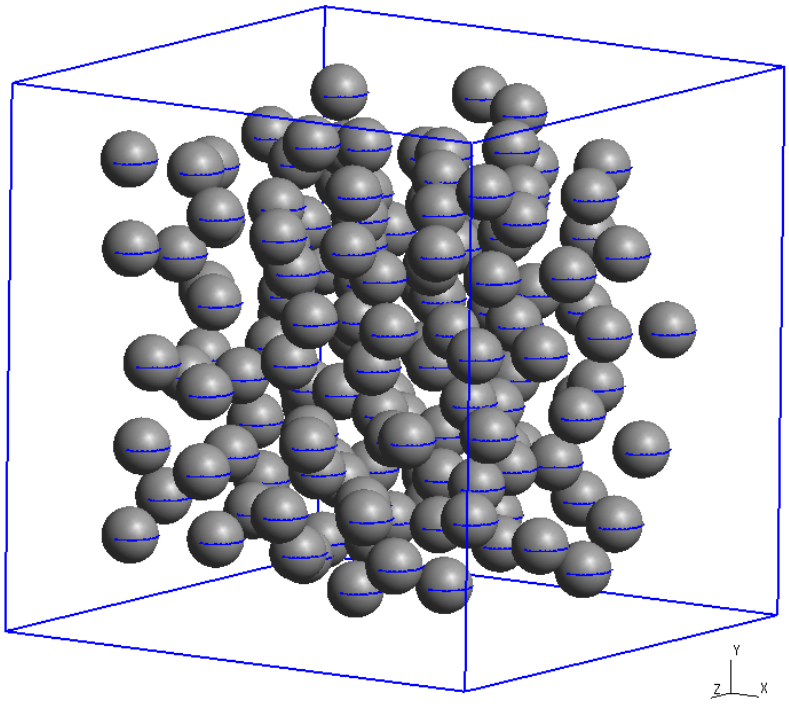

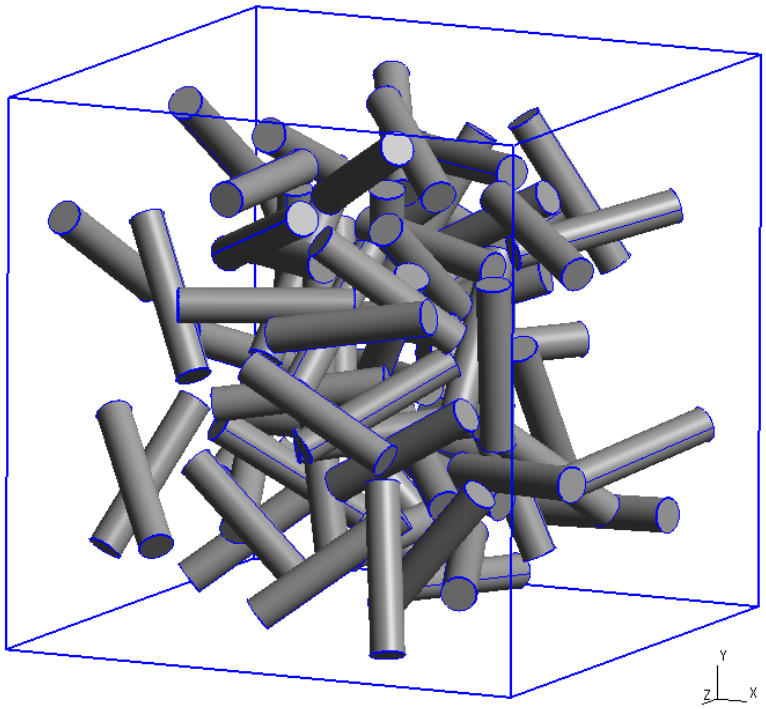
Y
Z
X

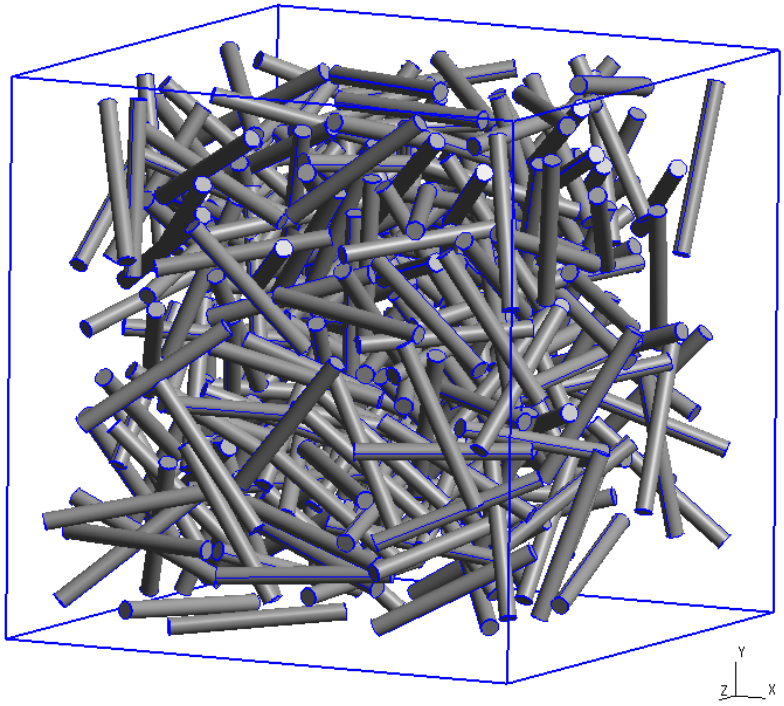
Y
Z
X

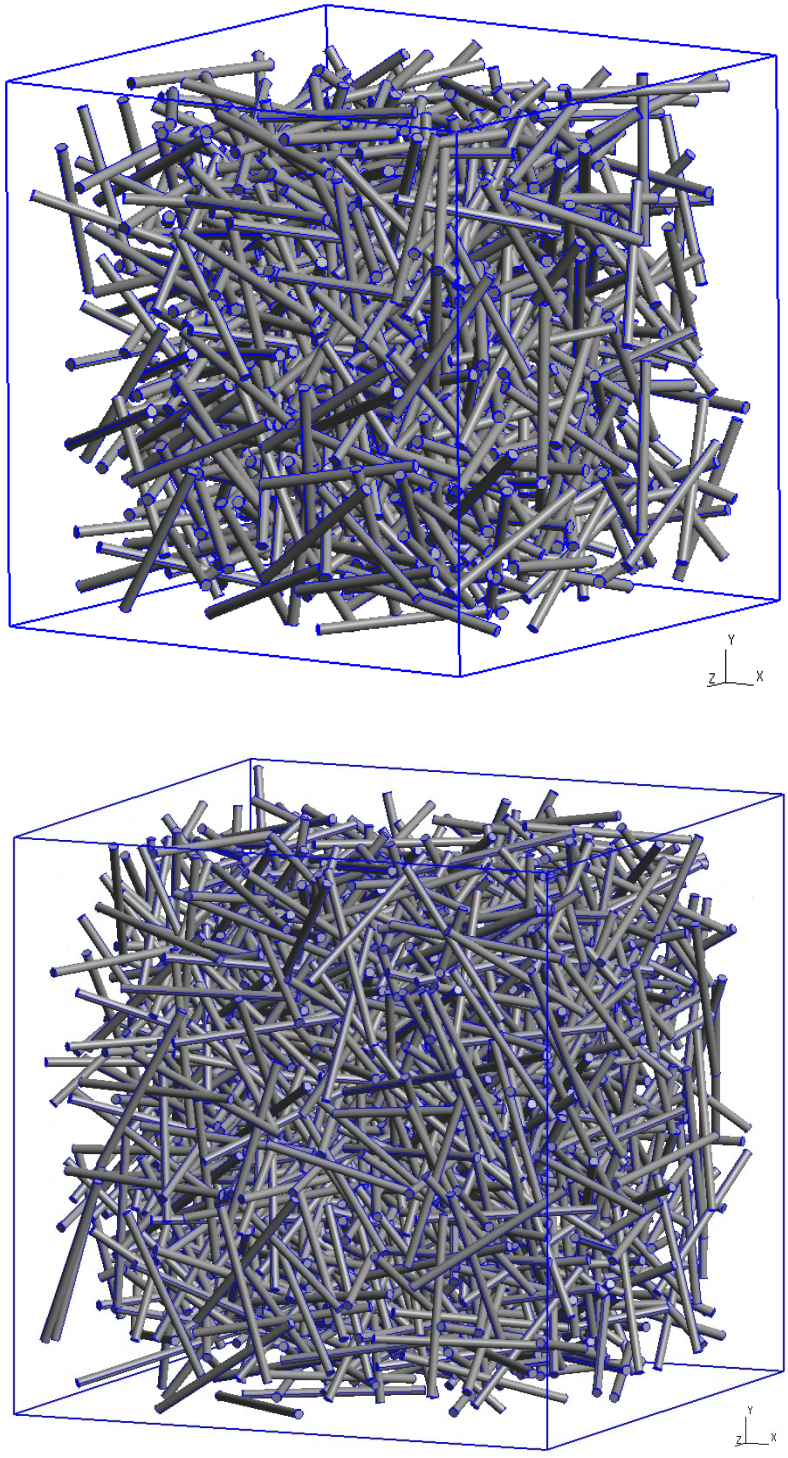

Figure 5-5. Geometry of particle distribution in criteria domain for particle elongation of: (a) 1, (b) 5, (c) 10, (d) 15, (e) 20.

The final orientation tensor for cylindrical particles inside criteria domain in each model is evaluated to make sure of uniformly isotropic distribution of fibers. Table 5-4, Table 5-5, Table 5-6, and Table 5-7 demonstrating orientation tensor for particles with elongation of relatively 5, 10, 15, and 20 all show a good isotropic distribution of particles.

Table 5-4. Orientation tensor for cylindrical particles L/D=5.

$$\begin{bmatrix} 0.337 & 0.005 & 0.001 \\ 0.005 & 0.330 & -0.006 \\ 0.001 & -0.006 & 0.331 \end{bmatrix}$$

Table 5-5. Orientation tensor for cylindrical particles L/D=10.

$$\begin{bmatrix} 0.367 & 0.048 & -0.002 \\ 0.048 & 0.335 & 0.005 \\ -0.002 & 0.005 & 0.297 \end{bmatrix}$$

Table 5-6. Orientation tensor for cylindrical particles L/D=15.

$$\begin{bmatrix} 0.329 & 0.009 & -0.002 \\ 0.009 & 0.332 & 0.0004 \\ -0.002 & 0.0004 & 0.338 \end{bmatrix}$$

Table 5-7. Orientation tensor for cylindrical particles L/D=20.

$$\begin{bmatrix} 0.354 & 0.007 & -0.001 \\ 0.007 & 0.336 & 0.008 \\ -0.001 & 0.008 & 0.340 \end{bmatrix}$$

Other techniques are also considered which belonged to the next steps and will be explained in the next sections.

5.2- Material properties of NFRPC

The material properties of constituents are gathered in Table 5-8.

Table 5-8. Material properties [106, 107].

Material	E (GPa)	G (GPa)	υ	ρ ($^{g}/_{cm^3}$)
Yellow birch fiber	13.90	0.95	0.42	0.62
HDPE	1.34	0.83	0.35	0.92

High-density polyethylene (HDPE)/birch fiber composites used in [106] are fabricated by thermomechanical pulping and compression molding. Yellow birch fibers are first extracted using a thermomechanical process, dried at 80 °C for 24 h, and ground to 20–60 mesh size. HDPE pellets are blended with malleated polyethylene as a compatibilizer to improve fiber–matrix adhesion. The fibers are then incorporated into the molten HDPE/compatibilizer blend using a Thermotron mixer at 170 °C, followed by repeated blending cycles to ensure homogeneity. The resulting sheets are compression molded under 5 MPa at 170 °C and cooled to below 60 °C under circulating water before being cut and polished into the required geometries.

The mechanical behavior of the composites was assessed by means of tensile and flexural testing. Table 5-9 summarizes the experimental test protocol used in this study. For the tensile tests, standardized dog-bone specimens were prepared according to ISO

527-2:2012 (Type 1A). The average specimen dimensions were 10 mm in width and 4 mm in thickness. The tests were performed on an Instron universal testing machine fitted with a 150 kN load cell. Strain was measured using a 25 mm extensometer placed on the gauge length. The loading rate was fixed at 2 mm/min, in accordance with ISO 527-1:2012. Six specimens were tested for each condition to ensure reproducibility of the results. For the flexural tests, rectangular specimens were cut following ASTM D790-10 requirements. The average dimensions were 12.2 mm in width and 3.1 mm in thickness, with a support span of 55 mm (span-to-depth ratio of 16 ± 1). A 10 kN load cell was selected to provide better accuracy given the compliance of the material. The crosshead speed was set at 1.5 mm/min, calculated according to Procedure A of the ASTM standard. Flexural modulus, flexural strength, and strain at break were determined.

Table 5-9. Summary of test protocol.

Test Type	Specimen Geometry	Standard	Key Dimensions (mm)	Load Cell (KN)	Loading Rate (mm/min)
Tensile	Dog-bone (Type 1A)	ISO 527-2:2012	10 width × 4 thickness	150	2
Flexural	Rectangular	ASTM D790-10	12.2 width × 3.1 thickness, 55 span	10	1.5

The experimental datasets obtained under these conditions are later used as benchmarks for validating the results of the numerical simulations.

5.3- Adaptations introduced into the mesh generation

For highly elongated particles, an alternative meshing technique is introduced to avoid the excessive generation of elements within the particles themselves, which would significantly increase computational costs. As previously mentioned, achieving higher elongation requires reducing the particle diameter. However, as the diameter decreases, the number of particles that need to be inserted into the model increases accordingly. This leads to a large number of small-diameter particles that must be meshed, resulting in an extremely high total element count, primarily due to the fine meshing required within the particles. Consequently, if the standard meshing approach is applied, the number of elements required to discretize just the particles can become impractically large.

To address this issue, a more efficient meshing approach is proposed. In the standard method, every circular cross-section and longitudinal edge is discretized into segments based on a size map (Figure 5-6a). This method initially creates nodes, progressively forming segments, triangles, and ultimately tetrahedrons through the whole model (Figure 5-6b). Conversely, the new approach involves fully meshing all cylinders without initially applying the size map, whereas the surrounding matrix continues to be meshed using the usual size map. Specifically, each circular section of the cylinder is discretized into only four equal segments (Figure 5-6c). The lengths of these segments are then uniformly applied to segment the cylinder along its entire length. The resulting segments serve as the basis for generating triangles and subsequently tetrahedrons throughout the cylinder volume(Figure 5-6d).

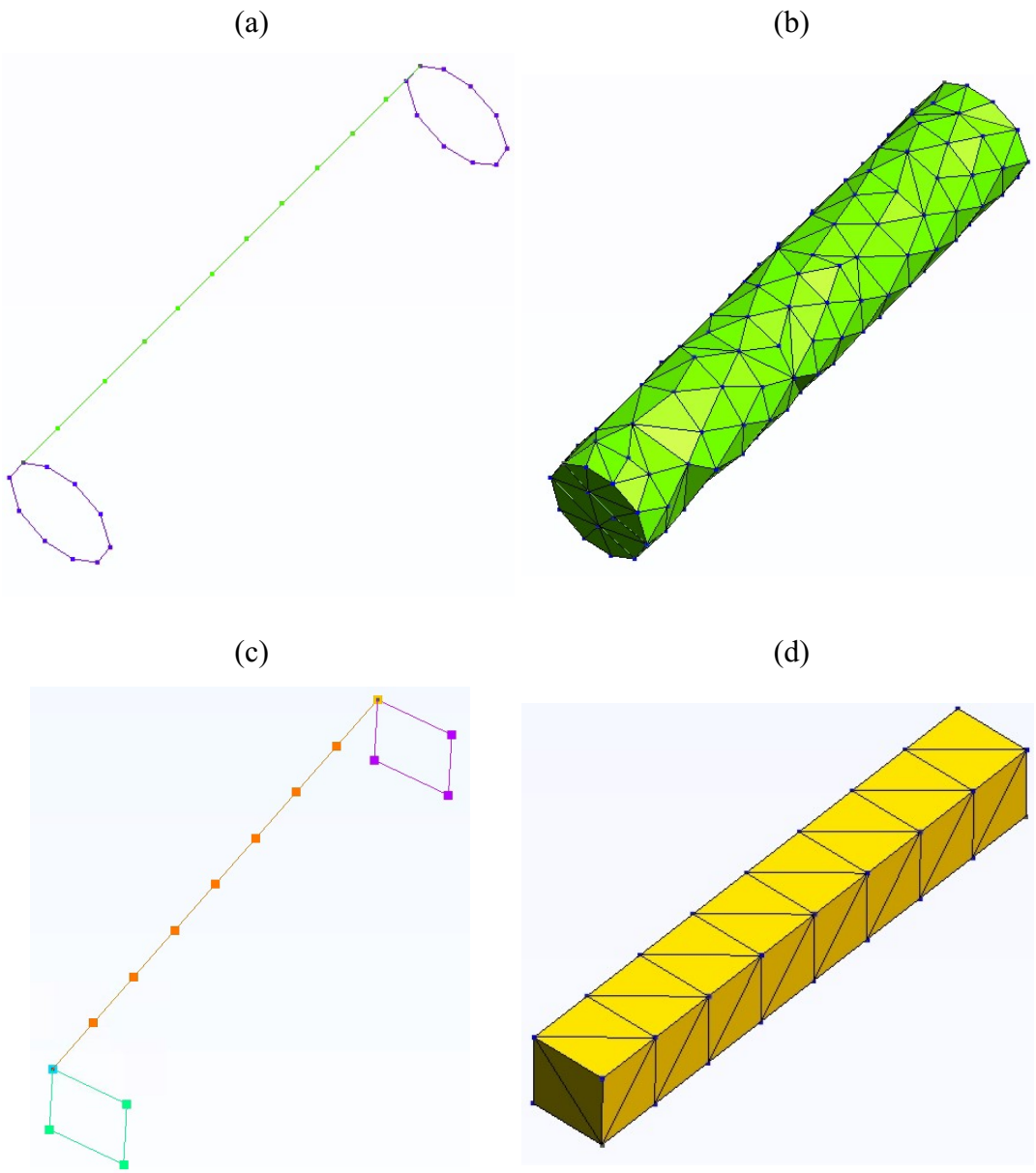

Figure 5-6. Particle segmentation and meshing process by: (a), (b) original and (c), (d) new method.

This approach dramatically reduces the initial segment count around and along each fiber, speeding up mesh generation while still delivering the fine resolution dictated by the size map. This method not only reduces the number of elements required to mesh an individual fiber but also minimizes the overall element density within the surrounding

matrix. Specifically, in usual meshing approaches, the need for extremely small elements near the fiber surface often dictates the global element size in the matrix, further increasing the total number of elements. By contrast, the proposed method alleviates this constraint, allowing for a more balanced and computationally manageable meshing process without compromising accuracy.

For instance, in the case of a particle with an elongation ratio of 10, a direct comparison is made between two different meshing strategies: (1) the conventional meshing method without partitioning, and (2) the proposed partitioning method, where the fiber's diameter is first split, and meshing is performed accordingly. The impact of each meshing technique on the total number of tetrahedral elements generated for a single fiber is analyzed. The results, summarized in Table 5-10, illustrate the effectiveness of the proposed method in significantly reducing the computational burden while maintaining meshing quality and accuracy.

Table 5-10. number of tetrahedral elements for one particle of elongation 10, with two meshing methods.

Meshing method	Number of tetras for one particle	Number of tetras for matrix
Conventional	800	32150
Elongated particle	90	31700

Figure 5-7a shows a particle being meshed by the conventional method and Figure 5-7b shows a particle being meshed by this new method. By the conventional method, for

a symbolic example, around 800 tetras will be created to mesh this particle in criteria domain before cutting. However, with this new technique, for the same size card and volume fraction of particles, this number goes down to around 90 tetras.

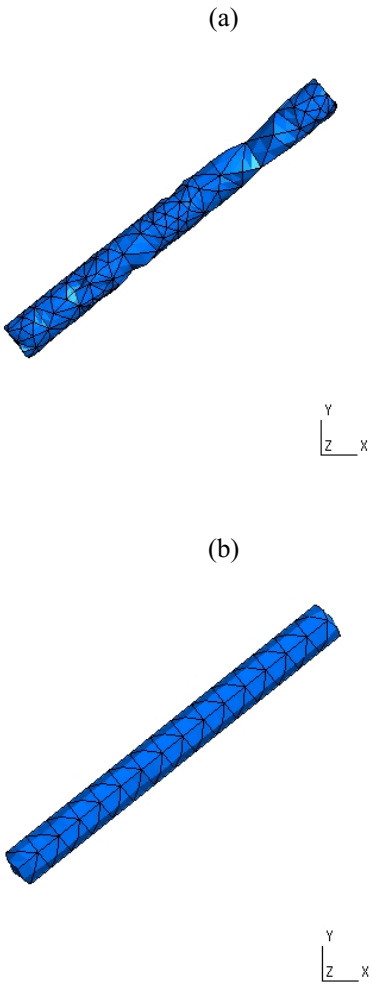

Figure 5-7. A particle meshed inside the SVE with: (a) conventional meshing method and (b) splitting meshing method.

By implementing this technique, not only is the meshing process optimized for elongated particles, but it also ensures that the matrix surrounding the fibers is meshed more efficiently, preventing an unnecessary increase in element count. This approach

proves particularly beneficial when dealing with high-volume fractions of fibers, where a balance between computational efficiency and meshing fidelity is essential for accurate finite element analysis.

Another aspect that affects the final volume fraction is the difference between linear and quadratic elements. This is well stablished in Figure 5-8 and also been evaluated in Table 5-11. Figure 5-8a and b demonstrate the transfer from a linear tetrahedral mesh to a quadratic tetrahedral mesh of a particle. Figure 5-8c and d demonstrate the same but for a conventional meshing technique.

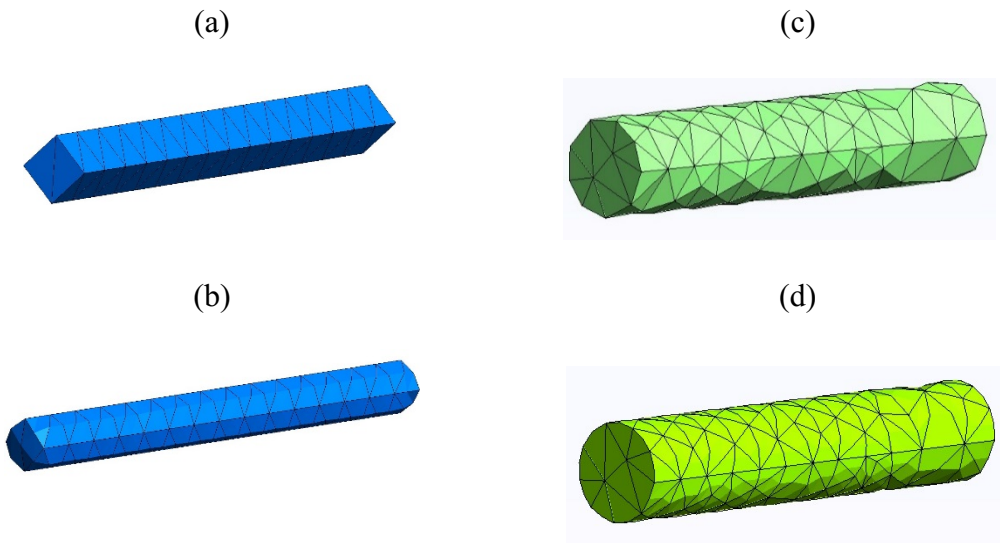

Figure 5-8. Transferring from linear to quadratic tetrahedral mesh for: (a) and (b) splitting meshing technique, (c) and (d) conventional meshing technique.

Switching to quadratic elements can lead to an increase in the achievable volume fraction. As shown in Table 5-11, for elongation values greater than 5, reaching the target volume fraction is only possible when using quadratic elements. For instance, at an

elongation of 10, the maximum attainable volume fraction with linear elements is approximately 10 %, whereas with quadratic elements, it exceeds 14 %.

This is because, at higher elongations, the particle splitting meshing method is employed, making the models more influenced by the quadratization of elements. This effect is illustrated in Figure 5-8 and Figure 5-9. Figure 5-9 shows a cross-section of a particle initially meshed with two linear elements, where the area covered by these elements is significantly smaller than the area covered when the same elements are quadratized. Additionally, in the quadratized mesh, the nodes shift toward the particle surface, enhancing geometric representation. The transition from a linear to a quadratic mesh improves accuracy in capturing curved geometries and fine details of particle boundaries, ultimately leading to better packing efficiency.

Table 5-11. Results of geometry and mesh generation.

Model	$\frac{L}{D}$	1	5	10	15	20
	No. SVE	15	15	15	5	1
Criteria Domain	No._particle	205 ± 5	110 ± 10	423 ± 62	1198 ± 23	1699 ± 83
	VF %	9.77 ± 0.19	7.77 ± 0.55	8.65 ± 0.63	8.76 ± 0.22	7.77
Unit cube	No. tetrahedral elements	~52000	~140000	~355000	~1140000	~1700000
	VF % with linear elements	10.36 ± 0.29	13.83 ± 0.42	10.47 ± 0.21	9.33 ± 0.41	8.28
	VF % with quadratic elements	14.54 ± 0.19	14.43 ± 0.78	14.59 ± 0.51	14.54 ± 0.22	11.85

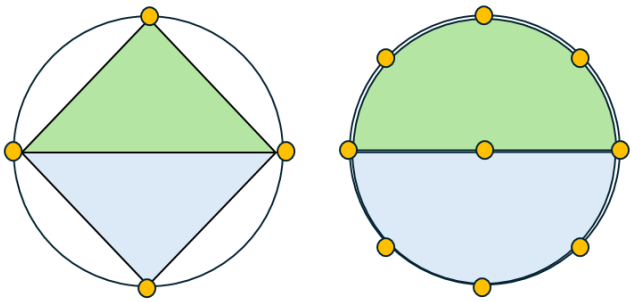

Figure 5-9. A particle cross-section meshed with left: linear elements, right: quadratic elements.

The final generated mesh for all five modeling is presented in Figure 5-10.

(a)

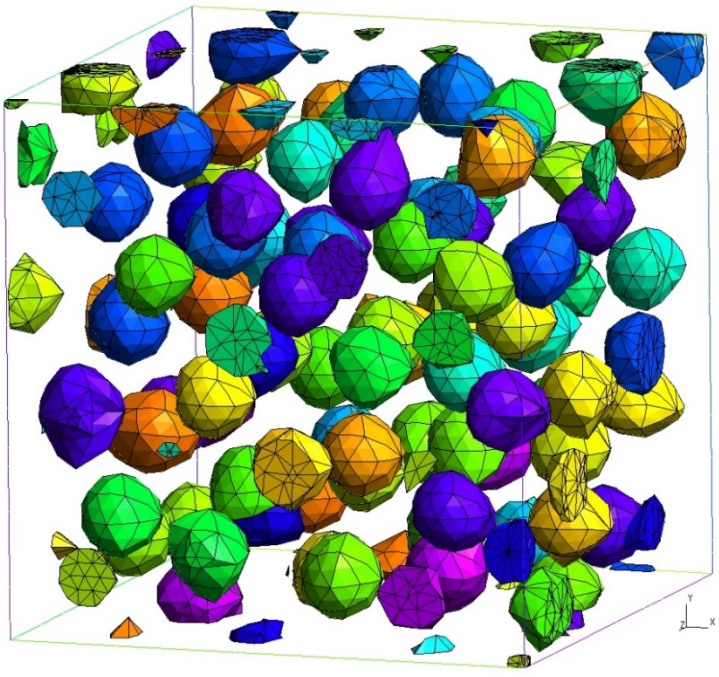

(b)

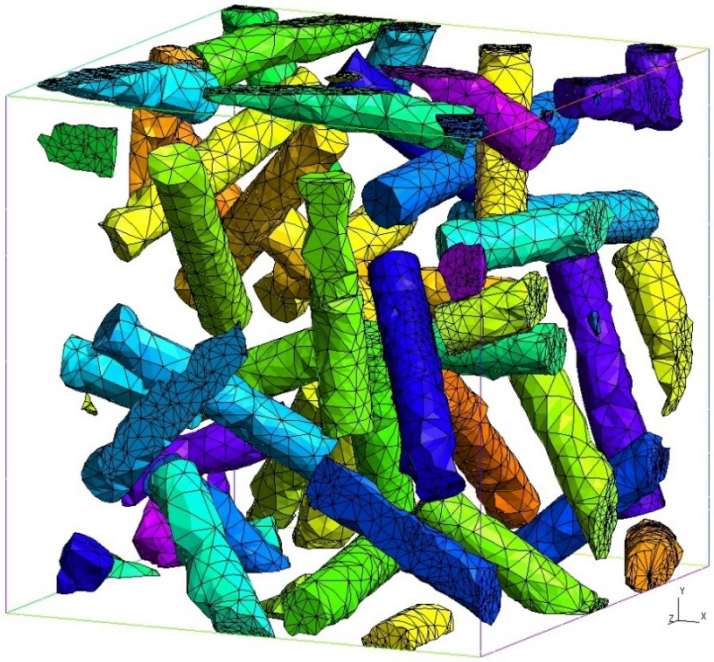

(c)

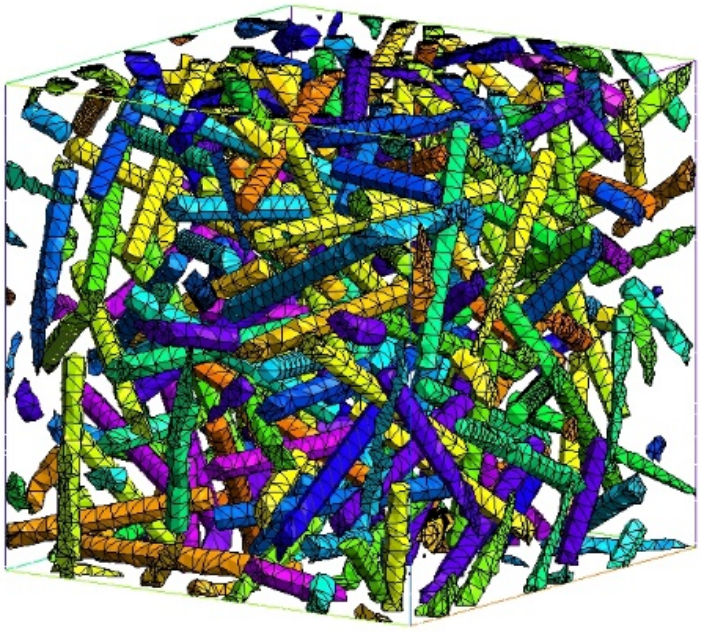

(d)

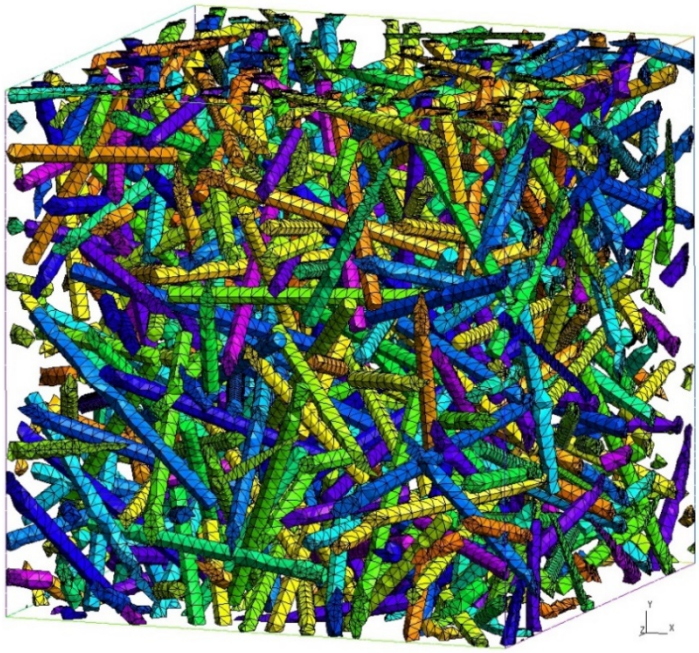

(e)

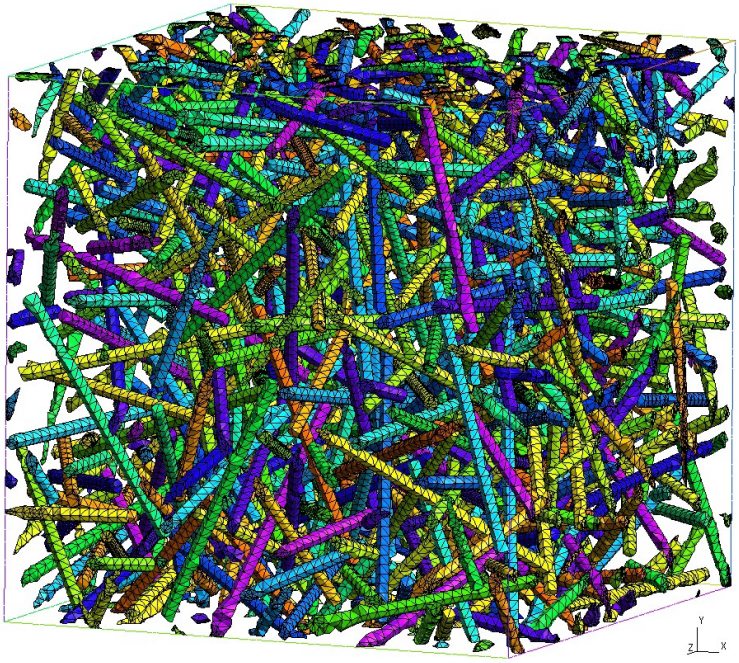

Figure 5-10. Quadratic mesh distribution on SVE with particle elongation of: (a) 1, (b) 5, (c) 10, (d) 15, (e) 20.

Next steps including applying two primary types of boundary conditions, KUBC and SUBC, then performing the finite element analysis, and finally homogenization to extract macroscopic properties from numerical simulations are as previously described in MCM description. By averaging the stress and strain responses obtained from multiple SVEs, homogenization techniques allow for the estimation of effective material properties such as elastic moduli and Poisson's ratio. Two commonly used homogenization methods are the volume averaging technique and the energy-based approach. The volume averaging method computes effective properties by integrating the local stress and strain fields over the entire SVE domain. The energy-based approach, on the other hand, determines the homogenized stiffness tensor by minimizing the difference between the strain energy of the heterogeneous material and that of an equivalent homogeneous medium. These homogenization strategies enable the translation of microstructural behaviors into macroscopic material properties, providing a reliable framework for material characterization and design. By combining automated boundary condition application with advanced numerical techniques and homogenization methods, this approach enhances the accuracy and reliability of finite element simulations for fiber-reinforced composite materials.

5.4- Results

The resulting elastic modulus for two different boundary conditions at various elongation values is reported in Table 5-12. For comparison with experiments, Table 5-12 also includes results obtained for birch fiber reinforced HDPE composites tested in [106].

In these tests, the fibers exhibited an average aspect ratio of approximately 20, with a volume fraction of 14.15 %. These conditions correspond to the experimental modulus values reported and serve as a validation benchmark for the numerical predictions. The results in Table 5-12 highlight that replacing spherical inclusions with cylindrical fibers leads to an increase in the elastic modulus, confirming the superior reinforcement efficiency of elongated particles. However, the effect of further increasing the fiber aspect ratio depends strongly on the boundary condition applied. Under KUBC, the elastic modulus generally remains nearly constant as fiber elongation increases. In certain cases, the over-constraining nature of KUBC can suppress local strain fluctuations and limit the ability of elongated fibers to effectively participate in carrying the applied load. By contrast, under SUBC, the elastic modulus increases with elongation ratio, showing that longer fibers are more effective reinforcements when the boundary conditions allow local deformations to develop. Despite these differences, in all cases the elastic modulus obtained with cylindrical inclusions remains higher than with spherical particles at the same volume fraction. This demonstrates that fiber geometry exerts a strong influence on the overall stiffness of the composite. Taken together, these results suggest that while KUBC provides consistent upper bounds, it may underestimate the reinforcement potential of elongated fibers, whereas SUBC predictions capture the expected trend of modulus enhancement with fiber elongation. This reinforces the importance of evaluating results under multiple boundary conditions to ensure that numerical predictions are both reliable and physically meaningful.

In addition, these findings align with existing studies in the literature, which consistently report that elongated fibers improve stiffness compared to spherical inclusions, although the magnitude of the effect depends on boundary conditions and microstructural assumptions.

However, simulating particles with an elongation of 20 at the target volume fraction of 14.15 % proved to be computationally expensive in terms of both time and memory, making it infeasible within the available resources. Instead, simulations were conducted at lower volume fractions for this particle shape. By leveraging an extrapolation approach, an estimation of the elastic modulus at the targeted volume fraction was obtained. This method provides a reasonable approximation while significantly reducing computational costs. To verify the accuracy of the extrapolation method, simulations were also performed for particles with an elongation of 15, progressively approaching the target volume fraction. The results for elongations of 15 and 20 were plotted together on the same graph in Figure 5-11 for both kinematic uniform boundary conditions and static uniform boundary conditions. As shown in this figure, the results obtained for the two different elongations exhibit close agreement under each boundary condition, thereby confirming the reliability of the extrapolation approach for estimating the elastic modulus at the targeted volume fraction.

Table 5-12. Resulting volume fraction and elastic modulus for different elongations.

$\frac{L}{D}$	Volume fraction with cut (%)	E_{KUBC} (GPa)	E_{SUBC} (GPa)	Calculation time for each SVE (day)	$E_{Expeimental}$ (for particles with $\frac{L}{D} = 20$, volume fraction=14.15 %) (GPa)
1	14.54 ± 0.19	1.81 ± 0.01	1.71 ± 0.01	< 1	1.92 ± 0.21
5	14.43 ± 0.78	1.93 ± 0.04	1.75 ± 0.02	< 1	
10	14.59 ± 0.51	1.91 ± 0.03	1.93 ± 0.02	1	
15	14.54 ± 0.22	1.90 ± 0.01	1.84 ± 0.01	4	
20	14.15	1.88 ± 0.02	1.82 ± 0.01	N/A	

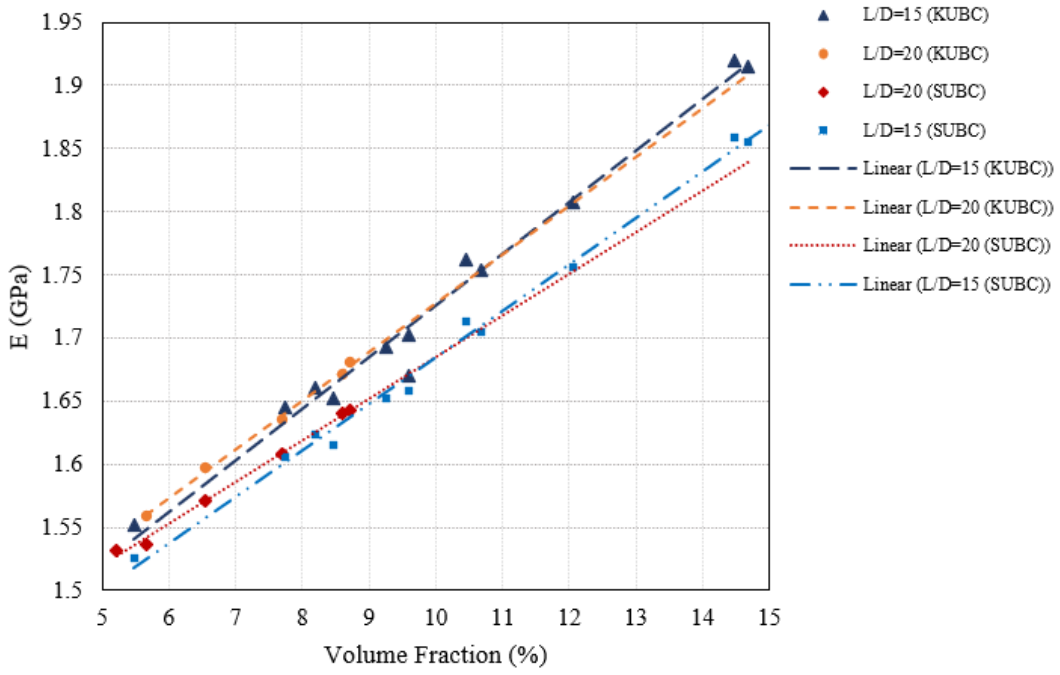

Figure 5-11. Elastic modulus scatter for different SVEs with particle elongation of 15 and 20.

The scatter in the elastic modulus for different elongations under both boundary conditions is illustrated in Figure 5-12. For each case, the results are compared with theoretical bounds, including the Reuss, Hashin-Shtrikman, and Voigt limits.

The most noticeable difference when comparing the results is the impact of particle shape on the elastic modulus. Specifically, transitioning from spherical to cylindrical particles leads to a distinct increase in the elastic modulus, bringing the results closer to the upper Hashin-Shtrikman bound. In contrast, for spherical particles, the computed elastic modulus remains noticeably below this upper bound. This indicates that particle elongation plays a significant contribution in increasing the stiffness of the composite material.

(a)

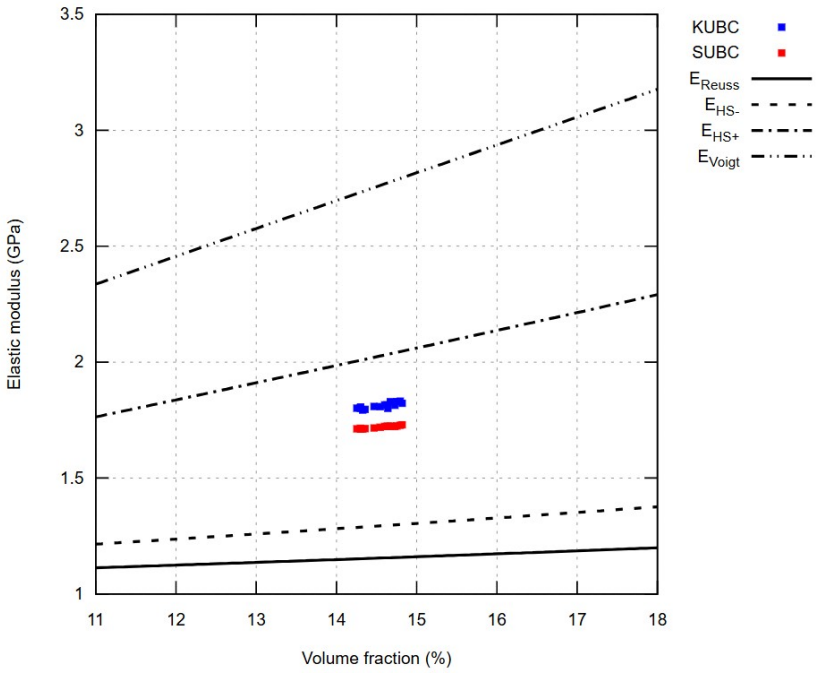

(b)

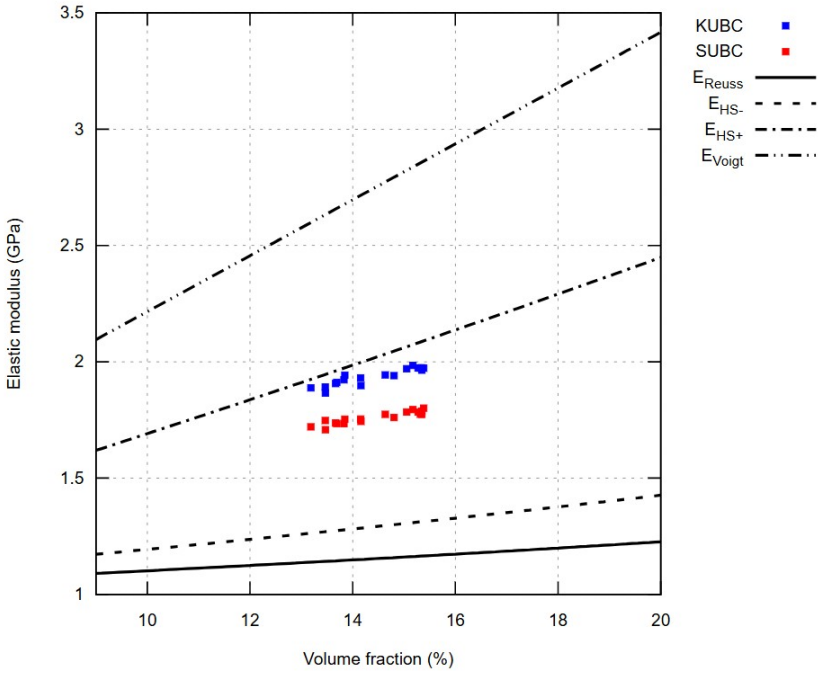
KUBC
SUBC
E_Reuss
E_HS-
E_HS+
E_Voigt
Elastic modulus (GPa)
Volume fraction (%)
3.5
3
2.5
2
1.5
1
10
12
14
16
18
20

(c)

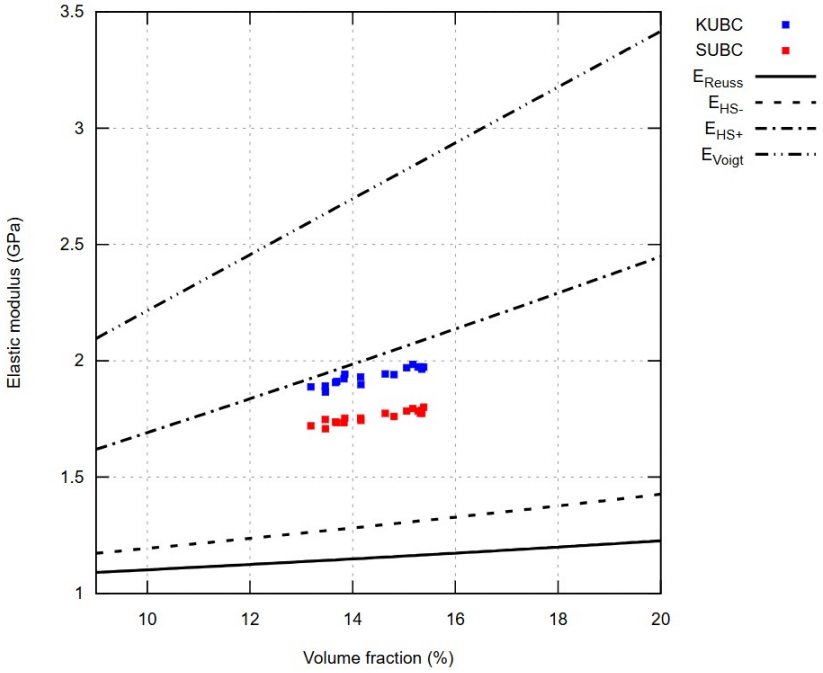
KUBC
SUBC
E_Reuss
E_HS-
E_HS+
E_Voigt
Elastic modulus (GPa)
Volume fraction (%)
3.5
3
2.5
2
1.5
1
10
12
14
16
18
20

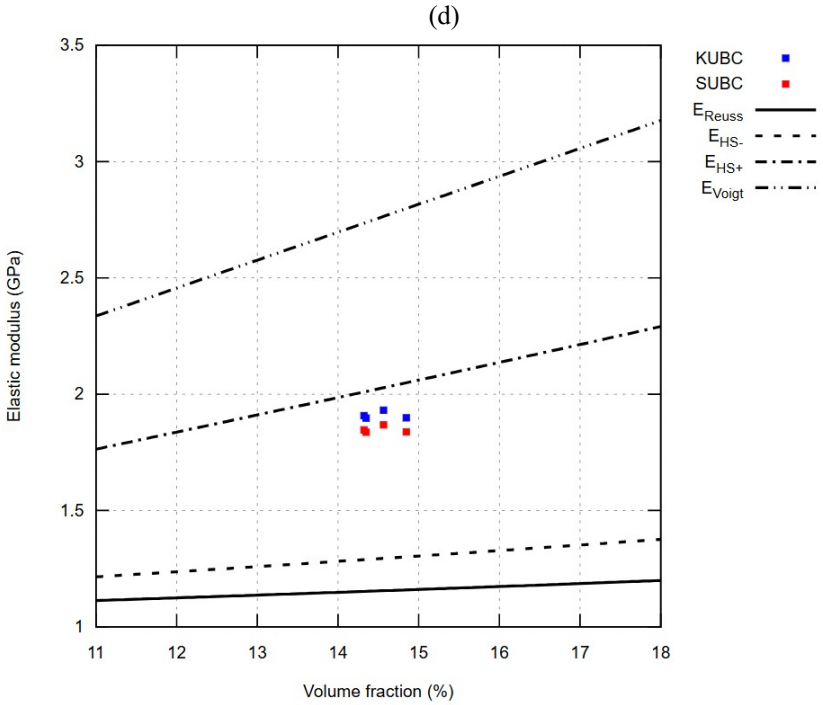

Figure 5-12. Elastic modulus scatter for different SVEs with particle elongation: (a) 1, (b) 5, (c) 10, (d) 15.

Furthermore, Figure 5-13 presents the variation of the elastic modulus through the core of the SVE as a function of volume fraction. A key observation is that as the particles become more elongated, the difference between the elastic modulus values obtained using KUBC and SUBC decreases. More specifically, the results under SUBC exhibit an increasing trend with elongation, whereas the values obtained with KUBC remain relatively stable. This suggests that SUBC is more sensitive to variations in SVE size, particle shape, and elongation, whereas KUBC provides more consistent results. While KUBC provides more consistent results, this does not necessarily imply higher accuracy.

(a)

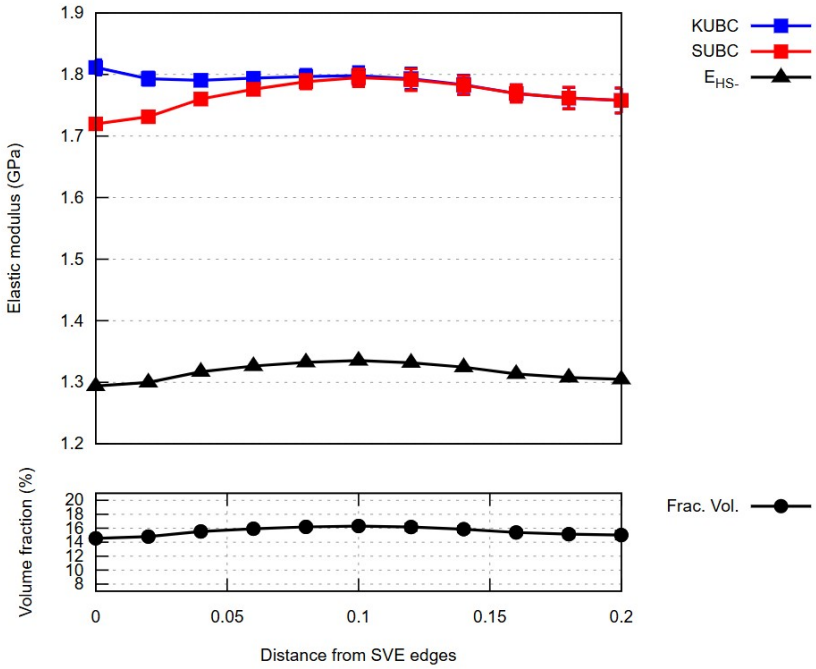
KUBC
SUBC
E_{HS-}
Elastic modulus (GPa)
1.9
1.8
1.7
1.6
1.5
1.4
1.3
1.2
Volume fraction (%)
20
18
16
14
12
10
8
Frac. Vol.
0
0.05
0.1
0.15
0.2
Distance from SVE edges

(b)

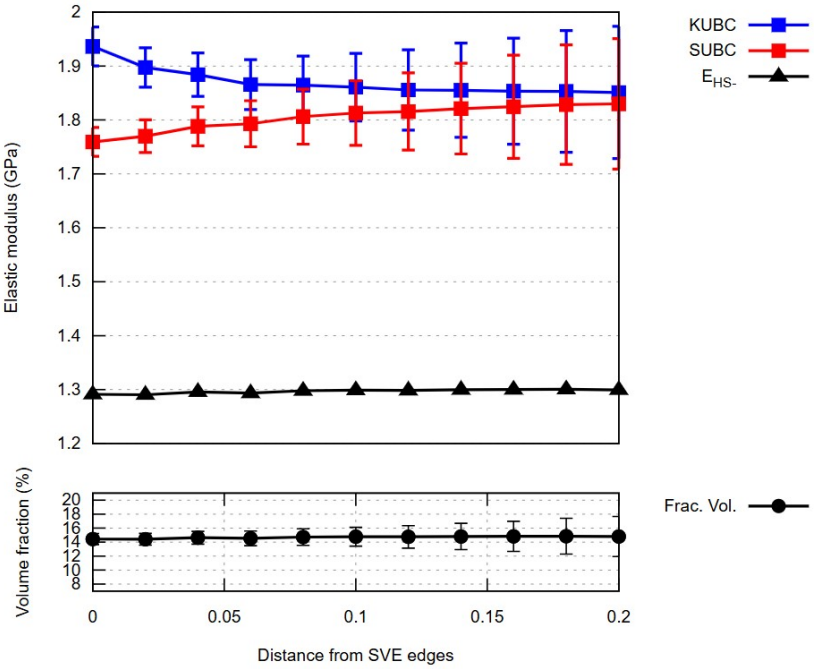
KUBC
SUBC
E_{HS-}
Elastic modulus (GPa)
2
1.9
1.8
1.7
1.6
1.5
1.4
1.3
1.2
Volume fraction (%)
20
18
16
14
12
10
8
Frac. Vol.
0
0.05
0.1
0.15
0.2
Distance from SVE edges

(c)

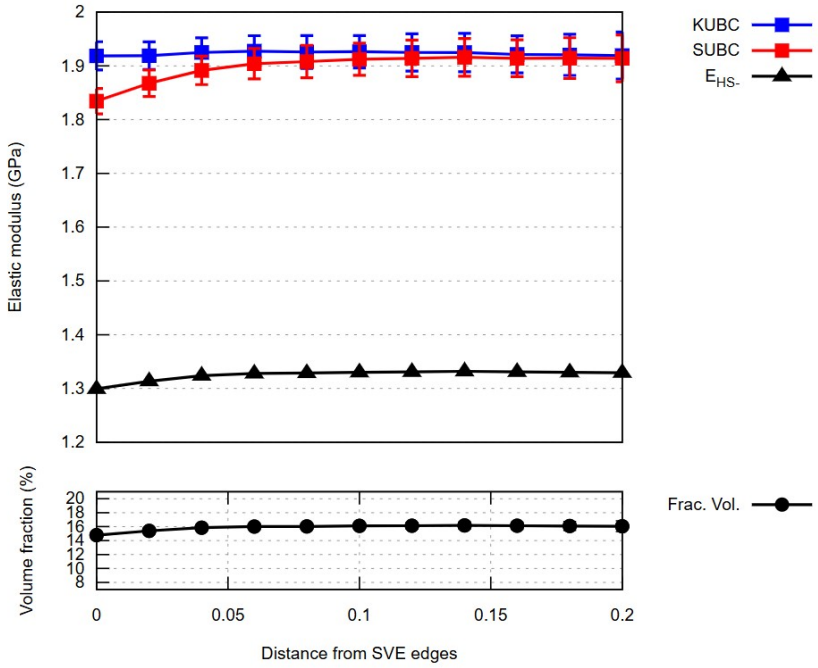

(d)

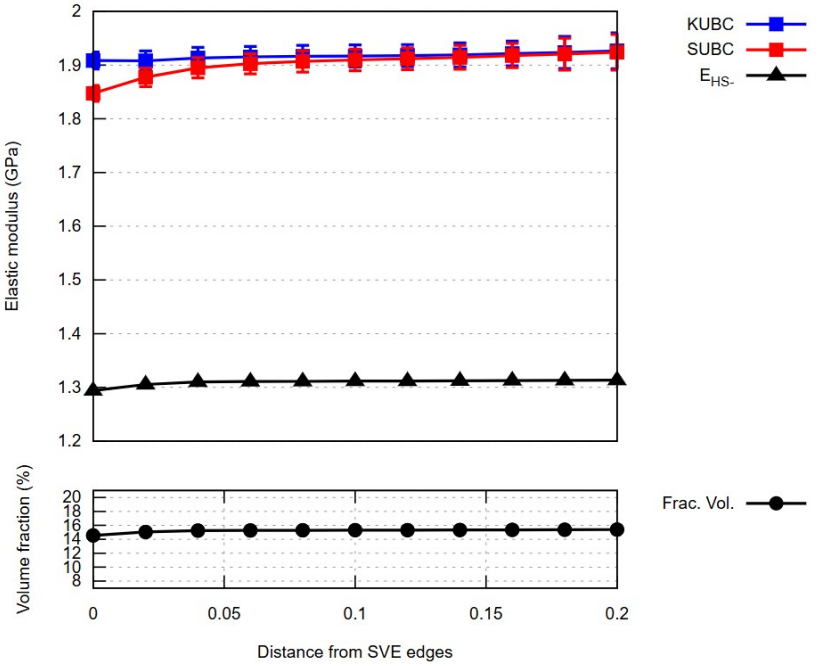

Figure 5-13. Elastic modulus scatter through the core of different SVEs with particle elongation of: (a) 1, (b) 5, (c) 10, (d) 15.

Additionally, the scatter in volume fraction through the core of the SVE demonstrates a uniform distribution of particles. As one moves through the core, the volume fraction curve stabilizes, showing no sudden or significant fluctuations. This indicates that the particles are well-distributed throughout the SVE, reinforcing the reliability of the microstructural representation used in the simulations.

The scatter in the elastic modulus for different elongations is illustrated within the same figure for each type of boundary condition in Figure 5-14, Figure 5-15, and Figure 5-16. It can be concluded that under KUBC, the difference between spherical and cylindrical particles is more pronounced, whereas only a small variation is observed between cylindrical particles of different elongations. On the other hand, by analyzing the Figure 5-14 and Figure 5-16, it is evident that under SUBC, the influence of particle elongation on the results becomes more clearly noticeable.

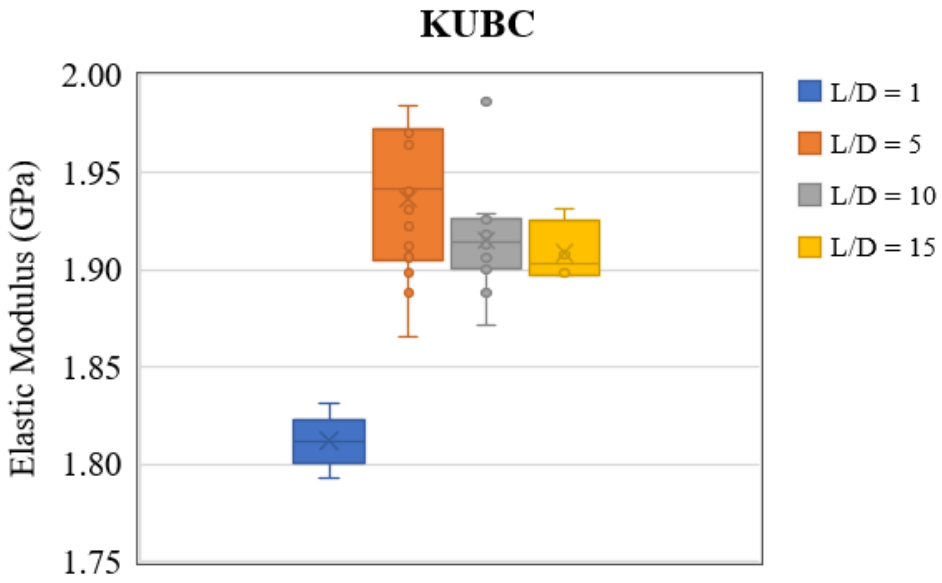

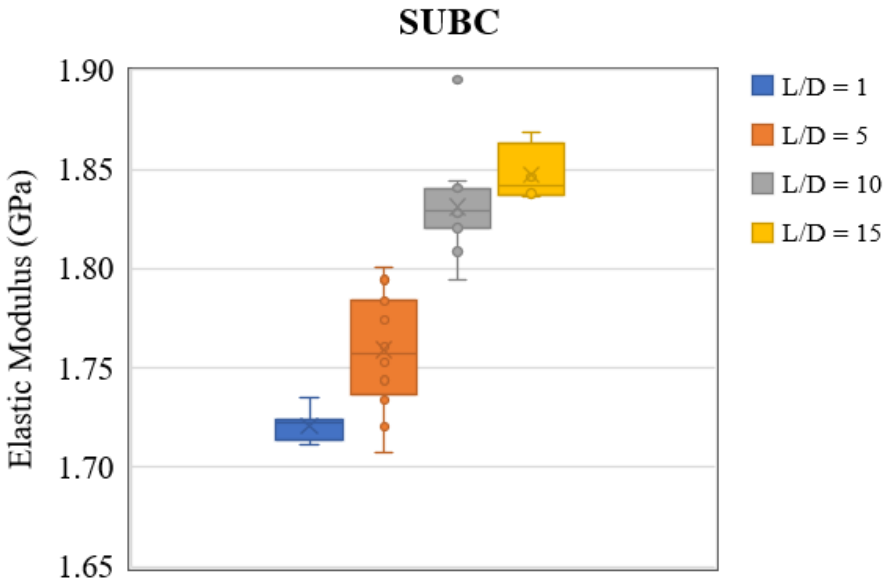

Figure 5-14. Elastic modulus scatter for different SVEs with various particle elongation with KUBC and SUBC.

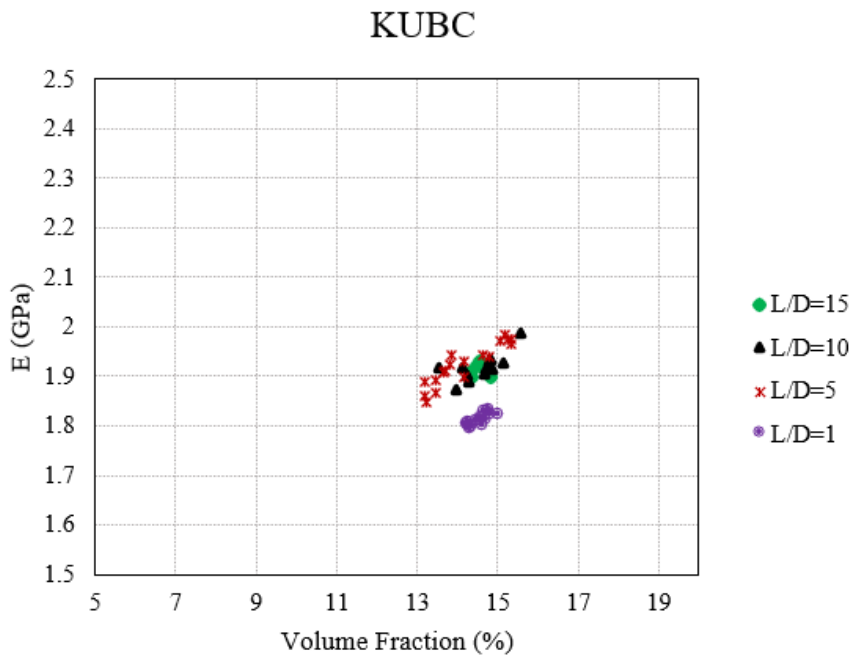

Figure 5-15. Comparison of elastic modulus for different SVEs and particle elongations with KUBC.

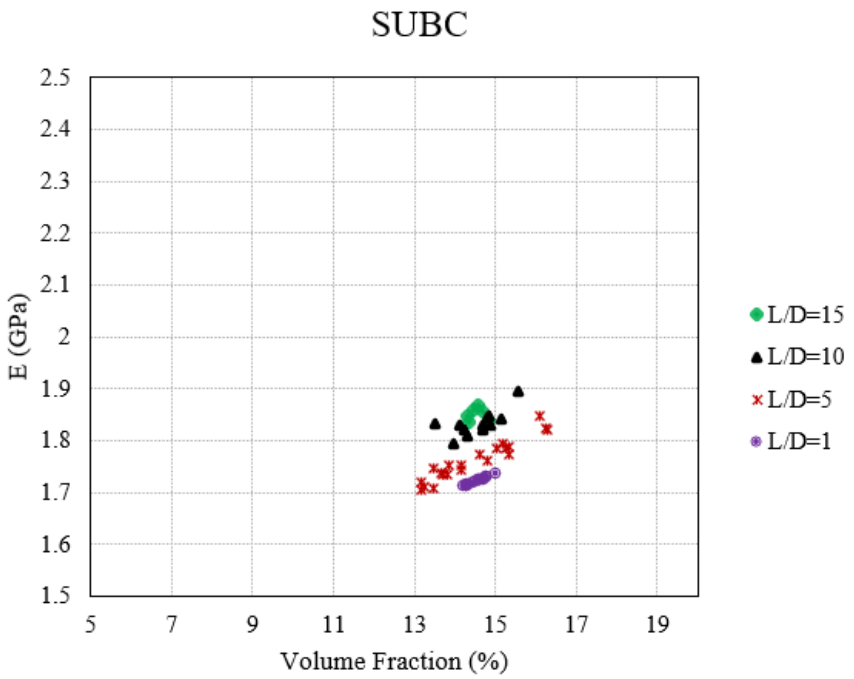

Figure 5-16. Comparison of elastic modulus for different SVEs and particle elongations with SUBC.

The comparison of data related to geometrical parameters is presented in Figure 5-17. Regarding cylindrical elongations, as the particle becomes more elongated, its volume decreases, requiring a greater number of particles to achieve the target volume fraction. However, when considering these results alongside the elastic modulus for all elongation types, it becomes evident that increased elongation leads to higher computational costs and resource consumption. Therefore, from a purely numerical perspective, lower aspect ratios are preferable since fewer particles are needed, which reduces meshing complexity and computational cost. However, this observation must be interpreted carefully in light of the trends obtained in the mechanical property predictions.

A particular case occurs when moving from spheres to cylinders with L/D=5. Here, the particle volume increases relative to spheres, meaning that fewer cylinders are required

to reach the same target volume fraction. For higher aspect ratios (L/D>5), the diameter decreases, and particle volume becomes smaller, which increases the number of particles required.

While lower aspect ratios provide a balance between accuracy and efficiency, realistic fiber geometries must be considered for predictive modeling of natural fiber composites. The combined analysis of Figure 5-15, Figure 5-16 and Figure 5-17 therefore shows that the choice of aspect ratio is a compromise: overly low values may underestimate stiffness, while highly elongated particles increase computational requirements. Moderate aspect ratios, such as L/D=5, appear to provide a reasonable balance while still reflecting the reinforcement mechanisms observed experimentally.

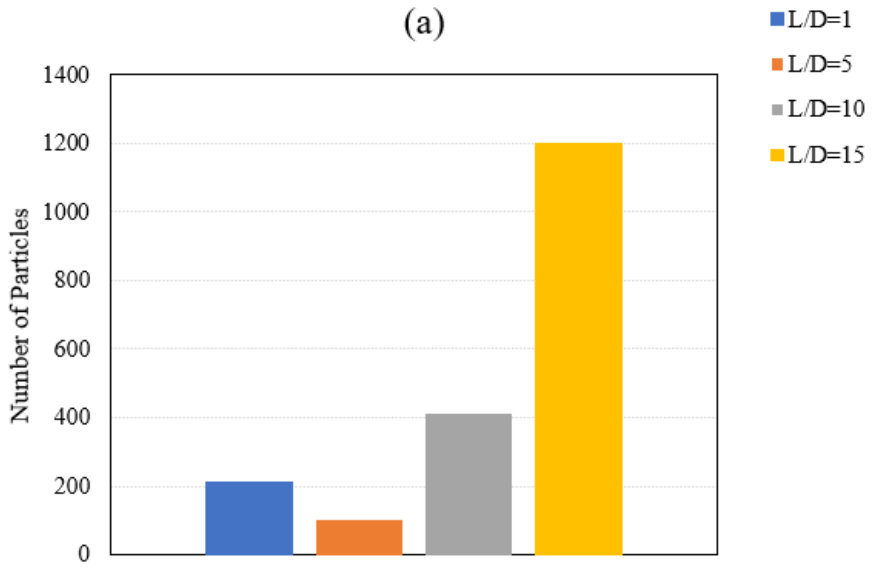

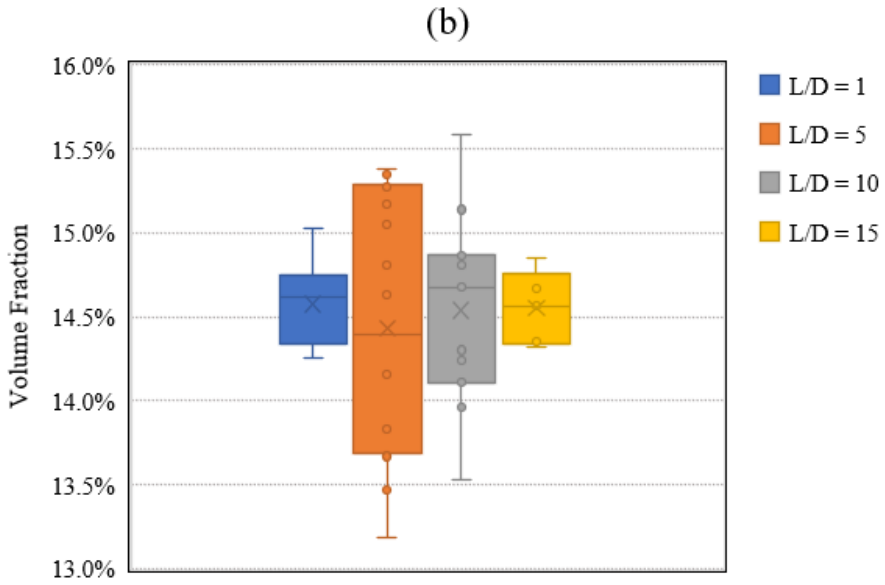

Figure 5-17. Comparison of (a) number of particles, (b) volume fraction, for various particle elongations.

This chapter applied the mesh cutting method to natural fiber reinforced composites and demonstrated its ability to model realistic microstructures at high volume fractions. The numerical results were compared with experimental data from birch fiber/HDPE composites and showed good agreement, validating the predictive capability of the method. The study highlighted the influence of fiber aspect ratio on the apparent elastic properties that replacing spheres with cylindrical fibers significantly increased stiffness. The study demonstrated that particle geometry strongly influences computational efficiency. Although low aspect ratios reduce computational cost, realistic elongations must be considered to capture the actual mechanical behavior of natural fiber composites. Taken together, these findings confirm that the mesh cutting method provides a robust and versatile framework for investigating the microstructure–property relationships of NFRCs, while also underlining the importance of balancing computational efficiency with physical representativeness

CHAPTER 6

CONCLUSIONS AND PERSPECTIVES

The research presented in this thesis advances the numerical modeling of particle-reinforced composites. By developing an automated framework that integrates geometry generation, meshing, FEA, and homogenization, this study enhances the efficiency and accuracy of evaluating the effective mechanical properties of these materials.

6.1- Conclusions

This thesis has focused on advancing the numerical modeling of particle-reinforced composites, with particular emphasis on high reinforcement fractions. It is important to clarify what is meant by high volume fraction in the context of this work. In experimental studies on particle-based composites, high reinforcement fractions can often exceed 50 % by volume, depending on the processing method and fiber packing efficiency. However, in numerical modeling, the definition of “high” must be adapted to reflect

computational constraints. Because of particle geometry, aspect ratio, and the inherent challenges of particle insertion, overlap correction, and mesh convergence, reinforcement levels of about 30 % already constitute high volume fractions in numerical modeling. This thesis therefore defines high volume fraction relative to modeling feasibility, and its contributions lie in extending those feasible limits.

The motivation stemmed from the need to overcome the shortcomings of existing microstructural modeling approaches, which often fail to balance geometric realism, computational efficiency, and predictive accuracy. The literature review highlights the strengths and weaknesses of analytical and numerical homogenization methods. Analytical approaches such as mean-field or variational models offer simplicity and efficiency but rely heavily on idealized geometries and assumptions of dilute or moderate reinforcement fractions. Numerical homogenization, on the other hand, provides higher fidelity by explicitly modeling microstructures but faces challenges at high volume fractions, particularly in meshing complex geometries. Classical particle generation strategies, such as RSA or Voronoi tessellation, were shown to suffer from convergence limitations, unrealistic particle morphologies, or incompatibility with finite element analysis. This review revealed a clear gap: the absence of an automated and robust methodology that could generate realistic microstructures with elongated particles at high volume fractions while preserving mesh quality.

To address this gap, two distinct methodologies are developed. The GCM was designed to resolve criteria (minimum distance and minimum angle) dissatisfaction

between geometrical entities by systematically adjusting particle size, position, and for elongated inclusions, orientation. The MCM, in contrast, operated on a larger generation domain, which was later trimmed into the desired representative element. MCM avoided edge empty spaces, preserved randomness, and ensured high-quality finite element meshes, supporting high fiber volume fractions.

The primary objective was to overcome the limitations of the erosion of results method, which relies on discarding boundary information, and to replace it with automated, robust methodologies capable of generating high-fraction representative volume elements without relying on erosion of results. Another objective was to validate these methodologies both numerically and experimentally in the context of natural fiber composites where high particle volume fractions and elongated geometries pose unique challenges. These objectives are achieved through the development of the GCM and the MCM, both of which provide innovative solutions to microstructural modeling challenges.

The robustness of the GCM algorithm is examined for both spherical and non-spherical particles. When applied to spheres, the algorithm can only rely on two adjustments: reducing the particle size or adjusting its position. Reducing particle size, however, decreases the actual inserted volume, which means that the increase in total volume fraction becomes less effective. Position adjustments can also be problematic in highly packed configurations, because moving one particle to resolve a violation may

generate a new overlap or boundary conflict with neighboring particles. These limitations explain why convergence becomes slower as density increases.

For non-spherical particles, especially elongated fibers, the algorithm has a third option which is adjusting orientation. This additional degree of freedom is very effective because even a small angular adjustment can create sufficient clearance to resolve criteria violations. However, repeated orientation adjustments may gradually promote partial alignment of fibers, as the algorithm tends to rotate particles in directions that favor further insertions. This tendency limits the effectiveness of the GCM when applied to elongated particles.

The performance of the MCM was analyzed in detail and compared with both the GCM and the erosion of results approach. The MCM proved more robust than both the GCM and the erosion of results approach. GCM, although efficient for moderate fractions and spherical particles, became less effective at very high densities, particularly for elongated fibers. Unlike GCM, MCM reliably achieved target fractions while maintaining isotropy and mesh quality. Compared with erosion, MCM produced smoother particle distributions and avoided the local volume fraction fluctuations that erosion could not eliminate. While erosion remains a practical and computationally efficient option for estimating elastic properties, especially when boundary effects are secondary, MCM provides a more accurate and physically representative framework. Furthermore, the MCM is extended to practical applications, specifically NFRCs. It is adapted to capture the elongated geometry of birch fibers embedded in HDPE and successfully applied to

generate realistic microstructures. Numerical homogenization results were compared against experimental data, demonstrating strong agreement in elastic properties. This validation provided crucial evidence that the developed methodology is not only theoretically sound but also applicable to real engineering materials.

A key finding of this research is the impact of particle elongation on mechanical performance. Finite element simulations demonstrate that cylindrical particles provide more accurate estimations of elastic properties compared to spherical particles when modeling elongated reinforcements. This highlights the importance of selecting appropriate particle shapes in numerical modeling to improve prediction accuracy.

Additionally, the results indicate that modeling highly elongated particles with aspect ratios greater than 5 leads to excessive computational costs and resource consumption. Consequently, it is more efficient to model elongated particles with moderate aspect ratios, rather than extreme elongations, to achieve a balance between accuracy and computational feasibility.

The results obtained with the GCM and MCM approaches can be better understood by comparing them to existing RVE/SVE generation and homogenization strategies. Traditional stochastic filling methods, such as RSA, are simple to implement but encounter convergence difficulties at high volume fractions due to frequent rejections of overlapping particles. Voronoi-volume-based techniques allow efficient packing of non-overlapping inclusions but are more suited to polycrystalline microstructures and often produce unrealistic particle shapes for fibrous composites. FFT-based homogenization

methods offer very high computational speed for large RVEs, but they require voxelized geometries and may struggle with complex particle boundaries or irregular morphologies. In contrast, the GCM and MCM approaches developed in this thesis achieve high fiber volume fractions with controlled particle placement, while preserving mesh quality suitable for finite element analysis. Their main advantage lies in balancing geometrical realism (arbitrary shapes, high elongation ratios) with computational tractability, avoiding the meshing artifacts and excessive rejection rates encountered in more conventional methods. This positions GCM and MCM as efficient and flexible tools for simulating NFRCs with complex microstructures, while remaining compatible with standard FEM workflows.

Beyond the specific case of natural fiber reinforced composites, the developed GCM and MCM tools have a more general scope and can be adapted to a wide variety of multiphase systems. The geometric correction strategy is not limited to spherical or cylindrical inclusions but can be extended to irregular shapes or particles with size gradients, making it suitable for modeling filled polymers, particle-reinforced metals, or biological composites. Similarly, the ability to generate SVEs with controlled morphology and high volume fractions open perspectives for studying multi-scale materials, where inclusions of different sizes or phases interact across length scales. This flexibility highlights the potential of the developed approaches as generic tools for microstructural modeling, capable of being tailored to different material classes.

Taken together, the work presented in this thesis fulfills its objectives and delivers several original contributions. First, it provides the community with two new automated methodologies, GCM and MCM, that overcome the limitations of existing RVE generation approaches, particularly the erosion of results method. Second, it advances understanding of the role of particle geometry, showing how aspect ratio controls both predictive accuracy and computational cost. Third, it validates the new methods against experimental data for NFRCs, bridging the gap between numerical and physical modeling. Fourth, it positions the framework as a general-purpose tool, adaptable to various classes of composites and multiphase materials.

The impact of this research is therefore both scientific and practical. Scientifically, it deepens knowledge of how microstructural features influence macroscopic properties, offering new insights into particle-packing strategies, boundary conditions, and geometric realism. Practically, it provides engineers and researchers with robust, automated tools for the design and optimization of sustainable composites. By eliminating the dependence on erosion methods, ensuring mesh quality, and validating against experiments, the framework offers a more accurate and efficient path to predicting composite performance.

6.2- Perspectives

Despite the significant progress achieved in this study, several important directions remain open for exploration. The current framework provides a solid foundation for the numerical characterization of particle-reinforced composites, yet additional developments can greatly expand its applicability and accuracy, particularly in the context of natural

fiber-reinforced composites, where microstructural complexity and interfacial behavior demand more sophisticated modeling tools.

One of the most promising extensions of this work lies in the deeper investigation of the geometry correction method. Further analysis could refine its capabilities for achieving higher volume fractions while maintaining random and isotropic distributions during particle insertion. For instance, systematic studies could explore the method's behavior under varying particle shapes, orientations, and aspect ratios to assess how it can be optimized without compromising geometric randomness or statistical homogeneity. A hybridization of GCM with the MCM also represents an attractive avenue, combining the strengths of both approaches into a single pre-processing tool capable of particle insertion, correction, and mesh preparation for complex geometries.

On assumption of the present framework is the statistically uniform particle distributions. In practice, manufacturing processes such as extrusion, compression molding, or injection molding often induce heterogeneities such as clustering, concentration gradients, or preferential fiber orientations. These effects can locally stiffen or weaken the material, altering global performance. Incorporating process-induced microstructural variability into the models would make predictions more representative of real composites.

Another direction involves the explicit modeling of the fiber-matrix interface. The present study assumes idealized perfect bonding between particles and matrix; however, this simplification may not be sufficient for natural fiber composites, where interfacial

adhesion, debonding, and surface treatments strongly affect mechanical performance. Introducing cohesive zone models or interfacial damage laws would provide insight into stress transfer, failure initiation, and the effect of surface treatments on durability.

Beyond elastic behavior, extending the framework to nonlinear regimes remains a critical step. Incorporating viscoelasticity, plasticity, and damage mechanics would allow simulation of creep, microcracking, fiber pull-out, and matrix degradation. Coupling mechanical and thermal effects would also enable thermo-elastic analyses, capturing coefficients of thermal expansion, residual stresses from fiber–matrix mismatches, and environmental degradation mechanisms. In the thermo-mechanical case, each phase can be described with temperature-dependent elastic properties and a thermal expansion tensor, while heat conduction is solved in parallel with the mechanical equilibrium. This makes it possible to compute not only the effective stiffness, but also effective thermal expansion coefficients and conductivities, while capturing residual stresses generated by thermal mismatches between fibers and matrix.

Beyond methodological advancements, several practical extensions can be explored using the existing modeling framework. These include incorporating large deformation simulations, which is relevant for materials capable of sustaining very high strains under normal loading, such as elastomers. In such cases, accounting for finite strains would improve the predictive capability of the framework. Additionally, fiber anisotropy can be introduced by assigning direction-dependent properties to the reinforcement phase, allowing for more accurate modeling of materials exhibiting

anisotropic mechanical behavior. The framework can also be adapted to model coated particles by introducing an additional material layer between the matrix and core particle. Similarly, porosities, whether arising during manufacturing or inherent to natural fibers, can be explicitly modeled as void inclusions to study their effects on mechanical performance.

Furthermore, future studies could investigate other forms of inclusions, such as platelets or irregularly shaped reinforcements, expanding the versatility of the approach for a wider range of composites. Finally, non-isotropic particle distributions, such as aligned or partially aligned reinforcements, could be examined to evaluate the directional dependence of composite properties and better match the behavior of real-world materials subjected to forming processes or preferential orientation during fabrication.

In summary, this thesis provides a strong and flexible approach for microstructural modeling of particle-reinforced composites, especially at high volume fractions. While it contributes to the optimization and design of sustainable composite materials, there are still many opportunities to expand and improve the work. Whether through improving the particle generation and meshing algorithms, modeling interfacial phenomena, capturing nonlinear or damage responses, or validating against experimental data, each of these future directions has the potential to significantly advance the field. Continued development in this area will enhance the design and optimization of next-generation sustainable composites, supporting their broader adoption in structural and functional applications.

BIBLIOGRAPHY

[1] J. Summerscales, N. P. Dissanayake, A. S. Virk, and W. Hall, "A review of bast fibres and their composites. Part 1–Fibres as reinforcements," *Composites Part A: Applied Science and Manufacturing,* vol. 41, no. 10, pp. 1329–1335, 2010.

[2] J. Summerscales, N. Dissanayake, A. Virk, and W. Hall, "A review of bast fibres and their composites. Part 2–Composites," *Composites Part A: Applied Science and Manufacturing,* vol. 41, no. 10, pp. 1336–1344, 2010.

[3] H. Ku, H. Wang, N. Pattarachaiyakoop, and M. Trada, "A review on the tensile properties of natural fiber reinforced polymer composites," *Composites Part B: Engineering,* vol. 42, no. 4, pp. 856–873, 2011.

[4] P. D. Pastuszak and A. Muc, "Application of composite materials in modern constructions," *Key Engineering Materials,* vol. 542, pp. 119–129, 2013.

[5] J.-C. Cuillière and V. Francois, "Integration of CAD, FEA and topology optimization through a unified topological model," *Computer-aided design and applications,* vol. 11, no. 5, pp. 493–508, 2014.

[6] M. Belmonte, "Advanced ceramic materials for high temperature applications," *Advanced engineering materials,* vol. 8, no. 8, pp. 693–703, 2006.

[7] W. Zhang, A. A. Dehghani-Sanij, and R. S. Blackburn, "Carbon based conductive polymer composites," *Journal of materials science,* vol. 42, pp. 3408–3418, 2007.

[8] R. Sanjinés, M. D. Abad, C. Vâju, R. Smajda, M. Mionić, and A. Magrez, "Electrical properties and applications of carbon based nanocomposite materials: An overview," *Surface and coatings technology,* vol. 206, no. 4, pp. 727–733, 2011.

[9] R. Hill, "Elastic properties of reinforced solids: some theoretical principles," *Journal of the Mechanics and Physics of Solids,* vol. 11, no. 5, pp. 357–372, 1963.

[10] E. Kröner, *Statistical continuum mechanics*, 1st ed. (Course held at the Department of General Mechanics). Springer, 1971.

[11] E. Sánchez-Palencia, *Non-Homogeneous Media and Vibration Theory*. Springer, 1980.

[12] Z. Hashin, "Analysis of composite materials," *J. appl. Mech,* vol. 50, no. 2, pp. 481–505, 1983.

[13] M. Avellaneda, "Optimal bounds and microgeometries for elastic two-phase composites," *SIAM Journal on Applied Mathematics,* vol. 47, no. 6, pp. 1216–1228, 1987.

[14] N. Charalambakis, "Homogenization techniques and micromechanics. A survey and perspectives," *Applied Mechanics Reviews,* vol. 63, no. 3, 2010.

[15] N. G. March, D. R. Gunasegaram, and A. B. Murphy, "Evaluation of computational homogenization methods for the prediction of mechanical properties of additively manufactured metal parts," *Additive Manufacturing,* vol. 64, p. 103415, 2023.

[16] R. Hill, "A self-consistent mechanics of composite materials," *Journal of the Mechanics and Physics of Solids,* vol. 13, no. 4, pp. 213–222, 1965.

[17] C. Huet, "Application of variational concepts to size effects in elastic heterogeneous bodies," *Journal of the Mechanics and Physics of Solids,* vol. 38, no. 6, pp. 813–841, 1990.

[18] W. Voigt, "Ueber die Beziehung zwischen den beiden Elasticitätsconstanten isotroper Körper," *Annalen der physik,* vol. 274, no. 12, pp. 573–587, 1889.

[19] A. Reuß, "Berechnung der fließgrenze von mischkristallen auf grund der plastizitätsbedingung für einkristalle," *ZAMM-Journal of Applied Mathematics and Mechanics/Zeitschrift für Angewandte Mathematik und Mechanik,* vol. 9, no. 1, pp. 49–58, 1929.

[20] K.-R. Qian, T. Liu, J.-Z. Liu, X.-W. Liu, Z.-L. He, and D.-J. Jiang, "Construction of a novel brittleness index equation and analysis of anisotropic brittleness characteristics for unconventional shale formations," *Petroleum Science,* vol. 17, no. 1, pp. 70–85, 2020.

[21] Z. Hashin and S. Shtrikman, "A variational approach to the theory of the elastic behaviour of multiphase materials," *Journal of the Mechanics and Physics of Solids,* vol. 11, no. 2, pp. 127–140, 1963.

[22] G. W. Milton and N. Phan-Thien, "New bounds on effective elastic moduli of two-component materials," *Proceedings of the Royal Society of London. A. Mathematical and Physical Sciences,* vol. 380, no. 1779, pp. 305–331, 1982.

[23] M. Bornert, C. Stolz, and A. Zaoui, "Morphologically representative pattern-based bounding in elasticity," *Journal of the Mechanics and Physics of Solids,* vol. 44, no. 3, pp. 307–331, 1996.

[24] S. Torquato, "Random heterogeneous media: microstructure and improved bounds on effective properties," *Applied Mechanics Reviews,* pp. 37–76, 1991.

[25] Y. Tomota, K. Kuroki, T. Mori, and I. Tamura, "Tensile deformation of two-ductile-phase alloys: Flow curves of α-γ Fe Cr Ni alloys," *Materials Science and Engineering,* vol. 24, no. 1, pp. 85‑94, 1976.

[26] R. Williamson, B. Rabin, and J. Drake, "Finite element analysis of thermal residual stresses at graded ceramic-metal interfaces. Part I. Model description and geometrical effects," *Journal of Applied Physics,* vol. 74, no. 2, pp. 1310–1320, 1993.

[27] S. Suresh, A. Giannakopoulos, and M. Olsson, "Elastoplastic analysis of thermal cycling: layered materials with sharp interfaces," *Journal of the Mechanics and Physics of Solids,* vol. 42, no. 6, pp. 979–1018, 1994.

[28] J. D. Eshelby, "The determination of the elastic field of an ellipsoidal inclusion, and related problems," *Proceedings of the royal society of London. Series A. Mathematical and physical sciences,* vol. 241, no. 1226, pp. 376–396, 1957.

[29] Y. Benveniste, "A new approach to the application of Mori-Tanaka's theory in composite materials," *Mechanics of materials,* vol. 6, no. 2, pp. 147–157, 1987.

[30] S. Torquato, "Effective stiffness tensor of composite media: II. Applications to isotropic dispersions," *Journal of the Mechanics and Physics of Solids,* vol. 46, no. 8, pp. 1411–1440, 1998.

[31] S. Torquato, "Morphology and effective properties of disordered heterogeneous media," *International journal of solids and structures,* vol. 35, no. 19, pp. 2385–2406, 1998.

[32] E. Kröner, "Berechnung der elastischen Konstanten des Vielkristalls aus den Konstanten des Einkristalls," *Zeitschrift für Physik,* vol. 151, no. 4, pp. 504–518, 1958.

[33] B. Budiansky, "On the elastic moduli of some heterogeneous materials," *Journal of the Mechanics and Physics of Solids,* vol. 13, no. 4, pp. 223–227, 1965.

[34] R. Christensen and K. Lo, "Solutions for effective shear properties in three phase sphere and cylinder models," *Journal of the Mechanics and Physics of Solids,* vol. 27, no. 4, pp. 315–330, 1979.

[35] Y. Yao, S. Chen, and P. Chen, "The effect of a graded interphase on the mechanism of stress transfer in a fiber-reinforced composite," *Mechanics of Materials,* vol. 58, pp. 35–54, 2013.

[36] F. Devries and F. Léné, "Homogenization at set macroscopic stress- Numerical implementation and application," *La Recherche Aerospatiale(English Edition),* no. 1, pp. 33–51, 1987.

[37] J. Guedes and N. Kikuchi, "Preprocessing and postprocessing for materials based on the homogenization method with adaptive finite element methods," *Computer methods in applied mechanics and engineering,* vol. 83, no. 2, pp. 143–198, 1990.

[38] K. Terada and N. Kikuchi, "Nonlinear homogenization method for practical applications," *American Society of Mechanical Engineers, Applied Mechanics Division, AMD,* vol. 212, pp. 1–16, 1995.

[39] S. Jansson, "Homogenized nonlinear constitutive properties and local stress concentrations for composites with periodic internal structure," *International journal of solids and structures,* vol. 29, no. 17, pp. 2181–2200, 1992.

[40] H. Moulinec and P. Suquet, "A fast numerical method for computing the linear and nonlinear mechanical properties of composites," *Comptes Rendus de l'Académie des sciences. Série II. Mécanique, physique, chimie, astronomie,* 1994.

[41] H. Moulinec and P. Suquet, "A numerical method for computing the overall response of nonlinear composites with complex microstructure," *Computer methods in applied mechanics and engineering,* vol. 157, no. 1-2, pp. 69–94, 1998.

[42] S. Lucarini, M. V. Upadhyay, and J. Segurado, "FFT based approaches in micromechanics: fundamentals, methods and applications," *Modelling and Simulation in Materials Science and Engineering,* vol. 30, no. 2, p. 023002, 2021.

[43] G. F. Pinder, *Numerical methods for solving partial differential equations: a comprehensive introduction for scientists and engineers*. John Wiley & Sons, 2017.

[44] S. R. Annapragada, D. Sun, and S. V. Garimella, "Prediction of effective thermo-mechanical properties of particulate composites," *Computational Materials Science,* vol. 40, no. 2, pp. 255–266, 2007.

[45] F. Municchi and M. Icardi, "Macroscopic models for filtration and heterogeneous reactions in porous media," *Advances in Water Resources,* vol. 141, p. 103605, 2020.

[46] J.-C. Michel, H. Moulinec, and P. Suquet, "Effective properties of composite materials with periodic microstructure: a computational approach," *Computer methods in applied mechanics and engineering,* vol. 172, no. 1-4, pp. 109–143, 1999.

[47] S. Mirkhalaf, F. A. Pires, and R. Simoes, "Determination of the size of the Representative Volume Element (RVE) for the simulation of heterogeneous polymers at finite strains," *Finite Elements in Analysis and Design,* vol. 119, pp. 30–44, 2016.

[48] W. J. Drugan and J. R. Willis, "A micromechanics-based nonlocal constitutive equation and estimates of representative volume element size for elastic composites," *Journal of the Mechanics and Physics of Solids,* vol. 44, no. 4, pp. 497–524, 1996.

[49] T. Kanit, S. Forest, I. Galliet, V. Mounoury, and D. Jeulin, "Determination of the size of the representative volume element for random composites: statistical and numerical approach," *International Journal of solids and structures,* vol. 40, no. 13-14, pp. 3647–3679, 2003.

[50] A. Couture, V. François, J.-C. Cuillière, and P. Pilvin, "Automatic statistical volume element modeling based on the unified topology model," *International Journal of Solids and Structures,* vol. 191, pp. 26–41, 2020.

[51] S. Nemat-Nasser and M. Hori, *Micromechanics: overall properties of heterogeneous materials*. Elsevier, 2013.

[52] R. DeHoff, E. Aigeltinger, and K. Craig, "Experimental determination of the topological properties of three-dimensional microstructures," *Journal of microscopy,* vol. 95, no. 1, pp. 69–91, 1972.

[53] O. Forsman, "Undersökning av rymdstrukturen hos ett kolstål av hypereutectoid sammansättning," *Jernkontorets Ann,* vol. 102, pp. 1–30, 1918.

[54] R. Brault, A. Germaneau, J.-C. Dupré, P. Doumalin, S. Mistou, and M. Fazzini, "In-situ analysis of laminated composite materials by X-ray micro-computed tomography and digital volume correlation," *Experimental Mechanics,* vol. 53, pp. 1143–1151, 2013.

[55] M. G. Lee, S. Lee, J. Cho, S. Bae, and J. Y. Jho, "Effect of the fluorination of graphene nanoflake on the dispersion and mechanical properties of polypropylene nanocomposites," *Nanomaterials,* vol. 10, no. 6, p. 1171, 2020.

[56] M. Anderson, G. Grest, and D. Srolovitz, "Computer simulation of normal grain growth in three dimensions," *Philosophical Magazine B,* vol. 59, no. 3, pp. 293–329, 1989.

[57] R. Qin and H. Bhadeshia, "Phase field method," *Materials science and technology,* vol. 26, no. 7, pp. 803–811, 2010.

[58] N. Provatas and K. Elder, *Phase-field methods in materials science and engineering*. John Wiley & Sons, 2011.

[59] C. E. Krill III and L.-Q. Chen, "Computer simulation of 3-D grain growth using a phase-field model," *Acta materialia,* vol. 50, no. 12, pp. 3059–3075, 2002.

[60] M. S. Salehi and S. Serajzadeh, "Simulation of static recrystallization in non-isothermal annealing using a coupled cellular automata and finite element model," *Computational Materials Science,* vol. 53, no. 1, pp. 145–152, 2012.

[61] D. Raabe, "Cellular automata in materials science with particular reference to recrystallization simulation," *Annual review of materials research,* vol. 32, no. 1, pp. 53–76, 2002.

[62] A. Okabe and B. Boots, "K. Sugihara. 1992. Spatial Tessellations. Concepts and applications of Voronoi diagrams," ed: Chichester: Wiley.

[63] K. Hitti, P. Laure, T. Coupez, L. Silva, and M. Bernacki, "Precise generation of complex statistical Representative Volume Elements (RVEs) in a finite element context," *Computational Materials Science,* vol. 61, pp. 224–238, 2012.

[64] B. Widom, "Random sequential addition of hard spheres to a volume," *The Journal of Chemical Physics,* vol. 44, no. 10, pp. 3888–3894, 1966.

[65] J. Feder, "Random sequential adsorption," *Journal of Theoretical Biology,* vol. 87, no. 2, pp. 237–254, 1980.

[66] S. Kari, H. Berger, and U. Gabbert, "Numerical evaluation of effective material properties of randomly distributed short cylindrical fibre composites," *Computational materials science,* vol. 39, no. 1, pp. 198–204, 2007.

[67] W. Tian, L. Qi, J. Zhou, J. Liang, and Y. Ma, "Representative volume element for composites reinforced by spatially randomly distributed discontinuous fibers and its applications," *Composite Structures,* vol. 131, pp. 366–373, 2015.

[68] A. Donev, S. Torquato, and F. H. Stillinger, "Neighbor list collision-driven molecular dynamics simulation for nonspherical hard particles. I. Algorithmic details," *Journal of computational physics,* vol. 202, no. 2, pp. 737–764, 2005.

[69] G. Li, F. Sharifpour, A. Bahmani, and J. Montesano, "A new approach to rapidly generate random periodic representative volume elements for microstructural assessment of high volume fraction composites," *Materials & Design,* vol. 150, pp. 124–138, 2018.

[70] B. D. Lubachevsky, "How to simulate billiards and similar systems," *Journal of Computational Physics,* vol. 94, no. 2, pp. 255–283, 1991.

[71] B. D. Lubachevsky, F. H. Stillinger, and E. N. Pinson, "Disks vs. spheres: Contrasting properties of random packings," *Journal of Statistical Physics,* vol. 64, pp. 501–524, 1991.

[72] W. Tian, X. Chao, M. Fu, and L. Qi, "An algorithm for generation of RVEs of composites with high particle volume fractions," *Composites Science and Technology,* vol. 207, p. 108714, 2021.

[73] A. Couture, V. François, J.-C. Cuillière, and P. Pilvin, "Automatic generation of statistical volume elements using multibody dynamics and an erosion-based homogenization method," *Computational Mechanics,* vol. 69, no. 4, pp. 1041–1066, 2022.

[74] A. Couture, "Automatisation de la modélisation numérique des microstructures de matériaux hétérogènes basée sur une intégration CAO-calcul," Doctoral dissertation, Université de Bretagne Sud; Université du Québec à Trois-Rivières, 2019.

[75] J.-C. Cuillière, *Introduction à la méthode des éléments finis-2e éd: Cours et exercices corrigés*. Dunod, 2023.

[76] S. Bargmann, B. Klusemann, J. Markmann, J. E. Schnabel, K. Schneider, C. Soyarslan, and J. Wilmers, "Generation of 3D representative volume elements for heterogeneous materials: A review," *Progress in Materials Science,* vol. 96, pp. 322–384, 2018.

[77] S. Kari, H. Berger, R. Rodriguez-Ramos, and U. Gabbert, "Computational evaluation of effective material properties of composites reinforced by randomly distributed spherical particles," *Composite structures,* vol. 77, no. 2, pp. 223–231, 2007.

[78] H. J. Böhm and A. Rasool, "Effects of particle shape on the thermoelastoplastic behavior of particle reinforced composites," *International Journal of Solids and Structures,* vol. 87, pp. 90–101, 2016.

[79] A. Rasool and H. J. Böhm, "Effects of particle shape on the macroscopic and microscopic linear behaviors of particle reinforced composites," *International Journal of Engineering Science,* vol. 58, pp. 21–34, 2012.

[80] A. El Moumen, T. Kanit, A. Imad, and H. El Minor, "Effect of reinforcement shape on physical properties and representative volume element of particles-reinforced composites: statistical and numerical approaches," *Mechanics of materials,* vol. 83, pp. 1–16, 2015.

[81] G. E. Rani, R. Murugeswari, S. Siengchin, N. Rajini, and M. A. Kumar, "Quantitative assessment of particle dispersion in polymeric composites and its effect on mechanical properties," *Journal of Materials Research and Technology,* vol. 19, pp. 1836–1845, 2022.

[82] J.-H. Yun, Y.-J. Jeon, and M.-S. Kang, "Numerical investigation of the elastic properties of polypropylene/ultra high molecular weight polyethylene fiber inside a composite material based on its aspect ratio and volume fraction," *Polymers,* vol. 14, no. 22, p. 4851, 2022.

[83] S. Siraj, A. H. Al-Marzouqi, M. Z. Iqbal, and W. Ahmed, "Impact of micro silica filler particle size on mechanical properties of polymeric based composite material," *Polymers,* vol. 14, no. 22, p. 4830, 2022.

[84] W. Tian, L. Qi, C. Su, J. Liang, and J. Zhou, "Numerical evaluation on mechanical properties of short-fiber-reinforced metal matrix composites: Two-step mean-field homogenization procedure," *Composite Structures,* vol. 139, pp. 96–103, 2016.

[85] I. Ezzaraa, N. Ayrilmis, M. Abouelmajd, M. K. Kuzman, A. Bahlaoui, I. Arroub, J. Bengourram, M. Lagache, and S. Belhouideg, "Numerical modeling based on finite element analysis of 3D-printed wood-polylactic acid composites: a comparison with experimental data," *Forests,* vol. 14, no. 1, p. 95, 2023.

[86] A. Kouassi, R. M. Boumbimba, M. Sangaré, Y. Koutsawa, A. Benelfellah, and V. Demais, "Dispersion and morphology analysis of PMMA/organoclay nanocomposites using the Ripley functions and determination of effective elastic properties," *Composite Structures,* vol. 312, p. 116881, 2023.

[87] N. Wolfsgruber, A. Tanda, V. M. Archodoulaki, and C. Burgstaller, "Influence of filler type and content on thermal conductivity and mechanical properties of thermoplastic compounds," *Polymer Engineering & Science,* vol. 63, no. 4, pp. 1094–1105, 2023.

[88] G. Afshar, A. Couture, V. François, J.-C. Cuillière, and É. Bourdier, "Modélisation de la microstructure de composites particulaires à haute teneur en fibres," in *16ème Colloque National en Calcul de Structures*, 2024.

[89] G. Foucault, J.-C. Cuillière, V. François, J.-C. Léon, and R. Maranzana, "Adaptation of CAD model topology for finite element analysis," *Computer-Aided Design,* vol. 40, no. 2, pp. 176–196, 2008.

[90] J.-C. Cuillière, S. Bournival, and V. François, "Contribution à l'automatisation des analyses par éléments-finis multidimensionnelles," *Mechanics & Industry,* vol. 12, no. 6, pp. 513–531, 2011.

[91] V. François and J.-C. Cuillière, "Automatic mesh pre-optimization based on the geometric discretization error," *Advances in Engineering Software,* vol. 31, no. 10, pp. 763–774, 2000.

[92] V. François and J.-C. Cuilliere, "3D automatic remeshing applied to model modification," *Computer-Aided Design,* vol. 32, no. 7, pp. 433–444, 2000.

[93] P. J. Frey and P.-L. George, "Mesh Generation: Application to Finite Elements." ISTE Ltd., 2008, ch. 19.

[94] G. Afshar, A. Couture, J.-C. Cuillière, and V. François, "Modeling the microstructure of a heterogeneous particle-based material with high-volume fraction," *Computational Mechanics,* pp. 1–18, 2025.

[95] S. D. Porumbescu, B. Budge, L. Feng, and K. I. Joy, "Shell maps," *ACM Transactions on Graphics (TOG),* vol. 24, no. 3, pp. 626–633, 2005.

[96] K. Erleben, H. Dohlmann, and J. Sporring, "The adaptive thin shell tetrahedral mesh," 2005.

[97] P. Areias and T. Rabczuk, "Steiner-point free edge cutting of tetrahedral meshes with applications in fracture," *Finite Elements in Analysis and Design,* vol. 132, pp. 27–41, 2017.

[98] C. P. Chrono. "An open source framework for the physicsbased simulation of dynamic systems." https://projectchrono.org/ (accessed.

[99] K. Terada, M. Hori, T. Kyoya, and N. Kikuchi, "Simulation of the multi-scale convergence in computational homogenization approaches," *International Journal of Solids and Structures,* vol. 37, no. 16, pp. 2285–2311, 2000.

[100] F. Larsson, K. Runesson, S. Saroukhani, and R. Vafadari, "Computational homogenization based on a weak format of micro-periodicity for RVE-problems," *Computer methods in applied mechanics and engineering,* vol. 200, no. 1-4, pp. 11–26, 2011.

[101] W. Tian, L. Qi, X. Chao, J. Liang, and M. Fu, "Periodic boundary condition and its numerical implementation algorithm for the evaluation of effective mechanical properties of the composites with complicated micro-structures," *Composites Part B: Engineering,* vol. 162, pp. 1–10, 2019.

[102] K. Schneider, B. Klusemann, and S. Bargmann, "Fully periodic RVEs for technological relevant composites: not worth the effort!," *Journal of mechanics of materials and structures,* vol. 12, no. 4, pp. 471–484, 2017.

[103] S. R. Mousavi, S. Estaji, A. Paydayesh, M. Arjmand, S. H. Jafari, S. Nouranian, and H. A. Khonakdar, "A review of recent progress in improving the fracture toughness of epoxy-based composites using carbonaceous nanofillers," *Polymer Composites,* vol. 43, no. 4, pp. 1871–1886, 2022.

[104] M. Y. Khalid, A. Al Rashid, Z. U. Arif, W. Ahmed, H. Arshad, and A. A. Zaidi, "Natural fiber reinforced composites: Sustainable materials for emerging applications," *Results in Engineering,* vol. 11, p. 100263, 2021.

[105] S. R. Mousavi, M. H. Zamani, S. Estaji, M. I. Tayouri, M. Arjmand, S. H. Jafari, S. Nouranian, and H. A. Khonakdar, "Mechanical properties of bamboo fiber-reinforced polymer composites: a review of recent case studies," *Journal of Materials Science,* vol. 57, no. 5, pp. 3143–3167, 2022.

[106] A. Koffi, F. Mijiyawa, D. Koffi, F. Erchiqui, and L. Toubal, "Mechanical properties, wettability and thermal degradation of HDPE/birch fiber composite," *Polymers,* vol. 13, no. 9, p. 1459, 2021.

[107] A. Koffi, D. Koffi, and L. Toubal, "Mechanical properties and drop-weight impact performance of injection-molded HDPE/birch fiber composites," *Polymer Testing,* vol. 93, p. 106956, 2021.